

ABSTRACT

MICHAELIS, ALLISON CLAIRE. Climate Change Effects on the Extratropical Transition of Tropical Cyclones in High-Resolution Global Simulations. (Under the direction of Dr. Gary M. Lackmann).

Tropical cyclones (TCs) undergoing extratropical transition (ET) can develop into intense cyclonic systems that bring high-impact weather to areas far removed from the original TC. While previous research has looked extensively at the ET process and climate change effects on TCs, the question of how climate change may affect ET has received considerably less attention. Here, we examine multi-seasonal global simulations representative of present-day and projected future thermodynamic environments using the Model for Prediction Across Scales-Atmosphere (MPAS) with high-resolution (15 km) throughout the Northern Hemisphere. We simulate ten years with varying phases of El Niño-Southern Oscillation (ENSO) using analyzed sea surface temperature (SST) patterns. Additionally, we created daily sea ice fields from climatological monthly-mean sea ice. Akin to pseudo-global warming methods, we apply changes from an ensemble of general circulation models (GCMs) to the SSTs and other fields for counterpart future simulations. We use TempestExtremes to track TCs as minima in sea-level pressure (SLP) with additional criteria to ensure a warm core structure. Next, we utilize the ExTraTrack ET tracker to continue TC trajectories into the extratropical phase based on local minima in SLP and identify ET events using the cyclone phase space (CPS). Our present-day simulations provide a reasonable reproduction of large-scale atmospheric features in the Northern Hemisphere such as the wintertime midlatitude storm tracks and annual precipitation patterns across the United States and the tropics. The simulations also adequately represent present-day TC and ET characteristics such as strength, location, and seasonal cycles for most Northern Hemispheric basins. The most significant changes in future ET events occur in the North Atlantic (NATL) basin. Here, a more favorable background environment, shift towards stronger TC warm cores, and a significant poleward shift in the latitude of TC genesis and location of peak intensity lead to a higher fraction of TCs undergoing ET; there is a ~40% increase in the number of NATL ET events while the fraction of TCs undergoing ET increases ~6%. Additionally, ET in the NATL occurs significantly farther north by ~4.5–5°N, and the resultant extratropical cyclones are significantly stronger; the median minimum SLP at this stage is ~6-hPa lower in the future simulations. Storm-relative composites of anomalous 500-hPa heights for NATL ET events show that this

increase in post-transition storm intensity is due to a strengthening of the upper-level trough and poleward shift in the storm center, which allows for strengthened trough-TC interactions after ET completion. Localized impacts associated with ET events, such as precipitation and near-surface wind speed, are also significantly more intense in the future ET events; 6-hourly precipitation for NATL events increases at a super-Clausius-Clapeyron rate. Furthermore, enhanced precipitation contributes to both enhanced lower-tropospheric potential vorticity (PV) and stronger upper-tropospheric outflow, which holds implications for more extreme impacts farther downstream.

Climate Change Effects on the Extratropical Transition of Tropical Cyclones in High-Resolution
Global Simulations

by
Allison Claire Michaelis

A dissertation submitted to the Graduate Faculty of
North Carolina State University
in partial fulfillment of the
requirements for the degree of
Doctor of Philosophy

Marine, Earth, and Atmospheric Sciences

Raleigh, North Carolina
2019

APPROVED BY:

Gary M. Lackmann
Committee Chair

Walter A. Robinson

Anantha Aiyyer

Kirankumar Alapaty

BIOGRAPHY

Allison was born and raised in Greensboro, NC. She has always been intrigued by weather for two reasons: (1) the Superstorm of 1993 brought several inches of snow to her hometown on her 4th birthday and (2) she has always been frightened by thunderstorms. In the fall of 2007, she came to Raleigh, NC to attend North Carolina State University (NCSU). After graduating Summa Cum Laude with undergraduate degrees in Mathematics and Meteorology, she continued at NCSU to pursue her master's in Atmospheric Science. As a master's student, Allison studied climate change effects on North Atlantic extratropical cyclones under the advisement of Dr. Gary Lackmann. Upon completion of her degree in May 2015, Allison completed an internship at the Environmental Protection Agency (EPA) before returning to NCSU once again to pursue her PhD with Dr. Gary Lackmann studying the extratropical transition of tropical cyclones in the context of climate change. During her master's and PhD studies, Allison worked as a teaching assistant for several introductory meteorology courses, solidifying her passion for teaching. Upon leaving NCSU, Allison will join the Center for Western Weather and Water Extremes in La Jolla, CA as postdoctoral scholar, after which she will pursue a career in academia.

ACKNOWLEDGMENTS

I would like to first thank my advisor, Dr. Gary Lackmann, for providing me with this research opportunity. I am extremely grateful for his immeasurable mentorship, support, and encouragement throughout the course of my graduate career. Special thanks are also extended to my committee member, Dr. Walt Robinson, for his extensive guidance throughout this research process. Additionally, I would like to thank my committee members, Dr. Anantha Aiyyer and Dr. Kiran Alapaty, for their valuable feedback contributing to the integrity and completion of this work.

This research was supported by the National Science Foundation (NSF) under grants AGS-1546743 and AGS-1560844, awarded to North Carolina State University (NCSSU). The Model for Prediction Across Scales (MPAS) and NCAR Command Language (NCL) used extensively in this research are made available by the National Center for Atmospheric Research (NCAR), sponsored by the NSF. High-performance computing support from Cheyenne (doi:10.5065/D6RX99HX) was provided by NCAR's Computational and Information System Laboratory, also sponsored by the NSF. Custom MPAS grid and additional MPAS support was provided by Michael Duda at NCAR. CMIP5 General Circulation Model (GCM) data is provided by the Program for Climate Model Diagnosis and Intercomparison (PCMDI). Additional thanks to Chunyong Jung at NCSU for creation of the CMIP5 GCM ensemble mean data and interpolation codes used in this study, and to Colin Zarzycki at Penn State University for the availability of and assistance on the tracking codes used in this research.

A big thank you to my current and past lab mates Ana Torres-Vasquez, Rebecca Miller, Jacob Radford, Chunyong Jung, Chris Marciano, Jennifer Tate, and Lindsay Blank who have been valuable sources of knowledge, advice, and support throughout this process. To Rowan Argent, Sofia Montalvo, Nicole Hoban, Rachel Atkins, Alex Gizzi, Michael Angus, and Keith Sherburn: thank you for your immense amount of friendship and support over the years. I am a better person for having you all in my life, and would not have gotten through this without each of you. To Dr. Sandra Yuter, I am tremendously lucky to call you my mentor and friend, thank you for your constant support and encouragement.

Last, I would like to thank my parents and step-mom, Sharon, Larry, and Sherry, brother, Benjamin, and numerous other family members for their continuous support through every step of college, graduate school, and life in general. I, literally and figuratively, would not be where I

am without you. An enormous thank you goes to my brilliant and talented husband, Tim, for his unwavering confidence throughout this process. Finally, I extend a special thank you to Kitty, who, over her 19 years of life, taught me the importance of curiosity, self-care, and always landing on your feet.

TABLE OF CONTENTS

LIST OF TABLES	viii
LIST OF FIGURES	xii
1. Introduction.....	1
1.1. Motivation	1
1.2. Synthesis of Prior Research.....	2
1.2.1. Extratropical Transition of Tropical Cyclones	2
1.2.1.1. Detection of Extratropical Transition.....	2
1.2.1.2. Transition and Reintensification Pathways	3
1.2.1.3. Northern Hemisphere Climatology of Extratropical Transition.....	5
1.2.2. Impacts of Climate Change.....	6
1.2.2.1. Tropical Cyclone Intensity	7
1.2.2.2. Sea Surface Temperatures	7
1.2.2.3. Upper-level Forcing	8
1.3. Science Questions and Hypotheses	9
2. Methods.....	11
2.1. Model Simulations	11
2.1.1. Model Configuration.....	12
2.1.2. Present-day and Future Climate Simulations.....	13
2.1.3. Surface Fields.....	14
2.1.4. Climate Change Representation.....	16
2.2. Tropical Cyclone Tracking.....	16
2.3. Detection of Extratropical Transition Events	17
2.3.1. Example Events	19
2.4. Storm-relative Composites	21
2.5. Assumptions and Limitations	22
3. Model Present-day Climatology	36
3.1. Precipitation and Midlatitude Features.....	36
3.1.1. Extratropical Storm Tracks	36
3.1.2. Large-scale Precipitation	37
3.1.3. CONUS Precipitation.....	37

3.2. Tropical Cyclones	38
3.2.1. Strength	38
3.2.2. Location	39
3.2.3. Seasonal Cycle	39
3.3. Extratropical Transition.....	40
3.3.1. Frequency and Seasonal Cycle	41
3.3.2. Location of ET	42
4. Present-day to Future Changes: Extratropical Transition Climatology	58
4.1. Background Environment.....	58
4.1.1. 850–200-hPa Vertical Wind Shear	58
4.1.2. 700-hPa Eady Growth Rate and Maximum Potential Intensity	60
4.2. Frequency and Seasonality	62
4.3. Location.....	63
4.4. Duration and Intensity	66
4.5. Cyclone Phase Space.....	67
4.6. Summary	68
5. Present-day to Future Changes: Storm-scale Dynamics.....	89
5.1. North Atlantic Basin.....	89
5.1.1. Overview of the Extratropical Transition Process	89
5.1.2. Statistical Changes	90
5.1.2.1. Intensity	90
5.1.2.2. Cyclone Phase Space.....	91
5.1.2.3. Duration.....	91
5.1.3. Dynamical Changes	91
5.1.3.1. Upstream Trough and Downstream Ridge	92
5.1.3.2. Tropical Cyclone Characteristics	93
5.1.3.3. Impacts	94
5.2. Western North Pacific Basin	95
5.2.1. Overview of the Extratropical Transition Process	95
5.2.2. Statistical Changes	96
5.2.2.1. Intensity	96

5.2.2.2. Cyclone Phase Space.....	96
5.2.2.3. Duration.....	97
5.2.3. Dynamical Changes	97
5.2.3.1. Upstream Trough and Downstream Ridge	97
5.2.3.2. Tropical Cyclone Characteristics	97
5.2.3.3. Impacts	98
5.3. Summary	98
6. Summary and Conclusions	138
REFERENCES.....	143

LIST OF TABLES

Table 2.1	Average Multivariate ENSO Index (MEI), Oceanic Niño Index (ONI), and corresponding ENSO phase during the tropical cyclone season (June–November) for the chosen simulation years.....	24
Table 2.2	List of 20 CMIP5 GCMs used to compute ensemble mean temperature “deltas” and sea ice fields	25
Table 2.3	TempestExtremes parameter choices.....	26
Table 3.1	Number of TCs, ET events, and percent of TCs that undergo transition in the North Atlantic and Western North Pacific basins over the 10 simulations years for IBTrACS and present-day MPAS simulations. The percent transition range of internal variability for IBTrACS is determined by calculating the percent of transitioning TCs for 100 10-yr samples.....	44
Table 3.2	Median latitude (°N) and longitude (°E) of ET for TCs that undergo transition in the North Atlantic and Western North Pacific basins over the 10 simulations years for IBTrACS and present-day MPAS simulations.....	44
Table 4.1	TC and ET frequency statistics over the ten simulation years for present-day and future simulations.....	70
Table 4.2	Median location of ET onset and completion. p-values are reported from the Wilcoxon Rank Sum statistical significance test. Italicized (bold) values indicate statistical significance at the 90% (95%) confidence level.....	70
Table 4.3	Median location of TC genesis and peak tropical intensity. p-values are reported from the Wilcoxon Rank Sum statistical significance test. Italicized (bold) values indicate statistical significance at the 90% (95%) confidence level.....	71
Table 4.4	Median duration (hrs) of various stages of the cyclone life cycle. p-values are reported from the Wilcoxon Rank Sum statistical significance test. Italicized (bold) values indicate statistical significance at the 90% (95%) confidence level.....	71
Table 4.5	Percentage of ET events that undergo slow and fast transition	72
Table 4.6	Median intensity (SLP; hPa) at various stages of the cyclone life cycle. p-values are reported from the Wilcoxon Rank Sum statistical significance test. Italicized (bold) values indicate statistical significance at the 90% (95%) confidence level	72
Table 4.7	Median intensity (SLP) change rate (hPa/6-h) between each stage of the	

	cyclone life cycle. p-values are reported from the Wilcoxon Rank Sum statistical significance test. Italicized (bold) values indicate statistical significance at the 90% (95%) confidence level.....	73
Table 4.8	Percentage of ET events that strengthen and weaken after completing ET	73
Table 5.1	Median intensity (SLP; hPa) at various stages of the cyclone life cycle for composited NATL ET events. p-values are reported from the Wilcoxon Rank Sum statistical significance test. Italicized (bold) values indicate statistical significance at the 90% (95%) confidence level.....	101
Table 5.2	Median duration (hrs) of various stages of the cyclone life cycle for composited NATL ET events. p-values are reported from the Wilcoxon Rank Sum statistical significance test. Italicized (bold) values indicate statistical significance at the 90% (95%) confidence level.....	101
Table 5.3	Absolute and percent changes in average and maximum positive and negative 500-hPa height anomaly values over the full composite area for NATL composite ET events. Changes for trough (ridge) calculated using all grid points to the west (east) of the storm center with negative (positive) values. Average and maximum values reported rounded to the nearest whole number. Percent change values computed using unrounded values, then reported rounded to the nearest whole percent	102
Table 5.4	Absolute and percent changes in average and maximum positive and negative θ'_{DT} values over the full composite area for NATL composite ET events. Changes for trough (ridge) calculated using all grid points to the west (east) of the storm center with negative (positive) values. Average and maximum values reported rounded to the nearest whole number. Percent change values computed using unrounded values, then reported rounded to the nearest whole percent.....	103
Table 5.5	Absolute and percent changes in average and maximum 900–700-hPa PV values over the composite area within 5° of the storm center for NATL composite ET events. Average and maximum values reported rounded to the nearest whole number. Percent change values computed using unrounded values, then reported rounded to the nearest whole percent	104
Table 5.6	Absolute and percent changes in average and maximum θ'_{2-m} values over the composite area within 5° of the storm center for NATL composite ET events. Average and maximum values reported rounded to the nearest whole number. Percent change values computed using unrounded values, then reported rounded to the nearest whole percent	105
Table 5.7	Absolute and percent changes in average and maximum 6-hourly precipitation values over the composite area within 10° of the storm center	

for NATL composite ET events. Average and maximum values reported rounded to the nearest whole number. Percent change values computed using unrounded values, then reported rounded to the nearest whole percent .. 106

Table 5.8 Absolute and percent changes in average and maximum 10-m wind speed values over the composite area within 10° of the storm center for NATL composite ET events. Average and maximum values reported rounded to the nearest whole number. Percent change values computed using unrounded values, then reported rounded to the nearest whole percent 107

Table 5.9 Median intensity (SLP; hPa) at various stages of the cyclone life cycle for composited WNP ET events. p-values are reported from the Wilcoxon Rank Sum statistical significance test. Italicized (bold) values indicate statistical significance at the 90% (95%) confidence level..... 108

Table 5.10 Median duration (hrs) of various stages of the cyclone life cycle for composited NATL ET events. p-values are reported from the Wilcoxon Rank Sum statistical significance test. Italicized (bold) values indicate statistical significance at the 90% (95%) confidence level..... 108

Table 5.11 Absolute and percent changes in average and maximum positive and negative 500-hPa height anomaly values over the full composite area for WNP composite ET events. Changes for trough (ridge) calculated using all grid points to the west (east) of the storm center with negative (positive) values. Average and maximum values reported rounded to the nearest whole number. Percent change values computed using unrounded values, then reported rounded to the nearest whole percent 109

Table 5.12 Absolute and percent changes in average and maximum positive and negative θ'_{DT} values over the full composite area for WNP composite ET events. Changes for trough (ridge) calculated using all grid points to the west (east) of the storm center with negative (positive) values. Average and maximum values reported rounded to the nearest whole number. Percent change values computed using unrounded values, then reported rounded to the nearest whole percent 110

Table 5.13 Absolute and percent changes in average and maximum 900–700-hPa PV values over the composite area within 5° of the storm center for WNP composite ET events. Average and maximum values reported rounded to the nearest whole number. Percent change values computed using unrounded values, then reported rounded to the nearest whole percent 111

Table 5.14 Absolute and percent changes in average and maximum θ'_{2-m} values over the composite area within 5° of the storm center for WNP composite ET events. Average and maximum values reported rounded to the nearest whole number. Percent change values computed using

unrounded values, then reported rounded to the nearest whole percent 112

Table 5.15 Absolute and percent changes in average and maximum 6-hourly precipitation values over the composite area within 10° of the storm center for WNP composite ET events. Average and maximum values reported rounded to the nearest whole number. Percent change values computed using unrounded values, then reported rounded to the nearest whole percent 113

Table 5.16 Absolute and percent changes in average and maximum 10-m wind speed values over the composite area within 10° of the storm center for WNP composite ET events. Average and maximum values reported rounded to the nearest whole number. Percent change values computed using unrounded values, then reported rounded to the nearest whole percent 114

LIST OF FIGURES

Figure 2.1	Variable resolution mesh and tropical cyclone basins	27
Figure 2.2	Example SST and sea ice fields	28
Figure 2.3	Difference in average annual 2-m temperature and zonal mean temperature between MPAS simulations and CMIP5 GCM ensemble mean	29
Figure 2.4	Overview of the cyclone phase space diagrams	30
Figure 2.5	Overview of an example ET event.....	31
Figure 2.6	Overview of an example partial ET event	32
Figure 2.7	Overview of an example subtropical event.....	33
Figure 2.8	Overview of an example tropical event	34
Figure 2.9	500-hPa height anomaly and SLP for the reference ET case.....	35
Figure 3.1	Average wintertime SLP variance for present-day MPAS simulations vs. ERA-I climatology	45
Figure 3.2	Average total annual precipitation for present-day MPAS simulations vs. TRMM climatology	46
Figure 3.3	Average summertime 700-hPa zonal wind speed for present-day MPAS simulations vs. ERA-I climatology.....	47
Figure 3.4	Average total precipitation for present-day MPAS simulations vs. PRISM climatology	48
Figure 3.5	Maximum 10-m wind speed vs. minimum SLP for observed and simulated TCs	49
Figure 3.6	Average number of observed and simulated TCs for the Northern Hemisphere and each Northern Hemisphere basin.....	50
Figure 3.7	TC track density for present-day MPAS simulations vs. IBTrACS	51
Figure 3.8	TC track density and 850–200-hPa vertical wind shear for present-day MPAS simulations vs. IBTrACS and ERA-I.....	52
Figure 3.9	Monthly average TC frequency for present-day MPAS simulations vs. IBTrACS	53

Figure 3.10	Average zonal wind anomalies at 850-hPa and 500-hPa for present-day MPAS simulations vs. ERA-I climatology	54
Figure 3.11	Total number of TCs, ET events, and ET percentage per month for present-day MPAS simulations vs. IBTrACS	55
Figure 3.12	Trajectories for all ET events for the present-day MPAS simulations vs. IBTrACS	56
Figure 3.13	Boxplots of ET location for present-day MPAS simulations vs. IBTrACS	57
Figure 4.1	Monthly averaged 850–200-hPa vertical wind shear for present-day vs. future simulations.....	74
Figure 4.2	Monthly averaged SST for present-day vs. future simulations.....	75
Figure 4.3	Monthly average 700-hPa Eady growth rate and MPI for present-day vs. future simulations.....	76
Figure 4.4	Monthly average MPI for present-day vs. future simulations	77
Figure 4.5	Monthly average TC and ET frequency and ET percentage for present-day vs. future simulations	78
Figure 4.6	Non-ET and ET track density for present-day vs. future simulations	79
Figure 4.7	Trajectories of ET events for present-day vs. future simulations	80
Figure 4.8	ET onset and completion density for present-day vs. future simulations	81
Figure 4.9	Boxplots of ET location for present-day vs. future simulations	82
Figure 4.10	Boxplots of TC genesis and maximum lifetime intensity location for present-day vs. future simulations	83
Figure 4.11	Boxplots of TC, ET, and total durations for present-day vs. future simulations	84
Figure 4.12	Boxplots of minimum SLP at various stages of the cyclone lifecycle for present-day vs. future simulations	85
Figure 4.13	Boxplots of SLP change rate between various stages of the cyclone lifecycle for present-day vs. future simulations.....	86
Figure 4.14	Cyclone phase space frequency diagrams for present-day vs. future NATL ET events	87

Figure 4.15	Cyclone phase space frequency diagrams for present-day vs. future WNP ET events	88
Figure 5.1	500-hPa height, SLP, and 850-hPa temperature showing an overview of the ET process for present-day and future NATL composite events.....	115
Figure 5.2	Time series of minimum SLP for present-day and future NATL composite ET events	116
Figure 5.3	Boxplots of minimum SLP at various stages of the cyclone lifecycle for present-day vs. future NATL composite ET events.....	117
Figure 5.4	Cyclone phase space frequency diagrams for present-day vs. future NATL composite ET events.....	118
Figure 5.5	Boxplots of TC and ET durations for present-day vs. future NATL composite ET events.....	119
Figure 5.6	500-hPa height anomaly for present-day vs. future NATL composite ET events at 24-h prior to ET onset, 12-h prior to ET onset, ET onset, ET completion, and 12-h after ET completion	120
Figure 5.7	Potential temperature anomaly and winds on the dynamic tropopause for present-day vs. future NATL composite ET events at 24-h prior to ET onset, 12-h prior to ET onset, ET onset, ET completion, and 12-h after ET completion.....	121
Figure 5.8	900–700-hPa layer average PV and SLP for present-day vs. future NATL composite ET events at 24-h prior to ET onset, 12-h prior to ET onset, ET onset, ET completion, and 12-h after ET completion.....	122
Figure 5.9	Vertical cross-section of PV for present-day vs. future NATL composite ET events at 24-h prior to ET onset, 12-h prior to ET onset, ET onset, ET completion, and 12-h after ET completion	123
Figure 5.10	θ'_{2-m} for present-day vs. future NATL composite ET events at 24-h prior to ET onset, 12-h prior to ET onset, ET onset, ET completion, and 12-h after ET completion	124
Figure 5.11	6-hourly precipitation and 10-m winds for present-day vs. future NATL composite ET events at 24-h prior to ET onset, 12-h prior to ET onset, ET onset, ET completion, and 12-h after ET completion.....	125
Figure 5.12	250-hPa wind speed for present-day vs. future NATL composite ET events at 24-h prior to ET onset, 12-h prior to ET onset, ET onset, ET completion, and 12-h after ET completion	126

Figure 5.13	500-hPa height, SLP, and 850-hPa temperature showing an overview of the ET process for present-day and future WNP composite events.....	127
Figure 5.14	Time series of minimum SLP for present-day and future WNP composite ET events	128
Figure 5.15	Boxplots of minimum SLP at various stages of the cyclone lifecycle for present-day vs. future WNP composite ET events	129
Figure 5.16	Cyclone phase space frequency diagrams for present-day vs. future WNP composite ET events	130
Figure 5.17	Boxplots of TC and ET durations for present-day vs. future WNP composite ET events	131
Figure 5.18	500-hPa height anomaly for present-day vs. future WNP composite ET events at 24-h prior to ET onset, 12-h prior to ET onset, ET onset, ET completion, and 12-h after ET completion	132
Figure 5.19	Potential temperature anomaly and winds on the dynamic tropopause for present-day vs. future WNP composite ET events at 24-h prior to ET onset, 12-h prior to ET onset, ET onset, ET completion, and 12-h after ET completion.....	133
Figure 5.20	900–700-hPa layer average PV and SLP for present-day vs. future WNP composite ET events at 24-h prior to ET onset, 12-h prior to ET onset, ET onset, ET completion, and 12-h after ET completion.....	134
Figure 5.21	Vertical cross-section of PV for present-day vs. future WNP composite ET events at 24-h prior to ET onset, 12-h prior to ET onset, ET onset, ET completion, and 12-h after ET completion	135
Figure 5.22	θ'_{2-m} for present-day vs. future WNP composite ET events at 24-h prior to ET onset, 12-h prior to ET onset, ET onset, ET completion, and 12-h after ET completion	136
Figure 5.23	6-hourly precipitation and 10-m winds for present-day vs. future WNP composite ET events at 24-h prior to ET onset, 12-h prior to ET onset, ET onset, ET completion, and 12-h after ET completion.....	137

1. Introduction

1.1. Motivation

The extratropical transition (ET) of tropical cyclones (TCs) occurs when a tropical cyclone translates into the midlatitudes, interacts with midlatitude features, such as an upper-level trough or extratropical cyclone (ETC), and undergoes a transformation from a symmetric, warm-core tropical system to an asymmetric, cold-core extratropical system (e.g., Jones et al. 2003). This process can induce modifications to the TC itself, such as expanded asymmetric distributions of wind and precipitation, which allow the system to impact a wider area as it transitions. TCs undergoing ET can develop into intense cyclonic systems that bring TC-like conditions (e.g., intense rainfall, strong winds, large waves) to areas far removed from the original TC (Malmquist 1999; Jones et al. 2003; Kitabatake 2011). Additional hazards associated with ET events include inland flooding, wind-induced wildfires, and sinking of ships (Arnott et al. 2004 and references therein). Transoceanic shipping routes in late summer and early autumn often shift poleward to benefit from shorter routes, calmer conditions, and avoidance of TCs; however, TCs that recurve poleward into these regions and undergo ET can pose serious threats (Harr and Elsberry 2000). Major cities such as Washington, D.C., New York, NY, and Boston, MA experience an ET event every two to four years; Western Europe is affected by an ET event every two years (Hart and Evans 2001). Recent examples of such events that affected the U.S. include Irene (2011) and Sandy (2012); the latter resulted in 2-m (~6.5-ft) of storm surge and over 900-mm (~3-ft) of snow across the northeast U.S. (Evans et al. 2017 and references therein). Additionally, these events can be associated with negative impacts on predictability on hemispheric scales, owing to downstream development of Rossby wave energy; the outflow from recurving or transitioning TCs can modify midlatitude flow and lead to high-impact weather events, such as cold-air outbreaks or heavy precipitation, downstream of the original TC (e.g., Harr and Dea 2009; Archambault et al. 2013; Archambault et al. 2015; Keller et al. 2018).

While previous research has looked extensively at the ET process and climate change effects on tropical cyclones, relatively few studies have looked into how ET events may be affected by climate change (Evans et al. 2017). Prior studies have hypothesized that warmer sea surface temperatures (SSTs) and a projected eastward extension of the North Atlantic hurricane development region could allow ET events to affect Western Europe more frequently in the future (Baatsen et al. 2015). Furthermore, TCs that undergo ET could have a higher chance of

regaining hurricane force winds in a future climate due to projected increases in moisture and subsequent latent heat release (Haarsma et al. 2013). ET events can produce devastating storm surges along coastlines, but research is lacking in how climate change will affect these hybrid events and subsequent impacts along the US East Coast (Colle et al. 2015; Booth et al. 2016). To fully realize the future impacts of these storms, we need to understand the how the location, frequency, transition periods, and the intensity of the ET events may change under future climate conditions, thus defining the goal of this dissertation research.

1.2. Synthesis of Prior Research

1.2.1. Extratropical Transition of Tropical Cyclones

The extratropical transition of tropical cyclones can be described as the process by which a system's existing tropical structure is replaced by a baroclinic structure (e.g., Arnott et al. 2004; Kofron et al. 2010b; Kitabatake 2011; Wood and Ritchie 2014). The environmental changes experienced by a TC during the transition process typically include increased baroclinicity, cooler SSTs, stronger SST gradients, and/or interactions with existing midlatitude troughs or cyclones (e.g., Jones et al. 2003; Kofron et al. 2010a). These environmental changes can produce structural modifications to the TC, such as loss of a symmetric inner core, expanded asymmetric distributions of wind and precipitation, and increased translation speeds (Klein et al. 2000; Jones et al. 2003; Wood and Ritchie 2014; Evans et al. 2017).

1.2.1.1. Detection of Extratropical Transition

Meteorological agencies, such as the National Hurricane Center (NHC) and the Japanese Meteorological Agency (JMA), typically declare the time of ET subjectively using SST data and satellite imagery to determine when the system begins to exhibit extratropical characteristics (Hart and Evans 2001; Kitabatake 2011). The shift in storm structure is most notably signified by a reduction in cloudiness and rainbands in the western quadrant of the storm, and the appearance of dry slots in rainbands in the southern quadrant, likely due to the equatorward advection of cold, dry air as the TC begins to interact with the baroclinic zone (Klein et al. 2000; Hart and Evans 2001; Kitabatake 2011). The reduced appearance of deep convection, disappearance of high-cloud canopy, exposure of the low-level circulation center, and development of a comma-shaped cloud pattern (i.e., frontal structure) are additional characteristics to consider when

subjectively detecting the transformation from a TC to an ETC using satellite imagery. Furthermore, an expansion of the radius of gale-force winds, appearance of asymmetric wind and precipitation fields, and cooler SSTs beneath TC can also indicate the system is undergoing transition (Jones et al. 2003). For example, Liu et al. (2017) showed that the rainfall distributions in TCs undergoing ET shift from a nearly circular distribution with the maximum to the right of the storm center to an asymmetric distribution with the majority of rainfall concentrated in the upper left quadrant.

Subjective identification techniques used, and records kept, by national centers, however, only include the declaration of ET once a system has fully undergone transition and thus, do not provide information on the timing between ET onset and completion, or what transition or reintensification pathway the storm took. Therefore, objective identification techniques, namely the cyclone phase space (CPS; Hart 2003) have become widely accepted methods for diagnosing ET (Evans et al. 2017) and are essential for analyzing ET using gridded datasets such as reanalyses or output from model simulations. The CPS uses geopotential height at various levels in the atmosphere to examine the symmetry of a cyclone along with the inner core temperature and strength; a symmetric, warm-core structure indicates a tropical system, and vice versa, an asymmetric, cold-core structure indicates an extratropical system. Furthermore, this method allows for visualization of how these parameters evolve over a storm's lifetime. Additional details regarding the calculation of CPS parameters are included in Section 2.3.

1.2.1.2. Transition and Reintensification Pathways

Previous research suggests that the majority of TCs begin the transition process in a similar manner; first there is a loss of symmetry, then a shallowing of the warm core before fully becoming a cold-core system (e.g., Hart et al. 2006). A wider variety of pathways, however, can occur during the post-transition or reintensification stages. Several known potential post-ET pathways include cold-core decay, cold-core intensification, warm-seclusion intensification, and non-ET events (Hart et al. 2006; Kofron et al. 2010a). Non-ET events include TCs that begin the ET process (e.g., begin to lose symmetry), but decay or merge with a pre-existing midlatitude cyclone before transition is completed, and those that undergo tropical transition back into a tropical cyclone (Harr and Elsberry 2000; Hart et al. 2006; Kofron et al. 2010a).

In some instances, the resultant extratropical cyclone from an ET event can reintensify into a storm that is stronger than the original TC (Kofron et al. 2010a). How the post-transition TC remnants interact with the midlatitude environment is thought to be a more important factor in determining whether or not the post-transition cyclone will reintensify compared to the strength of the original TC or pre-existing trough (Klein et al. 2002; Ritchie and Elsberry 2003; Hart et al. 2006; Ritchie and Elsberry 2007). For example, TCs in the Western North Pacific moving into a “northwest” synoptic pattern, defined when the primary pre-existing midlatitude trough or cyclone is located upstream of the TC remnants, were shown to be more likely to reintensify than “northeast” synoptic patterns, defined when the primary pre-existing midlatitude trough or cyclone is located downstream of the TC remnants (Harr and Elsberry 2000). Similarly, Klein et al. (2002) showed that if the upper-level outflow from the TC interacts appropriately with the upper jet, even a transitioning TC entering an otherwise unfavorable environment for cyclogenesis could still reintensify as an ETC. Additionally, the closer in proximity the TC remnants are to the pre-existing trough axis, the more likely reintensification is to occur (Hart et al. 2006; Ritchie and Elsberry 2007). More specifically, Ritchie and Elsberry (2007) found that TCs needed to be within 10-15° latitude of the trough axis in order to strongly or moderately intensify.

Two primary reintensification pathways are cold-core reintensification, also referred to as baroclinic reintensification, and warm-seclusion reintensification, also referred to as tropical reintensification (e.g., McTaggart-Cowan et al. 2003; McTaggart-Cowan et al. 2004; Hart et al. 2006; Kofron et al. 2010a). Baroclinic (cold-core) reintensification can occur when the TC remnants are positioned favorably in the right entrance region of the upper jet. Here, the west side of the system experiences cold advection, which helps break up the tropical convection in the southern quadrants, leading to the formation of frontal features (McTaggart-Cowan et al. 2003; McTaggart-Cowan et al. 2004). Warm-seclusion (tropical) reintensification cases are characterized by an elongated warm front and shallow warm core. While warm seclusion events typically form from cold-core cyclones, they can form during ET as the remnant TC warm core is incorporated into the system, and intrusion of dry air from the upper trough wraps around the system to form a shallow warm core (Baatsen et al. 2015). Additionally, if the TC remnants are located in the left exit region of the upper jet so that the east side of the system experiences enhanced warm advection, the storm’s environment can be preconditioned for warm-seclusion

reintensification. Furthermore, diabatic effects within the storm also lead to the formation, or enhancement, of a shallow warm core (Baatsen et al. 2015), which can aid in warm-seclusion intensification. Warm-seclusion reintensification cases exhibit a more rapid reintensification period and a more intense post-ET cyclone compared to the other reintensification cases (Kofron et al. 2010b). Because warm seclusion cyclones can result in severe storms, they are taken into particular consideration when evaluating future changes in European windstorms with a tropical origin (Maue 2010). In short, baroclinic (cold-core) reintensification is dominated by interactions between the upper trough and TC remnants, similar to Type-B cyclogenesis (Petterssen and Smebye 1971), while the enhanced diabatic processes during warm-seclusion (tropical) reintensification are more akin to Type-C cyclogenesis (Plant et al. 2003).

1.2.1.3. Northern Hemisphere Climatology of Extratropical Transition

Depending on the time period, dataset, and ET detection method, previous studies have found that, on average, 42–55% of TCs in the North Atlantic (NATL) basin, 5–23% of TCs in the Eastern North Pacific (ENP) basin, and 28–49% of TCs in the Western North Pacific (WNP) basin undergo extratropical transition (Klein et al. 2000; Hart and Evans 2001; Jones et al. 2003; Kitabatake 2011; Wood and Ritchie 2014; Zarzycki et al. 2017; Bieli et al. 2018, submitted). While the WNP tends to have the highest number of ET events, the NATL typically has the highest percentage of ET events (Jones et al. 2003). A subtropical ridge over southwest North America is the dominant upper-level pattern in the ENP region, which typically steers TCs westward into areas of cooler SSTs and stronger vertical wind shear, thus increasing the likelihood of dissipation before encountering an environment favorable for ET (Jones et al. 2003; Wood and Ritchie 2014). A possible explanation for why the highest percentage of ET events occurs in the NATL is that, on average, TCs reach peak warm-core structure 24-h prior to the start of ET, suggesting that once NATL TCs start to weaken, they only need to survive one more day before transition starts (Hart et al. 2006).

For the NATL, the number of ET events peaks in September, while the highest percentage of ET events occurs in the late fall (Hart and Evans 2001; Evans et al. 2017; Bieli et al. 2018, submitted). Hart and Evans (2001) discussed the relationship between “tropically favorable” regions, defined using the local maximum potential intensity (MPI) index, and “baroclinically favorable” regions, defined using the Eady growth rate (σ). The larger the

distance between these two regions, the longer a TC must survive in an unfavorable environment, thus lessening the chances for ET. These regions are in closest proximity to each other during the fall, which is why ET frequency tends to peak during this time in the NATL. The WNP shows a high percentage of ET events in both May and October (Kitabatake 2011; Bieli et al. 2018, submitted). The higher likelihood of ET during the fall in the WNP has been attributed to larger amounts of vertical wind shear and stronger air-sea temperature contrasts over the region during this time, which creates an environment that helps maintain the TC while also supporting its transition to an extratropical cyclone (Kitabatake 2011). As stated in Bieli et al. (2018, submitted), ET events in the ENP show no clear seasonal cycle due to the low frequency of events.

1.2.2. Impacts of Climate Change

To the author's knowledge, to date fewer than ten studies have examined climate change effects on ET (Evans et al. 2017). This is a complicated problem as it is affected by both changes in TCs (e.g., frequency, intensity, size) as well as changes in the midlatitude environment. Future climate simulations conducted by Liu et al. (2017) showed that warmer SSTs and reduced wind shear in the NATL tropical and subtropical regions create a more favorable environment for TC survival, allowing them to reach baroclinically favorable zones more often in the future, and resulting in a modestly significant increase in the percentage of ET events. Haarsma et al. (2013) and Baatsen et al. (2015) showed similar results in their future climate simulations; a projected increase in TC strength along with a poleward expansion and eastward shift of the NATL TC genesis region allow TCs to survive in the midlatitudes longer, thus increasing the frequency of ET events. Conversely, a case study of Typhoon Songda (2004) conducted by Ito et al. (2016) showed that weakening baroclinicity in the WNP created a less favorable environment for ET in the future.

Several factors affecting the ET process include the intensity and depth of the original TC, latitude of transition and underlying SSTs, scale of the pre-existing midlatitude trough, timing of the trough-TC interaction, and tilt of the upper-level trough (Hart et al. 2006). With limited knowledge on the ET process and climate change, it is beneficial to consider previous work regarding these parameters in the context of climate change.

1.2.2.1. Tropical Cyclone Intensity

As weaker TCs are more easily disrupted by the vertical wind shear in a midlatitude environment (Hart et al. 2006), it follows that stronger TCs are then more likely to survive the ET process. TC intensity is projected to increase with warming (e.g., Knutson et al. 2010; Hill and Lackmann 2011; Walsh et al. 2016; Bacmeister et al. 2018), which suggests a possible increase in the percent of TCs undergoing ET. On the other hand, an overall reduction in TC frequency has been projected (e.g., Knutson et al. 2010; Mallard et al. 2013b; Bacmeister et al. 2018), which would likely result in a subsequent decrease in ET frequency. It has been shown that the reduction in future TC frequency is primarily due to fewer weak TCs while the most intense TCs are projected to become more frequent (e.g., Knutson et al. 2010; Bacmeister et al. 2018). This increase in intense TCs could therefore offset the expected reductions in ET frequency due to decreases in TC frequency and result in an increase in such events.

1.2.2.2. Sea Surface Temperatures and Latitude of Transition

A poleward extension of the tropics, related to changes in vertical wind shear, potential intensity, SSTs, and the expansion of the Hadley Cell (e.g., Frierson et al. 2007; Lu et al. 2007; Previdi and Liepert 2007; Woollings 2010; Kang and Lu 2012; Zhao and Held 2012; Kossin et al. 2014), would act to reduce the gap between the “tropically favorable” and “baroclinically favorable” regions, thus enhancing the likelihood of ET and increasing ET frequency. However, a poleward shift in the midlatitude jet and storm track activity (e.g., Yin 2005; Bengtsson et al. 2006, 2009; Chang et al. 2012; De Vries et al. 2013; Simpson et al. 2014) would result in a poleward shift of the “baroclinically favorable” region, thus potentially offsetting the gap closure from the poleward expansion of the “tropically favorable” region, and theoretically resulting in little to no change in ET frequency.

The underlying SSTs can affect the speed of transition as well as the level of post-transition intensification; TCs over warmer waters experience slower transition periods and higher levels of reintensification (Hart et al. 2006). Climate change is expected to result in warmer SSTs, which would lead to slower transition times and a higher likelihood of post-transition reintensification in the future. Jung and Lackmann (2018, in review) saw evidence of slower transition periods in the future with their simulation of Hurricane Irene (2011). The projected warming maximum in the tropical upper-troposphere, however, could compensate for

the increases in storm intensity due to warmer SSTs (Knutson and Tuleya 2004; Hill and Lackmann 2011; Lackmann 2015), which would hinder the level of post-transition reintensification experienced by ET events in the future. Because the strongest upper-tropospheric warming is concentrated in the tropics and subtropics, future ET events could translate away from this mitigating effect, allowing the effect of warming SSTs on post-transition reintensification to dominate.

1.2.2.3. Upper-level Forcing

Projected increases in baroclinicity aloft, primarily in relation to tropical upper-tropospheric warming, could potentially be beneficial for the growth of upper-level disturbances. This would allow more interaction between surface and upper-level disturbances and therefore, would be beneficial to the ET process. However, reductions in lower-tropospheric baroclinicity, due to the reduction of the equator-to-pole temperature gradient by the polar amplification of global warming, and increases in lapse-rate stability in the tropics associated with tropical upper-tropospheric warming, could result in a decreased Rossby depth for surface disturbances, which would hinder the interaction between the trough and TC and limit ET frequency. It is unclear which change will be larger; it is also possible that these two effects will cancel out, resulting in little to no change in ET frequency. Additionally, these changes in stability primarily affect the tropics, so events that transition farther north may not be as susceptible to these effects. The debate on how the meridional amplitude of waves will change with warming is ongoing with some evidence existing that supports an increase in meridional wave amplitude during the TC season (Screen and Simmonds 2013; Di Caupa and Coumou 2016).

The timing of the trough-TC interaction affects how much influence the midlatitude feature has on the transition process and therefore, the degree of reintensification (Hart et al. 2006; Ritchie and Elsberry 2007). There is limited evidence of how upper-level jet and TC translation speeds are projected to change with warming, thus there are no concrete conclusion on how these factors will affect future trough-TC interactions. Jet position also influences the interaction between TCs and the midlatitude environment; this feature has been projected to shift poleward in the future (Yin 2005; De Vries et al. 2013; Simpson et al. 2014), which would act to shift the “baroclinically favorable” region poleward, as well.

1.3. Science Questions and Hypotheses

There remains a gap in the literature regarding climate change effects on the extratropical transition of tropical cyclones. This dissertation aims to build on this body of research and address the following research questions:

- Will the frequency, percentage, and geographical location of ET events change as a result of climate change? Are these changes significant?

Two components should be considered when answering this question: (1) changes in the strength and number of TCs and (2) changes in the background environment. As previously discussed, a reduction in TC frequency has been projected; however, if this decrease is primarily due to fewer weak storms, it may or may not result in a similar reduction in ET frequency. A shift towards more intense TCs under climate change conditions has also been projected, which could result in a higher frequency of ET events. In regards to changes in the background environment, the degree of expansion of the “tropically favorable” region compared to the poleward migration of the “baroclinically favorable” region will likely be important. While these two processes are linked, that does not necessarily imply they will occur at the same rate. Therefore, it is possible that the expansion of the “tropically favorable” region could occur faster than the poleward shift of the “baroclinically favorable” region, thus increasing ET frequency.

- Will the transition period and post-transition intensity of ET events be altered under climate change conditions? Will the reintensification pathways differ?

The frequency of post-transition reintensification, level of reintensification, and transition period are likely to increase under climate change conditions. Warmer SSTs have been linked to higher levels of post-ET reintensification and slower transition periods, and SSTs are projected to increase with climate change. While the effects of tropical upper-tropospheric warming may mitigate this change, this warming is maximized in the tropics and subtropics, meaning TCs undergoing ET may not be as susceptible to its compensating effect. There is additional potential for latent heat release to play a larger role in the reintensification of ET events, which could lead to tropical (warm-seclusion) reintensification becoming more likely. With enhanced diabatic influences, post-ET reintensification may be less reliant on

interactions with an upper-level trough in a future climate and therefore, be able to occur more frequently.

- How will the changes in the intensity of ET events (i.e., minimum sea-level pressure) compare with changes in the storm impacts (e.g., wind and precipitation)?

Even if we do not see significant changes in the post-transition intensity of ET events, it is likely the impacts associated with these systems will become more severe. For example, future projections of moisture increases, and subsequent latent heat release, could help TCs undergoing extratropical transition regain hurricane force winds post-transition while also increasing precipitation amounts, which would further increase the impact of these storms. Additionally, enhanced diabatic outflow from future ET events could result in more severe impacts downstream.

We aim to answer these research questions with novel high-resolution (15 km) multi-seasonal simulations conducted in present and future thermodynamic environments using the Model for Prediction Across Scales-Atmosphere (MPAS). Simulated tropical cyclones are tracked as minima in sea-level pressure (SLP) with the presence of a warm core structure. Candidate cyclone centers are connected using a nearest-neighbor approach to form TC trajectories; ET events are identified by first continuing TC trajectories, and then computing the CPS parameters at each time step. A storm-relative compositing approach is taken to examine the storm-scale dynamics of ET events under present and future climate conditions.

This dissertation continues as follows: Chapter 2 describes the methods and limitations of the aforementioned model simulations; Chapter 3 evaluates the present-day climate simulations; Chapter 4 presents future changes in the ET climatology; Chapter 5 examines future changes in the dynamics of ET events; and Chapter 6 includes a summary of results, concluding remarks, and ideas for future work.

2. Methods

The information in sections 2.1–2.2 and 2.5 is largely adapted from Michaelis et al. (2018, submitted).

2.1. Model Simulations

Numerical modeling is an important tool for determining the effects of climate change. With simulations spanning several centuries, multiple ensemble members, and the inclusion of atmosphere-ocean coupling, the latest generation of general circulation models (GCMs) from the Coupled Model Intercomparison Project Phase 5 (CMIP5) are common tools for research in this regard. However, due to current computational limitations, the grid spacing of these simulations is largely restricted to $\sim 1^\circ$ (~ 100 -km) or greater. While this coarse grid spacing is capable of representing large-scale atmospheric features such as polar amplification and teleconnections, it is insufficient for resolving weather extremes, especially those associated with smaller-scale systems such as tropical cyclones and convective storms (e.g., Mizielinski et al. 2014 and references therein; Small et al. 2014; Prein et al. 2015). These smaller-scale systems often result in significant socioeconomic impacts; therefore, in order to fully ascertain the societal impacts of climate change, it is essential to complement existing GCM simulations with simulations at resolutions sufficiently fine to capture these high-impact phenomena.

To date, several model downscaling techniques have been developed for this purpose. For example, regional downscaling (e.g., Wang et al 2004; Giorgi et al. 2009) computationally allows for finer grid spacings by employing a smaller domain, thus circumventing the resolution deficiency of traditional GCMs. However, the use of a regional domain presents the issue of how to specify lateral boundary conditions, preventing interactions with the larger-scale from being fully incorporated (Small et al. 2014). Global models eliminate the constraints of lateral boundaries, but, as previously discussed, can be expensive to run for long periods at high resolutions. Incorporating nests within a global domain, or using mesh refinement grids, however, can help alleviate this expense.

Another useful method for assessing how climate change can affect high-impact, small-scale weather systems is the “pseudo-global warming” (PGW) method, initially called “surrogate global warming” (e.g., Schär et al. 1996; Frei et al. 1998; Kimura and Kitoh 2007; Hara et al. 2008; Rasmussen et al. 2011; Mallard et al. 2013; Lackmann 2013, 2015; Trapp and Hoogewind

2016). In PGW experiments, high-resolution control simulations are conducted, typically replicating an observed weather event. The high-resolution initial and boundary conditions are then modified with “delta” fields derived from GCMs, and the event is re-simulated, allowing assessment of changes in the characteristics of the event as a function of larger-scale environmental change. An important advantage of the PGW method is that realistic, high-resolution synoptic-scale and mesoscale settings are guaranteed. This method is consistent with the “storyline” approach described by Shepherd (2016) and Trenberth et al. (2015). A limitation of PGW case studies is the inability to study the frequency of occurrence of such events. To alleviate this limitation, some investigators have conducted long-duration regional PGW simulations (e.g., Willison et al. 2015; Ban et al. 2014; Liu et al. 2017), which allow for analysis of statistical changes extending beyond a single case-study event. All regional PGW experiments, however, are limited by the need to impose lateral boundary conditions, which reduces the dynamical freedom of the simulation.

Given recent advances in computational power and data storage, several modeling groups have succeeded in performing long-term high-resolution global simulations, both with atmosphere-only and coupled atmosphere-ocean configurations (e.g., Small et al. 2014; Roberts et al. 2015 and references therein). Models that include coupling between the atmosphere and ocean have the advantage of two-way communication allowing the possibility of realistic atmosphere-ocean interactions; however, at long integration times, climatologies of coupled models have been known to suffer from biases due to the drift in sea surface temperatures, which can negatively affect regional climate projections (e.g., He and Soden 2016). Previous studies have determined that resolution is an important factor for a more accurate representation of synoptic and mesoscale phenomena (Willison et al. 2013; Small et al. 2014; Prein et al. 2015), and thus should be maximized whenever possible.

2.1.1. Model Configuration

In this study, we use the atmospheric component of MPAS, version 5.1 (Skamarock et al. 2012). MPAS is a non-hydrostatic global, atmosphere-only model that makes use of unstructured Voronoi meshes (Du et al. 1999) to create variable-resolution grids. This grid structure allows for localized areas of high-resolution to gradually transition to lower resolutions, thus alleviating the boundary issues associated with sharp transitions between domains in traditional nesting

approaches (Park et al. 2014). The focus of the simulations presented here is on Northern Hemispheric phenomena; therefore, we use a variable-resolution mesh with 15-km grid spacing over the Northern Hemisphere, expanding out to 60-km in the Southern Hemisphere (Fig. 2.1).

We selected ten simulation years with varying phases of El Niño-Southern Oscillation (ENSO), based on the Multivariate ENSO Index (MEI) and the Oceanic Niño Index (ONI) over the TC season (Table 2.1). These years also sample a range of tropical cyclone activity in the NATL, ENP, and WNP basins. Each simulation is integrated for 14.5 months, from 1 March of the first year through 14 May of the following year, with the first month discarded as spin-up; output is recorded every 6-h. The MPAS atmospheric physics suite includes a subset of physics schemes adapted from various versions of the Weather Research and Forecasting (WRF) model (Skamarock et al. 2008). The simulations presented here employ the following physics parameterizations: WRF Single-Moment 6 class (WSM6; as in WRF 3.8.1) for microphysics, Yonsei University (YSU; as in WRF 3.8.1) to represent the planetary boundary layer, Tiedtke (as in WRF 3.3.1) for sub-grid scale convection, Community Atmosphere Model (CAM; as in WRF 3.3.1) to represent shortwave and longwave radiation, and the Noah land surface model (as in WRF 3.3.1) for land surface processes. We selected the Tiedtke convective parameterization scheme due to its inclusion of convection momentum transport, which has been shown to be important for reducing model biases in surface winds and TC intensity (Zhang and McFarlane 1995; Han and Pan 2006; Hogan and Pauley 2007; Richter and Rasch 2008), as well as representation of features such as the Intertropical Convergence Zone (ITCZ; Zhang and Wang 2006; Kim et al. 2008). We completed a set of preliminary tests using a quasi-uniform 60-km mesh to further refine our physics choices (not shown).

We post-process model output to vertically interpolate fields to selected isobaric levels and horizontally interpolate from the native unstructured mesh to a $0.15^\circ \times 0.15^\circ$ latitude-longitude grid. Due to storage constraints, we saved limited number of variables for the Northern Hemisphere only; however, we archived monthly restart files, enabling replication of a particular period of time or event as needed.

2.1.2. Present-day and Future Climate Simulations

We used the ECMWF Interim Reanalysis (ERA-I; Dee et al. 2011) with a spectral T255 resolution ($\sim 0.7^\circ$ horizontal grid spacing) for present-day initial conditions for the initial spin-up

simulation only; SST and sea ice fields are updated daily. The configuration of these surface fields is discussed further in section 2.1.3. For the future climate spin-up simulation, we modify the ERA-I initial and lower boundary conditions by adding monthly-averaged temperature changes derived from a 20-member ensemble of CMIP5 GCMs. The GCMs included in this ensemble are listed in Table 2.2. These temperature changes are calculated by subtracting the 1980–1999 average temperature from the 2080–2099 average temperature following the Intergovernmental Panel on Climate Change (IPCC) Fifth Assessment Report (AR5) Representative Concentration Pathway (RCP) 8.5 emissions scenario and interpolated to the ERA-I grid. These change fields are then added to the existing temperature data at all atmospheric pressure and soil levels. The model adjusts geopotential height and specific humidity based on the imposed temperature changes; relative humidity is held constant. We set carbon dioxide (CO₂) concentrations in the future climate simulations to 936 ppm, the level projected by the RCP8.5 emissions scenario for 2100 (Meinshausen et al. 2011). Present-day CO₂ concentrations are based on analyzed values set according to the year.

Rather than running the simulations in chronological order, the simulation years are sorted from the smallest (most negative) MEI (ONI) to the largest (most positive) MEI (ONI) (Table 2.1). With the present-day and future initial conditions set, we conduct full simulations for a neutral ENSO year in each thermodynamic environment. These simulations are used as spin-up and therefore, excluded from our analysis. While we took this precaution to allow the model to come into equilibrium with the imposed warming for the future climate experiment, it was repeated for the present-day simulation to maintain consistency. We then used the output from 1 March, towards the end of the initial spin-up simulation, to initialize the first simulation year. This simulation method continues for both the present-day and future experiments by using the output from the latter part of one simulation to initialize the next. Applying this “daisy-chain” technique avoids the need for excessive spin-up times for each year; instead, only the output from the first month is discarded to allow any discontinuities arising from shifting SST patterns to come into equilibrium.

2.1.3. Surface Fields

As with the atmospheric initial conditions, the SST fields used in the simulations are taken primarily from the ERA-I. However, the SSTs in the ERA-I have been derived from

several different datasets over the years (Dee et al. 2011). For reanalysis times after February 2009, ERA-I SST and sea ice fields were taken from the Operational Sea Surface Temperature and Sea-Ice Analysis (OSTIA; Donlon et al. 2012). To maintain consistency between all simulations, the OSTIA SST, interpolated from its native 0.05° horizontal grid spacing to the ERA-I grid, is used for simulation years prior to 2009. Therefore, we effectively used OSTIA SST for all simulations.

The SSTs for the future climate simulations are altered in the same manner as the atmospheric and soil temperatures in the initial conditions (Fig. 2.2a–b). However, the same technique of adding a GCM delta field onto existing data cannot be used for sea ice. Instead, similar to Mizielinski et al. (2014), monthly-averaged CMIP5 ensemble mean sea ice fields are interpolated to create daily sea ice fields for both present-day (1980–1999) and future (2080–2099 under the RCP8.5 emissions scenario) time periods. An example of these sea ice fields is shown in Figure 2.2c–d. We then replaced the analyzed sea ice in the ERA-I data with these climatological fields for use in all model simulations. While the climatological present-day sea ice does not entirely match the analyzed field in the ERA-I (e.g., the sea ice edge is much more diffuse), handling the sea ice in this manner ensures that it is plausibly represented in the future climate simulations. The presence of an overly diffuse ice edge could result in unrealistically weak lower tropospheric baroclinicity during warm seasons.

Our technique for simulating a future climate is similar to the PGW approach in the sense that (1) the initial and lower boundary conditions are being altered using projected temperature changes from GCMs to represent future thermodynamic conditions, and (2) analyzed high-resolution SST fields are used to preserve realistic magnitudes of SST gradients, which have been shown to be important for midlatitude cyclone development and other regional climate changes (e.g., Brayshaw et al. 2011; Booth et al. 2012; Kirtman et al. 2012; He and Soden 2016; Siqueira and Kirtman 2016). However, by using a global model, one of the main limitations of PGW, the constraint of the lateral boundary conditions, is alleviated. The UPSCALE experiments described by Mizielinski et al. (2014) use a similar time-slice technique for simulating a future climate. By simulating a small ensemble of 26 years, UPSCALE samples a broad range of interannual variability and ENSO states; however, 25-km grid spacing is insufficient for resolving full strength tropical cyclones (Davis 2018). Therefore, our simulations

complement UPSCALE by offering sufficiently high resolution to better capture the atmospheric mesoscale.

2.1.4. Climate Change Representation

To ensure that our simulations are useful in studying climate change effects on ET, we must verify that the future climate simulations reproduce the large-scale warming patterns exhibited by the GCMs. Previous theoretical and modeling studies recognize that the Arctic region is warming at a faster rate than the rest of the globe in response to an increase in greenhouse gases (IPCC, 2013, §12.4.2.2). This polar amplification effect is captured in our simulations with portions of the Arctic experiencing temperature changes greater than 16-K compared to differences ≤ 10 -K elsewhere (Fig. 2.3a). We note, however, that Arctic temperatures in our present day simulations were colder compared to ERA-I, while the future simulations resulted in Arctic temperatures comparable to those produced by GCMs (not shown). As a result, the MPAS simulations produce a larger magnitude of warming in the Arctic compared to the GCM ensemble (Fig. 2.3a–b). Another result consistent with theory and previous modeling studies is the development of a warming maximum in the tropical upper-troposphere (IPCC, 2013, §12.4.3.2). This area of warming, which occurs between the ~ 400 -hPa and ~ 150 -hPa levels and which maximizes around the 250-hPa level (IPCC, 2013, §12.4.3.2), has been shown to mitigate projected changes in TC intensity (e.g., Knutson and Tuleya, 1999; Shen et al., 2000; Hill and Lackmann, 2011). As shown in Fig. 2.3c, this warming signature is replicated in the MPAS simulations.

2.2. Tropical Cyclone Tracking

We tracked simulated Northern Hemisphere tropical cyclones using the TempestExtremes objective, feature-based tracking algorithm (Ullrich and Zarzycki 2017; Zarzycki and Ullrich 2017). TCs are initially detected as minima in sea-level pressure, and then retained as candidate cyclone centers if certain criteria are met. Here, we required that TCs must have a 2-hPa closed SLP contour within 2° of the storm center and a 300–500-hPa geopotential thickness (DZ) maximum within 6° of the storm center to ensure that a warm core is present. Additionally, TCs must not travel more than 6° within a 6-h period, must have a lifetime of at least two days, must be located over water for at least 12-h, and must have at least two days of

10-m wind speed of at least 14 m/s (~31 mph). While we allow TempestExtremes to identify candidate centers as far north as 60°N to prevent the premature termination of trajectories, we post-process the tracks to eliminate TCs with a genesis latitude north of 45°N. Trajectories that end and begin within 12-h of each other are merged together to prevent broken tracks from being counted twice. A comprehensive list of tunable parameters for TempestExtremes, and our choices for each, is included in Table 2.3. Once TC tracks have been obtained, TCs are separated into basins (Fig. 2.1) based on their genesis location. Results of the TempestExtremes algorithm are most sensitive to the strength of the SLP minimum and warm core (Zarzycki and Ullrich 2017). We performed sensitivity tests adjusting these factors; results did not vary significantly from our chosen configuration (not shown).

2.3. Detection of Extratropical Transition Events

We use the ExTraTrack extratropical transition tracker (Zarzycki et al. 2017) to detect simulated ET events. ExTraTrack is an objective algorithm that continues TC trajectories from TempestExtremes based on local minima in SLP. Candidate centers are first identified as local minima in SLP compared to their eight surrounding neighbors. Due to the high-resolution of our model output, we implement a secondary local minimum check using neighboring grid points that are three grid points away from the candidate center. Additionally, candidate centers are discarded if the minimum SLP is greater than 1020-hPa, or if the center is over topography greater than 350-m. If multiple candidate centers are detected, the center with the lowest minimum SLP is retained. The storm propagation speed is limited to 40-ms⁻¹, which constrains the search radius for candidate centers, and changes in storm direction are restricted based on storm speed to prevent sharp changes in storm direction from occurring. ExTraTrack does not track TCs from TempestExtremes if they occur in the Northern Indian (NI) basin or dissipate south of 20°N.

The CPS (Hart 2003) is used to objectively detect and quantify simulated ET events through examination of storm structure. A cyclone's level of symmetry is determined by its 900–600-hPa thickness symmetry (B), calculated as:

$$B = \overline{Z_{600hPa} - Z_{900hPa}}_R - \overline{Z_{600hPa} - Z_{900hPa}}_L \quad (1)$$

where Z is the geopotential height at 600-hPa and 900-hPa levels, R and L indicate the right and left hemispheres of the storm relative to storm motion, respectively, and the overbar denotes an average value within a 500-km radius of the cyclone center is used. Generally, large values of B indicate an asymmetric nature, and vice versa, small values of B indicate a symmetric nature.

The temperature and strength of the cyclone core is determined by the lower-tropospheric (900–600-hPa) thermal wind ($-VLT$), calculated as:

$$-VLT = \left. \frac{\partial \Delta Z}{\partial \ln p} \right|_{900hPa}^{600hPa} \quad (2)$$

and the upper-tropospheric (600–300-hPa) thermal wind ($-VUT$), calculated as:

$$-VUT = \left. \frac{\partial \Delta Z}{\partial \ln p} \right|_{600hPa}^{300hPa} \quad (3)$$

where the vertical profiles of ΔZ are computed using pressure levels from 300-hPa to 900-hPa at 50-hPa intervals. A positive thermal wind signifies a warm-core cyclone. Likewise, a negative thermal wind indicates a cold-core structure.

Similar to previous studies, our simulated TCs have $B < 10$ and $-VLT > 0$, indicating a symmetric, warm-core structure, and simulated ETCs have $B > 10$ and $-VLT < 0$, signifying an asymmetric, cold-core structure (Fig. 2.4; Evans and Hart 2003; Hart et al. 2006; Kitabatake 2011). Cluster analysis of 19 ET events from 1998–2002 by Arnott et al. (2004) provides additional confidence in using these thresholds. Zarzycki et al. (2017) increased the B threshold to 15 to account for high-resolution data; however, preliminary analysis of ET events in our model output suggests that maintaining the B threshold at 10 is appropriate. The onset of transition occurs when either B first becomes greater than 10 or $-VLT$ first becomes negative; ET completion is declared when the alternate criteria is met. Satisfying both criteria indicates the cyclone has fully transitioned from a TC to an ETC (Evans and Hart 2003; Hart 2003; Haarsma et al. 2013; Wood and Ritchie 2014; Zarzycki et al. 2017).

ExTraTrack computes the aforementioned CPS parameters at each time step of the cyclone trajectory (i.e., every 6-h) to determine the storm structure throughout its life cycle. A 24-h running mean is used to smooth the CPS values prior to analysis. A cyclone must maintain

tropical characteristics (i.e., $B < 10$ and $-VLT > 0$) for at least the first 1.5 days of its trajectory. If this is not the case, the cyclone is categorized as a subtropical cyclone. Cyclones must fulfill the B and $-VLT$ criteria for 12 consecutive hours in order to be categorized as an ET event; storms that satisfy only one criterion are categorized as partial ET events. Partial ET events are generally storms that dissipate prior to ET completion, or transition back to a TC before completing ET. Last, cyclones detected by ExTraTracks that do not meet either ET criteria, or dissipate south of 20°N , are categorized as TCs. The former are generally weaker cyclones with shallow warm cores. Our analysis in the following chapters will focus primarily on cyclones in the ET category.

2.3.1. Example Events

A sequence of synoptic maps and CPS diagrams for an example storm in each category from the present-day MPAS simulations is shown in Figures 2.5–2.8 to help illustrate the evolutionary differences between the types of events. The example ET event in Figure 2.5 formed on 15 September 2010 at 00 UTC in the Western North Pacific between Guam and the Marshall Islands. It reached peak intensity as a tropical system on 14 September 2010 at 06 UTC. At this time, the cyclone begins to interact with the midlatitude flow, but is still primarily an independent feature in the 500-hPa height field (Fig. 2.5a), and remains associated with its own circulation in the dynamic tropopause wind field (Fig. 2.5d). This cyclone begins ET at 15 September 2010 at 00Z, when B first becomes larger than 10 (Fig. 2.5g); 18-h after ET onset, several of the closed 500-hPa height contours around the cyclone have merged with the midlatitude trough, leading to an open wave pattern in the 500-hPa height field (Fig. 2.5b). While the cyclone is still a distinguishable feature at this time, it is no longer independent from the midlatitude height field. Additionally, the circulation around the cyclone has weakened as the storm continues to interact with the upper-level trough building to the northwest (Fig. 2.5e). By ET completion at 06 UTC on 17 September 2010, when $-VLT$ becomes negative indicating a transition to a cold-core system (Fig. 2.5h), the cyclone is fully embedded in the midlatitude flow (Fig. 2.5c,f).

The example partial ET event (Fig. 2.6) evolves similarly to the ET event: the cyclone is a distinct feature in the 500-hPa field at the time of peak tropical intensity (Fig. 2.6a), becomes an open wave pattern in the 500-hPa field after ET onset (Fig. 2.6b), and is indistinguishable

from the midlatitude flow 24-h after beginning ET (Fig. 2.6c). However, the cyclone dissipates before completing ET and thus, does not fully become an ETC (Fig. 2.6g–h). The primary difference between this partial ET event and the previous ET example is the prevalence of an upper-level trough. In the previous example, the cyclone appears to merge with an upper-level trough, as evident by the 500-hPa height field (Fig. 2.5b–c) and the pattern of relatively cold potential temperatures on the dynamic tropopause (Fig. 2.5e–f). No such patterns are apparent here (Fig. 2.6b–c, e–f); instead, this partial ET event appears to be absorbed by a pre-existing midlatitude cyclone to the north (Fig. 2.6c).

At genesis time, the example subtropical cyclone has already begun to interact with the midlatitude flow, exhibiting an open wave pattern in the 500-hPa heights (Fig. 2.7a) and no clear independent circulation present (Fig. 2.7d). Interaction with an upper-level trough continues as the storm undergoes ET (Fig. 2.7b,e). 24-h after ET completion, the cyclone is fully incorporated into the midlatitude flow and has weakened substantially (Fig. 2.7c,f); it dissipates 12-h later. While this subtropical example storm mimics aspects of the example ET event, it is clear the cyclone does not spend as much time as a purely tropical system; there are a limited number of data points in the CPS tropical quadrants (Fig. 2.7g–h) and there is immediate interaction with the midlatitude environment at the time of TC genesis (Fig. 2.7a). One discriminating factor between this subtropical cyclone and the previous example storms is the latitude of TC genesis. In this example, the cyclone formed at 35.5°N compared to the other example storms forming below 20°N.

With the example TC case, the closed 500-hPa height contours around the storm center remain independent from the midlatitude flow throughout the duration of the event (Fig. 2.8a–c). Additionally, the TC remains a symmetric system with a warm core at upper and lower levels throughout its lifetime (Fig. 2.8g–h). Relatively cold potential temperatures on the dynamic tropopause and trough pattern in the 500-hPa heights northwest of the TC 12-h after peak tropical intensity (Fig. 2.8e and Fig. 2.8b, respectively) indicate the presence of an upper-level trough, and a midlatitude cyclone is evident to the northeast of the cyclone (Fig. 2.8b). However, the TC does not travel far enough poleward to interact with these features, and therefore, does not have the opportunity to undergo ET. Instead, the storm dissipates as a tropical system a few days after making landfall.

2.4. Storm-relative Composites

We utilize a storm-relative compositing approach to examine changes in the storm-scale dynamics of ET events in more detail. We chose which events to composite together based on the 500-hPa height anomaly field around the storm center. Here, we define “anomaly” as the deviation from the daily-varying time mean calculated over the ten simulation years, and we examine the height anomaly field within 40° to the west, 28° to the east, 30° to the north, and 10° to the south of the storm center 12-h prior to ET onset. Each ET case is compared to a reference case, taken as a NATL event that occurred in the present-day simulations on 20 October 2013, which features a prominent trough upstream of the TC and a substantial downstream ridge (Fig. 2.9); events with unweighted, centered pattern correlation coefficients of at least 0.3 are retained for compositing. This method results in 21 and 30 cases for the present-day and future NATL, respectively, and 32 and 31 for the present-day and future WNP, respectively. While reducing the correlation coefficient threshold increases the number of cases in the composites, it also results in significant variation between cases. Therefore, to preserve the synoptic pattern as best as possible, we opt for a higher correlation coefficient threshold and fewer cases.

Fields, such as wind speed or precipitation, are identified within a 5° or 10° radius of the cyclone center to assess impacts associated with the storms. The central point of the composite is defined as the location of minimum SLP at the time of ET onset; composites are also generated 24-h prior to ET onset, 12-h prior to ET onset, at the time of ET completion, and 12-h after ET completion. To examine changes in the synoptic environment, we generate composites of fields such as potential temperature on the dynamic tropopause within the previously discussed area around the storm center (e.g., 40° to the west, 28° to the east, etc.). At some composite times, particularly those post-transition, the composite domain is latitudinally restricted due to the far poleward location of the storm center. Additionally, the number of cases decreases for the post-transition composite times due to differences in storm lifetime. For this reason, post-transition composite times are limited to only 12-h after ET completion.

While storm-relative compositing allows us to identify common characteristics between similar types of ET events, and detect changes in these characteristics between present-day and future storms, variations in storm size, track lifetime, and propagation speed may result in smearing of some features.

2.5. Assumptions and Limitations

For our future climate simulations, we computed temperature delta values using the mean IPCC AR5 RCP8.5 emissions pathway. While other plausible scenarios exist, we selected a high emission pathway in order to maximize the signal-to-noise ratio in our simulations. Additionally, using the GCM ensemble mean temperature changes to alter our initial and lower boundary conditions diminishes the considerable amount of variability in the temperature changes projected by individual GCMs. However, computing an ensemble mean from a set of simulations using temperature change fields from each GCM is not likely to produce significantly different results (Hill 2010; Marciano 2014). With greater computational resources, we would seek to run a small ensemble of simulations in order to ensure robust results.

The adjustment of geopotential height based on the imposed temperature changes for the future climate simulation introduces some degree of imbalance between the model mass and wind fields. In previous studies, we utilized the Digital Filter Initialization (DFI) capability of the WRF model to reduce these imbalances. Since this feature is not included with MPAS, we conducted a full 14.5-month spin-up simulation to ensure imbalances between the mass and wind fields are minimized. We also maintain constant relative humidity between the present-day and future simulations in the initial conditions. While this assumption may be appropriate over ocean basins, it does not necessarily hold true over land areas (e.g., Sherwood and Fu, 2014); however, with no constraints on the lateral boundaries, the relative humidity within our model domain is allowed to evolve through the duration of the simulations.

While our treatment of sea ice in the model allows for a plausible representation of future conditions, we are using identical fields in each present-day and future simulation and therefore, are discounting the effects of interannual variability in sea ice. Several studies have highlighted the connection between sea ice variability and atmospheric circulations in the Northern Hemisphere (e.g., Deser et al. 2000; Overland and Wang 2010); however, our intention here is to minimize this influence and instead, focus on changes due to altered thermodynamics. Another limitation inherent in our methods is the assumption that future SST patterns will remain similar to what they are today. Nevertheless, we believe the benefits of using high-resolution SST analyses to preserve realistic SST gradients and alleviate regional biases associated with atmosphere-ocean coupling (e.g., He and Soden 2016) outweigh this limitation.

Many previous studies have shown that neglect of SST cooling results in TCs that are too strong (e.g., Schade and Emanuel 2009). Use of analyzed SST fields in our simulations does not allow for TC-generated cold wakes, which results in a positive TC intensity bias, and could lead to unrealistic temporal TC clustering. However, the use of convective parameterization, particularly the Tiedtke scheme, which adjusts momentum, tends to weaken TCs through momentum adjustment in a warm-core cyclonic structure, an effect opposite to that resulting from the neglect of SST cooling. Ideally, a grid length of 4-km or less would be used to fully capture the TC structure and intensity (e.g., Gentry and Lackmann 2010), but computational expense does not allow this for the Northern Hemisphere region of interest for the simulation durations needed for a sufficient statistical sample. A benefit of our configuration is that the resolution is sufficiently high to capture nearly the full range of TC intensity; preliminary testing highlighted the capability of 15-km to replicate realistic TC structures, such as spiral rain bands and a defined eye (not shown). We acknowledge that neglect of sea-surface cooling and use of parameterized convection represent limitations with our approach. These limitations are consistent between present-day and future simulations, allowing any differences found in TC intensity to remain meaningful.

We recognize that the methods employed in this study only account for projected changes due to increased anthropogenic greenhouse gases and therefore, do not represent other external climate forcings. Changes in other aspects of the climate system, such as aerosols, deep soil moisture, and vegetation, are also neglected in our simulations. Despite the limitations discussed, our method alleviates limitations associated with regional PGW and is much more computationally efficient than running high-resolution global models for long integration periods (e.g., centuries), resulting in controlled simulations to examine the effects of altered thermodynamics on high-impact weather events.

Table 2.1: Average Multivariate ENSO Index (MEI), Oceanic Niño Index (ONI), and corresponding ENSO phase during the tropical cyclone season (June–November) for the chosen simulation years.

Year	Multivariate ENSO Index (MEI) Rank: JJ–ON Average	Oceanic Niño Index (ONI): JJA–SON Average	ENSO Phase
2010	3.8	-1.2	Strong La Niña
1988	6.6	-1.2	Strong La Niña
2011	16.2	-0.7	Weak La Niña
2013	26.8	-0.2	Neutral
2001	31.8	-0.1	Neutral
2005	34.2	0.0	Neutral
1992	47.5	0.3	Neutral
1994	57.1	0.5	Weak El Niño
2015	64.8	1.7	Strong El Niño
1997	66.0	1.8	Strong El Niño

Table 2.2: List of 20 CMIP5 GCMs used to compute ensemble mean temperature “deltas” and sea ice fields.

Model	Modeling Center/Group	Grid Length
ACCESS1-0 ACCESS1-3	Commonwealth Scientific and Industrial Research Organization (CSIRO) and Bureau of Meteorology (BOM), Australia	1.25°x1.875°
CanESM2	Canadian Centre for Climate Modeling and Analysis	2.8°x2.8°
CMCC-CM	Centro Euro-Mediterraneo sui Cambiamenti Climatici (Euro-Mediterranean Center on Climate Change)	0.8°x0.8°
CNRM-CM5	National Centre of Meteorological Research, France	1.4°x1.4°
GISS-E2-H GISS-E2-H-CC GISS-E2-R-CC	NASA Goddard Institute for Space Studies	2°x2.5°
HadGEM2-AO HadGEM2-ES	Met Office Hadley Centre	1.25°x1.875°
INMCM4	Institute for Numerical Mathematics	1.5°x2.0°
IPSL-CM5A-MR IPSL-CM5B-LR	Institut Pierre Simon Laplace, France	1.25°x2.5° 1.8°x2.75°
MIROC-ESM MIROC-ESM-CHEM	Japan Agency for Marine-Earth Science and Technology, Atmosphere and Ocean Research Institute (The University of Tokyo), and National Institute for Environmental Studies	2.8°x2.8°
MPI-ESM-LR MPI-ESM-MR	Max Planck Institute for Meteorology	1.8°x1.8°
MRI-ESM1	Meteorological Research Institute, Japan	1.1°x1.1°
NorESM1-M NorESM1-ME	Norwegian Climate Center, Norway	1.9°x2.5°

Table 2.3: TempestExtremes parameter choices.

Parameter Definition	Value
Strength of local sea-level pressure (SLP) minimum	2-hPa
Allowable distance for SLP closed contour	2°
Strength of warm core anomaly (DZ)	15-m
Allowable distance for DZ closed contour	6°
Maximum separation between SLP minimum and DZ maximum	1.1°
Minimum allowable distance between two candidate centers	2°
Maximum travel distance for cyclone in 6-h	6°
Minimum cyclone lifetime	48-h
Maximum allowable gap in trajectory	12-h
Maximum latitude of SLP minimum	60°N
Minimum 10-m wind speed	14 m/s
Maximum topography directly under SLP minimum	100-m
Minimum time required over water	12-h

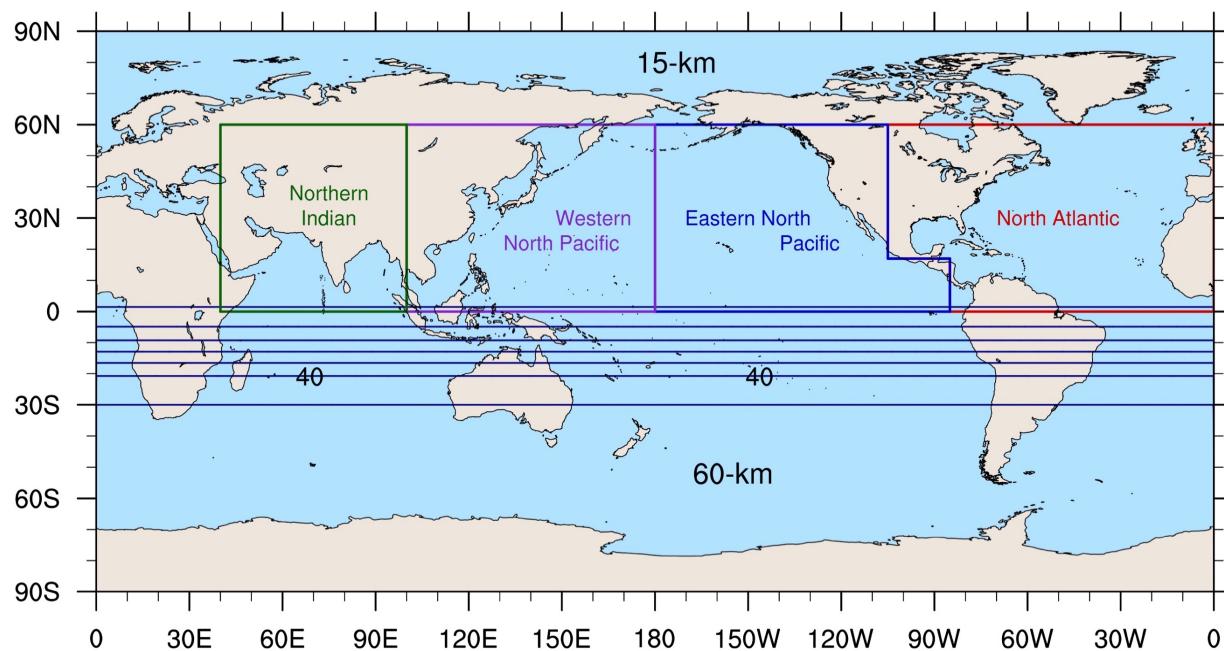


Figure 2.1: *Variable resolution mesh and tropical cyclone basins.* Variable-resolution mesh used in MPAS simulations and geographical regions of the tropical cyclone basins defined in this study.

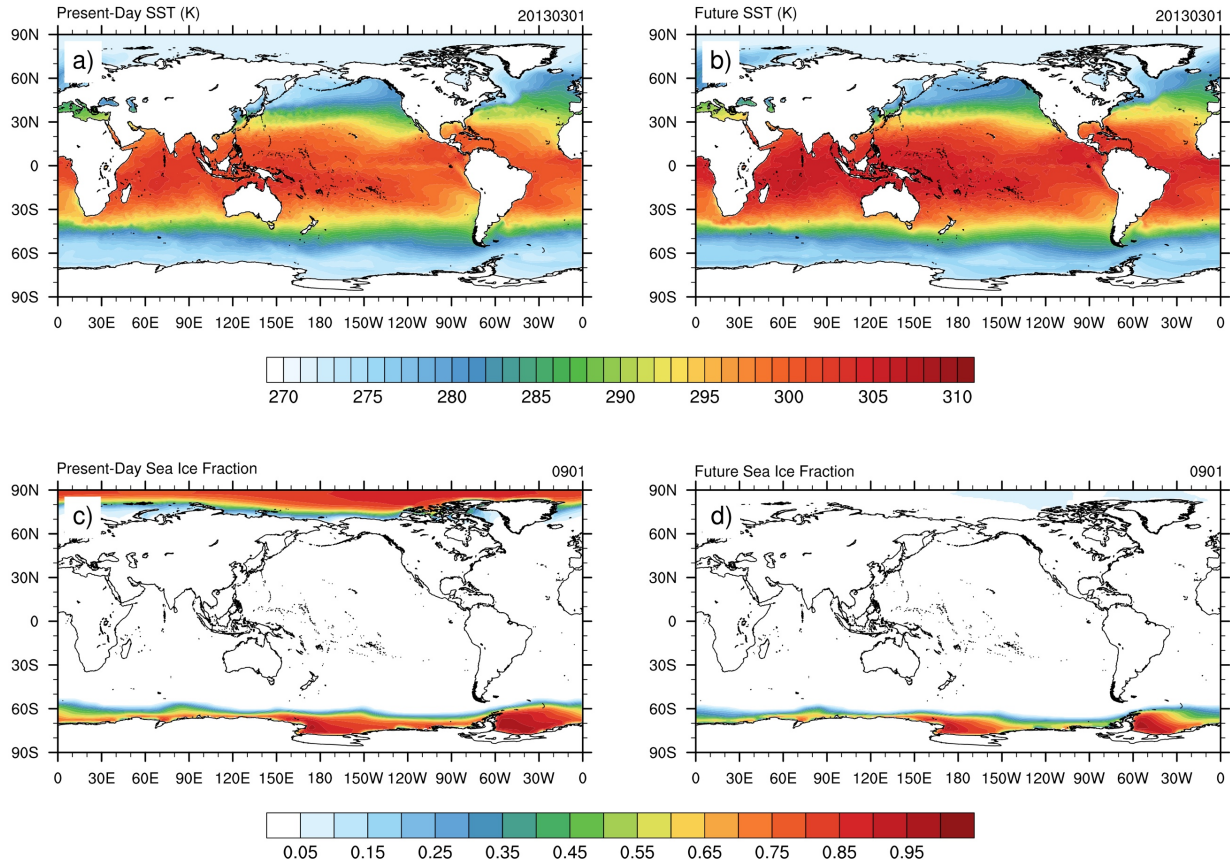


Figure 2.2: Example SST and sea ice fields. Example SST (K) on 1 March 2013 for (a) present-day MPAS simulation and (b) future and example sea ice fraction on 1 September for the (c) present-day MPAS simulations and (d) future MPAS simulations. Contours are shaded every 1-K in (a) and (b) and every 0.05 units in (c) and (d).

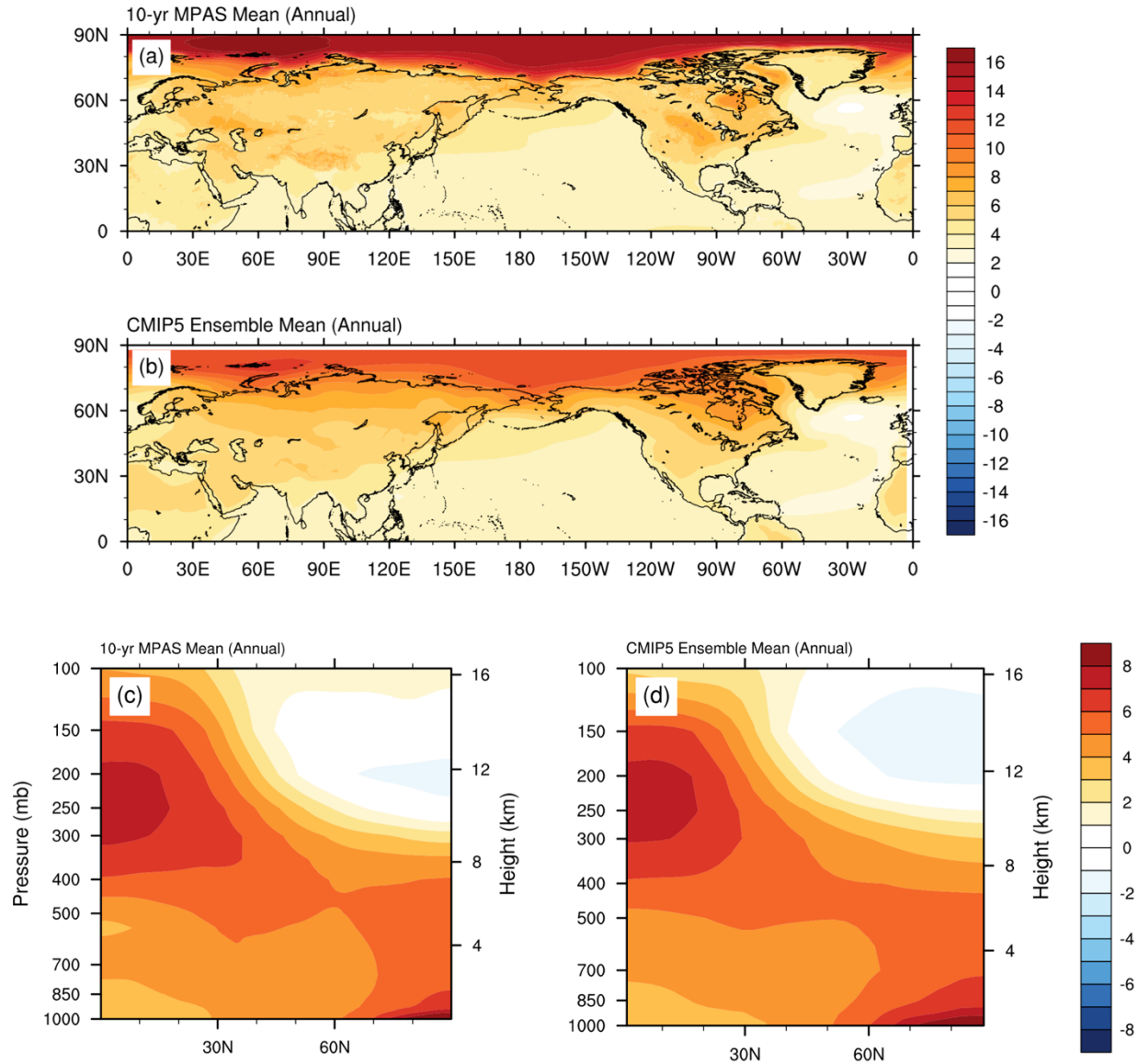


Figure 2.3: *Difference in average annual 2-m temperature and zonal mean temperature between MPAS simulations and CMIP5 GCM ensemble mean. (Top row) Average annual 2-m temperature difference (K; future minus current) for the (a) MPAS simulations and (b) CMIP5 GCM ensemble mean. (Bottom row) Average annual difference cross-section of zonal mean temperature (K; future minus current) for the (c) MPAS simulations and (d) CMIP5 GCM ensemble mean. Contours are shaded every 1-K in all panels.*

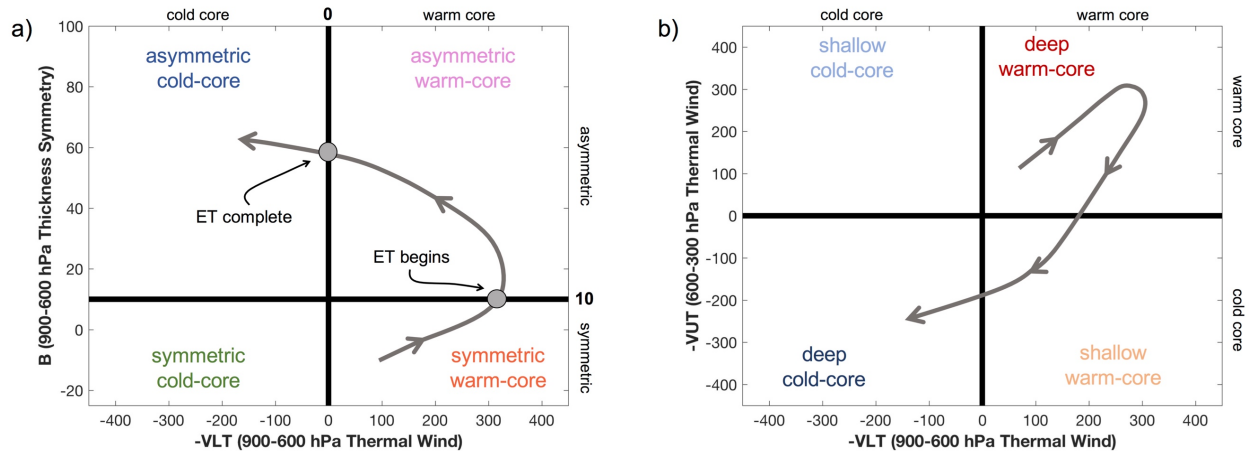


Figure 2.4: Overview of the cyclone phase space diagrams. Overview of the cyclone phase space (CPS) diagrams for (a) $-VLT$ vs. B and (b) $-VLT$ vs. $-VUT$.

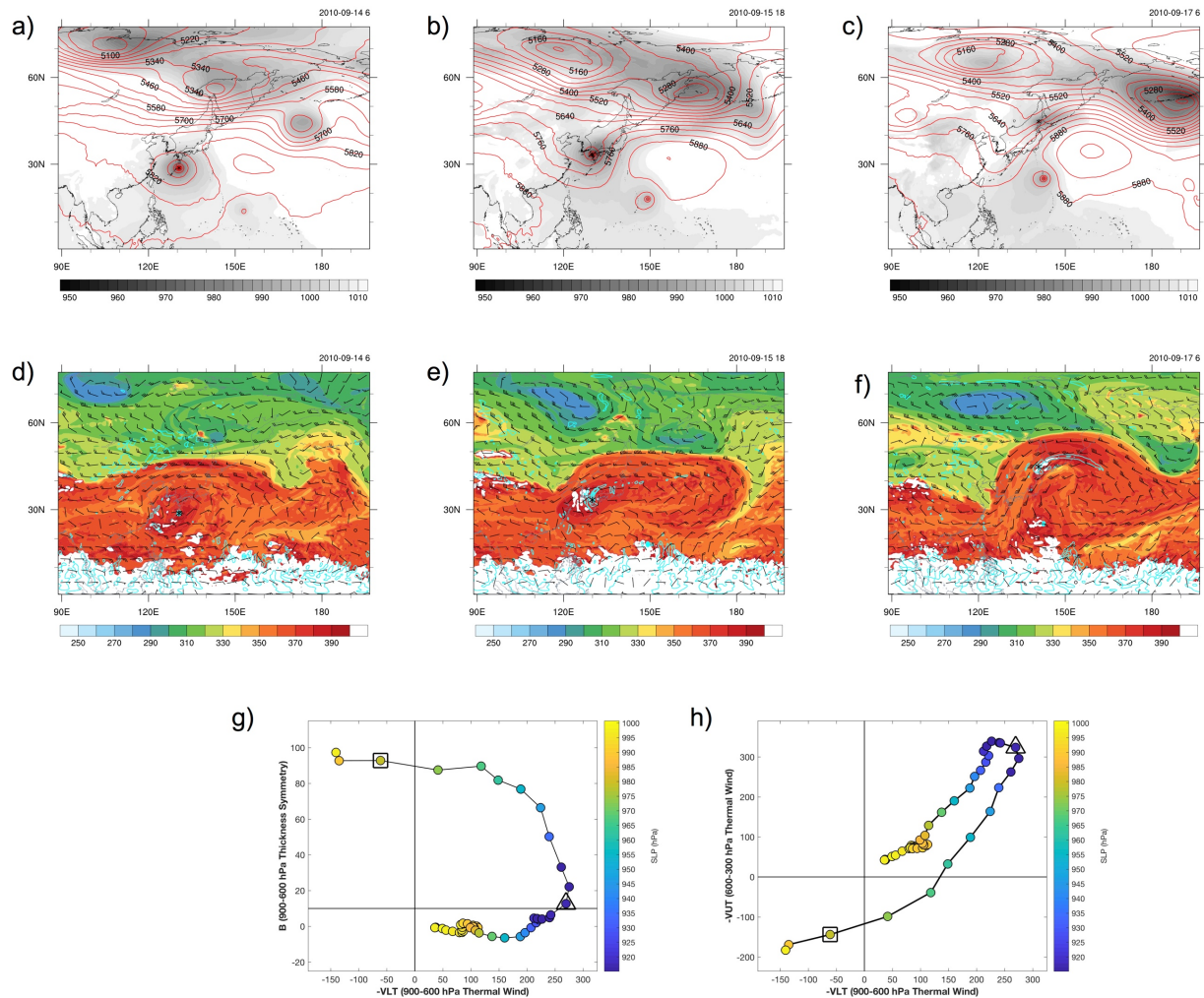


Figure 2.5: Overview of an example ET event. (a)–(c) 500-hPa heights (m; red contours) and SLP (hPa; shaded below 1010-hPa), (d)–(f) potential temperature on the dynamic tropopause (K; shaded), lower tropospheric potential vorticity (PVU; contoured from 0.5–2 PVU), and winds on the dynamic tropopause (barbs), and (g)–(h) CPS diagrams for an example ET event at the time of (left column) peak tropical intensity, (middle column) 18-h after ET onset, and (right column) ET completion. The black asterisks in (a)–(f) represent the cyclone center.

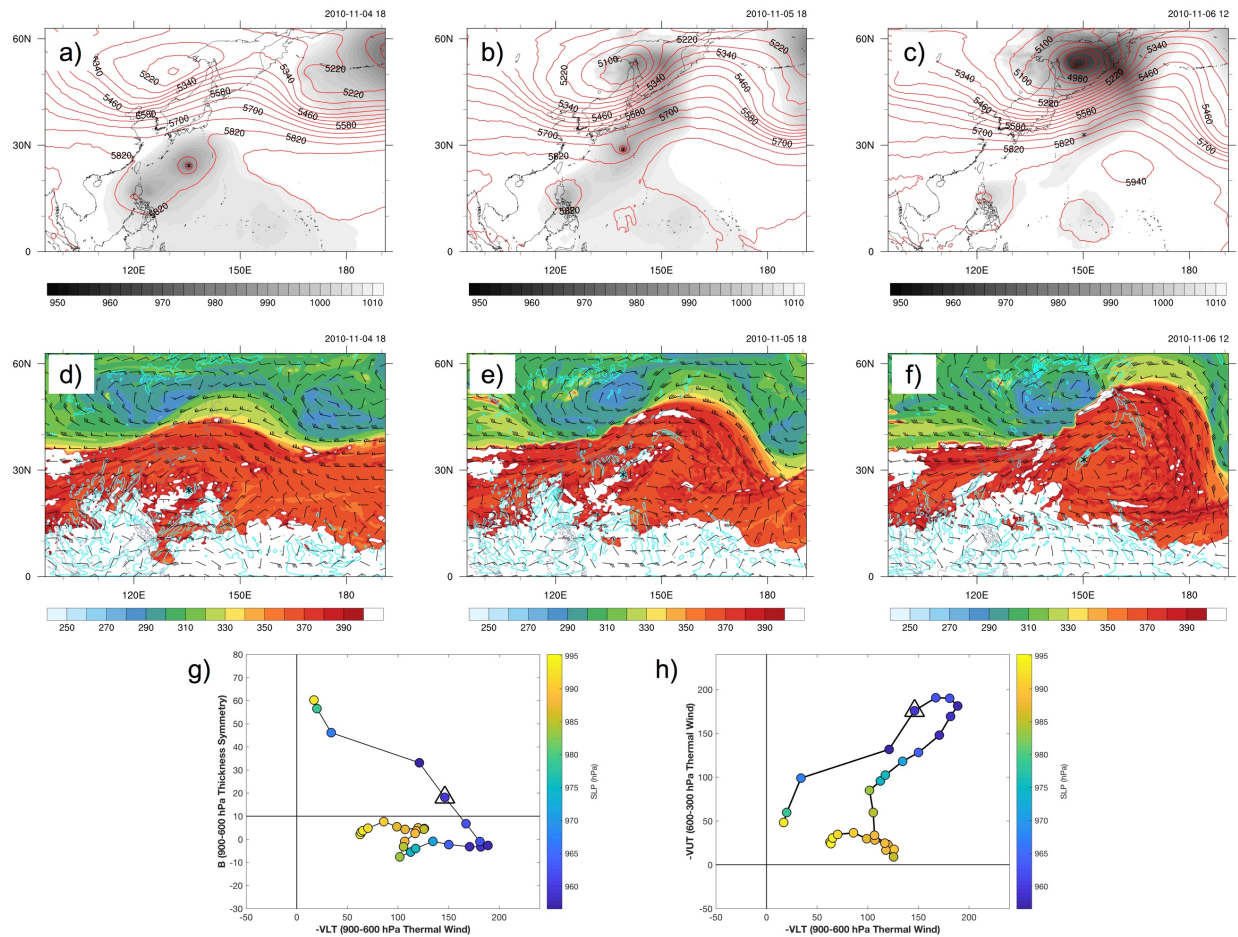


Figure 2.6: Overview of an example partial ET event. (a)–(c) 500-hPa heights (m; red contours) and SLP (hPa; shaded below 1010-hPa), (d)–(f) potential temperature on the dynamic tropopause (K; shaded), lower tropospheric potential vorticity (PVU; contoured from 0.5–2 PVU), and winds on the dynamic tropopause (barbs), and (g)–(h) CPS diagrams for an example partial ET event at the time of (left column) peak tropical intensity, (middle column) 6-h after ET onset, and (right column) the final time before dissipation. The black asterisks in (a)–(f) represent the cyclone center.

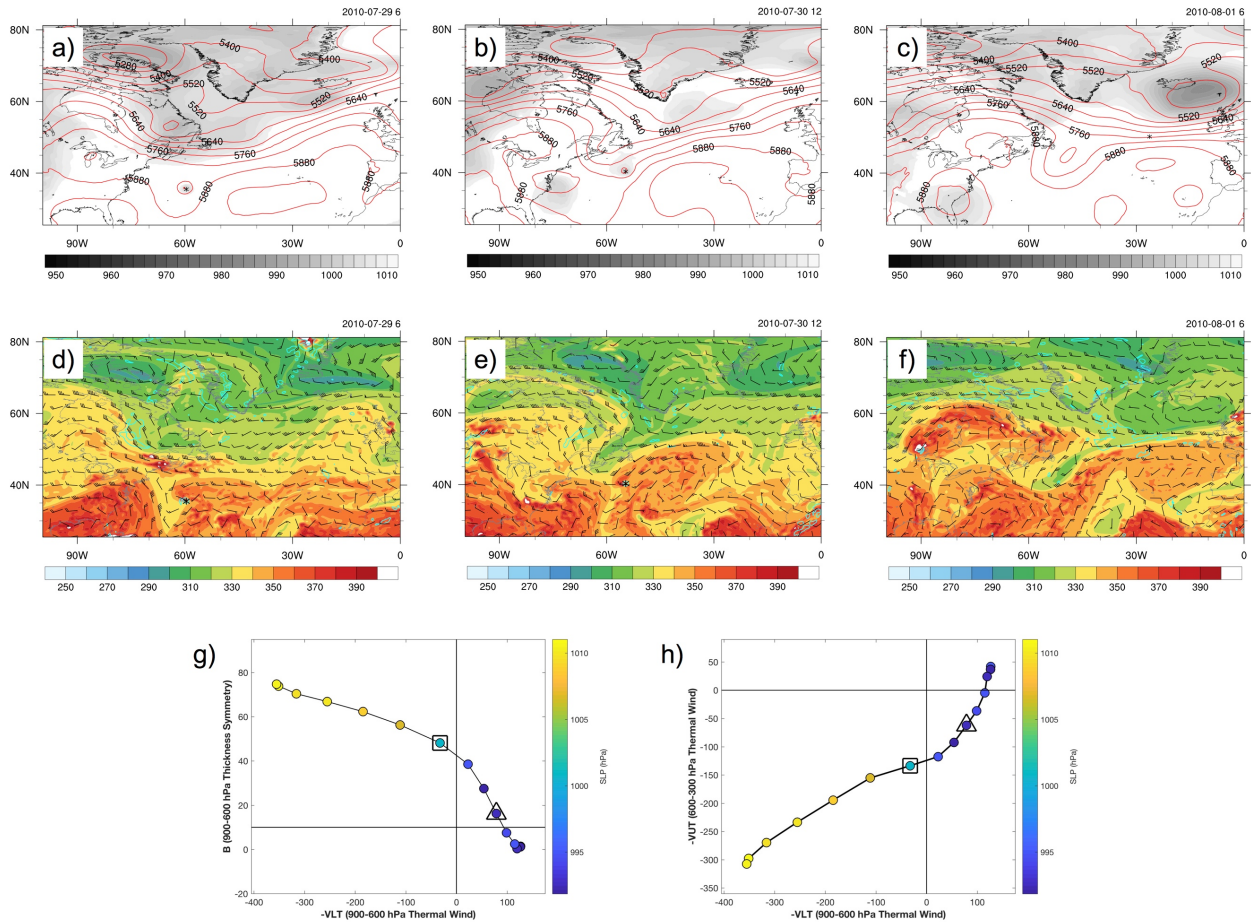


Figure 2.7: Overview of an example subtropical event. (a)–(c) 500-hPa heights (m; red contours) and SLP (hPa; shaded below 1010-hPa), (d)–(f) potential temperature on the dynamic tropopause (K; shaded), lower tropospheric potential vorticity (PVU; contoured from 0.5–2 PVU), and winds on the dynamic tropopause (barbs), and (g)–(h) CPS diagrams for an example subtropical event at the (left column) time of genesis, (middle column) time of ET onset, and (right column) 24-h after ET completion. The black asterisks in (a)–(f) represent the cyclone center.

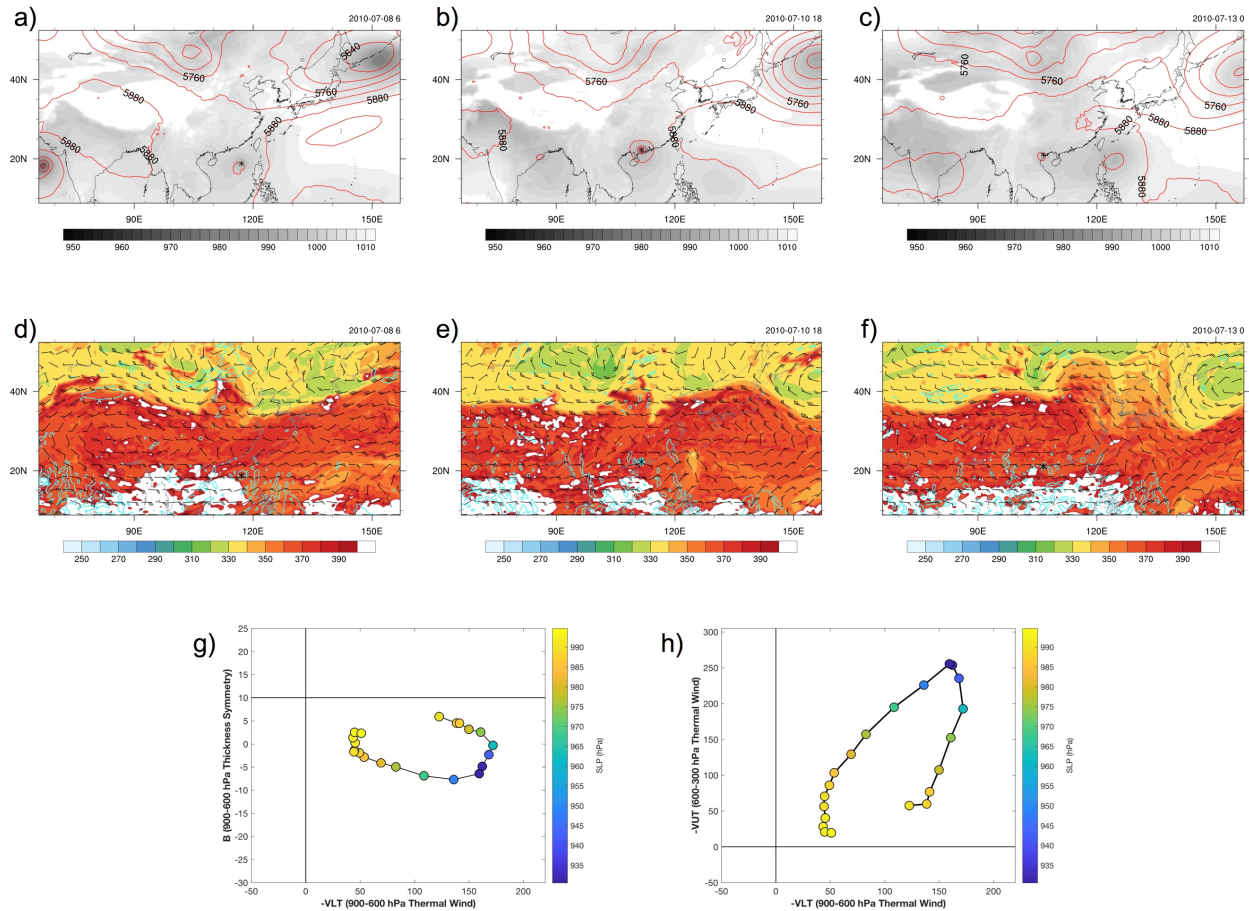


Figure 2.8: Overview of an example tropical event. (a)–(c) 500-hPa heights (m; red contours) and SLP (hPa; shaded below 1010-hPa), (d)–(f) potential temperature on the dynamic tropopause (K; shaded), lower tropospheric potential vorticity (PVU; contoured from 0.5–2 PVU), and winds on the dynamic tropopause (barbs), and (g)–(h) CPS diagrams for an example tropical event at the (left column) time of genesis, (middle column) time of ET onset, and (right column) 24-h after ET completion. The black asterisks in (a)–(f) represent the cyclone center.

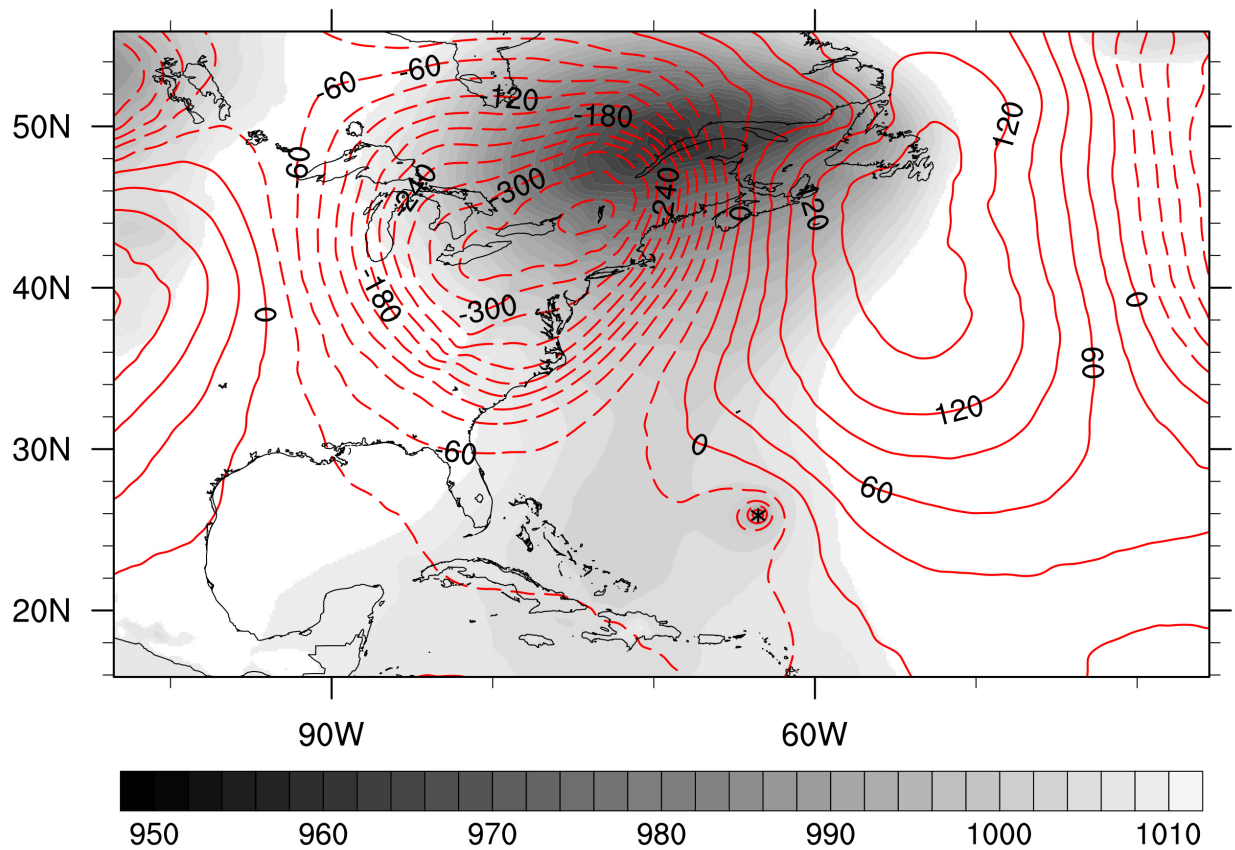


Figure 2.9: 500-hPa height anomaly and SLP for the reference ET case. 500-hPa height anomaly (m; red contours) and SLP (hPa; shaded below 1010-hPa) 12-h prior to ET onset for the 20 October 2013 reference case. Negative (positive) 500-hPa height anomaly contours are shown in dashed (solid) lines. The black asterisk represents the cyclone center.

3. Model Present-day Climatology

Sections 3.1–3.2 are largely adapted from Michaelis et al. (2018, submitted).

3.1. Precipitation and Midlatitude Features

3.1.1. Extratropical Storm Tracks

There are two primary midlatitude storm track regions in the Northern Hemisphere, the North Pacific and the North Atlantic, where baroclinic waves form over regions of enhanced temperature contrast linked to warm western boundary currents off the east coasts of Asia and North America and propagate eastward through downstream development (Chang et al. 2002). The extratropical cyclones in these regions play an essential role in the Earth’s climate system and contribute to everyday weather, including high-impact events. Therefore, it is important that they are well represented in model simulations.

As suggested by Chang and Fu (2003), variance in daily-mean fields can be used as proxies for storm track activity. Here, we use the 24-h variance of daily-mean SLP, calculated using equation (2) from Chang et al. (2013):

$$SLP \text{ variance} = \overline{[SLP(t + 24h) - SLP(t)]^2} \quad (3.1)$$

where the overbar indicates that the quantity is averaged over time, in this case over the winter season (December–February; DJF) when storm activity in the Northern Hemisphere is maximized (Chang et al. 2002; Brayshaw et al. 2009). Figure 3.1 shows the wintertime SLP variance for the MPAS simulations compared to the ERA-I. The ERA-I climatology in Fig. 3.1b is computed using only the ten simulation years. The North Pacific and North Atlantic storm track regions are clearly evident in the model simulations; the overall spatial correlation coefficient is greater than 0.98, indicating that general patterns of SLP variance are well reproduced in the MPAS simulations. As evident by the positive biases $\sim 35^\circ\text{N}$, 165°W and $\sim 40^\circ\text{N}$, 30°W (Fig. 3.1c), both storm track regions are shifted equatorward, and the North Pacific storm track is more zonally oriented in the MPAS simulations. Comparison with 100 random samples of 10-yr means from the ERA-I record indicates that these biases, primarily the shift in the North Pacific, likely represent true differences between the MPAS simulations and the real atmosphere. Negative biases in simulated storm activity occur east of Greenland, over

Scandinavia, and throughout central North America; these differences, however, fall within the range of observed variability (Fig. 3.1c).

3.1.2. Large-Scale Precipitation

Average precipitation over the ten simulation years compared to the 19-year (1998–2016) climatology from the Tropical Rainfall Measurement Mission (TRMM; Huffman et al. 2007) 3B42 product is shown in Figure 3.2. Because four of our ten simulation years occur before the TRMM record begins, we opted to use the full TRMM climatology for comparison. A pattern correlation coefficient of ~ 0.95 indicates that MPAS simulates the general spatial pattern of tropical precipitation well; the ITCZ in the equatorial Pacific and maxima along the west coast of India, over the Himalayas, and throughout northern South America are all well-represented by the model. The primary difference between the two precipitation fields is the overproduction of precipitation by MPAS in many areas (Fig. 3.2c), an issue common among high-resolution modeling studies (e.g., Bacmeister et al. 2014; Small et al. 2014). The overestimation in the southwestern Pacific basin (Fig. 3.2c) is primarily due to overproductions of summer and fall precipitation. The summer season is also responsible for the overproduction of precipitation through the Bay of Bengal and Gulf of Thailand, suggesting an overactive summer monsoon in the MPAS simulations. Another notable difference between MPAS and TRMM annual average precipitation is the westward shift of the heaviest precipitation along the ITCZ in the Atlantic basin. This shift in precipitation is likely related to a westward shift of the summertime African Easterly Jet (AEJ) maximum (Fig. 3.3).

3.1.3. CONUS Precipitation

An important aspect of our modeling study is the ability to represent climate regimes on a regional scale, such as precipitation patterns over the Contiguous United States (CONUS). Compared to the Parameter-elevation Regressions on Independent Slopes Model (PRISM) gridded precipitation data (Daly et al. 2008), MPAS simulates these precipitation patterns quite well with spatial correlation coefficients greater than 0.96 (Fig. 3.4a–f); orographic precipitation maxima in the Pacific Northwest and over the Appalachians, as well as maxima in precipitation along the Gulf Coast are clearly represented. The largest difference in annual precipitation is the model's general wet bias throughout the southern and western CONUS (Fig. 3.4g). This wet bias

is largely due to the overproduction of precipitation during the winter season. The absolute difference in DJF precipitation is most pronounced over terrain in the northwest and along the Gulf Coast (Fig. 3.4h), but the percent difference is largest throughout the central CONUS (Fig. 4.3k). On average, this positive bias during DJF amounts to ~65 mm, or a ~45% percent difference.

Summertime (June–August; JJA) precipitation (Fig. 3.4c,f), which is typically dominated by precipitation generated from organized convective systems, shows an apparent dry bias simulated by MPAS throughout the Great Plains and Florida (Fig. 3.4i,l). This dry bias over the Great Plains is a characteristic of several modeling studies (e.g., Klein et al. 2006; Bacmeister et al. 2014; Liu et al. 2017) and has been hypothesized to be a result of model deficiencies in reproducing the eastward propagation of organized mesoscale convective systems generated over the Rockies (Klein et al. 2006; Lee et al. 2008; Liu et al. 2017). Unfortunately, increasing resolution has not been shown to alleviate the issue (Bacmeister et al. 2014; Prein et al. 2015).

3.2. Tropical Cyclones

3.2.1. Strength

We compare simulated TC characteristics to the International Best Track Archive for Climate Stewardship (IBTrACS; Knapp et al. 2010). Only the IBTrACS for the ten simulated years (Table 2.1) are considered for comparison. Consistent with similar studies (e.g., Roberts et al. 2015), model storms are generally weaker than observed in terms of maximum 10-m wind speed; however, several simulated storms do attain a minimum SLP of less than 900 hPa (Fig. 3.5). Therefore, as in Roberts et al. (2015), storm intensity for the simulated TCs is measured by the minimum lifetime SLP of the storm in addition to maximum 10-m wind speed as defined by the Saffir-Simpson scale. Using the minimum SLP, categories are defined as >994-hPa for tropical storms (TS_p) and 980–994-hPa, 965–979-hPa, 945–964-hPa, 920–944-hPa, and <920-hPa for category (Cat_p) 1–5 equivalent tropical cyclones, respectively (Roberts et al. 2015). The subscript p is used to discriminate the SLP-based categories from those defined by the Saffir-Simpson wind speed thresholds. For IBTrACS, the maximum 10-m wind speed and minimum SLP across all reporting centers are used as the observed storm intensity for categorization.

Figure 3.6 shows the average TC frequency over the ten simulation years for the Northern Hemisphere as a whole, in addition to each basin. Our MPAS simulations generate an

excess of TC activity in the Northern Hemisphere, primarily due to the over-activity in the WNP basin. Simulated TC frequencies for the NATL, ENP, and NI basins are within the observed range. Across all basins, when categorizing TCs by minimum SLP (Fig. 3.6a), MPAS generally underestimates the number of weak systems (those with strengths less than Cat_p1), and overestimates the amount of Cat_p1 and Cat_p2 storms. The frequencies Cat_p3 TCs and stronger, on the other hand, are simulated reasonably well. With regard to TC categorization by maximum 10-m wind speed (Fig. 3.6b), MPAS simulates the frequency of TS strength TCs quite well in all basins. Strong storms (Cat4 and Cat5), however, are universally underestimated by the model in favor of Cat1–Cat3 TCs.

3.2.2. Location

Spatially, the model simulated TC track density compares reasonably well with observations; the pattern correlation coefficient is about 0.7 (Fig. 3.7). The most prominent difference is the lack of storm activity in the eastern portion of the NATL basin, which is common among several similar modeling studies (e.g., Bell et al. 2013; Strachan et al. 2013; Small et al. 2014; Roberts et al. 2015). TC genesis in this region typically occurs during August and September (Kossin et al. 2010; Daloz et al. 2015); comparison between the model and ERA-I monthly averaged 850–200-hPa vertical wind shear across the ten simulation years for these months shows a strong positive bias in the model over the NATL development region that is likely a primary factor in this lack of TC generation (Fig. 3.8). Fig. 3.7 does not show a strong track density bias in the Gulf of Mexico. Roberts et al. (2015) notes that a steady supply of vorticity in the Caribbean was a contributing factor to their overestimation of track density in this area; thus, it is possible that tracking TCs as SLP minima, rather than maxima in 850-hPa relative vorticity helps alleviate this bias. Unlike Small et al. (2014) and Roberts et al. (2015), we do not find a positive track density bias in the central North Pacific; instead, we see a slight underrepresentation of TC activity in that area.

3.2.3. Seasonal Cycle

Aside from the underestimation in August and September (likely attributed to the lack of TC genesis in the eastern portion of the basin), MPAS simulates the present-day seasonal TC cycle for the NATL reasonably well; TC activity increases during the spring and summer seasons

and reaches a maximum in the fall (Fig. 3.9a). For the ENP, MPAS produces too many storms in the springtime (April and May) and too few storms during the summer months (Fig. 3.9b). As defined by Camargo et al. (2008), cluster 2 type ENP TCs generate off the coast of Mexico, travel towards the northwest along the coastline, and have a bimodal seasonal distribution with peaks in late spring/early summer and early fall, similar to the modeled cycle in Fig. 3.9b. Compared to the ERA-I ten-year climatology, enhanced westerlies at 500-hPa and 850-hPa between 0–20°N in the eastern portion of the ENP basin for May (Fig. 3.10) suggest that our simulations may be in a regime more conducive to cluster 2 storms. For the WNP (Fig. 3.9c), MPAS correctly simulates the fall peak in TC activity; however, there is a secondary peak in April that does not match observations. Although there is a general overestimation of storm activity in the NI basin, the model does replicate the shape of the seasonal cycle with both the early summer and mid-fall peaks represented, albeit the fall peak occurs a month earlier than observed (Fig. 3.9d).

3.3. Extratropical Transition

Due to the low frequency of ET in the ENP (e.g., Wood and Ritchie 2014; Bieli et al. 2018, submitted), we only evaluate the present-day MPAS ET climatology for the NATL and WNP basins in this chapter; Chapters 4 and 5 will examine future changes in ET. As discussed in Section 2.3, an MPAS cyclone must maintain tropical characteristics for at least the first 1.5 days of its lifetime, and satisfy both CPS criteria ($B > 10$ and $-VLT < 0$) for at least 12-h to be considered an ET event. For IBTrACS, the “ET” tag in the recorded track defines a storm as an ETC; therefore, we use the “ET” tag as a declaration of ET completion. Here, we include all IBTrACS cyclones that were categorized as an ETC at any point during their lifetime, excluding first 1.5 days to be consistent with our MPAS definition (i.e., a TC is not included for analysis if it begins as an ETC and undergoes tropical transition). IBTrACS ET declaration is based on various forecasters subjective interpretation of satellite imagery and surface observations (e.g., Hart and Evans 2001; Kitabatake 2011; Zarzycki et al. 2017); detection of ET in the MPAS simulations is objective using the CPS. As in Section 3.2, only the IBTrACS for the ten simulated years (Table 2.1) are considered for comparison with the present-day MPAS simulations. Additionally, any unnamed storms are removed from IBTrACS prior to analysis to remain consistent with previous work (e.g., Zarzycki et al. 2017).

3.3.1. Frequency and Seasonal Cycle

The number of TCs, ET events, and percentage of TCs that undergo ET are recorded in Table 3.1. For the NATL, the IBTrACS 10-yr ET percentage is lower than range of previously published estimates for this basin (~35% compared to 42–55%; Hart and Evans 2001; Jones et al. 2003; Zarzycki et al. 2017; Bieli et al. 2018, submitted). However, calculation of percent transition for IBTrACS from 1980–2002 resulted in 46% of TCs undergoing ET, consistent with Zarzycki et al. (2017). Additionally, the IBTrACS 10-yr ET percentage is well within the range of observed variability (Table 3.1). For the WNP, the IBTrACS 10-yr percent transition is within the range of published estimates (~37% compared to 28–49%; Klein et al. 2000; Kitabatake 2011; Bieli et al. 2018, submitted). The ET percentages for the present-day MPAS simulations are slightly lower than IBTrACS for both the NATL and WNP basins, but still fall well within range of variability (Table 3.1).

In the NATL, the number of ET events in the present-day MPAS simulations increases from June to July, reaches a maximum in September, and decreases thereafter (Fig. 3.11a). This seasonal cycle in the latter portion of the TC season is consistent with IBTrACS (Fig. 3.11c) and previous studies (Hart and Evans 2001; Zarzycki et al. 2017; Bieli et al. 2018, submitted). MPAS does produce too many ET events in the shoulder months surrounding the TC season, primarily due to the overproduction of TCs. There is little correlation in the seasonality of the fraction of TCs undergoing ET between IBTrACS and MPAS (Fig. 3.11a,c). For example, a secondary maximum in IBTrACS ET percentage occurs in June when the fraction of TCs that undergo ET is at an absolute minimum in the MPAS simulations. The seasonality in percent transition produced by the MPAS simulations somewhat resembles the ERA-I seasonal cycle presented by Zarzycki et al. (2017, their Fig. 7) with maxima in July and September and minimums in June and October. Studholme et al. (2015) also showed a seasonal cycle for the NATL with relatively high ET percentages from July through October (their Fig. 13), not unlike what is shown here for the MPAS simulations (Fig. 3.11a). According to Hart and Evans (2001), the highest percentage of ET events occurs in the late fall when the baroclinically favorable and tropically favorable regions are closest together. Our MPAS simulations instead show ET percentage maximized in late summer/early fall. Overall, there is large variation in the literature regarding the seasonality of percent transition for the NATL (Hart and Evans 2001; Studholme et al 2015; Zarzycki et al. 2017; Bieli et al. 2018, submitted).

With the exception of April, which has too many TCs and ET events, the seasonality in the number of ET events in the WNP simulated by MPAS compares well with IBTrACS; there is an increase in frequency through the beginning of the TC season, reaching a maximum in August, and declining thereafter (Fig. 3.11b,d). For the MPAS simulations, the highest fraction of TCs undergoing ET occurs in June; May, July–September, and November also have relatively high percentages. The fraction of ET events is lowest in December and October (Fig. 3.11b). The IBTrACS ET percentages over the ten simulation years are also highest in May, June, August, and September, and lowest in December (Fig. 3.11d). One of the largest discrepancies between the simulated and observed seasonality of percent transition occurs in the late spring/early summer where the fraction of TCs undergoing ET declines from May to June in IBTrACS, but increases over the same time period in the MPAS simulations. Additionally, IBTrACS shows a consistent decrease in ET percentage from August through November; the MPAS simulations, with a local maximum occurring in November, do not. While variations in the seasonality of percent transition are apparent throughout the literature, one consistent pattern for the WNP is a peak in ET percentage occurring around May–June and a secondary maximum occurring in September or October (Kitabatake 2011; Studholme et al. 2015; Bieli et al. 2018, submitted). This same pattern is evident in the MPAS simulations (Fig. 3.11b), albeit we also see a tertiary maximum in November.

3.3.2. Location of ET

Upon initial visual inspection, there does not appear to be a systematic latitudinal difference in the location of ET completion between IBTrACS and MPAS. The tracks of ET events in the MPAS simulations do extend farther east, particularly in the WNP, leading to an apparent larger zonal variation in the location of ET completion (Fig. 3.12). Because we categorize cyclones into basins based on genesis location, there are a small number of storms in the MPAS simulations that generate in the NATL, but propagate into the ENP. However, these storms represent a small fraction of the total ET events (<5%) and therefore, should not significantly influence our results.

Comparison of the median latitude and longitude of ET completion for all ET events over the ten simulation years quantitatively highlights potential biases. Generally, the distributions of ET completion location compare well between IBTrACS and MPAS (Fig. 3.13a–b). In both

NATL and WNP basins, ET does occur slightly farther south (by 0.5° and 1.2°, respectively) and east (by 8° and 3°, respectively) in the MPAS simulations (Table 3.2), but these changes are not found to be statistically significant. Additionally, the MPAS simulations present a larger amount of variation in ET location (Fig. 3.13a–b). Zarzycki et al. (2017) also showed a larger range in the location of ET in their model simulations compared to reanalyses (their Fig. 9).

With the exception of June, the IBTrACS seasonal cycle for latitude of ET completion in the NATL shows an increase from July to August, a maximum in September, and a decrease from September to November (Fig. 3.13c). This seasonality is similar to Bieli et al. (2018, submitted, Fig. 9). The seasonal cycle simulated by MPAS for the NATL is different; the latitude of ET completion remains fairly steady from July through October, and then decreases thereafter (Fig. 3.13c). Establishing a robust seasonal cycle of ET completion latitude, however, is difficult given that sample sizes for both IBTrACS and MPAS are small (e.g., most months including less than ten ET events).

The ET completion latitude seasonality in IBTrACS over the ten simulation years for the WNP basin generally shows an increase from June to September, a peak in September, and a decrease from September to December (Fig. 3.13d). Again, this seasonal cycle is similar to that shown by Bieli et al. (2018, submitted, their Fig. 9), except their maximum latitude is reached in August. The seasonality simulated by MPAS for the WNP mimics IBTrACS and Bieli et al. (2018, submitted, their Fig. 9) with an increase in ET completion latitude through the summer, a maximum in August, and a decrease thereafter (Fig. 3.13d). Sample sizes for the WNP are larger than the NATL for both IBTrACS and MPAS, but there are still several months with less than ten storms; larger sample sizes would allow for a better representation of a seasonal cycle in the latitude of ET completion.

Table 3.1: Number of TCs, ET events, and percent of TCs that undergo transition in the North Atlantic and Western North Pacific basins over the 10 simulations years for IBTrACS and present-day MPAS simulations. The percent transition range of internal variability for IBTrACS is determined by calculating the percent of transitioning TCs for 100 10-yr samples.

Basin	Data Source	Number of TCs	Number of ET Events	% Transition	% Transition: Range of Observed Variability
North Atlantic	IBTrACS	141	49	34.8	20.4–47.1
	MPAS	189	60	31.7	
Western North Pacific	IBTrACS	300	112	37.3	29.9–43.8
	MPAS	475	154	32.4	

Table 3.2: Median latitude (°N) and longitude (°E) of ET for TCs that undergo transition in the North Atlantic and Western North Pacific basins over the 10 simulations years for IBTrACS and present-day MPAS simulations.

Basin	Data Source	Median Latitude (°N)	Median Longitude (°E)
North Atlantic	IBTrACS	40.4	304.5
	MPAS	39.9	312.5
Western North Pacific	IBTrACS	38.7	149.9
	MPAS	37.5	152.9

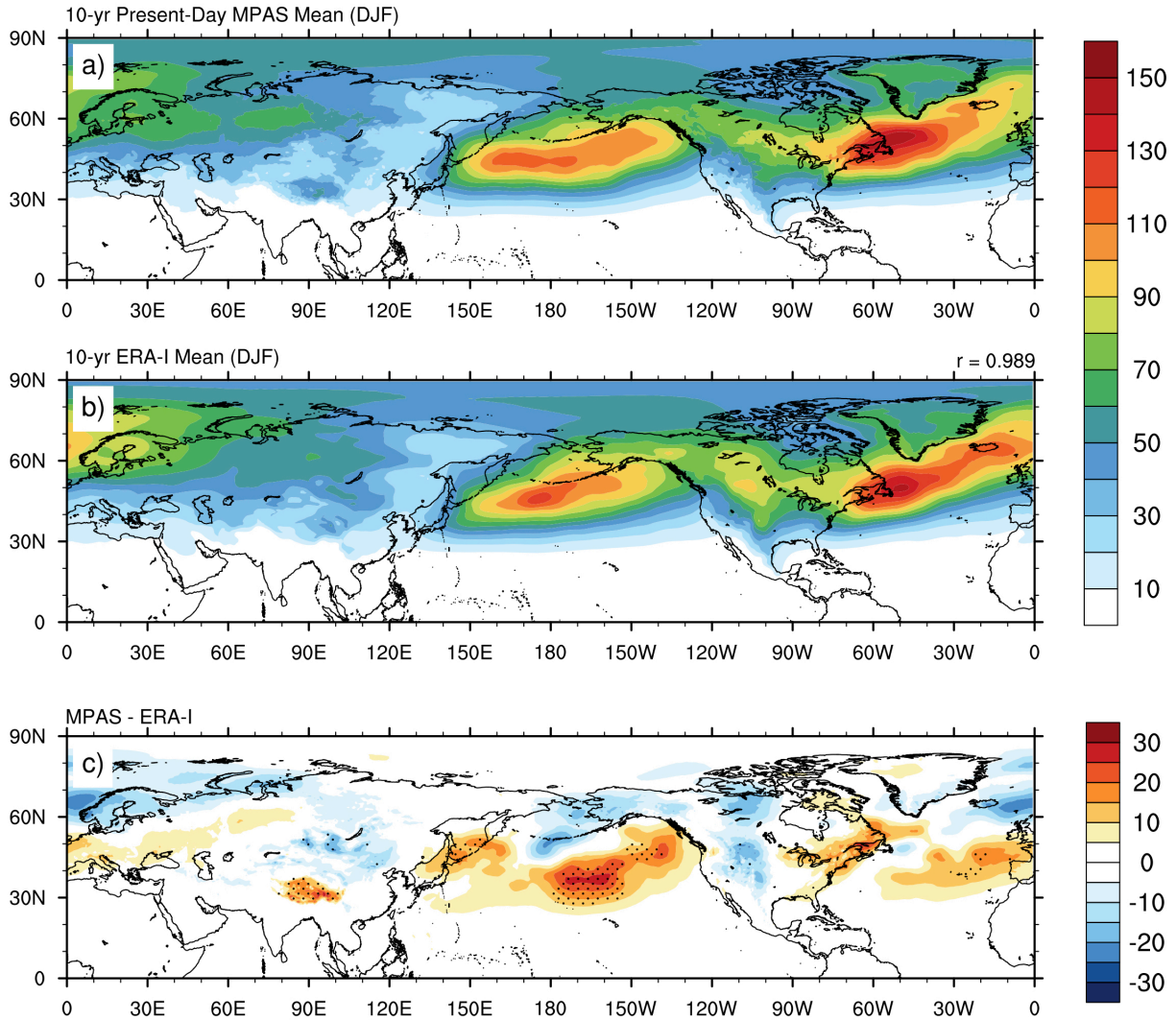


Figure 3.1: Average wintertime SLP variance for present-day MPAS simulations vs. ERA-I climatology. Average wintertime (DJF) SLP variance (hPa^2) over the ten simulation years for (a) present-day MPAS simulations, (b) ERA-I 10-yr climatology, and (c) the model bias (MPAS minus ERA-I). Contours are shaded every 10 hPa^2 in (a) and (b) and every 5 hPa^2 in (c). MPAS output were linearly interpolated to the ERA-I grid for point-to-point comparison. The pattern correlation coefficient is reported at the top-right of (b). Stippling in (c) indicates locations where the MPAS 10-yr mean exceeds the range computed from 100 random samples of 10-yr means from ERA-I by more than 5% ($\sim 7 \text{ hPa}^2$).

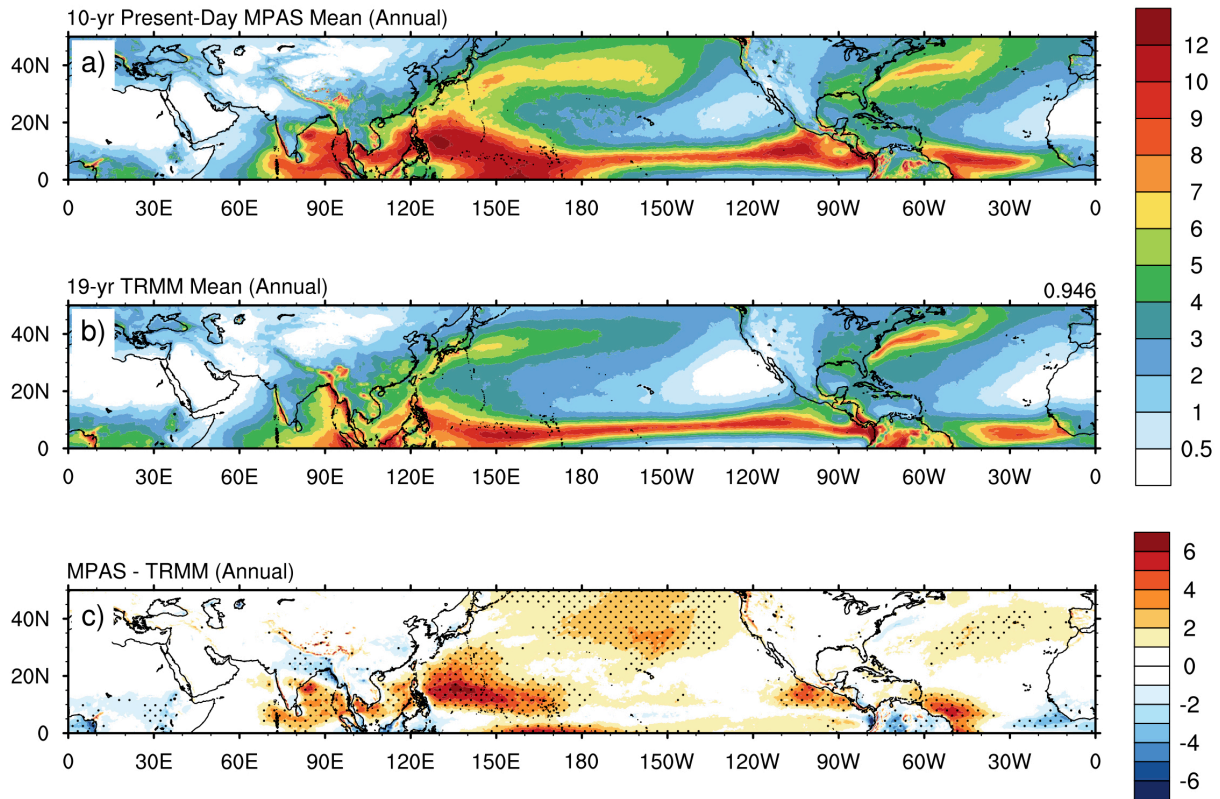


Figure 3.2: Average total annual precipitation for present-day MPAS simulations vs. TRMM climatology. Average total annual precipitation (mm/day) for (a) present-day MPAS simulations, (b) TRMM 19-yr climatology, and (c) the model bias (MPAS minus TRMM). MPAS output were linearly interpolated to the TRMM grid for point-to-point comparison. Pattern correlation coefficient is reported in the top-right of (b). Stippling in (c) indicates locations where the MPAS 10-yr mean exceeds the range computed from 100 random samples of 10-yr means from TRMM by more than 5% (~1.2 mm/day).

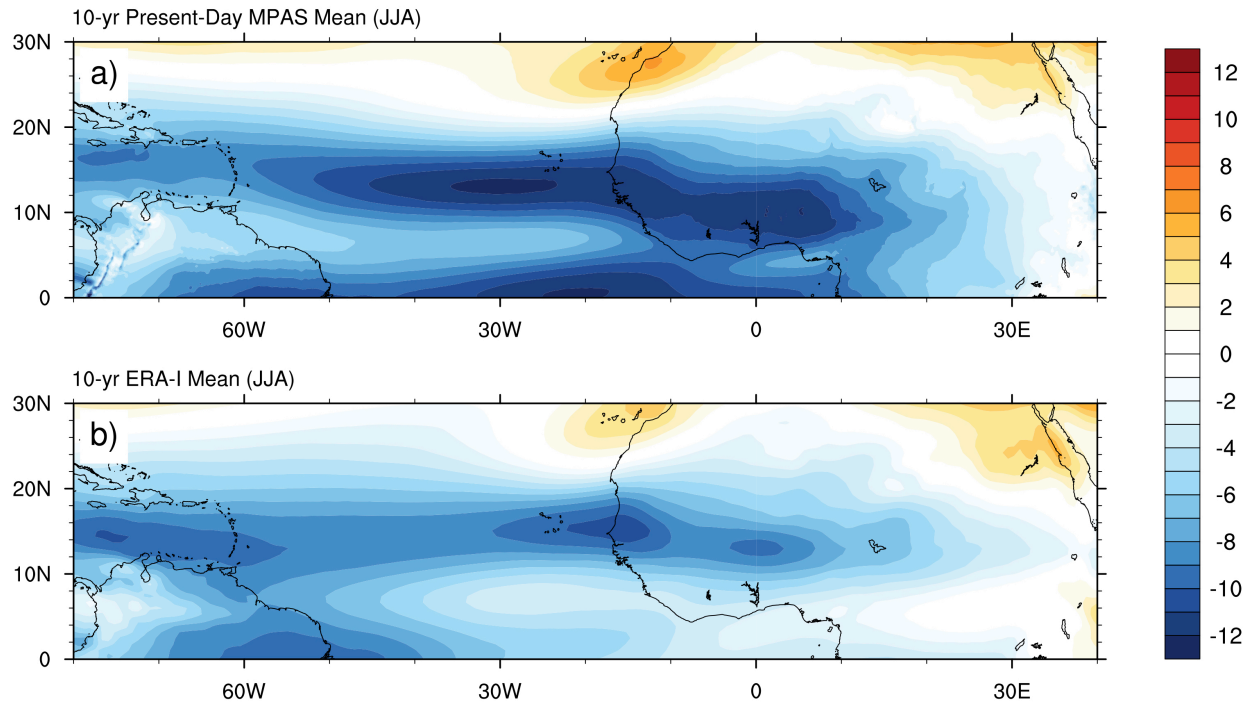


Figure 3.3: Average summertime 700-hPa zonal wind speed for present-day MPAS simulations vs. ERA-I climatology. Summertime (JJA) average 700-hPa zonal wind speed (m/s) over the ten simulation years for (a) present-day MPAS simulations and (b) ERA-I 10-yr climatology. Contours are shaded every 1-m/s.

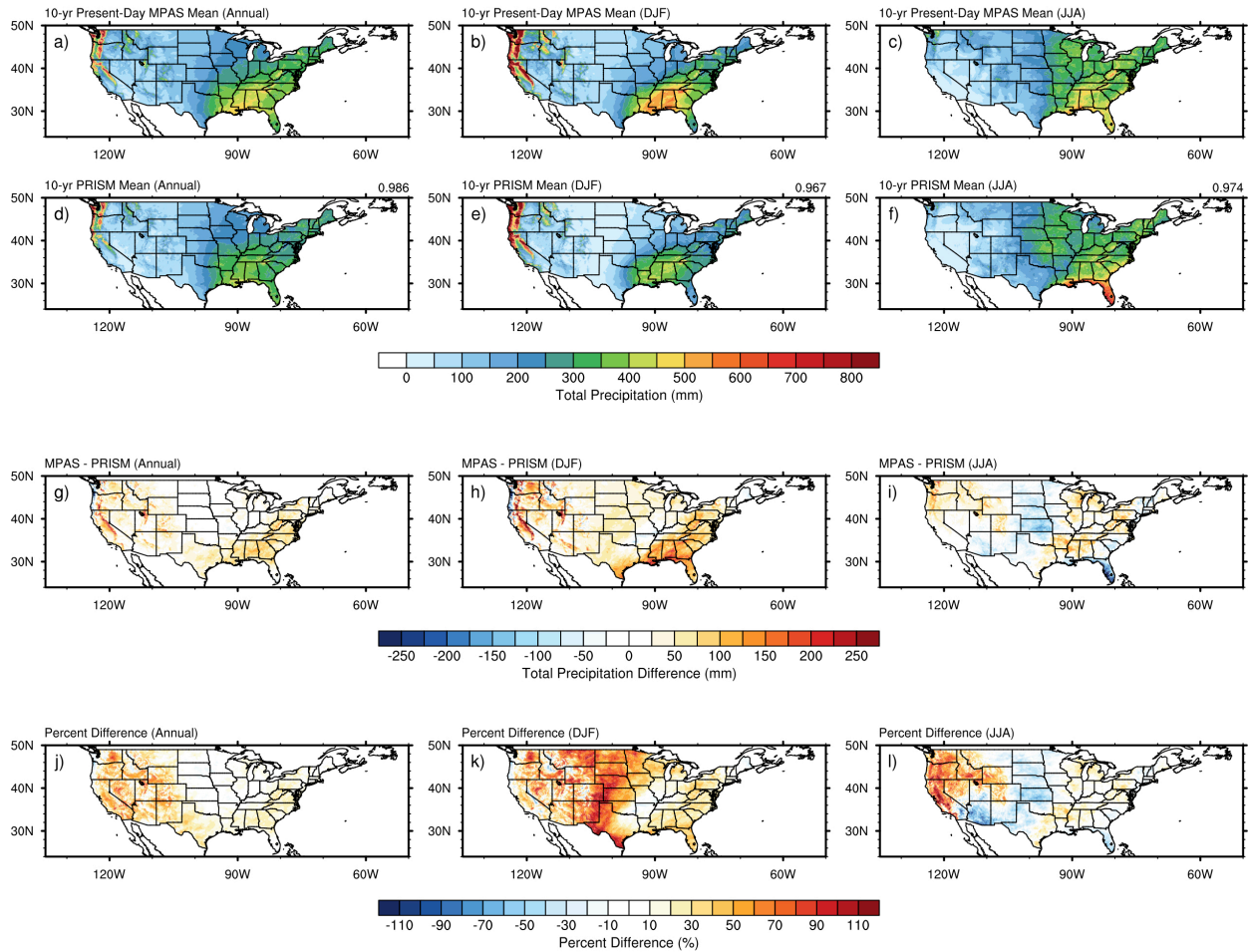


Figure 3.4: Average total precipitation for present-day MPAS simulations vs. PRISM climatology. Average total precipitation (mm) over the ten simulation years for (a)–(c) present-day MPAS simulations, (d)–(f) PRISM 10-yr climatology, (g)–(h) model bias (MPAS minus PRISM), and (j)–(l) model percent difference for (left column) annual precipitation, (middle column) wintertime (DJF) precipitation, and (right column) summertime (JJA) precipitation. PRISM data were linearly interpolated to the MPAS grid for point-to-point comparisons. Pattern correlation coefficients are reported in the top-right of panels (d)–(f).

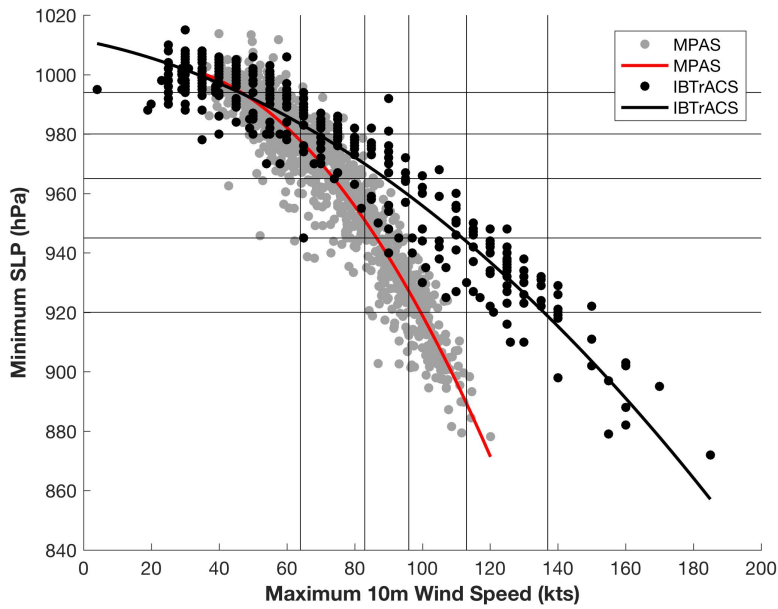


Figure 3.5: *Maximum 10-m wind speed vs. minimum SLP for observed and simulated TCs.* Scatter plot of maximum 10-m wind speed (kts) versus minimum SLP (hPa) for IBTrACS (black) and present-day MPAS (gray) Northern Hemispheric TCs. The lines of best fit for each (IBTrACS in black and MPAS in red) were computed using a second-order polynomial. The wind (SLP) category thresholds are indicated by the vertical (horizontal) lines.

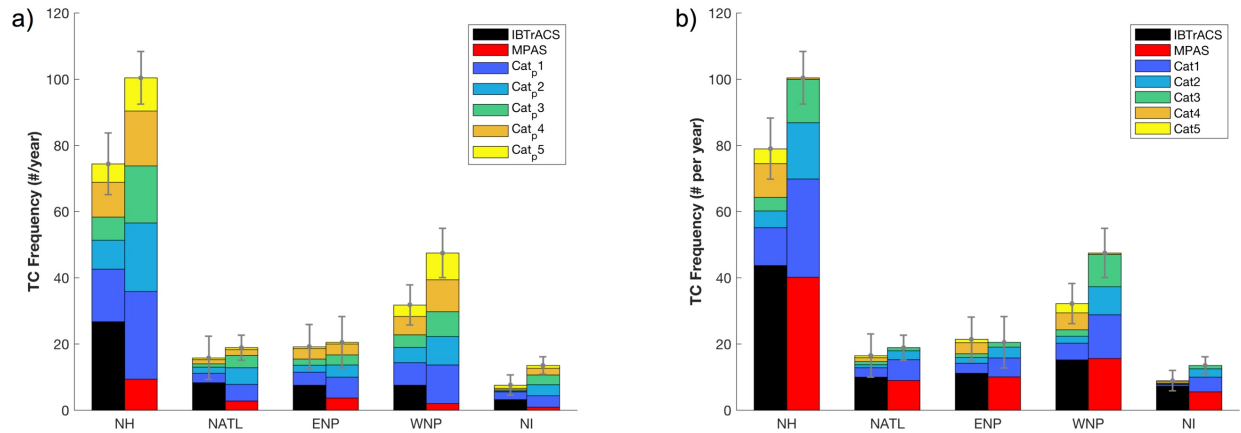


Figure 3.6: Average number of observed and simulated TCs for the Northern Hemisphere and each Northern Hemisphere basin. Average number of TCs over the ten simulation years for the Northern Hemisphere and each Northern Hemisphere basin. Columns are colored by intensity categories based on (a) minimum lifetime SLP and (b) maximum lifetime 10-m wind speed. The bottom color represents intensities of tropical storm strength or less for IBTrACS and MPAS in the first and second columns, respectively. Categories 1–5 are shaded for both data sets according to the legend. The error bars indicate the interannual standard deviation. The number of TCs for IBTrACS varies based on strength metric due to the lack of SLP records for a select number of storms.

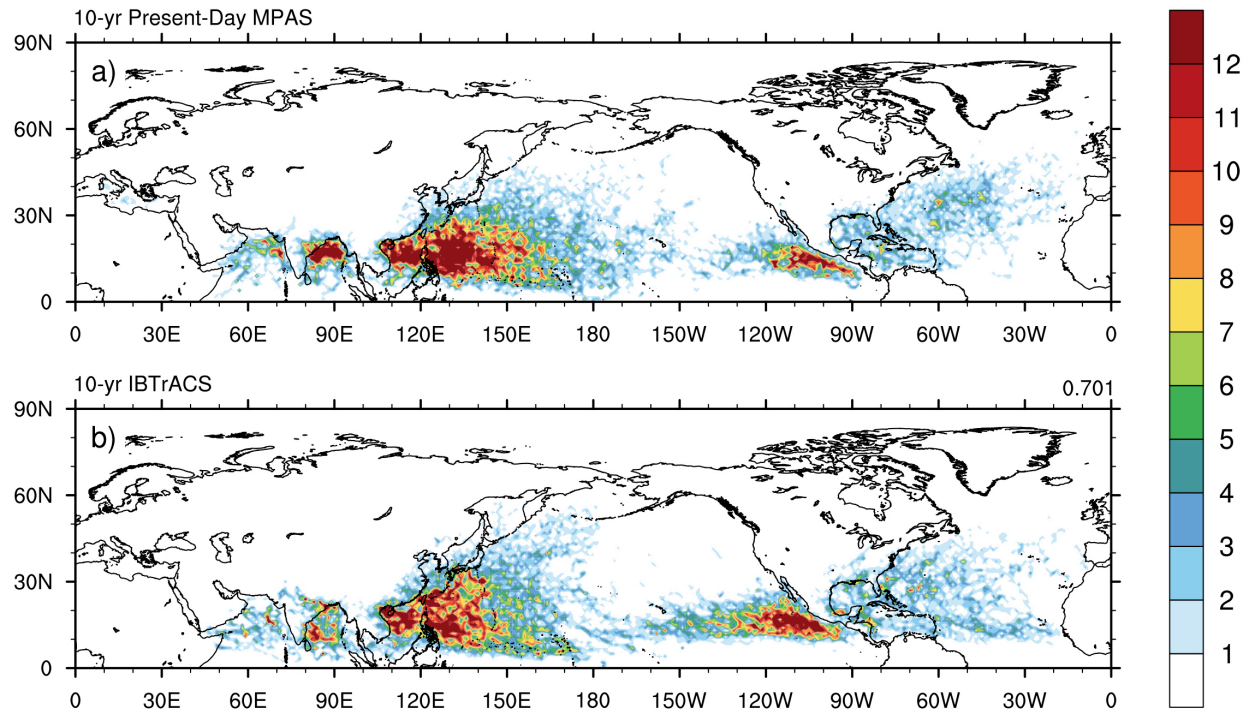


Figure 3.7: TC track density for present-day MPAS simulations vs. IBTrACS. Track density (number of cyclone tracks per $1^\circ \times 1^\circ$ area) over the ten simulated years for (a) present-day MPAS simulations and (b) IBTrACS. Contours are shaded every 1 count.

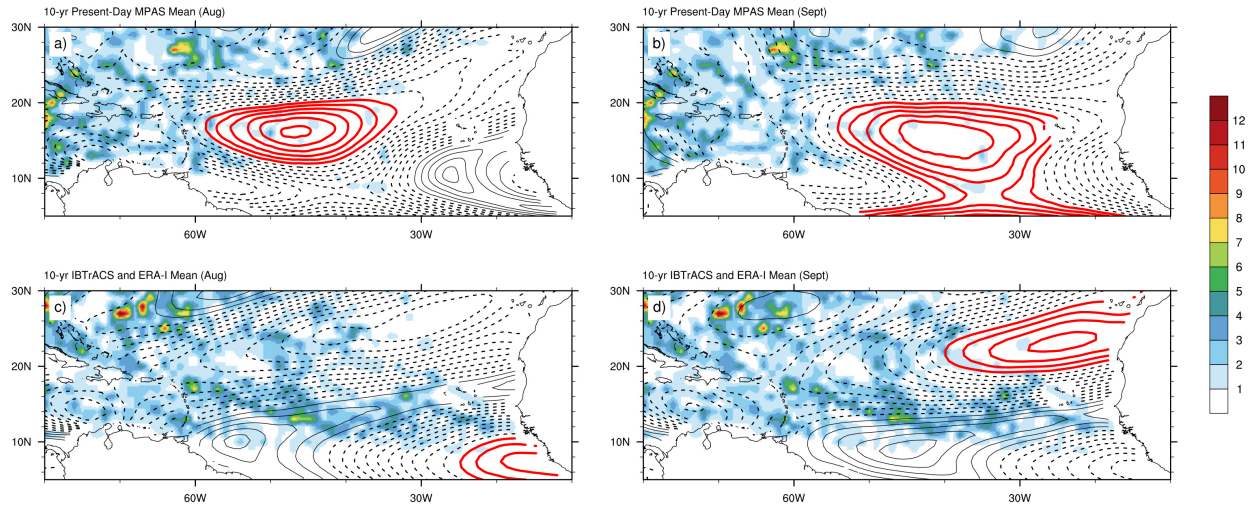


Figure 3.8: TC track density and 850–200-hPa vertical wind shear for present-day MPAS simulations vs. IBTrACS and ERA-I. Track density (number of cyclone tracks per $1^\circ \times 1^\circ$ area; shaded) and 850–200-hPa vertical wind shear (m/s; contoured) over the ten simulated years for (a)–(b) present-day MPAS simulations and (c)–(d) IBTrACS and ERA-I for (left column) August and (right column) September. Track density is shaded every 1 count. Vertical wind shear is contoured every 1-m/s. Vertical wind shear values less than 5-m/s are contoured in solid black lines, values between 5-m/s and 15-m/s are contoured in dashed black lines, and values greater than 15-m/s are contoured in solid red lines.

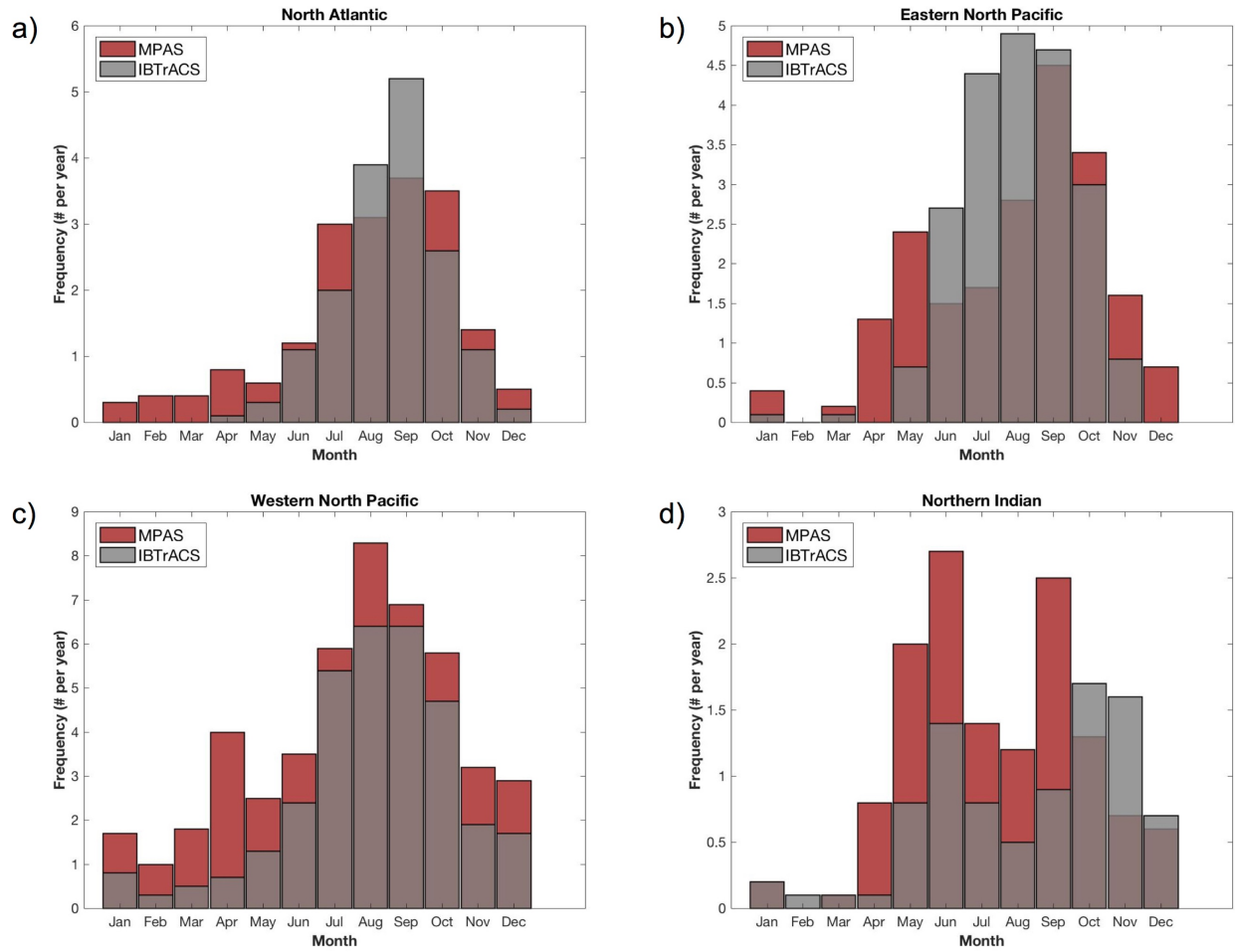


Figure 3.9: Monthly average TC frequency for present-day MPAS simulations vs. IBTrACS. Monthly average TC frequency over the ten simulated years for the (a) North Atlantic, (b) Eastern North Pacific, (c) Western North Pacific, and (d) Northern Indian basins. The frequencies for IBTrACS (MPAS simulations) are shown in the gray (red) bars.

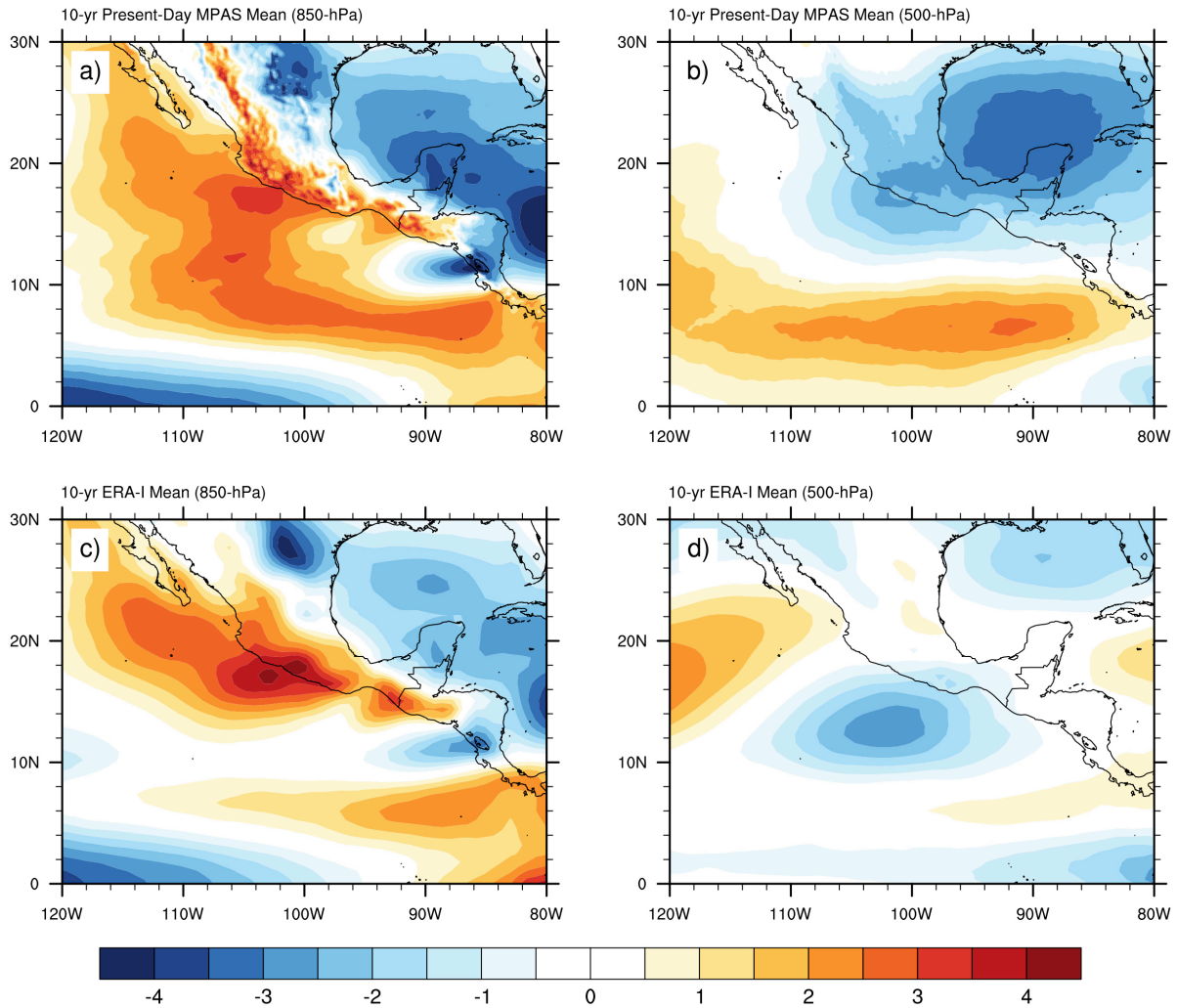


Figure 3.10: Average zonal wind anomalies at 850-hPa and 500-hPa for present-day MPAS simulations vs. ERA-I climatology. Average zonal wind anomalies (m/s) over the ten simulation years for the month of May at (left column) 850-hPa and (right column) 500-hPa for (a)–(b) present-day MPAS simulations and (c)–(d) ERA-I 10-yr climatology. Contours are shaded every 0.5-m/s.

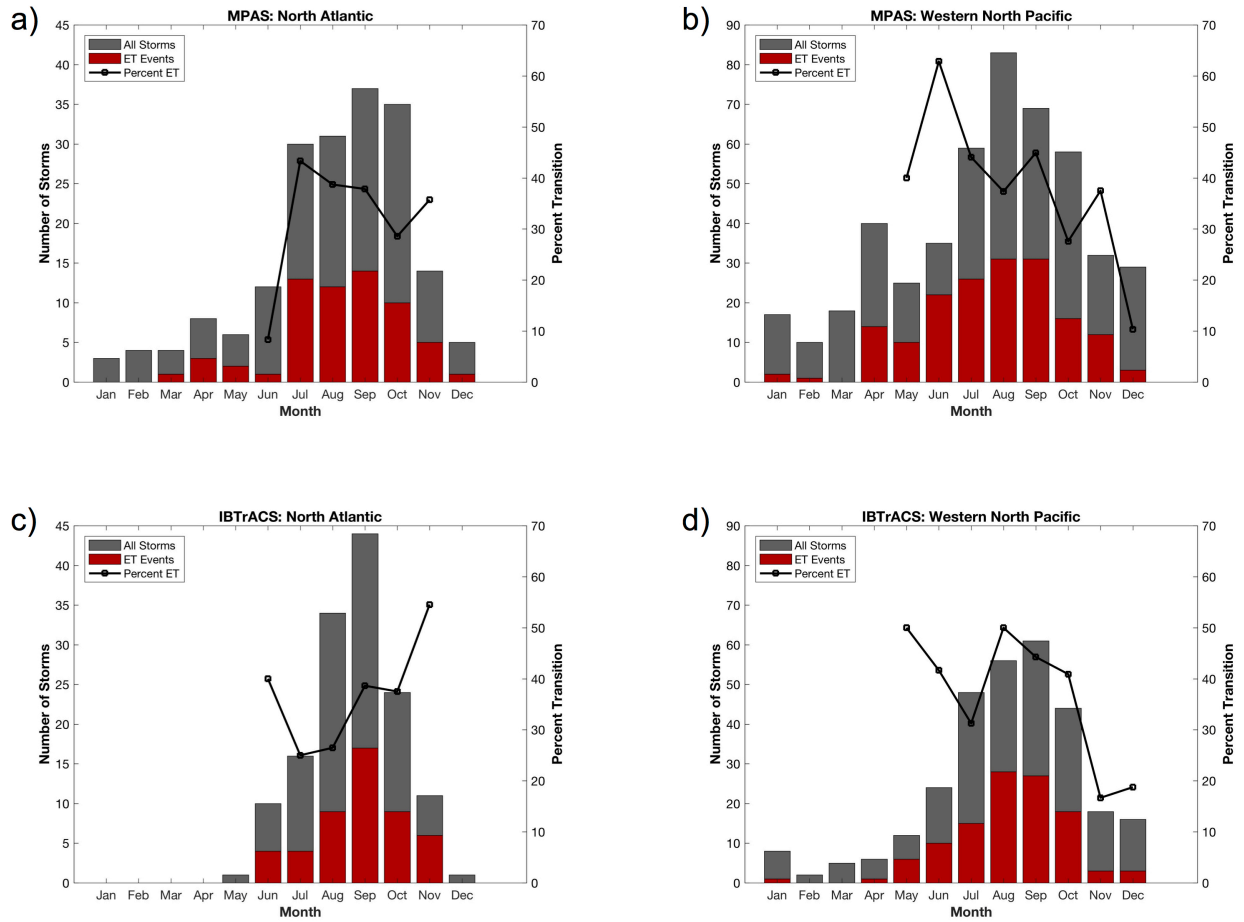


Figure 3.11: Total number of TCs, ET events, and ET percentage per month for present-day MPAS simulations vs. IBTrACS. Total number of TCs (gray bars), ET events (red bars), and percent of TCs that undergo transition (black line) per month over the 10 simulation years in the (left column) North Atlantic and (right column) Western North Pacific basins for (a)–(b) IBTrACS and (c)–(d) present-day MPAS simulations. Unnamed storms are excluded from IBTrACS counts. Percent transition is only calculated for months with at least 10 storms in both data sets.

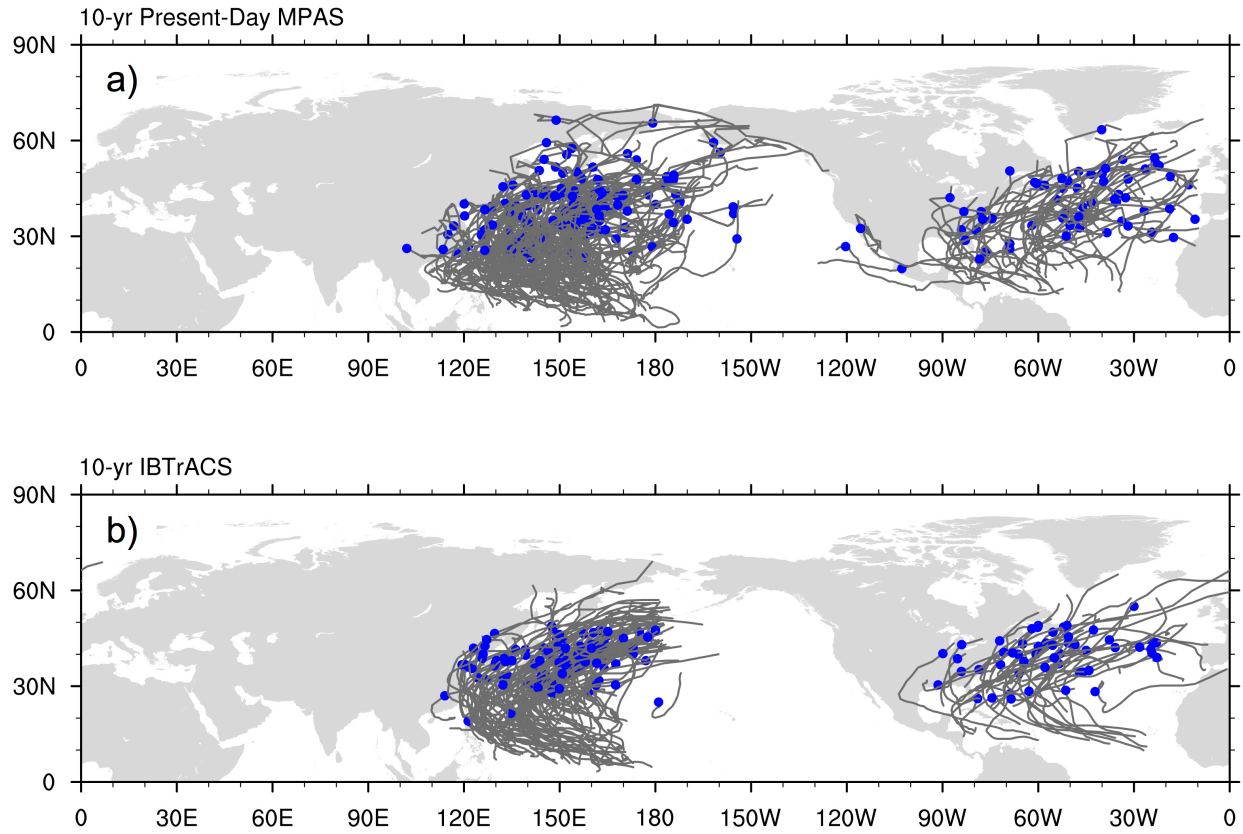


Figure 3.12: Trajectories for all ET events for the present-day MPAS simulations vs. IBTrACS. Trajectories for all ET events for the (a) present-day MPAS simulations and (b) IBTrACS over the ten simulation years. Blue circles indicate the location of ET completion.

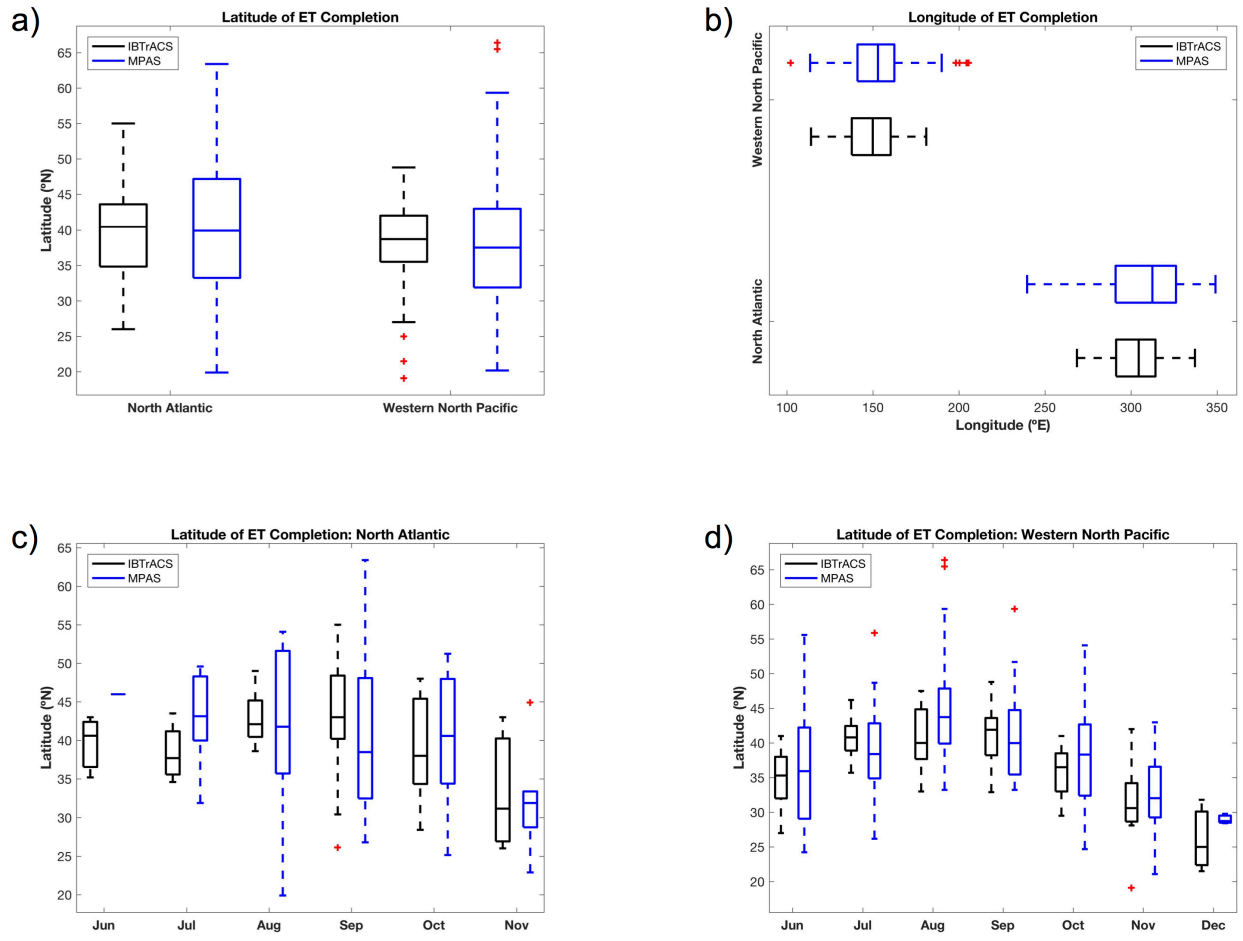


Figure 3.13: *Boxplots of ET location for present-day MPAS simulations vs. IBTrACS.* Boxplots of (a) latitude ($^{\circ}$ N) and (b) longitude ($^{\circ}$ E) of ET completion for all ET events over the ten simulation years. Boxplots showing the seasonal cycle of ET completion latitude ($^{\circ}$ N) for (c) North Atlantic and (d) Western Pacific basins. In all panels, statistics for IBTrACS (MPAS) are shown in black (blue).

4. Present-day to Future Changes: Extratropical Transition Climatology

Here, we examine how the ET climatology responds to a warming climate. Quantities of interest include the frequency and seasonality of ET events, the location of transition and ET events, the timing between each stage of the transition process, and intensity changes throughout the cyclone lifetime, particularly during and after the transition period. We will further examine storm-scale dynamics and impacts, such as near-surface wind speed and precipitation, in Chapter 5.

4.1. Background Environment

Characteristics of the background environment (e.g., level of vertical wind shear, strength of baroclinicity, SSTs, etc.) affect the behavior of TCs and ET; therefore, changes in the background environment in the future simulations will inform expected changes in TCs and ET events. Section 4.2 examines these changes in ET frequency and track density in more detail.

4.1.1. 850–200-hPa Vertical Wind Shear and Sea Surface Temperatures

Large amounts of vertical wind shear are detrimental for TC development and intensification (e.g., Vecchi and Soden 2007 and references therein), while warm SSTs are a necessary ingredient for TC formation and growth. Using a set of GCMs under the IPCC Fourth Assessment Report (AR4) mid-range A1B emissions scenario, Vecchi and Soden (2007) found significant increases in vertical wind shear in the NATL basin over the TC season (June–November) by the end of the 21st century; Haarsma et al. (2013) and Liu et al. (2017), on the other hand, using the comparable IPCC AR5 RCP4.5 emissions scenario, found a reduction in wind shear magnitude throughout most of the NATL over the same time period. There is also a general consensus that SSTs are expected to increase under future climate conditions, which would further contribute to an environment favorable for sustained tropical activity and therefore, ET.

Here, we compute the magnitude of vertical wind shear using the vector difference between monthly-mean winds at 850-hPa and 200-hPa. Using monthly-mean winds rather than daily winds in this calculation should not produce drastically different results (Vecchi and Soden 2007). The general patterns of climatological monthly vertical wind shear averaged over June–November look similar between present-day and future climates; maxima off the East Coast of

North America, over the northern Pacific, and off the western coast of Africa are apparent in both simulations (Fig. 4.1a,b). However, changes in magnitude are clearly evident (Fig. 4.1c).

In the NATL, there are two distinct areas with stronger vertical wind shear in the future: (1) the tropical Atlantic between $\sim 0^{\circ}$ – 20° N and (2) throughout the Caribbean Sea and southern Gulf of Mexico. Vertical wind shear in the tropical Atlantic increases, on average, by ~ 1.5 -m/s, with maxima between 3 – 3.5 -m/s occurring in some areas. Throughout the Caribbean, vertical wind shear increases by ~ 2 -m/s, on average, with maxima ~ 4.5 – 5 -m/s. Stronger vertical wind shear in these regions likely acts to inhibit TC activity in the future simulations (e.g., Fig. 5.14 from Torres-Vasquez 2018). On the contrary, vertical wind shear in the subtropical and lower midlatitudes of the NATL basin decreases by an average ~ 1.2 -m/s in the future simulations, with several areas experiencing reductions between 2 – 3 -m/s. This reduction in vertical wind shear is consistent with previous work (e.g., Haarsma et al. 2013; Liu et al. 2017), and implies a more favorable environment for future tropical activity. Creating a more supportive environment for TCs in the subtropics likely increases the chances of TCs reaching the midlatitudes intact, thus making ET more likely in the future simulations.

Changes in vertical wind shear throughout the WNP are comparatively less robust. There is an area of slight increase $\sim 0^{\circ}$ – 20° N, which averages ~ 0.3 -m/s stronger in the future simulations, with some areas increasing ~ 1.5 – 2 -m/s. While an increase in vertical wind shear could act to hinder TC development, this change is relatively small, and therefore, may not have a substantial effect on WNP TC activity. A larger area of reduction in vertical wind shear occurs to the north, between $\sim 20^{\circ}$ – 35° N. Here, vertical wind shear is reduced by ~ 1.2 -m/s on average, with a maximum of ~ 2 – 2.5 -m/s towards the eastern portion of the basin. This magnitude of vertical wind shear decrease is comparable to the subtropical NATL, but does not extend as far poleward. Therefore, while a reduction in subtropical wind shear could raise the chances for WNP TCs to undergo ET in the future simulations, it is possible this effect may be greater in the NATL.

Changes in SST, on the other hand, are fairly similar between the two basins (Fig. 4.2c). Both the NATL and WNP show overall increased SSTs, and exhibit a warming maximum north of Gulf Stream and Kuroshio currents, respectively. This enhanced warming creates weaker SST gradients in these regions, which can aid in the survival of TCs in the midlatitudes, and therefore,

increase the chance of ET. Additionally, the amount of warming is comparable between the two areas; on average across the basins, SSTs increase ~ 3 -K in both regions.

4.1.2. 700-hPa Eady Growth Rate and Maximum Potential Intensity

As in Hart and Evans (2001), we define the region favorable for tropical development and intensification using the monthly-mean theoretical maximum potential intensity (MPI), calculated following Emanuel (1995), and the region supportive of baroclinic development using the monthly-mean 700-hPa Eady growth rate (σ), calculated as:

$$\sigma = 0.31 \frac{fU_z}{N} \quad (4.1)$$

where f is the Coriolis parameter, U_z is the vertical wind shear of the zonal wind calculated using a center finite differencing method at each level, and N is the Brunt-Väisälä frequency. We measure the extent of these regions using the 960-hPa MPI contour and the 0.25 day^{-1} σ contour; the smaller the distance between these two regions, or the greater the overlap, the higher the chances for extratropical transition (Hart and Evans 2001).

Figure 4.3 shows the average tropically favorable and baroclinically favorable regions over the TC season (June–November) for the present-day and future simulations. Generally, there is a substantial amount of overlap between the baroclinically favorable (gray areas) and the tropical favorable (red contour) regions during the TC season in both climates. Throughout the WNP, there is a northward extension of both regions (Fig. 4.3c,d), albeit the amount of shift in the baroclinic zone is relatively small. Even still, these changes result in the area of overlap between the tropical and baroclinic zones increasing by $\sim 570,000\text{-km}^2$ in the future simulations. primarily due to changes in the tropical region. There is substantial overlap in the interannual variability of the 960-hPa MPI contour, but it appears that, as whole, the future boundary is shifted slightly poleward (Fig. 4.3d).

In the NATL, there are three regions with small changes in the extent of the baroclinically favorable region in the future simulations: over the Gulf of Mexico, the western portion of the basin from the East Coast to $\sim 50^\circ\text{W}$ and the far eastern part of the basin from $\sim 30^\circ\text{W}$ to the African coast (Fig. 4.3c). These areas also see little to no change in the extent of the tropically favorable region (Fig. 4.3d). In the central NATL basin, the tropically supportive region expands poleward by $\sim 5^\circ$ (Fig. 4.3d). This expansion of the tropics is consistent with previous work (e.g., Kossin et al. 2013, 2014), and alone, would act to reduce the gap between

the baroclinic and tropical zones, thus increasing the chances of ET. However, the baroclinically favorable region in the central NATL is extended toward the northeast between $\sim 30^{\circ}$ – 40° N, which reduces the overlap between the tropical and baroclinic zones. On the other hand, a westward extension of the baroclinic region between 20° – 30° N increases the area of intersection between the two zones. Examining the area between the 960-hPa MPI and 0.25-day^{-1} contours between the present-day and future climate shows an increase in the amount of overlap by $\sim 630,000\text{-km}^2$, and an increase in the amount of separation by $\sim 40,000\text{-km}^2$, resulting in a net increase in the area of overlap by $\sim 590,000\text{-km}^2$. This increase suggests that climatologically, the environment is more conducive for ET in the future simulations. While there is some overlap in the interannual variability of the southern boundary of the baroclinic region, there does appear to be a clear northeastward extension of this region $\sim 30^{\circ}$ – 40° W in the future simulations (Fig. 4.3c). Similarly, despite overlap in the spread, the northern boundary of the tropically favorable region does exhibit a slight northward shift in the future NATL.

Comparison of the full MPI field, in terms of minimum potential SLP, shows a reduction in minimum potential SLP (i.e., stronger potential intensity) in the both basins, albeit this change is more substantial in the NATL (Fig. 4.4). On average over the full NATL and WNP basins, from 0 – 60° N, the MPI is reduced by $\sim 9\text{-hPa}$ and $\sim 8\text{-hPa}$ in the future, respectively. Over only the tropical regions, however, there is a $\sim 13\text{-hPa}$ reduction in MPI in the NATL compared to a $\sim 5\text{-hPa}$ decrease in the WNP. As shown in Fig. 4.2 and discussed above, the change in SST over this time period and region is similar between the two basins, which suggests that another factor, such as changes in CAPE, could be a larger contributor to these basin-dependent changes in MPI.

Reduced vertical wind shear, warmer SSTs, lower MPI in terms of minimum SLP, and a greater amount of overlap between the regions supportive of tropical and baroclinic development in the central NATL, suggests that the future MPAS climate is more favorable for ET of NATL TCs. The same can be said for the WNP, but the changes are comparatively less robust. While examining the average vertical wind shear, baroclinicity, and MPI over the primary TC season, when the fraction of TCs undergoing ET is generally highest, gives us a general idea of how favorable an environment is for ET, and how that favorability may change in the future, whether or not an individual TC undergoes ET is largely dependent on the local conditions during the lifetime of the storm.

4.2. Frequency and Seasonality

Table 4.1 shows the TC and ET frequency statistics over the ten simulation years for present-day and future simulations. Both the NATL and WNP basins see an increase in the overall number of TCs in the future. In the NATL, there is a ~18% increase in the number of TCs from 189 in the present-day simulations to 222 in the future simulations. The WNP experiences a smaller change, a ~5% increase from 475 present-day TCs to 500 in the future. The number of ET events in the NATL increases by ~40% in the future from 60 events to 84 events. The fraction of TCs that undergo ET in the NATL is also higher in the future; ~38% of TCs undergo ET in the future simulations compared to ~32% in the present-day. A higher percentage of ET events in the future NATL is consistent with the results discussed in Section 4.1; reduced subtropical vertical wind shear, warmer SSTs, and an increase in the area of overlap between the tropical and baroclinic zones creates an environment more conducive to ET in the future. There are ~5% more ET events in the WNP in the future, but the fraction of TCs that undergo ET is similar in present-day and future climates. Even though environmental conditions are also more favorable for ET in the WNP basin in the future, we see little to no change in ET percentage. It is worth noting that the percent transition in the future simulations for both basins is within one standard deviation of the present-day ET percentage; therefore, the observed shifts in percent transition may not be statistically significant. Both basins have a smaller standard deviation of percent transition in the future climate simulations indicating less interannual variability in the future; thus future TCs appear to be undergoing ET more consistently year-to-year.

The seasonal cycle in the number of ET events for the NATL is similar between present-day and future simulations with an increase in frequency through the beginning of the TC season, a peak in September, and a decrease in frequency through December (Fig. 4.5a,c). The springtime (MAM) ET frequency is also similar with several events occurring during each month in both sets of simulations. January, however, has more TCs and ET events in the future simulations; there are no January ET events in the present-day simulations (Fig. 4.5a,c). The seasonality in NATL ET percentage is not drastically different between the present-day and future simulations (Fig. 4.5e). The present-day simulations have a higher ET percentage in the spring while the future simulations have a higher ET percentage throughout the remainder of the year. The largest differences in NATL percent transition occur in January, where no storms

undergo ET in the present-day climate and ~14% of TCs undergo ET in the future simulations, and in June, where ~50% of TCs undergo ET in the future climate, compared to only ~8% in the present-day simulations. Relatively small sample sizes for several months, however, leads to a high level of uncertainty in whether or not the observed differences in the seasonal cycle are robust.

For the WNP, the present-day and future seasonal cycles in the number of ET events are also similar; there is an increase in frequency from June to August, a peak in August/September, and a decrease in frequency thereafter (Fig. 4.5b,d). Additionally, both present-day and future simulations generate several ET events in January and February. The future seasonal cycle does not show as strong of a peak during April for either TCs or ET events; instead, ET frequency is fairly consistent throughout MAM (Fig. 4.5b,d). The primary difference in the seasonality of ET percentage in the WNP is that the percent transition is more consistent throughout the year in the future, particularly during the main TC season (June–November; Fig. 4.5f). For example, over the TC season, the present-day percent transition varies from a maximum of 63% in June to a minimum of 28% in October, a range of 35%. The future ET percentage over the same time period varies from a maximum of 42% in July to a minimum of 30% in November, a range of only 13%. Additionally, the present-day seasonality shows three distinct local maxima in June, September, and November; the future seasonality, on the other hand, shows a more consistent pattern (Fig. 4.5f). As with the NATL, small sample sizes suggest these differences are likely insignificant.

4.3. Location

The track density of ET and non-ET events (e.g., purely tropical systems, partial ET events, etc.) for the present-day and future simulations is shown in Figure 4.6. Generally, in both present-day and future climates, non-ET events in the WNP form farther east and travel more zonally compared to ET events (Fig. 4.6a–b,d–e). The differences between track density patterns of non-ET and ET events in the NATL are not as distinct; both non-ET and ET events occur throughout the basin, albeit the northern edge of the track density for ET events does extend farther poleward (Fig. 4.6a–b,d–e).

In the NATL, there is a clear increase in both non-ET and ET events around 30°–40°N in the future simulations (Fig. 4.6c,f). This increase, coupled with a reduction in TC activity in the

Gulf of Mexico, primarily exhibited by non-ET events (Fig. 4.6c), suggests a potential eastward shift in NATL storm activity. Haarsma et al. (2013) and Liu et al. (2017) also indicate a potential eastward shift in future NATL TC activity due to warming SSTs. In addition to warming SSTs, our simulations show increased vertical wind shear over the Gulf of Mexico and the Caribbean (Fig. 4.1c) as an additional factor contributing to reduced TC activity in this area. Although not evident in the difference field due to smoothing and the chosen contour interval, there are several more storms that reach the United Kingdom (U.K.) in the future simulations (Fig. 4.6a–b,d–e).

The climate change signal in the WNP is less clear (Fig. 4.6c,f). There is an increase in the frequency of non-ET events east of Japan as well as an area of track density increase farther east into the basin, around 180°E (Fig. 4.6c). These increases, coupled with a reduction in activity of non-ET events northeast of the Philippines in the Philippine Sea (Fig. 4.6c), suggest a potential northeast shift of storm activity in the future. ET events, on the other hand, show a slight reduction in activity east of Japan and increases along the east coast of China, over Taiwan and Japan, and east of the Philippines (Fig. 4.6f). While the changes in the overall number of TCs and ET events in the WNP are small (Table 4.1), there are potential shifts in where storms occur. However, the track density differences in the WNP are noisier and therefore, less robust than the signals in the NATL, and should be interpreted as such.

By looking at the individual trajectories rather than the track density (Fig. 4.7), the increase in ET events reaching the U.K. is apparent. Similarly, tracks extend further towards Western Europe in the NATL and towards eastern Asia in the WNP. As previously mentioned, these changes are relatively small, on the order of around one additional event per year, or less. Upon initial visual inspection of Figure 4.7, we can see a northward, and slight eastward, shift in both ET onset and ET completion location in the NATL. In the WNP, there is no obvious shift in the location of ET onset. ET completion, on the other hand, does appear to occur farther south in the future.

These present-day-to-future differences in ET onset and completion location are more pronounced in Figure 4.8, which shows the density of ET onset and completion. As in Figure 4.7, there is a clear northward shift, and slight eastward extension, in the location of ET onset and completion in the NATL in the future simulations (Fig. 4.7c,f). Again, the signal in the WNP is not as robust. Here, the ET onset density shows two areas of slightly positive change, one to the west of Japan over North Korea and South Korea, and the other towards the southeastern

portion of the basin $\sim 20^{\circ}\text{N}$, 165°W (Fig. 4.8c). The difference in ET completion density shows a similar pattern; there are areas of increase in the East China Sea and in the southeastern portion of the basin with a region of decreasing density in between (Fig. 4.8f). These changes in ET location suggest that ET occurs both farther inland and farther offshore in the future simulations. However, the prevalence of noise in the differences fields for the WNP indicates that results should be interpreted with caution.

Examination of box-and-whisker plots relating the distributions of ET onset and completion location in the present-day and future simulations allows for a more quantitative comparison (Fig. 4.9). The latitude of ET onset (Fig. 4.9a) and ET completion (Fig. 4.9c) in the NATL show the largest differences. The median latitudes of ET onset and completion in the NATL occur 4.6° and 5° farther north in the future simulations, respectively. These northward shifts are both statistically significant at the 95% confidence level as indicated by the Wilcoxon Rank Sum significance test (Table 4.2). This poleward shift in ET location is consistent with a significant poleward shift in the latitude of TC genesis and peak tropical intensity for NATL ET events (Table 4.3; Fig. 4.10), as well as a poleward shift in the latitude of TC genesis and location of lifetime maximum intensity for all NATL TCs (Torres-Vasquez 2018); all poleward shifts are consistent with a poleward expansion of the tropically favorable region indicated by the 960-hPa MPI contour (Fig. 4.3d). ET onset and completion of NATL ET events occur farther east in the future simulations by 5.9° and 1.8° , respectively; however, neither of these eastward shifts is statistically significant (Table 4.2). Similarly, the longitude of TC genesis and peak tropical intensity of NATL ET events is shifted eastward, but neither shift is found to be statistically significant (Table 4.3; Fig. 4.10). ET onset and completion locations in the WNP show slight northwest and southwest shifts in the future, respectively (Table 4.2; Fig. 4.9). Due to the dipole pattern exhibited by the changes in ET onset and completion location in the WNP (Fig. 4.8c,f), it is unsurprising that these changes are not found to be statistically significant (Table 4.2). While there is a slight poleward expansion in the region favorable for tropical development in the WNP (Fig. 4.3d), it is evidently not enough to elicit a significant response in the location of TC genesis or peak tropical intensity for future WNP ET events (Table 4.3; Fig. 4.10), or in the locations of TC genesis and lifetime maximum intensity for WNP TCs as a whole (Torres-Vasquez 2018).

4.4. Duration and Intensity

NATL ET events in the future simulations, on average, spend 7-h less as tropical systems, undergo the transition process 3-h faster, and experience total lifetimes that are 3-h shorter than their present-day climate counterparts; however, these changes are relatively small and not found to be statistically significant (Table 4.4; Fig. 4.11). On the other hand, we find a larger fraction of NATL ET events experience slow transition periods (i.e., transition periods ≥ 48 -h as in Hart et al. 2006) in the future, while the fraction of fast transitioning events (i.e., those with transition periods ≤ 12 -h as in Hart et al. 2006) is reduced (Table 4.5). Therefore, even though the median duration of ET is largely unchanged in the future simulations, there is evidence supporting a shift towards more NATL storms experiencing slow transition periods.

The median location of ET onset in the WNP is shifted slightly north while the median ET completion location is shifted slightly south, albeit insignificantly, which suggests that ET events are potentially traveling shorter distances between onset and completion in the WNP in the future simulations. The median distance between ET onset and completion in this basin is ~ 190 -km, or $\sim 1.7^\circ$, shorter in the future simulations, but this change is not statistically significant ($p = 0.28$). Even still, a shorter distance between onset and completion could imply faster durations of ET in the future simulations, or slower translation speeds. Additionally, a higher frequency of ET events interacting with land could also result in storms undergoing ET more quickly. The median duration of ET (e.g., time between ET onset and ET completion) is 6-h faster in the future simulations for WNP ET events; however, this shift is not found to be statistically significant (Table 4.4). Similar to NATL events, there are no significant changes in the time spent as a tropical cyclone before ET onset, or in the total duration of the storm from TC genesis to lysis as an ETC (Table 4.4; Fig. 4.11a,c). Additionally, there is little to no change in the fraction of events experiencing relatively slow or fast transition periods (Table 4.5).

NATL ET events in the future simulations are generally stronger at each stage of the cyclone lifecycle (Fig. 4.12); the median peak tropical intensity (i.e., minimum SLP reached prior to ET onset) is 6-hPa lower, the median SLP 12-h prior to ET onset is 3-hPa lower, the median SLP at ET onset is 3-hPa lower, the median SLP at ET completion is 2.7-hPa lower, and the median peak intensity as an ETC (i.e., minimum SLP reached after ET completion) is 6.1-hPa lower. The shifts towards lower SLPs at ET completion and towards stronger post-transition storms are statistically significant at the 90% and 95% confidence level, respectively (Table 4.6).

The minimum SLP reached by ET events in WNP during the tropical phase is significantly lower by 11.8-hPa in the future simulations (Table 4.6). Differences in intensity between the present-day and future storms at the other lifecycle stages are small, and not statistically significant (Table 4.6; Fig. 4.12)

Overall, present-day and future ET events in both the NATL and WNP undergo similar intensity changes during each lifecycle stage (Fig. 4.13). Therefore, while storms are significantly stronger in the latter two lifecycle stages in the future simulations, NATL ET events do not experience significantly different intensification or weakening rates between each stage. The only significant difference occurs with WNP storms; future ET events have a significantly stronger weakening rate from the time of peak tropical intensity to the time of ET onset (Table 4.7), likely because WNP ET events are significantly stronger as tropical systems in the future simulations (Table 4.6).

As expected, the majority of ET events in both basins weaken from ET onset to ET completion as the cyclone is undergoing structural changes (Fig. 4.13b). A slightly higher fraction of NATL ET events strengthen after transition is completed in the present-day simulations (Table 4.8). However, because there are more ET events in the future simulations, there are a larger number of events that undergo post-transition strengthening (26 in the present-day vs. 34 in the future). In the WNP, the fraction of events to strengthen after ET completion occurs is about the same between the present-day and future simulations (Table 4.8).

4.5. Cyclone Phase Space

Figure 4.14 shows composite CPS diagrams for all NATL ET events in the present-day and future simulations. The present-day diagrams (Fig. 4.14a,d) are comparable to Zarzycki et al. (2017, their Fig. 11). The general structure for both present-day and future events is similar; storms spend the most time as tropical systems (i.e., frequencies are highest in the bottom-right quadrant of the top row and the top-right quadrant of the bottom row). Figure 4.14c shows a shift towards larger $-VLT$ and more positive B values in the bottom-right quadrant for future storms. This indicates that, as tropical systems, future NATL ET events are more asymmetric with stronger lower-level warm cores. The locations of TC genesis, peak tropical intensity, and ET for NATL ET events shift significantly poleward in the future, which is likely contributing factor to their increase in asymmetric structure. Decreases in frequency near the origin of Figure 4.14f,

and small increases in the top-right quadrant, also indicate a stronger warm core at upper and lower levels for future ET events early in their lifecycle. A stronger warm core structure in future NATL ET events is consistent with expected increases in moisture and enhanced latent heat release. Furthermore, stronger warm cores could be a contributing factor in a higher fraction of NATL TCs undergoing ET in the future simulations; TCs with an enhanced warm core structure are likely able to survive in unfavorable conditions for longer periods of time, thus increasing the probability of undergoing ET.

Similar to NATL ET events, ET events in the WNP also spend most of their life as tropical systems (Fig. 4.15). Unlike NATL storms, though, there are not drastic differences in the composite CPS diagrams between present-day and future storms. The bottom-right and top-right quadrants of Figure 4.15c and Figure 4.15f show a dipole pattern in the difference field indicating that some storms experience stronger warm cores in the future simulations, while others experience weaker warm cores. Similarly, the pattern in Figure 4.15c shows increases in the frequency of both more positive and more negative B values, rather than a systematic shift in one direction. These changes in symmetry are consistent with the pattern of track density change for WNP ET events (Fig. 4.6f), which shows both poleward and equatorward increases in storm activity, suggesting a greater geographic range of storm activity in the future simulations.

4.6. Summary

One of the most significant changes in the ET climatology is that a higher fraction of NATL TCs undergo ET in the future simulations (Table 4.1). There are three factors contributing to this increase in ET percentage: (1) the magnitude of 850–200-hPa vertical wind shear is reduced throughout the NATL subtropics (Fig. 4.1), SSTs are warmer (Fig. 4.2), there is a greater amount of overlap between the tropically favorable and baroclinically favorable zones (Fig. 4.3), and the minimum potential SLP (i.e., MPI) is lower (Fig. 4.4), which, climatologically, creates an environment more conducive for ET in the future, (2) NATL ET events experience stronger warm cores as tropical systems (Fig. 4.14), which likely increases the chances of survival in unfavorable conditions, thus increasing the likelihood of ET, and (3) there is a significant poleward shift in the latitude of TC genesis and location of peak intensity for NATL ET events (Table 4.3; Fig. 4.10), which reduces the distance needed to travel in an unfavorable environment, and therefore, like (2), increases the chances of ET.

While similar changes in the climatological background environment occur in the WNP, there is little to no change in the fraction of TCs that undergo ET in the future simulations. This could be because WNP ET events do not show a systematic shift towards stronger warm cores during the tropical phase of the cyclone lifecycle, nor is there a significant poleward shift in the location of TC genesis or peak intensity, suggesting that future WNP TCs are just as susceptible to the negative effects of unfavorable conditions during the propagation to the midlatitudes as their present-day counterparts.

The locations of ET onset and completion of NATL ET events shift significantly poleward in the future (Table 4.2; Fig. 4.9), consistent with a poleward shift in the latitude of TC genesis and peak tropical intensity (Table 4.3; Fig. 4.10), as well as a poleward expansion of the tropically favorable region (Fig. 4.3). In regards to changes intensity, ET events in the NATL are stronger at the time of ET completion, and reach lower minimum SLPs as ETCs after ET is completed (Table 4.6; Fig. 4.12), but do not show significant changes in the intensification or weakening rates between lifecycle stages (Table 4.7; Fig. 4.13). WNP ET events are more intense during the tropical phase of the cyclone lifecycle (Table 4.6; Fig. 4.12), and thus weaken between reaching peak tropical intensity and ET onset at a significantly faster rate (Table 4.7; Fig. 4.13). There are no significant changes in the median duration of ET for ET events in either basin, but a higher percentage of future NATL ET events do experience slow transition periods (Table 4.5), consistent with storms having stronger warm cores.

Table 4.1: TC and ET frequency statistics over the ten simulation years for present-day and future simulations.

Basin	Climate	Number of TCs	Number of ET Events	% Transition	% Transition σ	% Transition $\pm 1\sigma$
North Atlantic	Current	189	60	32	17	15–49
	Future	222	84	38	9	29–47
Western North Pacific	Current	475	154	32	14	18–46
	Future	500	161	32	5	27–37

Table 4.2: Median location of ET onset and completion. p-values are reported from the Wilcoxon Rank Sum statistical significance test. Italicized (bold) values indicate statistical significance at the 90% (95%) confidence level.

Basin	Climate	Median Latitude ($^{\circ}$ N) of ET Onset	Median Longitude ($^{\circ}$ E) of ET Onset	Median Latitude ($^{\circ}$ N) of ET Completion	Median Longitude ($^{\circ}$ E) of ET Completion
North Atlantic	Current	34.7	302.6	39.9	312.5
	Future	39.3	308.5	44.9	314.3
	p-value	0.003	0.18	0.001	0.41
Western North Pacific	Current	30.8	143.0	37.5	152.9
	Future	31.3	141.7	36.4	149.6
	p-value	0.72	0.99	0.37	0.61

Table 4.3: Median location of TC genesis and peak tropical intensity. p-values are reported from the Wilcoxon Rank Sum statistical significance test. Italicized (bold) values indicate statistical significance at the 90% (95%) confidence level.

Basin	Climate	Median Latitude (°N) of TC Genesis	Median Longitude (°E) of TC Genesis	Median Latitude (°N) of Maximum Tropical Wind Speed	Median Longitude (°E) of Maximum Tropical Wind Speed
North Atlantic	Current	23.0	301.8	29.0	300.3
	Future	29.3	305.4	33.0	305.2
	p-value	0.004	0.72	0.02	0.50
Western North Pacific	Current	15.4	152.2	22.1	141.0
	Future	16.0	151.0	22.4	141.2
	p-value	0.95	0.96	0.99	0.85

Table 4.4: Median duration (hrs) of various stages of the cyclone life cycle. p-values are reported from the Wilcoxon Rank Sum statistical significance test. Italicized (bold) values indicate statistical significance at the 90% (95%) confidence level.

Basin	Climate	Median Time (hr) Between TC Genesis and ET Onset	Median Time (hr) Between ET Onset and ET Completion	Median Total Cyclone Lifetime (hr)
North Atlantic	Current	108	24	171
	Future	99	21	168
	p-value	0.71	0.48	0.98
Western North Pacific	Current	144	30	216
	Future	150	24	222
	p-value	0.65	0.56	0.62

Table 4.5: Percentage of ET events that undergo slow and fast transition.

Basin	Climate	# (%) of Slow Transition Events (ET Duration \geq 48-h)	# (%) of Fast Transition Events (ET Duration \leq 12-h)
North Atlantic	Current	12 (20)	24 (40)
	Future	24 (29)	31 (37)
Western North Pacific	Current	43 (28)	44 (29)
	Future	45 (28)	48 (30)

Table 4.6: Median intensity (SLP; hPa) at various stages of the cyclone life cycle. p-values are reported from the Wilcoxon Rank Sum statistical significance test. Italicized (bold) values indicate statistical significance at the 90% (95%) confidence level.

Basin	Climate	Median Minimum Tropical SLP (hPa)	Median SLP (hPa) 12-h Prior to ET Onset	Median SLP (hPa) at ET Onset	Median SLP (hPa) at ET Completion	Median Minimum Post-ET SLP (hPa)
North Atlantic	Current	974.5	991.1	991.6	999.7	999.8
	Future	968.5	988.1	988.6	997.0	993.7
	p-value	0.42	0.29	0.22	<i>0.07</i>	0.04
Western North Pacific	Current	953.1	978.5	980.5	996.6	996.2
	Future	941.3	979.6	983.2	994.8	995.1
	p-value	0.02	0.57	0.57	0.35	0.50

Table 4.7: Median intensity (SLP) change rate (hPa/6-h) between each stage of the cyclone life cycle. p-values are reported from the Wilcoxon Rank Sum statistical significance test. Italicized (bold) values indicate statistical significance at the 90% (95%) confidence level.

Basin	Climate	Median Intensity Change Rate (hPa/6-h) between Peak Tropical and ET Onset	Median Intensity Change Rate (hPa/6-h) between ET Onset and ET Completion	Median Intensity Change Rate (hPa/6-h) between ET Completion and Post-ET
North Atlantic	Current	1.4	2.3	0.3
	Future	1.5	2.1	0.5
	p-value	0.92	0.52	0.79
Western North Pacific	Current	2.0	2.9	1.5
	Future	2.8	2.7	1.4
	p-value	0.01	0.89	0.88

Table 4.8: Percentage of ET events that strengthen and weaken after completing ET.

Basin	Climate	# (%) of ET Events to Strengthen Post-ET	# (%) of ET Events to Weaken Post-ET
North Atlantic	Current	26 (43)	30 (50)
	Future	34 (41)	44 (52)
Western North Pacific	Current	47 (31)	103 (67)
	Future	52 (32)	102 (63)

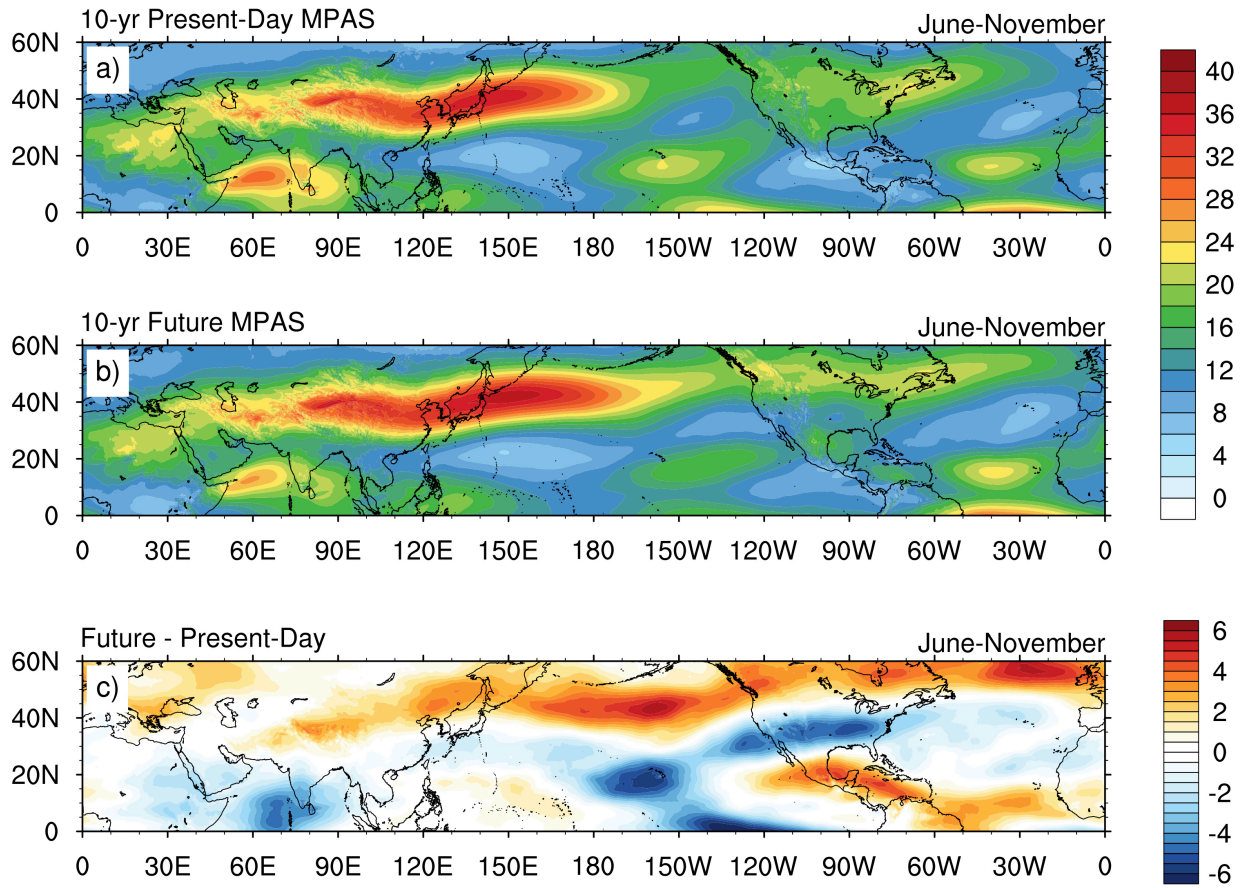


Figure 4.1: Monthly averaged 850–200-hPa vertical wind shear for present-day vs. future simulations. 10-yr monthly-mean 850–200-hPa vertical wind shear (m/s) averaged over June–November for (a) present-day simulations, (b) future simulations, and (c) future minus present-day. Contours are shaded every 2-m/s in (a)–(b) and every 0.5-m/s in (c).

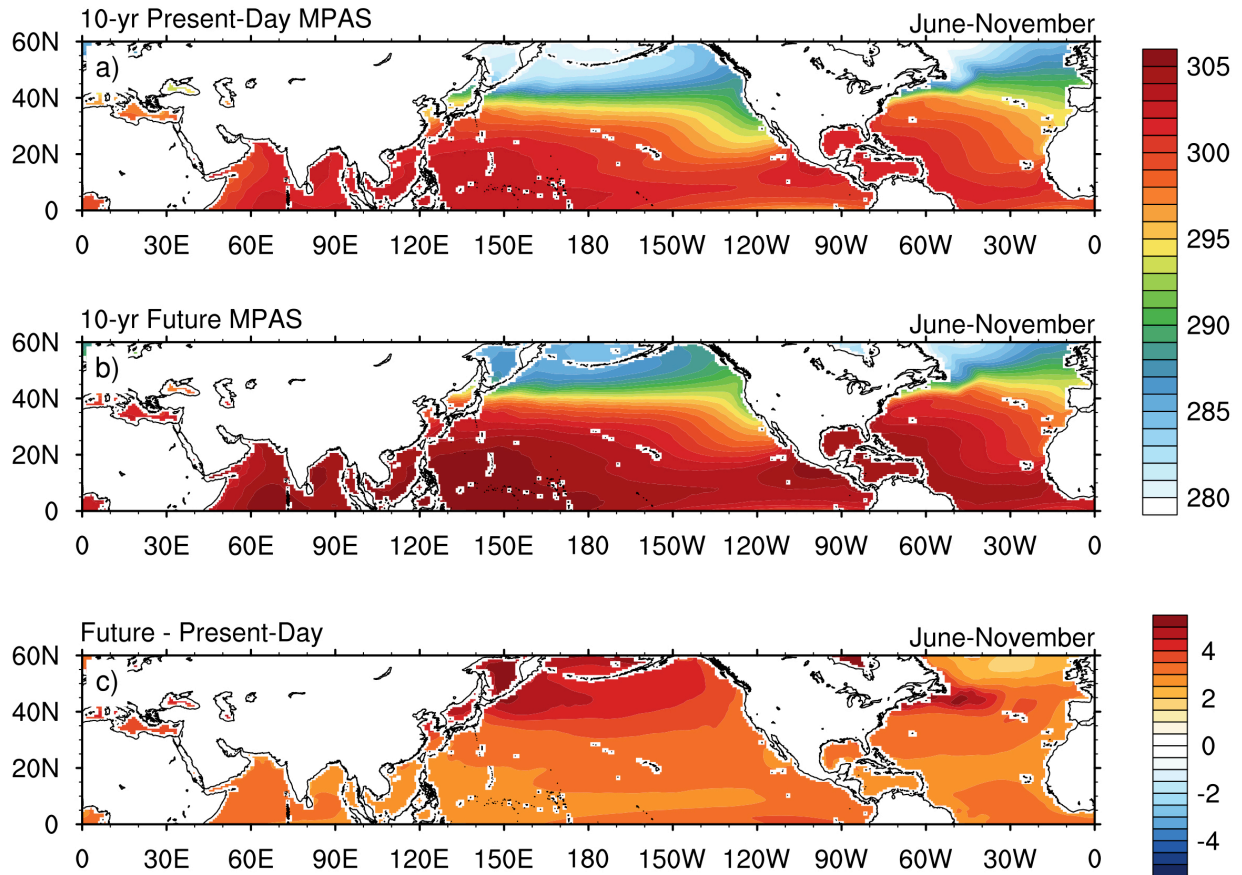


Figure 4.2: Monthly averaged SST for present-day vs. future simulations. 10-yr monthly-mean SST (K) averaged over June–November for (a) present-day simulations, (b) future simulations, and (c) future minus present-day. Contours are shaded every 1-K in (a)–(b) and every 0.5-K in (c).

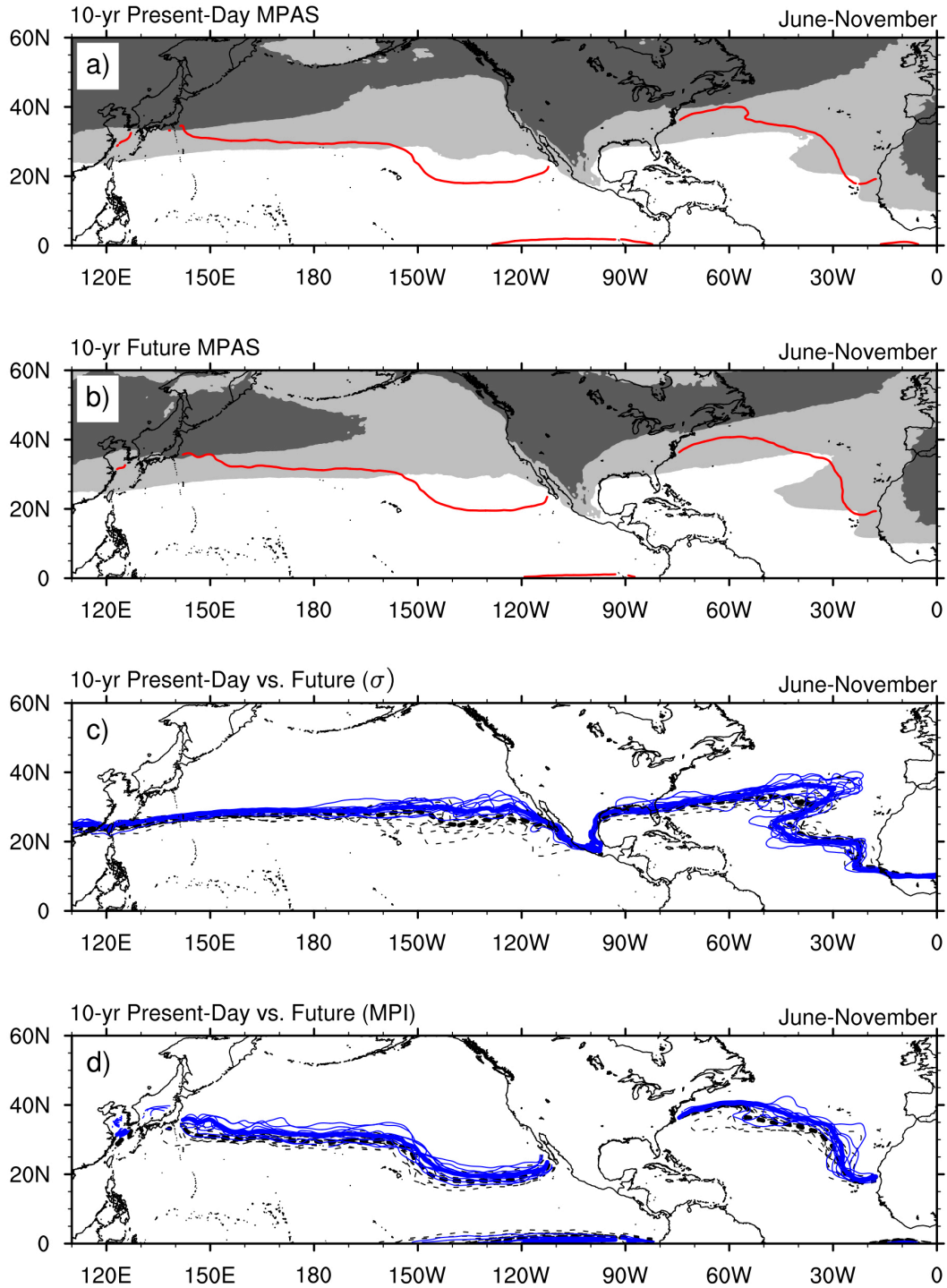


Figure 4.3: Monthly average 700-hPa Eady growth rate and MPI for present-day vs. future simulations. 10-yr monthly-mean 700-hPa σ (shaded at 0.25-day^{-1} (light gray) and 0.5-day^{-1} (dark gray)) and MPI (960-hPa contour in red) averaged over June–November for (a) present-day simulations and (b) future simulations. Comparison of seasonal mean (c) 0.25-day^{-1} σ contour and (d) 960-hPa MPI contour for present-day (dashed black) and future (solid blue) simulations. Contours for each of the ten simulation years are shown as faded contours (present-day in dashed black; future in solid blue) in (c) and (d).

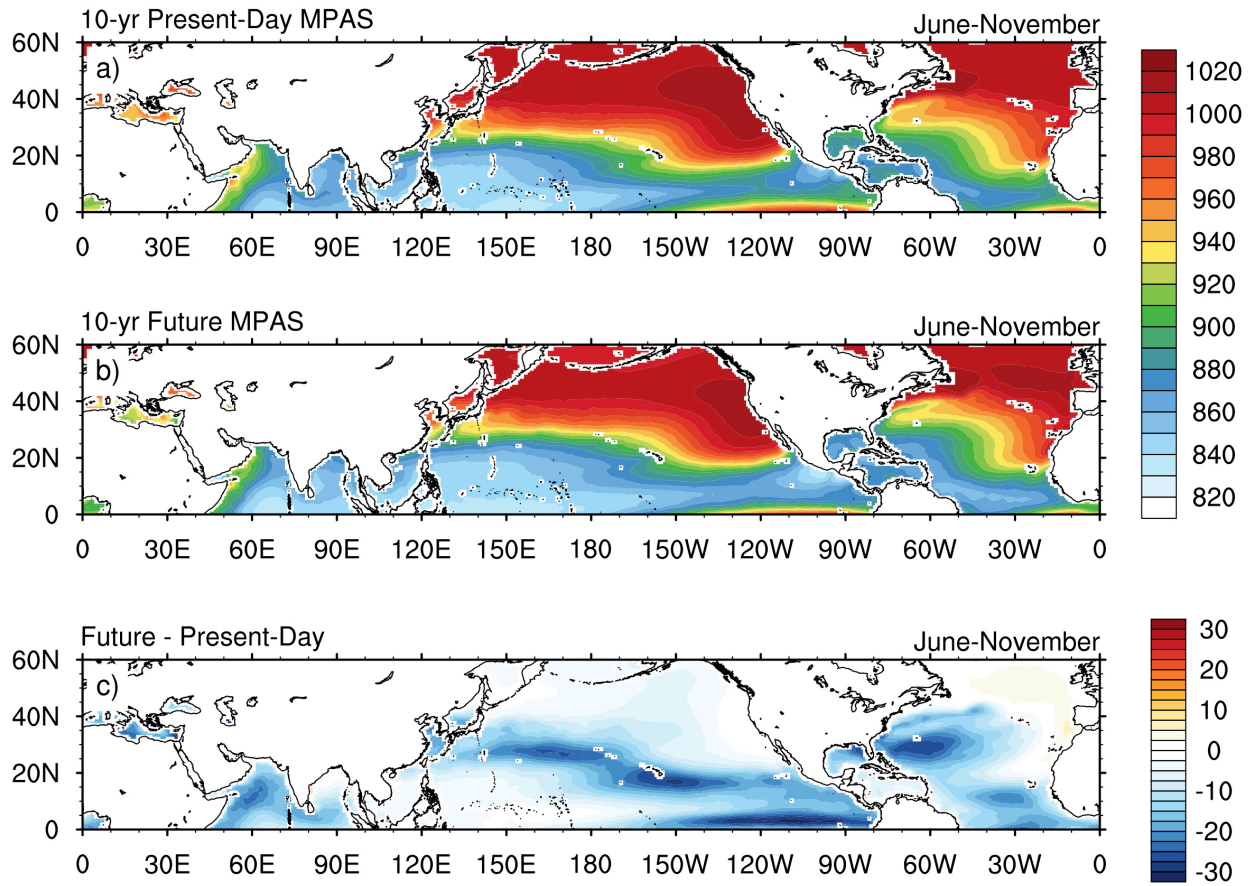


Figure 4.4: Monthly average MPI for present-day vs. future simulations. 10-yr monthly-mean MPI (minimum SLP; hPa) averaged over June–November for (a) present-day simulations, (b) future simulations, and (c) future minus present-day. Contours are shaded every 10-hPa in (a)–(b) and every 2.5-hPa in (c).

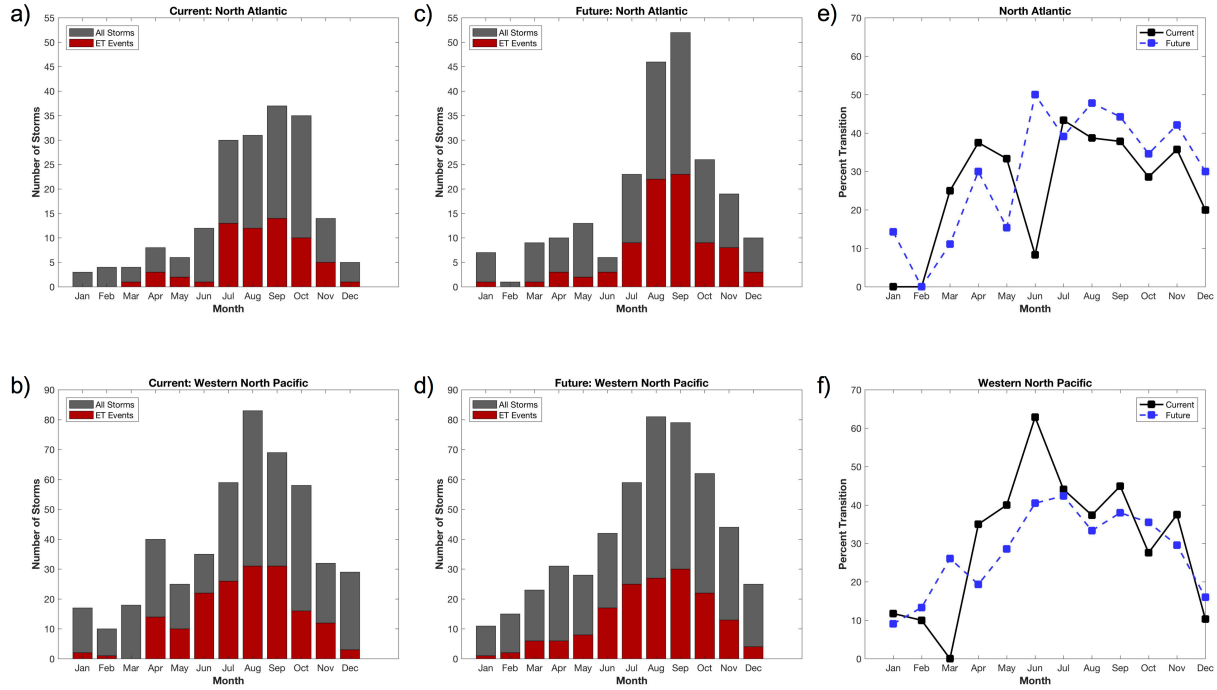


Figure 4.5: Monthly average TC and ET frequency and ET percentage for present-day vs. future simulations. (a)–(d) Monthly average TC (gray bars) and ET (red bars) frequency over the ten simulation years for (a)–(b) present-day and (c)–(d) future MPAS simulations in the (top row) North Atlantic and (bottom row) Western North Pacific basins. (e)–(f) Present-day (black line) and future (blue line) monthly average percent transition over the ten simulation years for the (e) North Atlantic and (f) Western North Pacific basins.

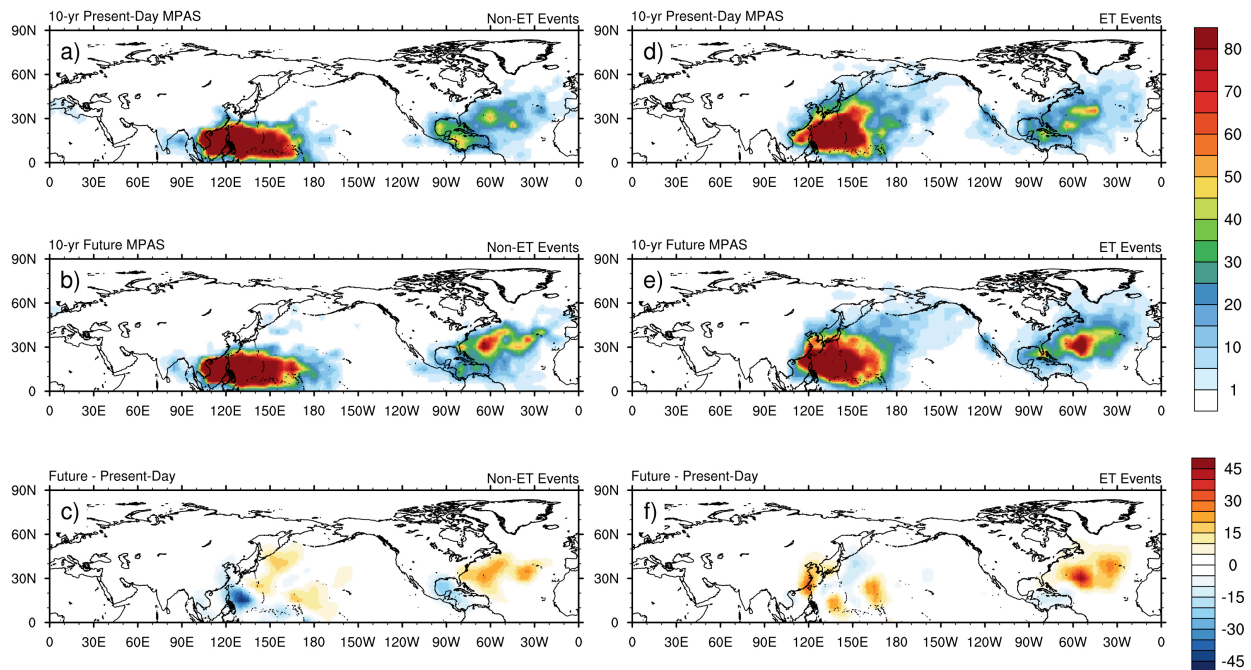


Figure 4.6: *Non-ET and ET track density for present-day vs. future simulations.* Track density (number of storms per $5^{\circ} \times 5^{\circ}$ box) of (a)–(c) non-ET and (d)–(f) ET events over the ten simulation years for the (top row) present-day simulations, (middle row) future simulations, and (bottom row) future minus present-day. Contours are shaded every 5 count in all panels.

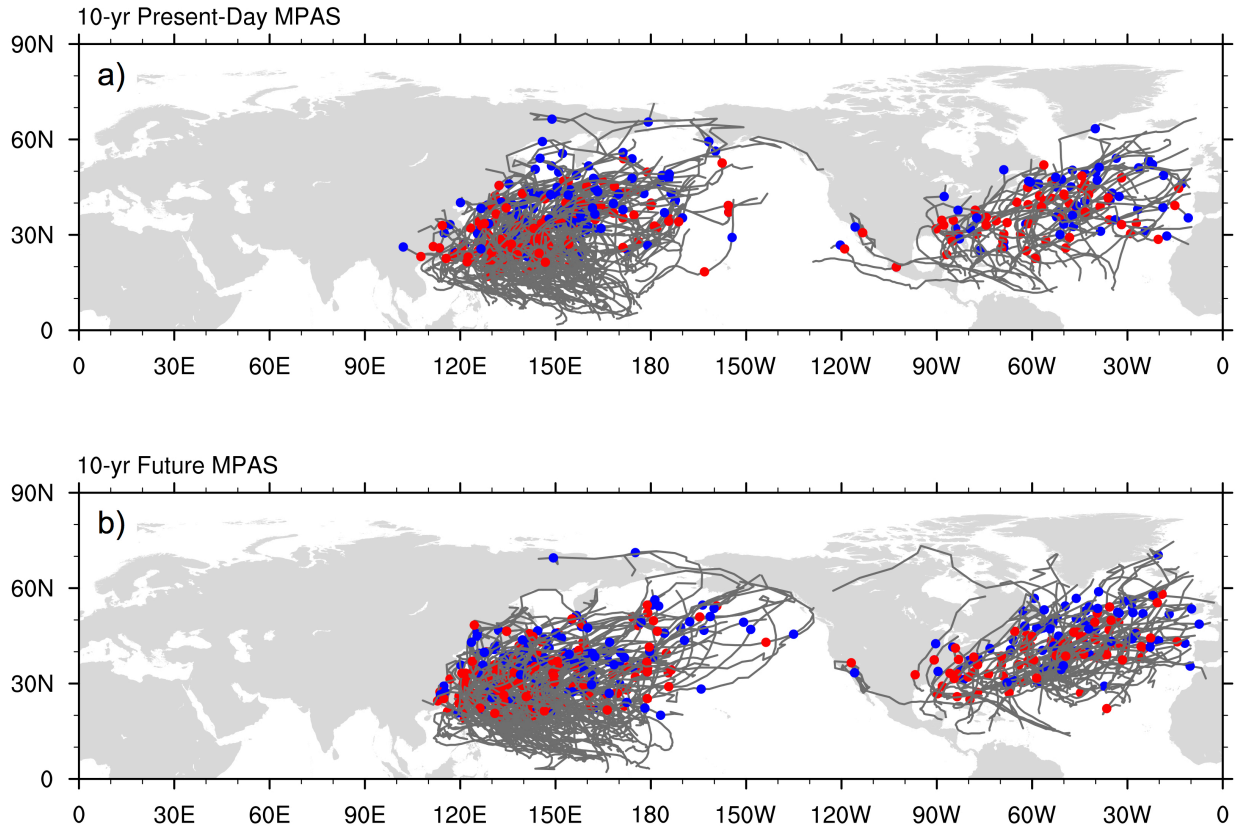


Figure 4.7: Trajectories of ET events for present-day vs. future simulations. Objective tracked storm trajectories of ET events over the ten simulation years in the (a) present-day and (b) future simulations. Location of ET onset (completion) for each track is denoted by the red (blue) circle.

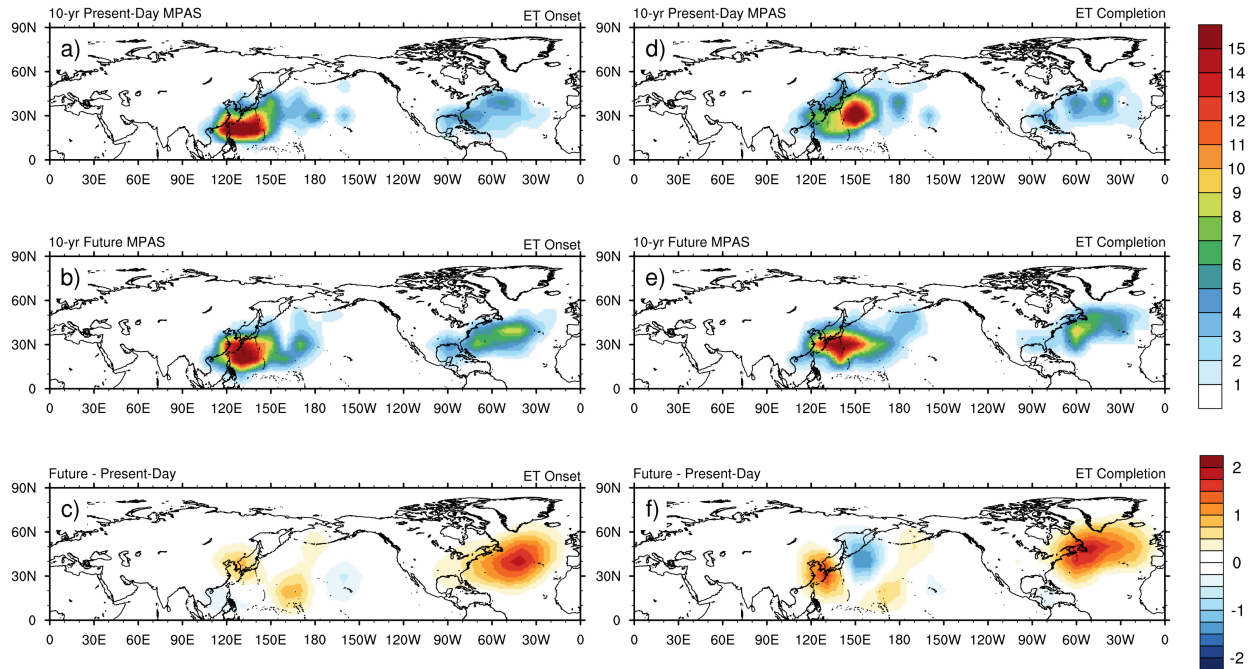


Figure 4.8: *ET onset and completion density for present-day vs. future simulations.* (a)–(c) ET onset and (d)–(f) ET completion density (number of storms per $10^\circ \times 10^\circ$ box) over the ten simulation years for the (top row) present-day simulations, (middle row) future simulations, and (bottom row) future minus present-day. Contours are shaded every 1 count in the top two rows and every 0.5 count in the bottom row.

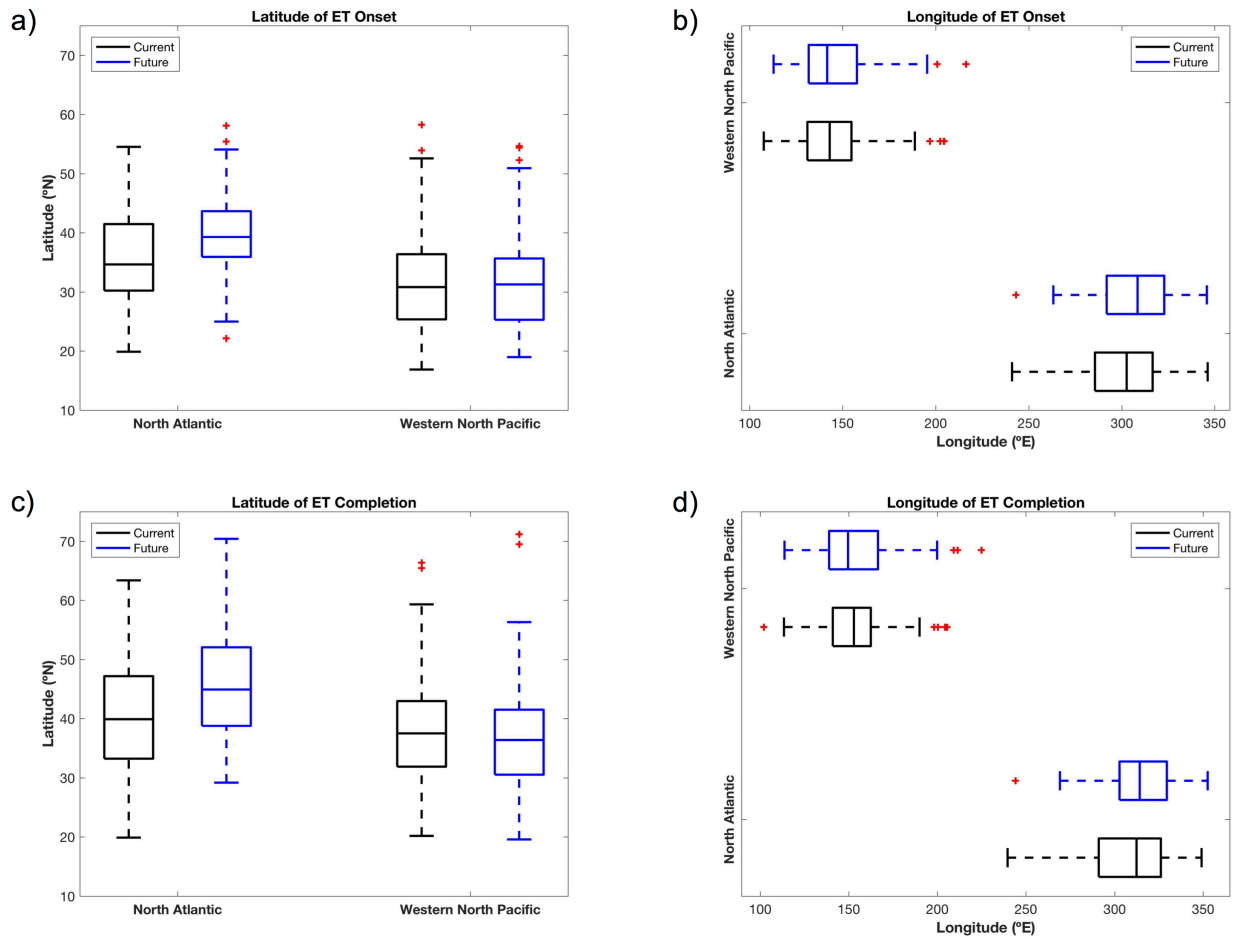


Figure 4.9: Boxplots of ET location for present-day vs. future simulations. Boxplots showing (a) latitude and (b) longitude of ET onset and (c) latitude and (d) longitude of ET completion in the North Atlantic and Western North Pacific basins. Present-day (future) distributions are shown in black (blue). The bottom (left-most) whisker indicates the minimum latitude (longitude). The top (right-most) whisker indicates the maximum latitude (longitude). The bottom, middle, and top (left, middle, and right) lines associated with each box represent the 25th, 50th, and 75th percentile latitude (longitude). The red asterisks represent outliers that fall outside of $\pm 2.7\sigma$ range.

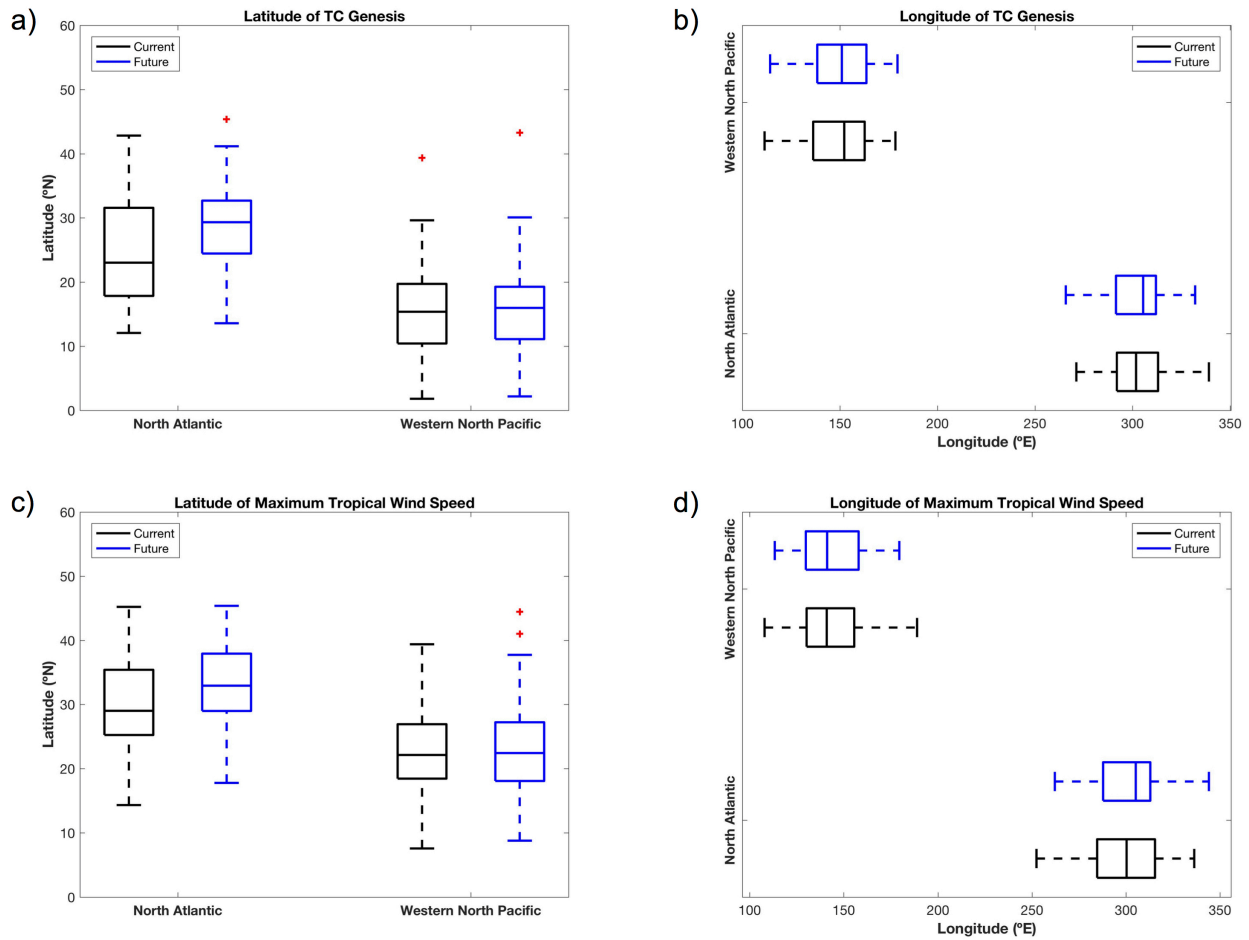


Figure 4.10: Boxplots of TC genesis and maximum lifetime intensity location for present-day vs. future simulations. Boxplots showing (a) latitude and (b) longitude of TC genesis and (c) latitude and (d) longitude of peak tropical intensity for ET events in the North Atlantic and Western North Pacific basins. Present-day (future) distributions are shown in black (blue). The bottom (left-most) whisker indicates the minimum latitude (longitude). The top (right-most) whisker indicates the maximum latitude (longitude). The bottom, middle, and top (left, middle, and right) lines associated with each box represent the 25th, 50th, and 75th percentile latitude (longitude). The red asterisks represent outliers that fall outside of $\pm 2.7\sigma$ range.

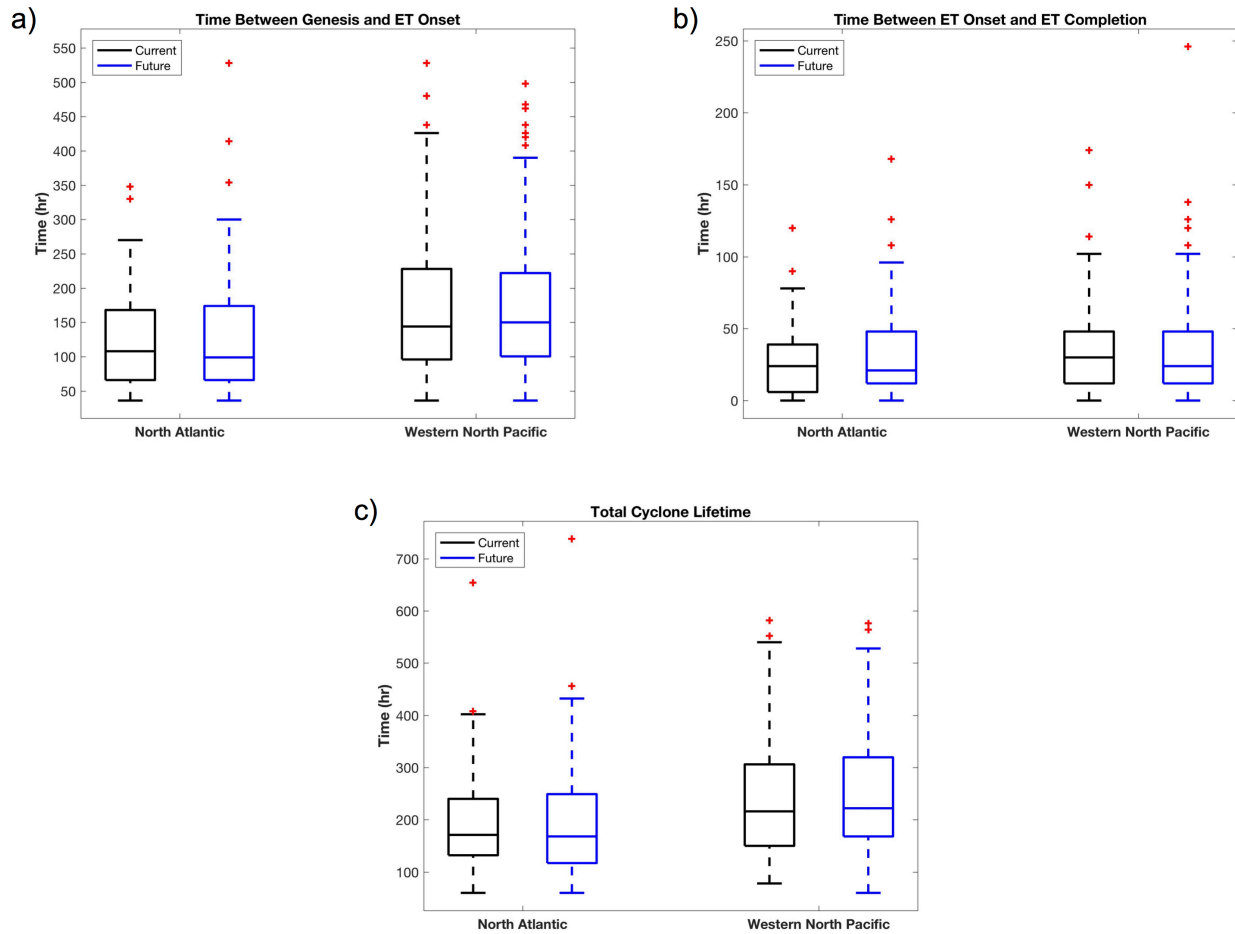


Figure 4.11: Boxplots of TC, ET, and total durations for present-day vs. future simulations. Boxplots showing (a) time (hr) between TC genesis and ET onset, (b) time (hr) between ET onset and ET completion, and (c) total cyclone lifetime (hr) for all storms over the ten simulation years in the North Atlantic and Western North Pacific basins. Present-day (future) distributions are shown in black (blue). The bottom whisker indicates the minimum duration. The top whisker indicates the maximum duration. The bottom, middle, and top lines associated with each box represent the 25th, 50th, and 75th percentile duration. The red asterisks represent outliers that fall outside of $\pm 2.7\sigma$ range.

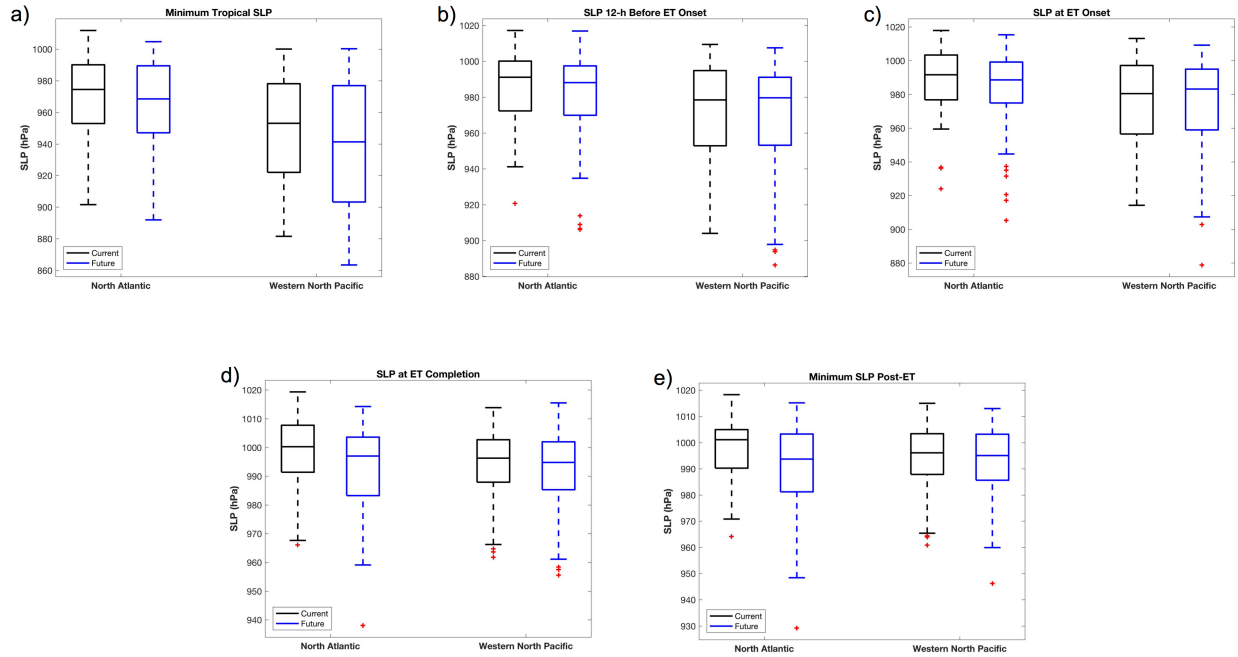


Figure 4.12: *Boxplots of minimum SLP at various stages of the cyclone lifecycle for present-day vs. future simulations.* Boxplots showing (a) minimum SLP (hPa) reached as a tropical cyclone before ET onset, (b) SLP (hPa) 12-h prior to ET onset, (c) SLP (hPa) at the time of ET onset, (d) SLP (hPa) at the time of ET completion, and (e) minimum SLP (hPa) reached as an extratropical cyclone after ET completion for all storms over the ten simulation years in the North Atlantic and Western North Pacific basins. Present-day (future) distributions are shown in black (blue). The bottom whisker indicates the minimum intensity. The top whisker indicates the maximum intensity. The bottom, middle, and top lines associated with each box represent the 25th, 50th, and 75th percentile intensity. The red asterisks represent outliers that fall outside of $\pm 2.7\sigma$ range.

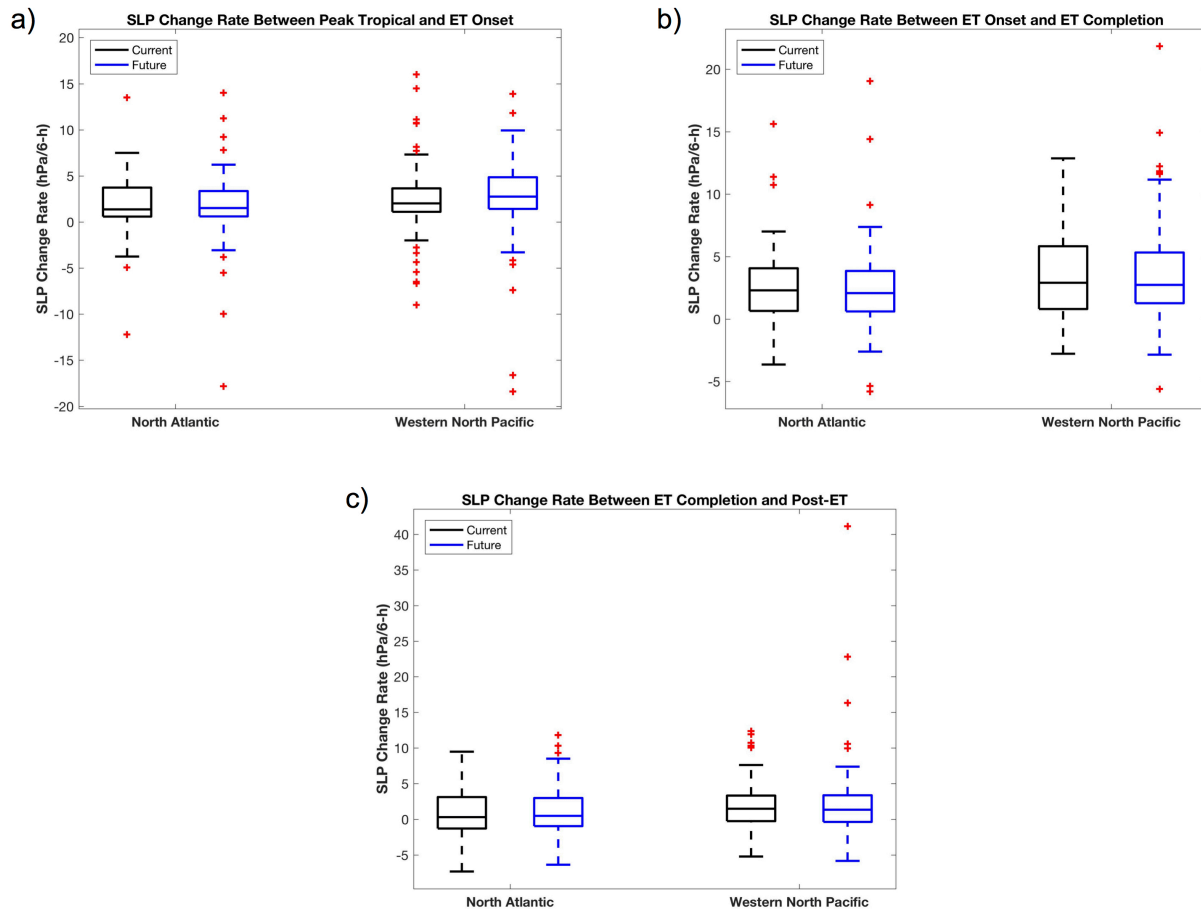


Figure 4.13: Boxplots of SLP change rate between various stages of the cyclone lifecycle for present-day vs. future simulations. Boxplots showing SLP change rate (hPa/6-h) between (a) peak intensity as a tropical cyclone and ET onset, (b) ET onset and ET completion, and (c) ET completion and peak intensity as an extratropical cyclone for all storms over the ten simulation years in the North Atlantic and Western North Pacific basins. Present-day (future) distributions are shown in black (blue). The bottom whisker indicates the minimum intensity change. The top whisker indicates the maximum intensity change. The bottom, middle, and top lines associated with each box represent the 25th, 50th, and 75th percentile intensity change. The red asterisks represent outliers that fall outside of $\pm 2.7\sigma$ range.

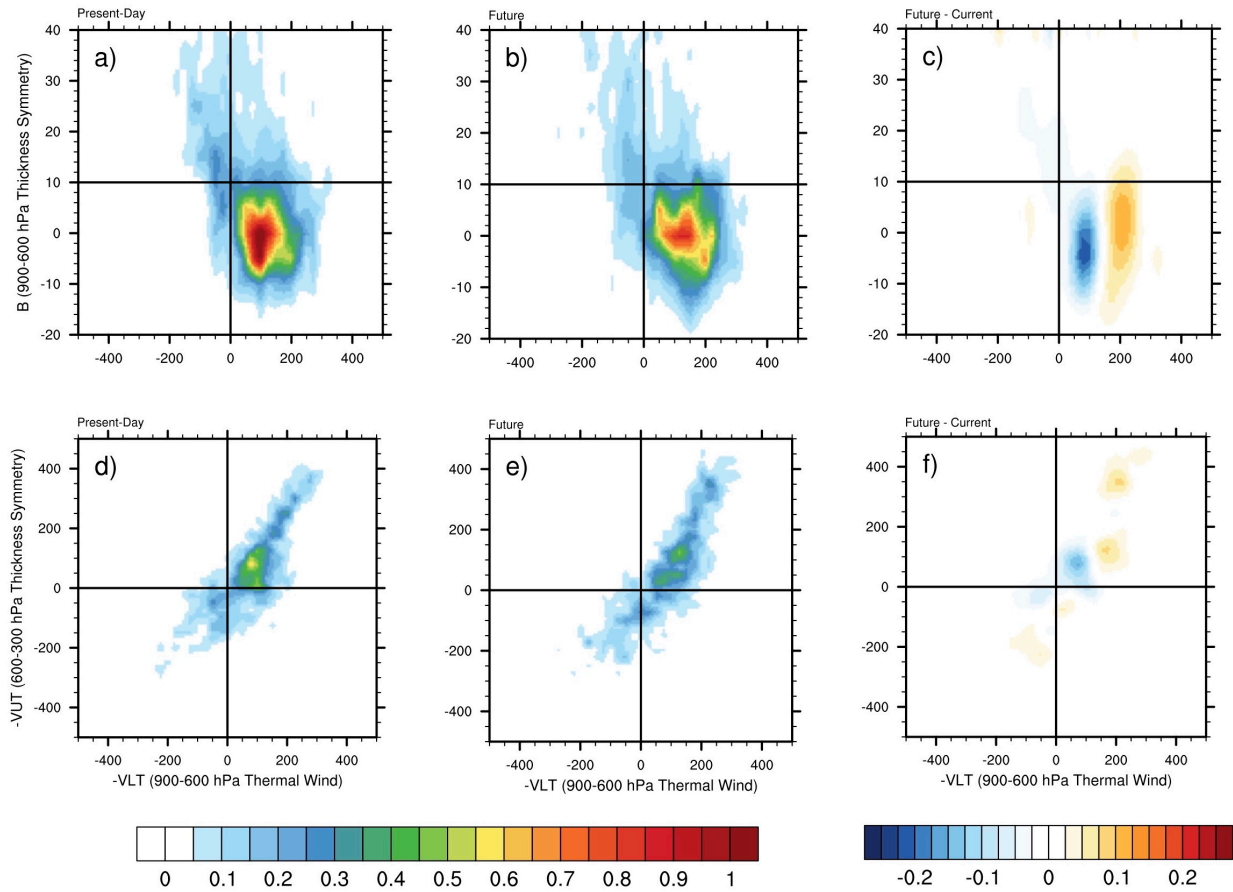


Figure 4.14: Cyclone phase space frequency diagrams for present-day vs. future NATL ET events. Cyclone phase space frequency diagrams for all NATL ET events in the (a,d) present-day simulations, (b,e) future simulations, and (c,f) future minus present-day. $-VLT$ vs. B is shown on the top row. $-VLT$ vs. $-VUT$ is shown on the bottom row. Frequencies are normalized by the number of storms.

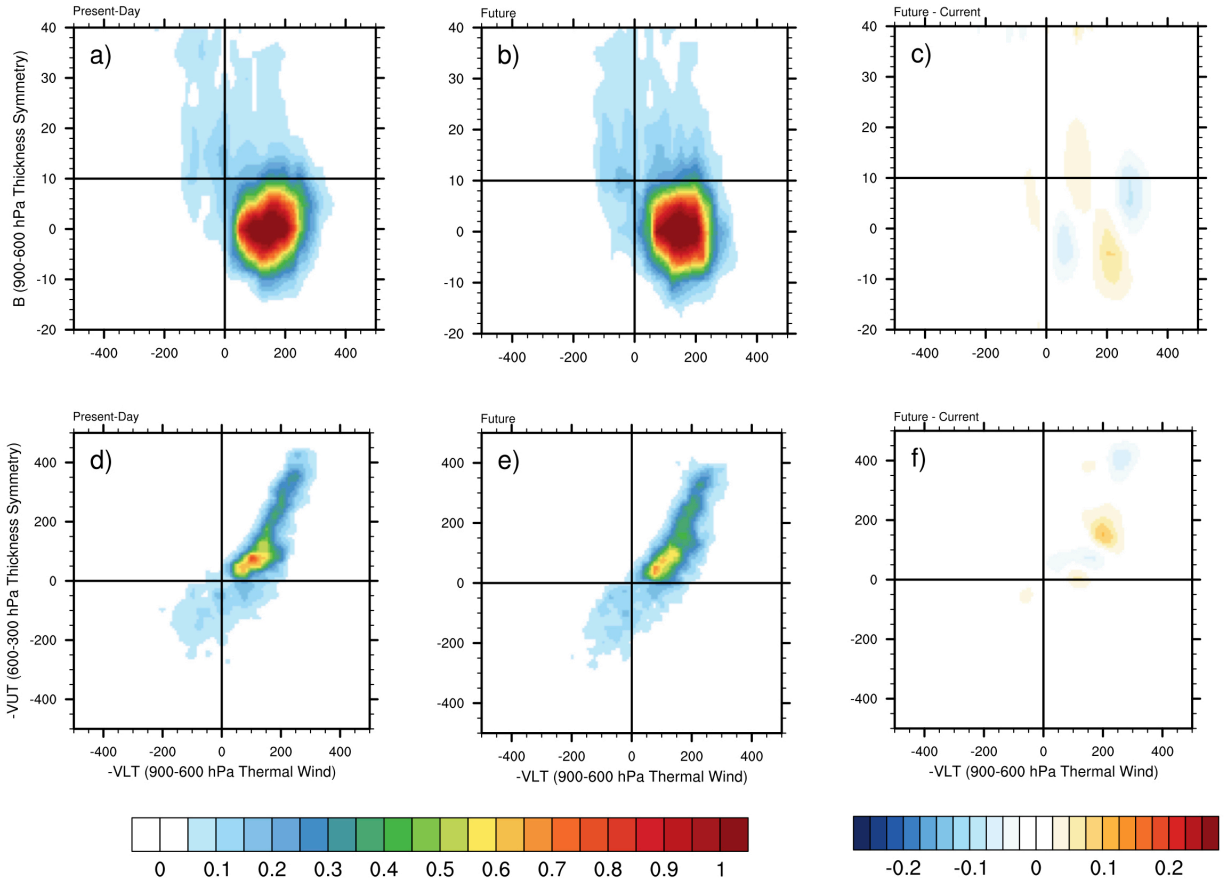


Figure 4.15: *Cyclone phase space frequency diagrams for present-day vs. future WNP ET events.* Cyclone phase space frequency diagrams for all WNP ET events in the (a,d) present-day simulations, (b,e) future simulations, and (c,f) future minus present-day. $-VLT$ vs. B is shown on the top row. $-VLT$ vs. $-VUT$ is shown on the bottom row. Frequencies are normalized by the number of storms.

5. Present-day to Future Changes: Storm-scale Dynamics

In this chapter, we examine composite ET events from the present-day and future simulations to assess potential changes in storm-scale dynamics and impacts associated with these systems. As discussed in Section 2.4, we generate the composites using cases whose 500-hPa height anomaly field correlates strongly ($r \geq 0.3$) with a reference case (Fig. 2.8). We use the same reference case to select events for the NATL and WNP composites in both the present-day and future simulations. Unless otherwise stated, the present-to-future changes presented in this Chapter refer to changes exhibited only by the composited population of ET events. The present-day and future NATL composite includes 21 and 30 cases, respectively; the present-day and future WNP composite includes 32 and 31, respectively. First, changes found for the NATL composite ET events are presented. A similar discussion of the WNP composite events will follow in Section 5.2.

5.1. North Atlantic Basin

5.1.1. Overview of the Extratropical Transition Process

The ET process for the composite ET events is best illustrated using the full 500-hPa height and 850-hPa temperature fields. Note that due to the imposed warming in the future simulations, both of these quantities will be higher in the future composite. For the purpose of providing an overview of the ET process, we will focus on the patterns exhibited by the height and temperature fields rather than their respective magnitudes. The magnitudes of features such as the upper-level trough and downstream ridge will be examined in more detail using anomaly fields in Section 5.1.3.

The present-day NATL composite ET event undergoes the transition process as expected. 24-h prior to ET onset, the TC is located in an area of weak temperature gradients with a clearly defined warm core, and is a separate feature in the 500-hPa height field (Fig. 5.1a–b). By ET onset, a distinct warm core is still apparent, but the storm has moved into a more baroclinic region as indicated by the stronger temperature gradients to the northwest, and has further interacted with the upper-level trough to the west (Fig. 5.1i–j). By ET completion, an isolated warm core is no longer visible (Fig. 5.1n); 12-h later, the SLP field around the resultant storm has substantially broadened and the TC remnants (i.e., resultant ETC) have been fully embedded in the baroclinic environment (Fig. 5.1q–r).

The overall process is generally the same for the future NATL composite event with the TC starting as a separate feature in the 500-hPa height field with a distinct warm core at 24-h prior to ET onset (Fig. 5.1c–d), interacting with an upper-level trough and stronger temperature gradients (Fig. 5.1g–h,k–l,o–p) to the northwest, and eventually losing its isolated warm core structure and merging completely into the midlatitude flow by 12-h after ET completion (Fig. 5.1s–t). While the process is the same, there are a few differences between the present-day and future NATL composite events. First, the interaction between the TC and upper-level trough at ET onset appears to be stronger in the future composite. At this time, the future composite storm shares multiple contours with the upper-level trough, and has become a clear open wave in the 500-hPa height field while the current composite storm has not yet reached this point in the trough-TC interaction (Fig. 5.1i,k). Second, the upstream trough is more amplified and better defined at ET completion and 12-h after ET completion in the future composite (Fig. 5.1m,o,q,s); the downstream ridge in the future composite is also broader and more organized after ET completion (Fig. 5.1q,s). Last, in terms of minimum SLP, the resultant ETC at 12-h after ET completion in the future composite is more intense (Fig. 5.1q–s). At this time, the future composite ETC is ~10-hPa stronger with a minimum SLP in the present-day composite of ~1002-hPa compared to ~992-hPa in the future.

5.1.2. Statistical Changes

Here, we examine changes in the quantities discussed in Chapter 4 (e.g., storm intensity, duration, etc.), but for only the composited population of ET events.

5.1.2.1. Intensity

Both present-day and future NATL ET events weaken during the ET process, but the future composite storm is stronger at all composite times. While the future composite storm weakens more during the 24-h prior to ET onset, it weakens comparatively less during ET and in the 12-h after ET completion (Fig. 5.2).

Looking more closely at the distributions of SLP for composited events at each time, we see that, similar to the full population of ET events, future NATL composited ET events reach significantly lower SLPs as ETCs after the ET process is completed compared to their present-day counterparts. At all other times, however, differences in intensity between present-day and

future composited storms are not significant (Fig. 5.3; Table 5.1). This lack of statistical significance could be in part due to our small sample sizes ($n_{\text{present-day}} = 21$, $n_{\text{future}} = 30$); while the inclusion of more events could increase the precision of the estimated error and thus, yield more significant results, the large amount of overlap between the distributions (e.g., Fig. 5.2–5.3) suggest this is unlikely.

5.1.2.2. Cyclone Phase Space

Similar to the full population of storms, the average CPS diagram for composited NATL ET events shows a shift towards larger (more positive) – VLT and B values (Fig. 5.4c) indicating that the future ET events within the composite are more symmetric with stronger warm cores, particularly during the tropical phase (lower-right quadrant). Compared to the full population of NATL ET events (Fig. 4.12c), the future composite shows a stronger shift towards larger B values. Furthermore, the area of increased frequency is larger and extends farther into upper-right quadrant for the composited subset of NATL ET events, suggesting that these future events show a stronger signal for maintaining their warm-core structure for longer durations compared to current events.

5.1.2.3. Duration

The median time between TC genesis and ET onset for the composited subset of NATL ET events is 15 h less for the future events, while the duration of transition is 6 h longer, although neither change is statistically significant (Table 5.2; Fig. 5.5). The slight shift towards stronger pre-transition storms (Table 5.1), albeit an insignificant shift, along with future events exhibiting stronger warm cores, is consistent with longer duration periods. The shorter amount of time spent as a tropical system (i.e., time between TC genesis and ET onset) is consistent with the future poleward shift in NATL ET events (Tables 4.2–4.3); existing farther poleward increases the asymmetry of the storm, and subsequently its B value, allowing it to reach the B CPS threshold sooner.

5.1.3. Dynamical Changes

As previously mentioned, full fields such as geopotential height and temperature include changes due to the warming imposed in the future simulations (e.g., higher heights, warmer

temperatures, increased moisture content); therefore, to assess changes in the magnitude of features associated with our composite ET events, like the upper-level trough and downstream ridge, we will examine anomaly fields. Here, we define an anomaly as the deviation from a daily-varying time mean computed over the ten simulation years. In Tables 5.3–5.4, changes in the trough are calculated using all grid points to the west of the storm center with negative values. Likewise, changes in the ridge are calculated using only positive values to the east of the storm center.

5.1.3.1. Upstream Trough and Downstream Ridge

The anomalous 500-hPa height and potential temperature on the dynamic tropopause (θ'_{DT}) fields are useful in examining changes in the strength and structure of the upper-level trough (negative anomaly) and downstream ridge (positive anomaly) for the composite ET events. Similar to the full 500-hPa heights, the ET process is demonstrated in the height anomaly field for both present-day and future NATL events with the TC as a separate entity 24-h prior to ET and then eventually merging with the trough approaching from the west (Fig. 5.6). In the future composite, however, there appears to be a stronger interaction between the TC and upper-level trough in that the future TC begins sharing a contour with the trough 12-h prior to ET onset, and continues to be a part of the negative anomaly through ET completion and post-completion (Fig. 5.6e,h,k,n). While there is still interaction between the TC and trough in the present-day composite, the TC does not become as incorporated into the negative anomaly.

Through ET onset, the average strength of the negative 500-hPa height anomaly changes less than 1% while the maximum strength of the trough increases by ~25% over this time period (Table 5.3). The most significant change in the upper trough through ET onset, however, is the strengthening to the south and west of the storm center at 12-h prior to ET onset and at the time of ET onset (Fig. 5.6f,i). Additionally, at these times, the future composite TC is located ~3° farther north. Therefore, the increased TC-trough interaction in the future composite is likely correlated with this significant equatorward shift of the upstream trough maximum (i.e., increased meridional amplitude) and the poleward shift of the storm center; the closer the proximity of the two entities, the stronger the interaction (Hart et al. 2006; Ritchie and Elsberry 2007). The upstream trough also appears less zonally extended (i.e., “thinner”) in the future composite through ET onset (Fig. 5.6a–b,d–e,g–h), which could further enhance the trough-TC

interaction and speed up the transition process (Hart et al. 2006). Previous work has shown limited evidence for increased meridional trough amplitude in a future climate (e.g., Screen and Simmonds 2013). While our results appear to be consistent with this finding, they could also be an artifact of our sampling method, and thus, not represent a true dynamical change. Therefore, it is necessary to compare this result against a larger sample of ET events before it can be considered robust.

At ET completion and 12-h after ET completion, the negative anomaly is significantly stronger and more organized in the future composite (Fig 5.6j–o). Over these two time periods, the average and maximum strength of the trough increases by $\sim 179\%$ and $\sim 160\%$, respectively (Table 5.3). A stronger upper-level trough again suggests more interaction between the trough and post-transition ETC in the future, which is consistent with the significant increase in strength shown for the future composite event at 12-h after ET completion (Table 5.1). A poleward shift of $\sim 5^\circ$ in the storm center after ET completion also enables strengthened and continued trough-TC interactions.

The other significant change in the 500-hPa height anomaly field for the composite NATL ET events is the strengthening and broadening of the downstream ridge, particularly from ET onset through post-completion, likely indicating stronger diabatic outflow from the ET event in the future, or stronger southerly advection of low-PV air due to the stronger circulation of the composite cyclone. On average over the compositing times, the average and maximum strength of the positive height anomaly increases $\sim 13\%$ and 20% , respectively (Table 5.3). This enhanced downstream ridge is reinforced in the θ'_{DT} field (Fig. 5.7). Here, the change is especially apparent at 12-h after ET completion (Fig. 5.7q–s) where the average strength of the positive anomaly increases $\sim 84\%$ and the maximum strength increases $\sim 48\%$ (Table 5.4). Additionally, wind speed on the dynamic tropopause is significantly stronger on the north side of the ridge at most composite times (Fig. 5.7d,h,l,p,t). A broader, stronger ridge and associated outflow in the future has implications for downstream effects to be more severe in the future (Harr and Dea 2009; Archambault et al. 2013; Archambault et al. 2015; Keller et al. 2018).

5.1.3.2. Tropical Cyclone Characteristics

Next, we examine the 900–700-hPa layer average potential vorticity (lower-level potential vorticity; LPV), the vertical structure of PV, and the 2-m potential temperature anomaly

(θ'_{2-m}) to further assess changes in the strength of the pre-existing TC and resultant post-transition ETC. We generate composites of LPV and θ'_{2-m} within a 5° radius of the storm center to get the best view of the storm structure. For the NATL composite ET events, there is a clear increase in LPV at all times in the future with the largest increases occurring near the storm center 24-h and 12-h prior to ET onset (Fig. 5.8). While a large portion of the increases in LPV surrounding the storm center are significant, especially prior to ET completion, the intensification in the direct vicinity of the storm center is not (Fig. 5.8c,f,i,l,o). Over all composite times, the average and maximum LPV increase by $\sim 20\%$ and $\sim 19\%$, respectively (Table 5.5), a portion of which is likely due to the poleward shift in storm location. Taking a vertical cross-section through the storm center, we see that the PV tower associated with the TC through ET onset is noticeably stronger and taller in the future composite; the 2-PVU contour extends well into the troposphere and the maximum PV in the mid-levels is at least 1-PVU greater (Fig. 5.9a–f). After ET onset, however, differences between the present-day and future composites are less drastic; the PV is still generally stronger in the future composite, but the PV tower near the storm center is less organized (Fig. 5.9g–j).

Like the LPV, θ'_{2-m} is also stronger at all composite times in the future (Fig. 5.10). Over the composite times, the average θ'_{2-m} increases $\sim 65\%$ and the maximum increases $\sim 24\%$ (Table 5.6). The changes are most significant, though, after ET completion (Fig. 5.10m–o) where the average and maximum θ'_{2-m} are $\sim 167\%$ and $\sim 92\%$ stronger, respectively (Table 5.6). Overall, enhanced θ'_{2-m} , LPV, and PV tower suggest a generally stronger and deeper NATL storm in the future.

5.1.3.3. Impacts

Intense precipitation and strong near-surface winds are among the primary impacts associated with ET events, both of which are generally stronger in the future for the NATL composite events. Over the composite times, the average and maximum 6-hourly precipitation increases by $\sim 30\%$ and $\sim 54\%$, respectively (Table 5.7), while the average 10-m wind speed increases by $\sim 21\%$ (Table 5.8). The change in the maximum 10-m wind speed is less drastic, increasing only $\sim 4\%$ on average (Table 5.8).

While the general structure of precipitation is similar between the NATL present-day and future composites at most times, there are large increases in precipitation near the storm center at

all composite times (Fig. 5.11), similar to the changes in LPV (Fig. 5.8). The most significant increases, however, occur to the northwest of the storm center at ET completion and to the north and east of the storm center 12-h after ET completion (Fig. 5.11p,t). Overall increases in precipitation are consistent with strengthening LPV. In both the present-day and future composites, the storm center is located in the right-entrance region of the upper-level jet at all times (Fig. 5.12a–b,d–e,g–h,j–k,m–n), which is an area favorable for ascent and heavy precipitation. A significantly stronger jet occurs in the future composite (Fig. 5.12c,f,l,i,o), leading to enhanced forcing for ascent in the simulated future storms and likely contributing to the observed increased 6-hourly precipitation. Over the composite times, the average increases in area-average and maximum 6-hourly precipitation (Table 5.7) correspond to a ~ 3 -K increase in the area-average 850-hPa temperature. Following the Clausius-Clapeyron relation, this increase in temperature should result in a $\sim 21\%$ increase in water vapor; therefore, both the maximum 6-hourly precipitation and average precipitation over the composite area increase at a super-Clausius-Clapeyron rate. Jung and Lackmann (2018, in review) found that due to enhanced moisture flux convergence and evaporation from the surface, precipitation associated with Hurricane Irene (2011) also increased at a super-Clausius-Clapeyron rate.

In the future composite, there are significant increases in 10-m wind speed to the south of the storm center prior to ET onset, but the largest and most significant change is the strengthening to the southeast of the storm center at 12-h after ET completion (Fig. 5.11d,h,t). At this time, the maximum and average 10-m wind speed over the composite area increase by $\sim 22\%$ and $\sim 48\%$, respectively (Table 5.8). Stronger low-level winds, particularly at ET completion and post-completion are consistent with the apparent tighter SLP gradient in the future NATL composite (Fig. 5.8).

5.2. Western North Pacific Basin

5.2.1. Overview of the Extratropical Transition Process

As with the NATL, we will discuss the ET process for the composite ET events using the full 500-hPa height and 850-hPa temperature fields. The magnitudes of features such as the upper-level trough and downstream ridge will be examined in more detail using anomaly fields in Section 5.2.3.

The ET process for the WNP present-day and future composite events is similar to that shown for the NATL events (Fig. 5.13). The differences between the present-day and future composite storms discussed for the NATL events, however, are not the same as the differences we see for the WNP composite events. For example, the future NATL composite event appeared to have a stronger interaction with the upper-level trough earlier in the ET process (i.e., at ET onset, the future NATL TC was comparatively more embedded in the midlatitude flow; Fig. 5.1i,k). With the WNP event, the opposite is true: at 24-h and 12-h prior to ET onset, the TC in the future composite appears to be comparatively less incorporated into the midlatitude flow (Fig. 5.13a,c,e,g). Additionally, while the upstream trough, downstream ridge, and resultant ETC were all noticeably stronger or more amplified in future NATL composite at ET completion and post-completion (Fig. 5.1m,o,q,s), the upper-level trough in the WNP composite is less amplified, the downstream ridge is not noticeably different, and the resultant ETC is weaker in the future (Fig. 5.13m,o,q,s).

5.2.2. Statistical Changes

5.2.2.1. Intensity

Similar to the NATL composite, present-day and future WNP ET events also generally weaken during the ET process. The intensity is similar between present-day and future composite storms for the WNP, with the future composite being slightly weaker at all composite times. The future WNP composite event weakens less during the 24-h prior to ET onset, but weakens slightly more during ET. Both present-day and future composite events weaken at the same rate between ET completion and 12-h after ET completion (Fig. 5.14). At all composite times, future WNP ET events are weaker on average, but no differences are statistically significant (Fig. 5.15; Table 5.9). Again, sample sizes are small ($n_{\text{present-day}} = 32$, $n_{\text{future}} = 31$), but there is already a considerable amount of overlap between the present-day and future distributions (Fig. 5.14–5.15).

5.2.2.2. Cyclone Phase Space

As with the full population of WNP ET events (Fig. 4.13), the patterns exhibited in the average CPS by the composited WNP ET events are noisy and show no prominent signal (Fig. 5.16).

5.2.2.3. Duration

Unlike the NATL, the suggestion of potentially weaker WNP ET events in the future (Table 5.9) could correlate with shorter ET durations; the median time between ET onset and completion is 6-h shorter for the future composited events. Additionally, the future median time between TC genesis and ET onset is also shorter by 9 h (Table 5.10; Fig. 5.17). Like the full population of storms, however, these shifts in timing between various stages of the TC cycle are not significant.

5.2.3. Dynamical Changes

5.2.3.1. Upstream Trough and Downstream Ridge

For the WNP, the downstream ridge and associated flow to the north are significantly enhanced in the future composite (Figs. 5.18–5.19). Over all composite times, the average and maximum strength of the positive anomaly in the 500-hPa height field increases by ~63% and ~55%, respectively (Table 5.11). The changes in the θ'_{DT} positive anomaly are less extreme with the average strength increasing ~37% and the maximum strength increasing only ~6% (Table 5.12). Over the composite times, the magnitude of the upper-level trough in the height anomaly field is not drastically different in the future composite (Table 5.11; Fig. 5.18). There is, however, a small area of significant weakening of the upper-level trough to the northwest of the storm center at ET onset, which appears to be associated with a slight poleward shift in the trough maximum in the future composite (Fig. 5.18g–i). At ET onset, the present-day event has a greater interaction with the upstream trough (Fig 5.18g–h), likely due to this poleward shift limiting the interaction between the trough and TC in the future composite.

5.2.3.2. Tropical Cyclone Characteristics

Changes in LPV and θ'_{2-m} for the WNP composite ET events are much less significant than those found for the NATL. There are slight changes in LPV at all composite times with small areas of strengthening around the TC center prior to ET onset, but general weakening at the storm center, all of which are largely insignificant (Fig. 5.20). Over all composite times, the LPV increases by a modest ~3% while the maximum LPV is reduced by ~12% (Table 5.13). The PV tower associated with the TC is slightly deeper through ET onset in the future, but is also generally weaker (Fig. 5.21a–f). After ET onset, there is little difference in the PV tower around

the storm center, but upper-level PV between 300–150-hPa is noticeably weaker in the future composite (Fig. 5.21g–j). Similar to LPV, changes in θ'_{2-m} for the WNP composite events are small and largely insignificant (Fig. 5.22). There are slight increases in θ'_{2-m} to the southeast of the storm center prior to ET onset (Fig. 5.22c,f), then an area of significant reduction to the north of the storm center at ET completion (Fig. 5.22i). Over all composite times, the average and maximum θ'_{2-m} weaken by $\sim 11\%$ and $\sim 17\%$, respectively (Table 5.14); small changes in θ'_{2-m} and LPV are consistent with insignificant changes in storm intensity (Table 5.1).

5.2.3.3. Impacts

Changes in 6-hourly precipitation and 10-m wind speed for the WNP composite events are generally less drastic than those shown for the NATL. While large increases in precipitation occur just to the south of the storm center through ET onset, the most significant changes are the reductions in precipitation to the east and west of the storm center at ET completion and 12-h after ET completion (Fig. 5.23c,g,k,o,s). Over the composite times, the area-average and maximum 6-hourly precipitation increase by $\sim 10\%$ and $\sim 8\%$, respectively (Table 5.15). These changes in precipitation correspond to average increase in area-average 850-hPa temperature of $\sim 4.6\text{-K}$, which suggests a $\sim 32\%$ increase in water vapor as dictated by the Clausius-Clapeyron relation. Therefore, unlike the NATL composite events, precipitation in the WNP composite events increases at a sub-Clausius-Clapeyron rate.

Like 6-hourly precipitation, the present-to-future changes in 10-m wind speed are also small and largely insignificant. The most substantial changes are the localized areas of reduction to the south-southeast of the storm center at ET completion and post-completion (Fig. 5.23p,t). On average over the composite times, the area-average and maximum 10-m wind speed decrease by $\sim 1\%$ and $\sim 10\%$, respectively (Table 5.16). Small changes in near-surface winds are consistent with no noticeable difference in SLP gradient for the WNP composites (Fig. 5.20).

5.3. Summary

As demonstrated by the composite events, the overall ET process is virtually unchanged in the future simulations; the pre-existing tropical cyclone interacts with an upper-level trough approaching from the west and eventually becomes fully incorporated into the midlatitude flow (Figs. 5.1; Fig. 5.13). With the exception of the significant increase in strength for future NATL

storms at 12-h after ET completion, the intensity of the composite ET events is also largely unchanged throughout the ET process in both basins (Table 5.1; Fig. 5.3). Composited NATL ET events do show a shift towards storms being more asymmetric with a stronger warm core structure, particularly during the tropical phase (Fig. 5.4). Despite a more intense and vertically extended PV tower through ET onset in the future NATL composite (Fig. 5.9), no significant changes in timing between TC genesis and ET onset and between ET onset and ET completion are found; changes in durations for the WNP composite events are also insignificant (Table 5.2; Table 5.10; Fig. 5.5; Fig. 5.17). With that said, several important changes between the present-day and future ET events do occur.

For one, the future NATL composite ET event appears to have a stronger interaction with the upper-level trough throughout the ET process, likely attributed to the significant equatorward shift in the trough maximum beginning at 12-h prior to ET onset (Fig. 5.6d–i) and a poleward shift in the storm center location. Furthermore, the upstream trough in the future composite is substantially stronger and more organized at ET completion and post-completion (Fig. 5.6j–o), allowing for continued interaction between the trough and resultant ETC, and is consistent with NATL ET events reaching lower minimum SLPs as ETCs in the future (Table 5.1).

Secondly, for both NATL and WNP events, the downstream ridge is significantly stronger and extended farther east in the future composite (Figs. 5.6–5.7; Figs. 5.18–5.19). Additionally, the wind speed on the dynamic tropopause is enhanced to the north of the downstream ridge (Fig. 5.7; Fig. 5.19), indicating that future ET events in both basins appear to be accompanied by stronger diabatic outflow. This is consistent with significantly enhanced LPV in broad areas around the storm center for the future NATL event at all composite times (Fig. 5.8). The composite WNP event also experiences areas of increased LPV in the future, but the significance of these changes is less widespread (Fig. 5.20).

The primary impacts associated with ET events, precipitation and near-surface winds, are more intense in the future for the NATL composite, particularly after ET completion (Table 5.7–5.8; Fig. 5.11s–t). Significant strengthening of θ'_{2-m} after ET completion (Fig. 5.10o) is consistent with a stronger cyclonic circulation. On average, 6-hourly precipitation in the future NATL composite increases at a super-Clausius-Clapeyron rate. On the other hand, small changes in, and even slight reductions at later times of, θ'_{2-m} (Table 5.14; Fig. 5.22) in the WNP composite are consistent with small changes (and slight reductions) in 10-m wind speed (Table

5.16; Fig. 5.23). While precipitation does, on average, increase in the future WNP composite (Table 5.15), it does so at a sub-Clausius-Clapeyron rate.

Table 5.1: Median intensity (SLP; hPa) at various stages of the cyclone life cycle for composited NATL ET events. p-values are reported from the Wilcoxon Rank Sum statistical significance test. Italicized (bold) values indicate statistical significance at the 90% (95%) confidence level.

Basin	Climate	Median SLP (hPa) 24-h Prior to ET Onset	Median SLP (hPa) 12-h Prior to ET Onset	Median SLP (hPa) at ET Onset	Median SLP (hPa) at ET Completion	Median SLP (hPa) 12-h After ET Completion
North Atlantic	Current	994.6	997.3	994.1	999.5	1002.2
	Future	986.4	985.1	990.9	993.5	996.6
	p-value	0.28	0.41	0.44	0.23	0.04

Table 5.2: Median duration (hrs) of various stages of the cyclone life cycle for composited NATL ET events. p-values are reported from the Wilcoxon Rank Sum statistical significance test. Italicized (bold) values indicate statistical significance at the 90% (95%) confidence level.

Basin	Climate	Median Time (hr) Between TC Genesis and ET Onset	Median Time (hr) Between ET Onset and ET Completion
North Atlantic	Current	108	12
	Future	93	18
	p-value	0.62	0.75

Table 5.3: Absolute and percent changes in average and maximum positive and negative 500-hPa height anomaly values over the full composite area for NATL composite ET events. Changes for trough (ridge) calculated using all grid points to the west (east) of the storm center with negative (positive) values. Average and maximum values reported rounded to the nearest whole number. Percent change values computed using unrounded values, then reported rounded to the nearest whole percent.

			ET onset – 24-h	ET onset – 12-h	ET onset	ET completion	ET completion +12-h	Average
Negative Anomaly (Trough)	Average	Current	-43-m	-43-m	-38-m	-22-m	-12-m	-32-m
		Future	-39-m	-42-m	-41-m	-37-m	-46-m	-41-m
		Abs. Change	+4-m	+1-m	-3-m	-15-m	-34-m	-9-m
		% Change	+8%	+3%	-9%	-74%	-284%	-71%
	Maximum	Current	-158-m	-140-m	-114-m	-52-m	-28-m	-98-m
		Future	-202-m	-174-m	-143-m	-89-m	-98-m	-141-m
		Abs. Change	-44-m	-34-m	-29-m	-37-m	-70-m	-43-m
		% Change	-27%	-24%	-26%	-73%	-246%	-79%
Positive Anomaly (Ridge)	Average	Current	+48-m	+58-m	+62-m	+56-m	+42-m	+53-m
		Future	+55-m	+65-m	+65-m	+62-m	+51-m	+60-m
		Abs. Change	+7-m	+7-m	+3-m	+6-m	+9-m	+6-m
		% Change	+16%	+12%	+4%	+11%	+23%	+13%
	Maximum	Current	+101-m	+118-m	+123-m	+120-m	+80-m	+108-m
		Future	+120-m	+144-m	+147-m	+137-m	+101-m	+130-m
		Abs. Change	+19-m	+26-m	+24-m	+17-m	+21-m	+21-m
		% Change	+19%	+21%	+20%	+14%	+26%	+20%

Table 5.4: Absolute and percent changes in average and maximum positive and negative θ'_{DT} values over the full composite area for NATL composite ET events. Changes for trough (ridge) calculated using all grid points to the west (east) of the storm center with negative (positive) values. Average and maximum values reported rounded to the nearest whole number. Percent change values computed using unrounded values, then reported rounded to the nearest whole percent.

		ET onset – 24-h	ET onset – 12-h	ET onset	ET completion	ET completion +12-h	Average	
Negative Anomaly (Trough)	Average	Current	-5-K	-4-K	-4-K	-3-K	-3-K	-4-K
		Future	-4-K	-4-K	-4-K	-3-K	-3-K	-4-K
		Abs. Change	+1-K	0-K	0-K	0-K	0-K	0-K
		% Change	+14%	+6%	+18%	+8%	-12%	+7%
	Maximum	Current	-15-K	-16-K	-15-K	-10-K	-10-K	-13-K
		Future	-16-K	-20-K	-15-K	-11-K	-11-K	-15-K
		Abs. Change	-1-K	-4-K	0-K	-1-K	-1-K	-1-K
		% Change	-4%	-25%	-5%	-4%	-3%	-8%
Positive Anomaly (Ridge)	Average	Current	+5-K	+7-K	+7-K	+7-K	+5-K	+6-K
		Future	+7-K	+8-K	+9-K	+9-K	+10-K	+9-K
		Abs. Change	+2-K	+1-K	+2-K	+2-K	+5-K	+2-K
		% Change	+29%	+21%	+28%	+37%	+84%	+40%
	Maximum	Current	+20-K	+26-K	+25-K	+25-K	+21-K	+23-K
		Future	+26-K	+26-K	+31-K	+28-K	+31-K	+28-K
		Abs. Change	+6-K	0-K	+6-K	+3-K	+10-K	+5-K
		% Change	+30%	+1%	+27%	+12%	+48%	+24%

Table 5.5: Absolute and percent changes in average and maximum 900–700-hPa PV values over the composite area within 5° of the storm center for NATL composite ET events. Average and maximum values reported rounded to the nearest whole number. Percent change values computed using unrounded values, then reported rounded to the nearest whole percent.

		ET onset – 24-h	ET onset – 12-h	ET onset	ET completion	ET completion +12-h	Average
Average	Current	0.4-PVU	0.4-PVU	0.5-PVU	0.6-PVU	0.7-PVU	0.5-PVU
	Future	0.5-PVU	0.5-PVU	0.6-PVU	0.7-PVU	0.8-PVU	0.6-PVU
	Abs. Change	+0.1-PVU	+0.1-PVU	+0.1-PVU	+0.1-PVU	+0.1-PVU	+0.1-PVU
	% Change	+24%	+24%	+24%	+12%	+16%	+20%
Maximum	Current	3-PVU	3-PVU	3-PVU	2-PVU	1-PVU	2-PVU
	Future	4-PVU	4-PVU	3-PVU	2-PVU	1-PVU	3-PVU
	Abs. Change	+1-PVU	+1-PVU	0-PVU	0-PVU	0-PVU	0-PVU
	% Change	+42%	+35%	+15%	0%	+3%	+19%

Table 5.6: Absolute and percent changes in average and maximum θ'_{2-m} values over the composite area within 5° of the storm center for NATL composite ET events. Average and maximum values reported rounded to the nearest whole number. Percent change values computed using unrounded values, then reported rounded to the nearest whole percent.

		ET onset – 24-h	ET onset – 12-h	ET onset	ET completion	ET completion +12-h	Average
Average	Current	1-K	2-K	2-K	1-K	1-K	1-K
	Future	1-K	2-K	2-K	2-K	2-K	2-K
	Abs. Change	0-K	0-K	0-K	1-K	1-K	0-K
	% Change	+21%	+19%	+29%	+90%	+167%	+65%
Maximum	Current	4-K	4-K	5-K	4-K	2-K	4-K
	Future	4-K	4-K	5-K	4-K	5-K	4-K
	Abs. Change	0-K	0-K	0-K	0-K	3-K	1-K
	% Change	+5%	-4%	+1%	+24%	+92%	+24%

Table 5.7: Absolute and percent changes in average and maximum 6-hourly precipitation values over the composite area within 10° of the storm center for NATL composite ET events. Average and maximum values reported rounded to the nearest whole number. Percent change values computed using unrounded values, then reported rounded to the nearest whole percent.

		ET onset – 24-h	ET onset – 12-h	ET onset	ET completion	ET completion +12-h	Average
Average	Current	2-mm	2-mm	2-mm	2-mm	1-mm	2-mm
	Future	2-mm	2-mm	3-mm	3-mm	3-mm	3-mm
	Abs. Change	0-mm	0-mm	+1-mm	+1-mm	+2-mm	+1-mm
	% Change	-1%	+6%	+22%	+39%	+85%	+30%
Maximum	Current	41-mm	41-mm	34-mm	17-mm	13-mm	29-mm
	Future	56-mm	53-mm	44-mm	35-mm	21-mm	42-mm
	Abs. Change	+15-mm	+12-mm	+10-mm	+18-mm	+8-mm	+13-mm
	% Change	+37%	+30%	+31%	+107%	+67%	+54%

Table 5.8: Absolute and percent changes in average and maximum 10-m wind speed values over the composite area within 10° of the storm center for NATL composite ET events. Average and maximum values reported rounded to the nearest whole number. Percent change values computed using unrounded values, then reported rounded to the nearest whole percent.

		ET onset – 24-h	ET onset – 12-h	ET onset	ET completion	ET completion +12-h	Average
Average	Current	5-ms ⁻¹	5-ms ⁻¹	5-ms ⁻¹	4-ms ⁻¹	4-ms ⁻¹	5-ms ⁻¹
	Future	5-ms ⁻¹	5-ms ⁻¹	6-ms ⁻¹	6-ms ⁻¹	5-ms ⁻¹	5-ms ⁻¹
	Abs. Change	0-ms ⁻¹	0-ms ⁻¹	+1-ms ⁻¹	+2-ms ⁻¹	+1-ms ⁻¹	+1-ms ⁻¹
	% Change	+8%	+8%	+7%	+32%	+48%	+21%
Maximum	Current	23-ms ⁻¹	23-ms ⁻¹	24-ms ⁻¹	15-ms ⁻¹	10-ms ⁻¹	19-ms ⁻¹
	Future	23-ms ⁻¹	23-ms ⁻¹	22-ms ⁻¹	16-ms ⁻¹	12-ms ⁻¹	19-ms ⁻¹
	Abs. Change	0-ms ⁻¹	0-ms ⁻¹	-2-ms ⁻¹	+1-ms ⁻¹	+2-ms ⁻¹	0-ms ⁻¹
	% Change	+3%	-2%	-7%	+5%	+22%	+4%

Table 5.9: Median intensity (SLP; hPa) at various stages of the cyclone life cycle for composited WNP ET events. p-values are reported from the Wilcoxon Rank Sum statistical significance test. Italicized (bold) values indicate statistical significance at the 90% (95%) confidence level.

Basin	Climate	Median SLP (hPa) 24-h Prior to ET Onset	Median SLP (hPa) 12-h Prior to ET Onset	Median SLP (hPa) at ET Onset	Median SLP (hPa) at ET Completion	Median SLP (hPa) 12-h After ET Completion
North Atlantic	Current	974.4	976.2	985.2	995.9	998.9
	Future	982.5	980.1	988.6	999.4	1002.0
	p-value	0.68	0.58	0.79	0.29	0.28

Table 5.10: Median duration (hrs) of various stages of the cyclone life cycle for composited WNP ET events. p-values are reported from the Wilcoxon Rank Sum statistical significance test. Italicized (bold) values indicate statistical significance at the 90% (95%) confidence level.

Basin	Climate	Median Time (hr) Between TC Genesis and ET Onset	Median Time (hr) Between ET Onset and ET Completion
North Atlantic	Current	159	30
	Future	150	24
	p-value	0.91	0.81

Table 5.11: Absolute and percent changes in average and maximum positive and negative 500-hPa height anomaly values over the full composite area for WNP composite ET events. Changes for trough (ridge) calculated using all grid points to the west (east) of the storm center with negative (positive) values. Average and maximum values reported rounded to the nearest whole number. Percent change values computed using unrounded values, then reported rounded to the nearest whole percent.

			ET onset – 24-h	ET onset – 12-h	ET onset	ET completion	ET completion +12-h	Average
Negative Anomaly (Trough)	Average	Current	-33-m	-37-m	-38-m	-30-m	-30-m	-34-m
		Future	-35-m	-32-m	-31-m	-25-m	-24-m	-29-m
		Abs. Change	-2-m	+5-m	+7-m	+5-m	+6-m	+4-m
		% Change	-7%	+13%	+19%	+16%	+17%	+12%
	Maximum	Current	-265-m	-225-m	-161-m	-63-m	-60-m	-155-m
		Future	-240-m	-205-m	-158-m	-66-m	-44-m	-143-m
		Abs. Change	+25-m	+20-m	+3-m	-3-m	+16-m	+12-m
		% Change	+9%	+9%	+2%	-5%	+26%	+8%
Positive Anomaly (Ridge)	Average	Current	+22-m	+28-m	+34-m	+33-m	+27-m	+29-m
		Future	+42-m	+51-m	+51-m	+48-m	+38-m	+46-m
		Abs. Change	+20-m	+23-m	+17-m	+15-m	+11-m	+17-m
		% Change	+97%	+82%	+51%	+45%	+38%	+63%
	Maximum	Current	+50-m	+68-m	+82-m	+68-m	+61-m	+66-m
		Future	+93-m	+116-m	+123-m	+102-m	+75-m	+102-m
		Abs. Change	+43-m	+48-m	+41-m	+34-m	+14-m	+36-m
		% Change	+86%	+70%	+50%	+50%	+21%	+55%

Table 5.12: Absolute and percent changes in average and maximum positive and negative θ'_{DT} values over the full composite area for WNP composite ET events. Changes for trough (ridge) calculated using all grid points to the west (east) of the storm center with negative (positive) values. Average and maximum values reported rounded to the nearest whole number. Percent change values computed using unrounded values, then reported rounded to the nearest whole percent.

			ET onset – 24-h	ET onset – 12-h	ET onset	ET completion	ET completion +12-h	Average
Negative Anomaly (Trough)	Average	Current	-5-K	-5-K	-5-K	-3-K	-3-K	-4-K
		Future	-6-K	-6-K	-5-K	-4-K	-3-K	-5-K
		Abs. Change	-1-K	-1-K	0-K	-1-K	0-K	-1-K
		% Change	-36%	-25%	-9%	-26%	-29%	-25%
	Maximum	Current	-26-K	-18-K	-17-K	-14-K	-14-K	-18-K
		Future	-33-K	-27-K	-18-K	-16-K	-19-K	-23-K
		Abs. Change	-7-K	-9-K	-1-K	-2-K	-5-K	-5-K
		% Change	-30%	-53%	-4%	-13%	-37%	-27%
Positive Anomaly (Ridge)	Average	Current	+6-K	+7-K	+8-K	+9-K	+7-K	+7-K
		Future	+9-K	+10-K	+11-K	+11-K	+8-K	+10-K
		Abs. Change	+3-K	+3-K	+3-K	+2-K	+1-K	+2-K
		% Change	+49%	+52%	+40%	+31%	+15%	+37%
	Maximum	Current	+49-K	+41-K	+27-K	+29-K	+28-K	+35-K
		Future	+36-K	+42-K	+34-K	+35-K	+30-K	+35-K
		Abs. Change	-13-K	+1-K	+7-K	+6-K	+2-K	+1-K
		% Change	-25%	+3%	+24%	+18%	+8%	+6%

Table 5.13: Absolute and percent changes in average and maximum 900–700-hPa PV values over the composite area within 5° of the storm center for WNP composite ET events. Average and maximum values reported rounded to the nearest whole number. Percent change values computed using unrounded values, then reported rounded to the nearest whole percent.

		ET onset – 24-h	ET onset – 12-h	ET onset	ET completion	ET completion +12-h	Average
Average	Current	0.4-PVU	0.4-PVU	0.5-PVU	0.6-PVU	0.7-PVU	0.5-PVU
	Future	0.4-PVU	0.5-PVU	0.5-PVU	0.6-PVU	0.6-PVU	0.5-PVU
	Abs. Change	0-PVU	+0.1-PVU	0-PVU	0-PVU	-0.1-PVU	0-PVU
	% Change	+5%	+5%	+9%	+2%	-5%	+3%
Maximum	Current	4-PVU	4-PVU	3-PVU	1-PVU	1-PVU	3-PVU
	Future	3-PVU	3-PVU	3-PVU	1-PVU	1-PVU	2-PVU
	Abs. Change	-1-PVU	-1-PVU	0-PVU	0-PVU	0-PVU	0-PVU
	% Change	-16%	-16%	-16%	-6%	-6%	-12%

Table 5.14: Absolute and percent changes in average and maximum θ'_{2-m} values over the composite area within 5° of the storm center for WNP composite ET events. Average and maximum values reported rounded to the nearest whole number. Percent change values computed using unrounded values, then reported rounded to the nearest whole percent.

		ET onset – 24-h	ET onset – 12-h	ET onset	ET completion	ET completion +12-h	Average
Average	Current	1-K	1-K	1-K	2-K	2-K	1-K
	Future	1-K	1-K	1-K	1-K	1-K	1-K
	Abs. Change	0-K	0-K	0-K	-1-K	-1-K	0-K
	% Change	+3%	+30%	-17%	-42%	-29%	-11%
Maximum	Current	5-K	5-K	5-K	4-K	4-K	5-K
	Future	4-K	4-K	4-K	3-K	3-K	4-K
	Abs. Change	-1-K	-1-K	-1-K	-1-K	-1-K	-1-K
	% Change	-9%	-14%	-20%	-26%	-15%	-17%

Table 5.15: Absolute and percent changes in average and maximum 6-hourly precipitation values over the composite area within 10° of the storm center for WNP composite ET events. Average and maximum values reported rounded to the nearest whole number. Percent change values computed using unrounded values, then reported rounded to the nearest whole percent.

		ET onset – 24-h	ET onset – 12-h	ET onset	ET completion	ET completion +12-h	Average
Average	Current	3-mm	3-mm	3-mm	3-mm	2-mm	3-mm
	Future	3-mm	4-mm	4-mm	3-mm	2-mm	3-mm
	Abs. Change	0-mm	+1-mm	+1-mm	0-mm	0-mm	0-mm
	% Change	+12%	+19%	+16%	-1%	+6%	+10%
Maximum	Current	71-mm	64-mm	56-mm	23-mm	12-mm	45-mm
	Future	79-mm	62-mm	60-mm	24-mm	14-mm	48-mm
	Abs. Change	+8-mm	-1-mm	+4-mm	+1-mm	+2-mm	+3-mm
	% Change	+10%	-4%	+8%	+7%	+17%	+8%

Table 5.16: Absolute and percent changes in average and maximum 10-m wind speed values over the composite area within 10° of the storm center for WNP composite ET events. Average and maximum values reported rounded to the nearest whole number. Percent change values computed using unrounded values, then reported rounded to the nearest whole percent.

		ET onset – 24-h	ET onset – 12-h	ET onset	ET completion	ET completion +12-h	Average
Average	Current	7-ms ⁻¹	7-ms ⁻¹	7-ms ⁻¹	6-ms ⁻¹	5-ms ⁻¹	6-ms ⁻¹
	Future	7-ms ⁻¹	7-ms ⁻¹	7-ms ⁻¹	5-ms ⁻¹	4-ms ⁻¹	6-ms ⁻¹
	Abs. Change	0-ms ⁻¹	0-ms ⁻¹	0-ms ⁻¹	-1-ms ⁻¹	-1-ms ⁻¹	0-ms ⁻¹
	% Change	+7%	+5%	0%	-7%	-9%	-1%
Maximum	Current	26-ms ⁻¹	25-ms ⁻¹	23-ms ⁻¹	16-ms ⁻¹	11-ms ⁻¹	20-ms ⁻¹
	Future	25-ms ⁻¹	23-ms ⁻¹	21-ms ⁻¹	13-ms ⁻¹	10-ms ⁻¹	18-ms ⁻¹
	Abs. Change	-1-ms ⁻¹	-2-ms ⁻¹	-2-ms ⁻¹	-3-ms ⁻¹	-1-ms ⁻¹	-2-ms ⁻¹
	% Change	-6%	-8%	-11%	-16%	-10%	-10%

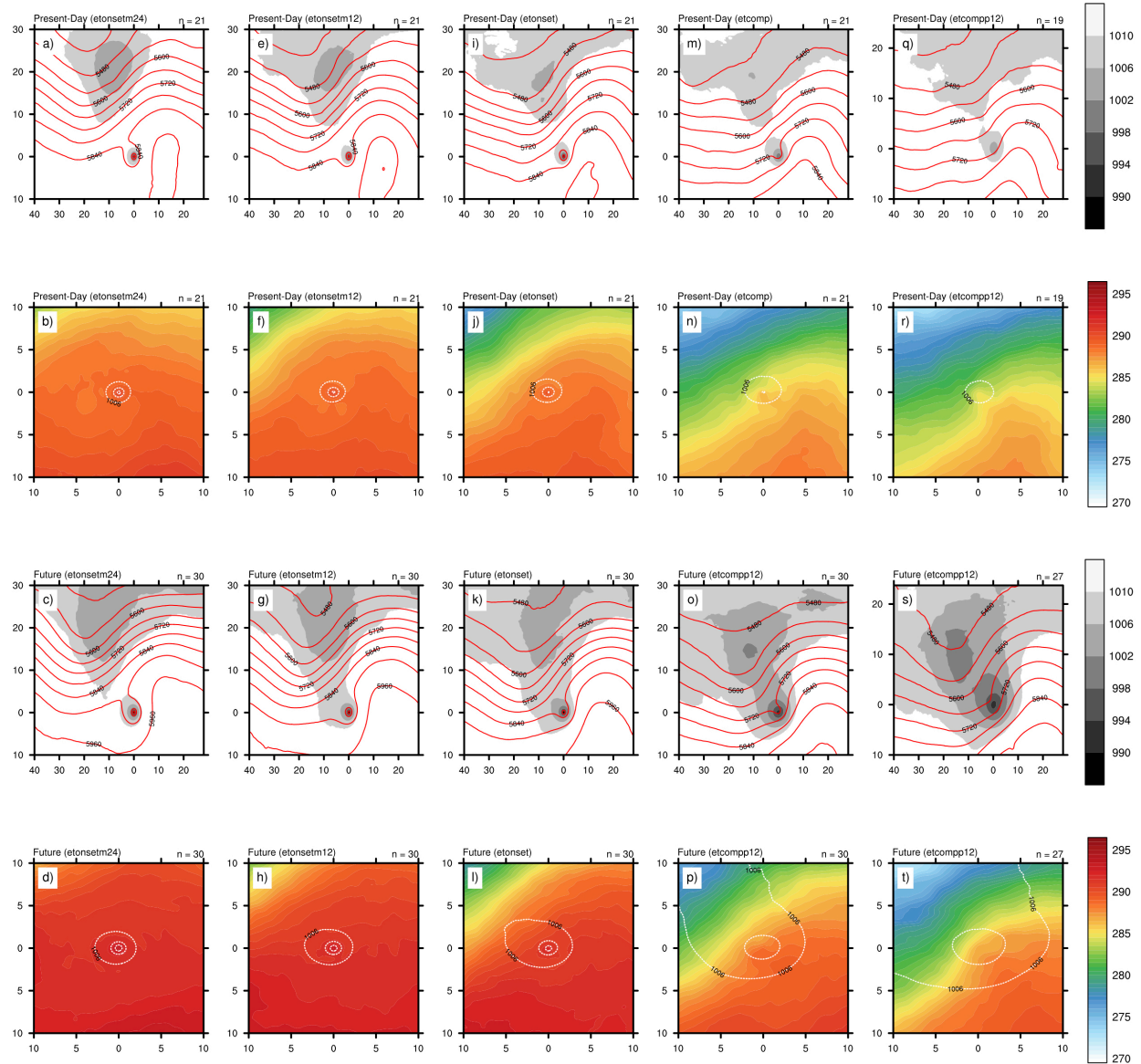


Figure 5.1: 500-hPa height, SLP, and 850-hPa temperature showing an overview of the ET process for present-day and future NATL composite events. (first and third rows) 500-hPa heights (m; red contours; every 60-m) and SLP (hPa; shaded below 1010-hPa; every 4-hPa) and (second and fourth rows) 850-hPa temperature (K; shaded; every 0.5-K) and SLP (hPa; dashed contours; every 8-hPa) for NATL (top two rows) present-day and (bottom two rows) future composite ET events at (a)–(d) 24-h prior to ET onset, (e)–(h) 12-h prior to ET onset, (i)–(l) time of ET onset, (m)–(p) time of ET completion, and (q)–(t) 12-h after ET completion. Distance from the storm center in degrees are shown on the ordinate and abscissa with (0,0) marking the storm center. The number of cases included in each composite is shown at the top-right of each panel.

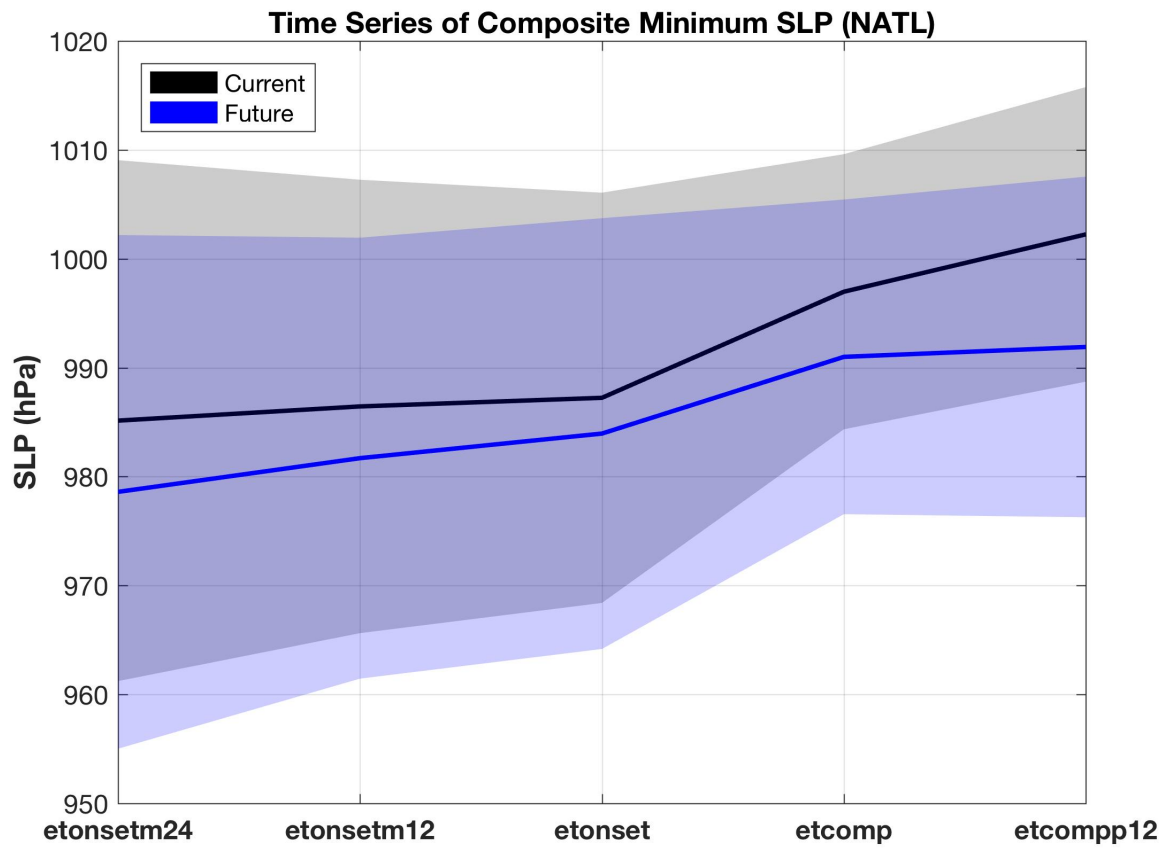


Figure 5.2: Time series of minimum SLP for present-day and future NATL composite ET events. Time series of minimum SLP (hPa) over all composite times for the NATL composite ET events. Present-day (future) time series is shown in black (blue). Shading indicates ± 1 -standard deviation.

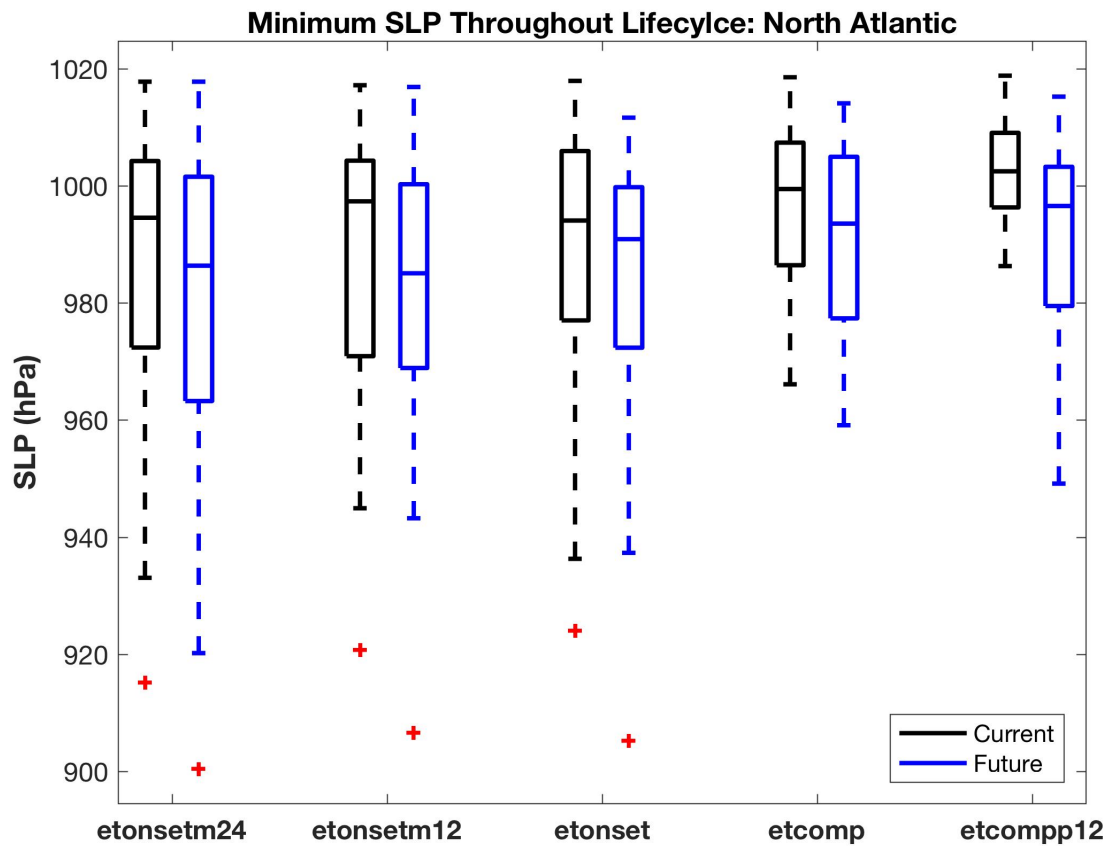


Figure 5.3: *Boxplots of minimum SLP at various stages of the cyclone lifecycle for present-day vs. future NATL composite ET events.* Boxplots showing SLP (hPa) reached 24-h prior to ET onset, 12-h prior to ET onset, at the time of ET onset, at the time of ET completion, and 12-h after ET completion for the NATL composited ET events. Present-day (future) distributions are shown in black (blue). The bottom whisker indicates the minimum intensity. The top whisker indicates the maximum intensity. The bottom, middle, and top lines associated with each box represent the 25th, 50th, and 75th percentile intensity. The red asterisks represent outliers that fall outside of $\pm 2.7\sigma$ range.

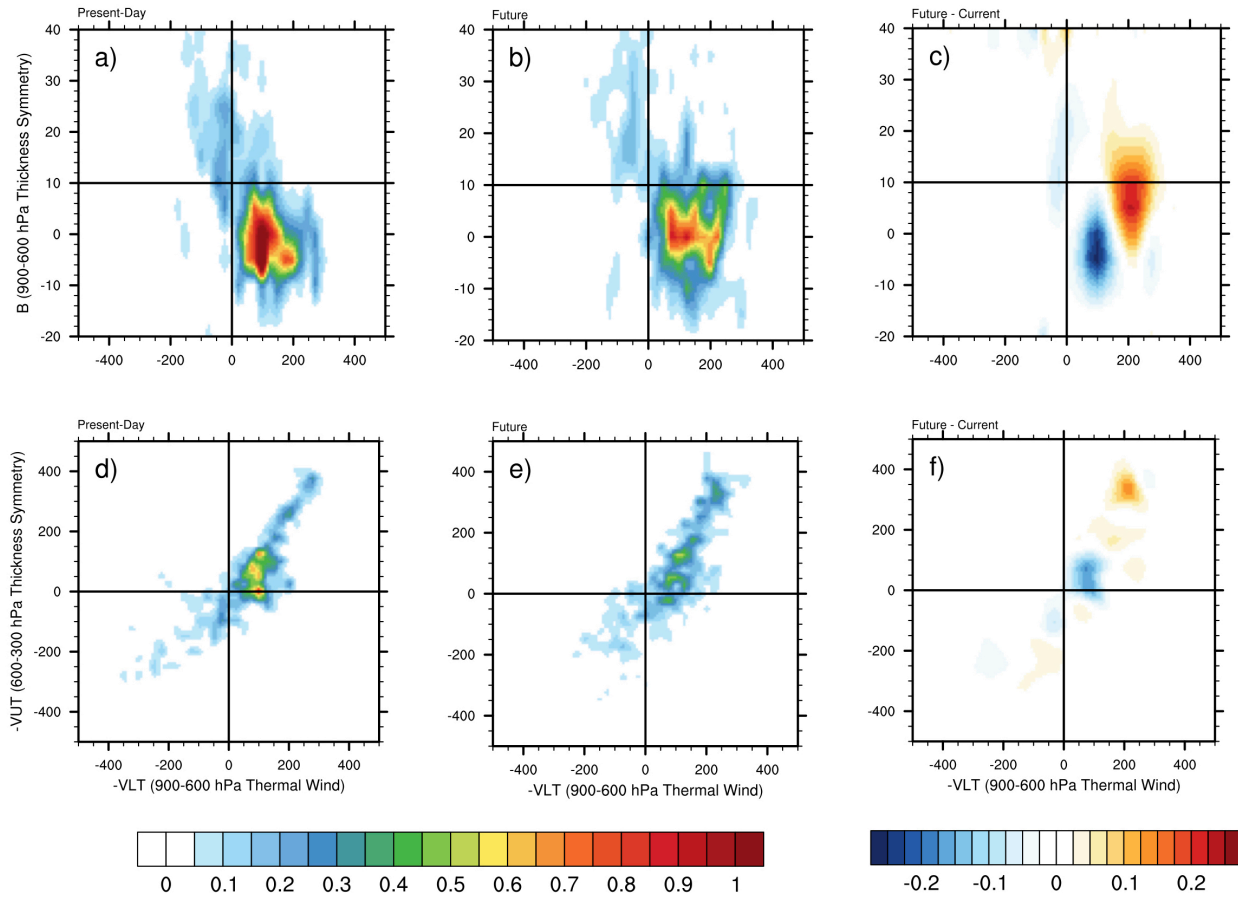


Figure 5.4: Cyclone phase space frequency diagrams for present-day vs. future NATL composite ET events. Cyclone phase space frequency diagrams for composited NATL ET events in the (a,d) present-day simulations, (b,e) future simulations, and (c,f) future minus present-day. $-VLT$ vs. B is shown on the top row. $-VLT$ vs. $-VUT$ is shown on the bottom row. Frequencies are normalized by the number of storms.

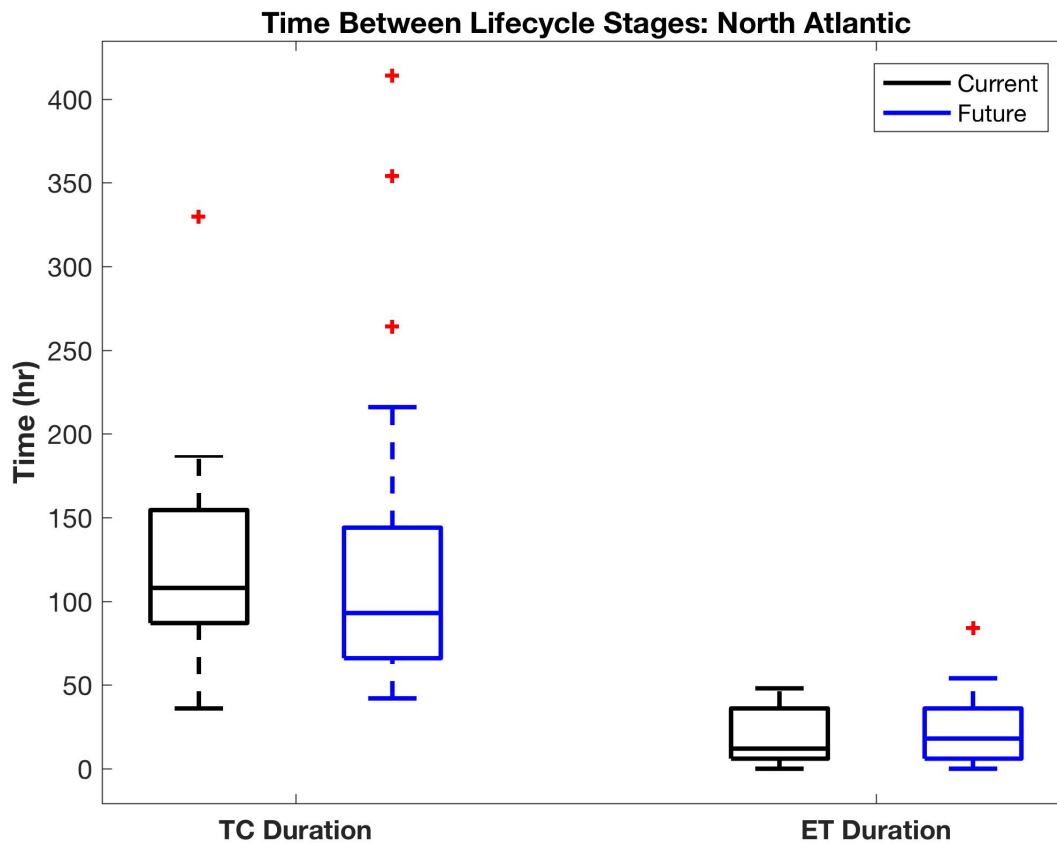


Figure 5.5: *Boxplots of TC and ET durations for present-day vs. future NATL composite ET events.* Boxplots showing time (hr) between TC genesis and ET onset (TC duration) and ET onset and ET completion (ET duration) for the NATL composited ET events. Present-day (future) distributions are shown in black (blue). The bottom whisker indicates the minimum duration. The top whisker indicates the maximum duration. The bottom, middle, and top lines associated with each box represent the 25th, 50th, and 75th percentile duration. The red asterisks represent outliers that fall outside of $\pm 2.7\sigma$ range.

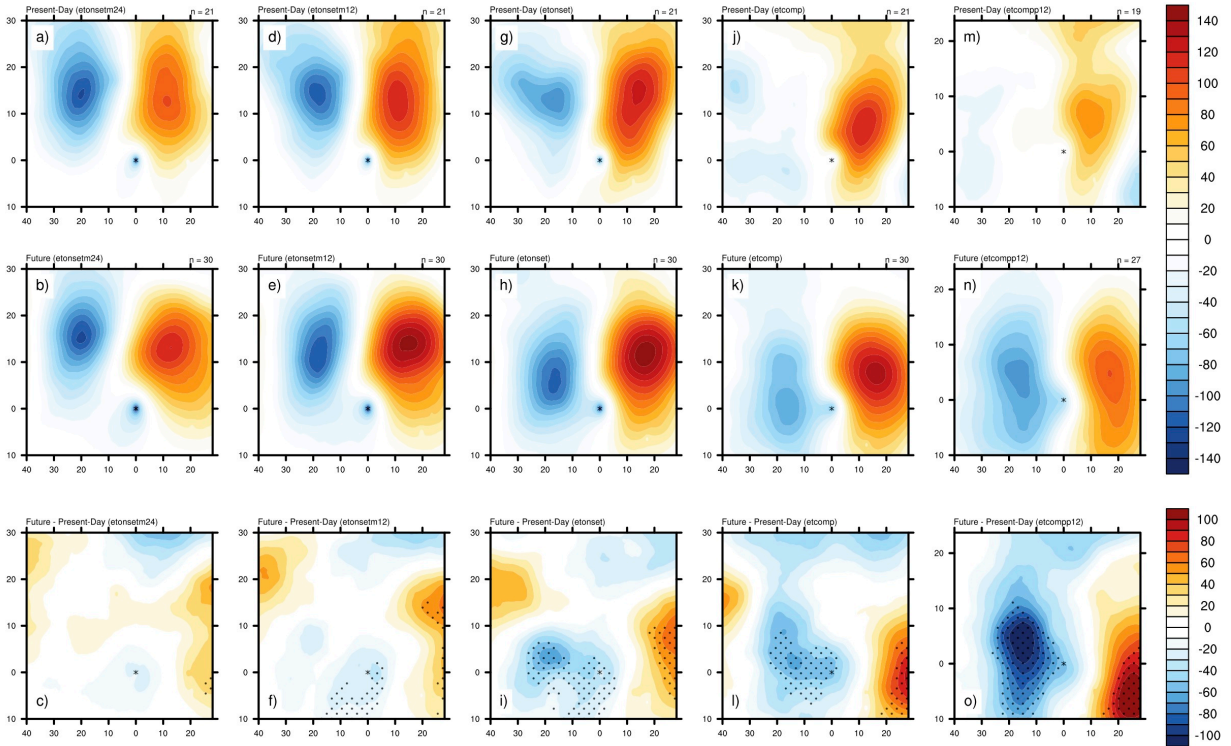


Figure 5.6: 500-hPa height anomaly for present-day vs. future NATL composite ET events at 24-h prior to ET onset, 12-h prior to ET onset, ET onset, ET completion, and 12-h after ET completion. 500-hPa height anomaly (m) for NATL (top row) present-day, (middle row) future, and (bottom row) future minus present-day composite ET events at (a)–(c) 24-h prior to ET onset, (d)–(f) 12-h prior to ET onset, (g)–(i) time of ET onset, (j)–(l) time of ET completion, and (m)–(o) 12-h after ET completion. Distance from the storm center in degrees are shown on the ordinate and abscissa with an asterisk at (0,0) marking the storm center. The number of cases included in each composite is shown at the top-right of each panel in the top two rows. Contours are shaded every 10-m in all panels. Stippling in the bottom row panels indicate where the differences are significant at the 95% confidence level using the Wilcoxon rank sum significance test.

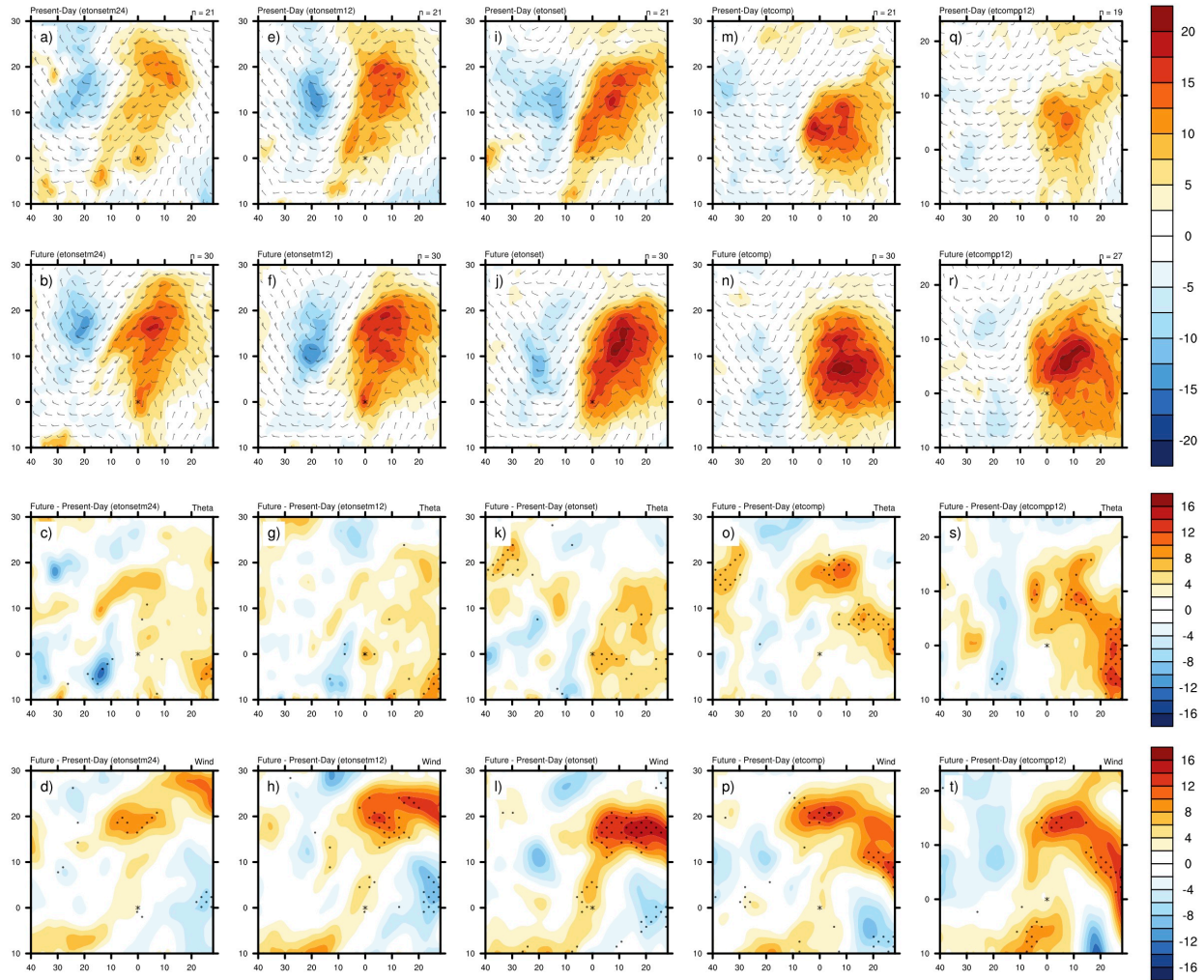


Figure 5.7: Potential temperature anomaly and winds on the dynamic tropopause for present-day vs. future NATL composite ET events at 24-h prior to ET onset, 12-h prior to ET onset, ET onset, ET completion, and 12-h after ET completion. Potential temperature (θ) anomaly (K; shaded) and winds (m s^{-1} ; vectors) on the dynamic tropopause for NATL (top row) present-day, (second row) future, (third row) future minus present-day (θ) and (bottom row) future minus present-day (wind speed) composite ET events at (a)–(d) 24-h prior to ET onset, (e)–(h) 12-h prior to ET onset, (i)–(l) time of ET onset, (m)–(p) time of ET completion, and (q)–(t) 12-h after ET completion. Distance from the storm center in degrees are shown on the ordinate and abscissa with an asterisk at (0,0) marking the storm center. The number of cases included in each composite is shown at the top-right of each panel in the top two rows. Contours are shaded every 2.5-K in the top two rows, every 2-K in the third row, and every 2- m s^{-1} in the bottom row. Stippling in the bottom row panels indicate where the differences are significant at the 95% confidence level using the Wilcoxon rank sum significance test.

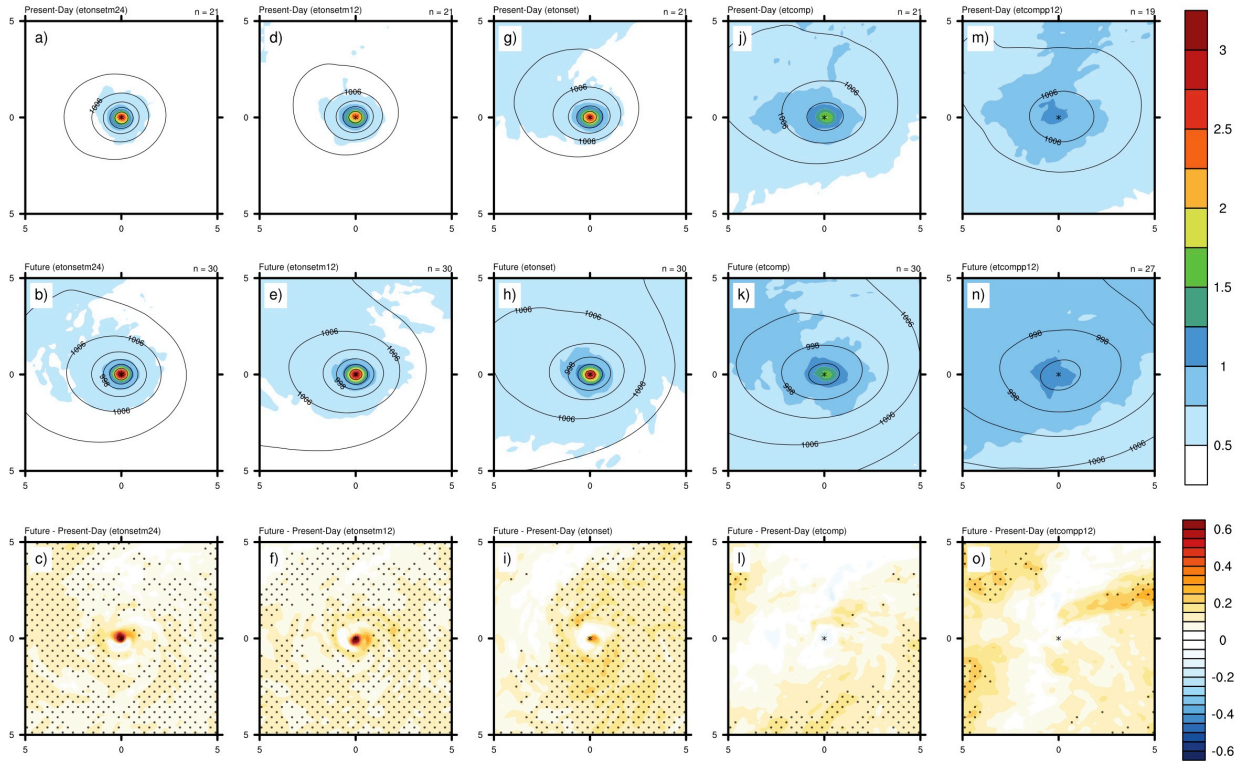


Figure 5.8: 900–700-hPa layer average PV and SLP for present-day vs. future NATL composite ET events at 24-h prior to ET onset, 12-h prior to ET onset, ET onset, ET completion, and 12-h after ET completion. 900–700-hPa layer average PV (PVU; shaded) and SLP (hPa; contours) for NATL (top row) present-day, (middle row) future, and (bottom row) future minus present-day composite ET events at (a)–(d) 24-h prior to ET onset, (e)–(h) 12-h prior to ET onset, (i)–(l) time of ET onset, (m)–(p) time of ET completion, and (q)–(t) 12-h after ET completion. Distance from the storm center in degrees are shown on the ordinate and abscissa with an asterisk at (0,0) marking the storm center. The number of cases included in each composite is shown at the top-right of each panel in the top two rows. PV contours are shaded every 0.25-PVU and SLP contours are drawn every 4-hPa in the top two rows; PV contours are shaded every 0.05-PVU in the bottom row. Stippling in the bottom row panels indicate where the differences are significant at the 95% confidence level using the Wilcoxon rank sum significance test.

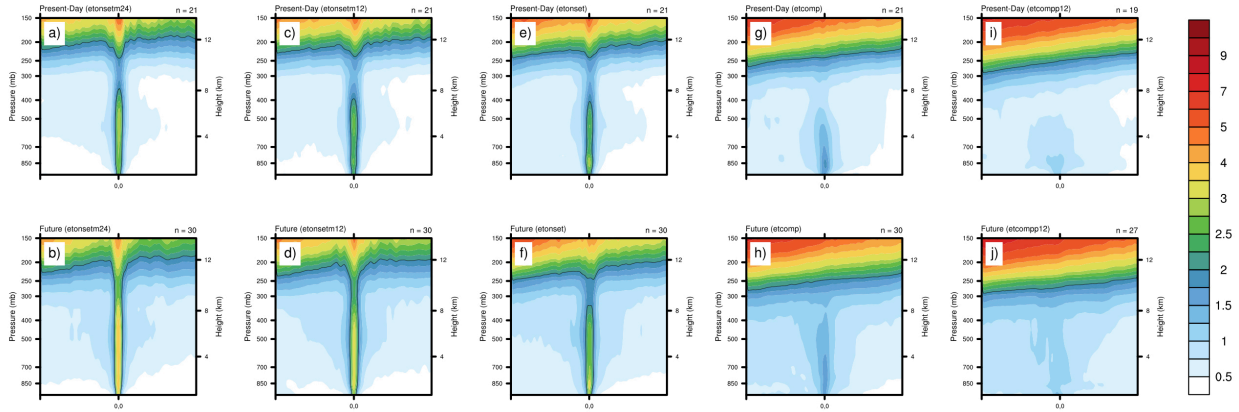


Figure 5.9: Vertical cross-section of PV for present-day vs. future NATL composite ET events at 24-h prior to ET onset, 12-h prior to ET onset, ET onset, ET completion, and 12-h after ET completion. Vertical northwest-to-southeast cross-section of PV (PVU) for NATL (top row) present-day and (bottom row) future composite ET events at (a)–(b) 24-h prior to ET onset, (c)–(d) 12-h prior to ET onset, (e)–(f) time of ET onset, (g)–(h) time of ET completion, and (i)–(j) 12-h after ET completion. Distance from the storm center in degrees are shown on the ordinate and abscissa with (0,0) marking the storm center. The number of cases included in each composite is shown at the top-right of each panel in the top two rows. PV contours are shaded every 0.25-PVU from 0.5-PVU to 3-PVU, every 0.5-PVU from 3-PVU to 5-PVU, and every 1-PVU from 5-PVU to 10-PVU.

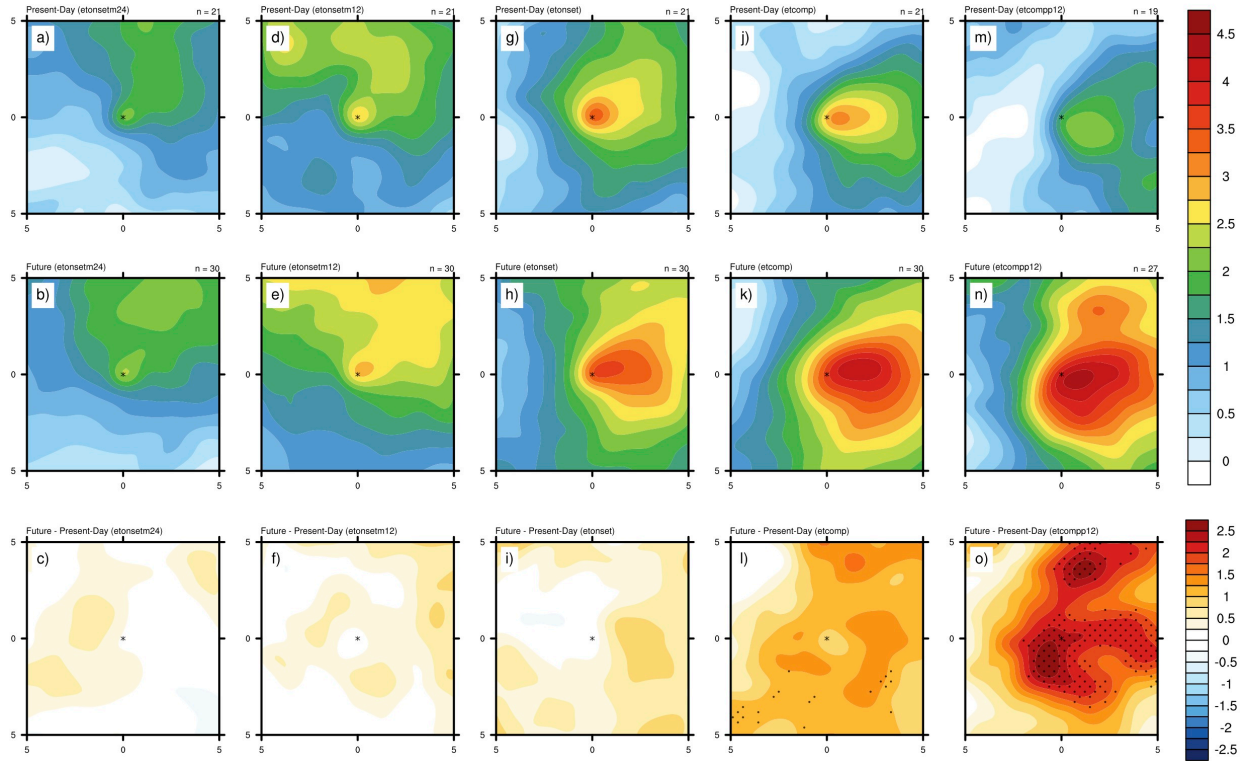


Figure 5.10: θ'_{2-m} for present-day vs. future NATL composite ET events at 24-h prior to ET onset, 12-h prior to ET onset, ET onset, ET completion, and 12-h after ET completion. θ'_{2-m} (K) for NATL (top row) present-day, (middle row) future, and (bottom row) future minus present-day composite ET events at (a)–(c) 24-h prior to ET onset, (d)–(f) 12-h prior to ET onset, (g)–(i) time of ET onset, (j)–(l) time of ET completion, and (m)–(o) 12-h after ET completion. Distance from the storm center in degrees are shown on the ordinate and abscissa with an asterisk at (0,0) marking the storm center. The number of cases included in each composite is shown at the top-right of each panel in the top two rows. Contours are shaded every 0.25-K in all panels. Stippling in the bottom row panels indicate where the differences are significant at the 95% confidence level using the Wilcoxon rank sum significance test.

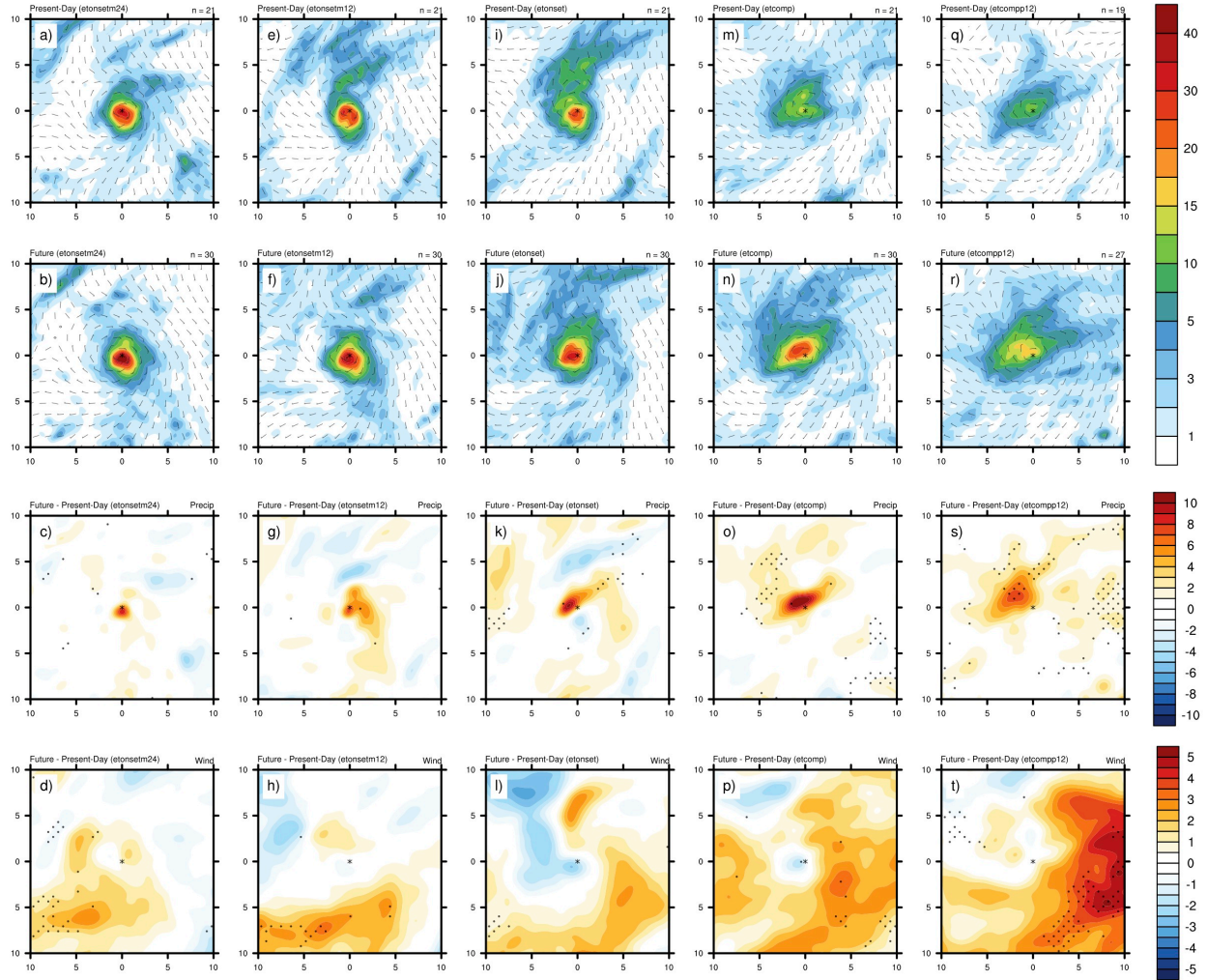


Figure 5.11: 6-hourly precipitation and 10-m winds for present-day vs. future NATL composite ET events at 24-h prior to ET onset, 12-h prior to ET onset, ET onset, ET completion, and 12-h after ET completion. 6-hourly precipitation (mm; shaded) and 10-m winds (ms^{-1} ; vectors) for NATL (top row) present-day, (second row) future, (third row) future minus present-day (precipitation) and (bottom row) future minus present-day (wind speed) composite ET events at (a)–(d) 24-h prior to ET onset, (e)–(h) 12-h prior to ET onset, (i)–(l) time of ET onset, (m)–(p) time of ET completion, and (q)–(t) 12-h after ET completion. Distance from the storm center in degrees are shown on the ordinate and abscissa with an asterisk at (0,0) marking the storm center. The number of cases included in each composite is shown at the top-right of each panel in the top two rows. Contours in the top two rows are shaded every 1-mm from 1-mm to 5-mm, every 2.5-mm from 5-mm to 20-mm, and every 5-mm from 20-mm to 40-mm. Contours in the third row are shaded every 1-mm. Contours in the last row are shaded every 0.5- m s^{-1} in the bottom row. Stippling in the bottom row panels indicate where the differences are significant at the 95% confidence level using the Wilcoxon rank sum significance test.

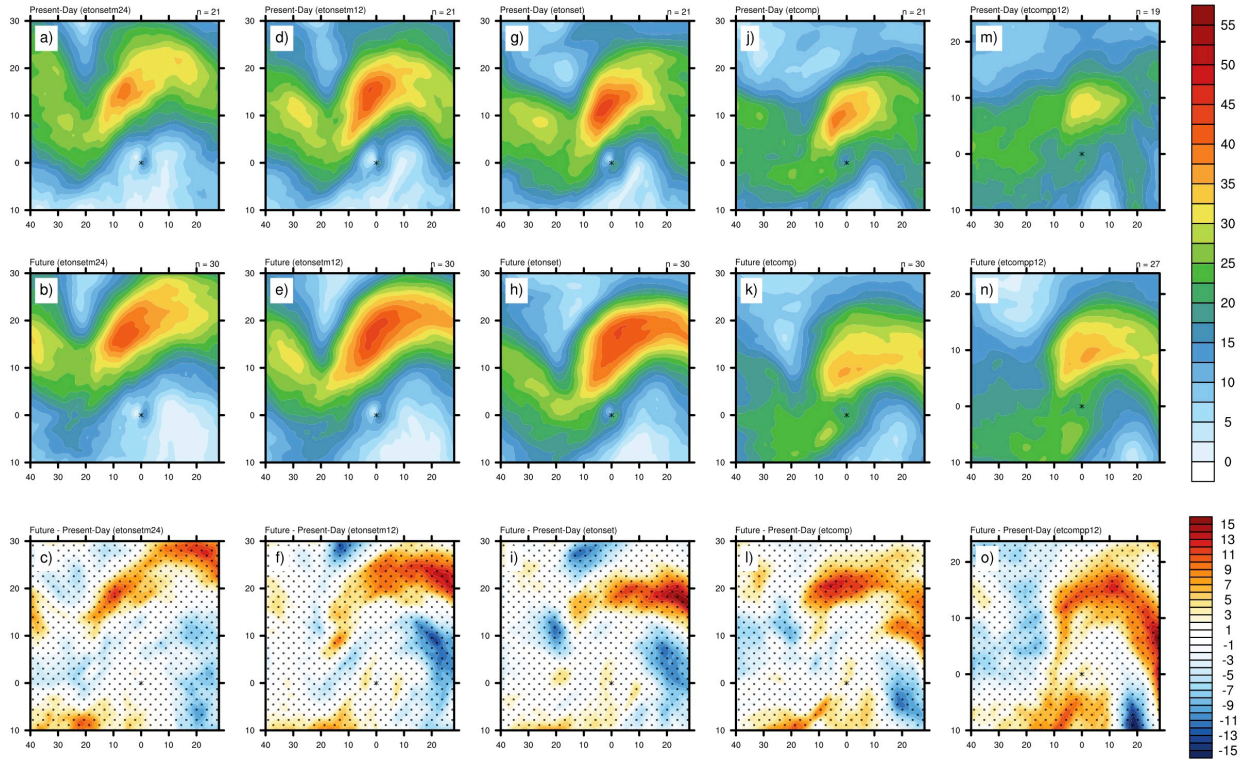


Figure 5.12: 250-hPa wind speed for present-day vs. future NATL composite ET events at 24-h prior to ET onset, 12-h prior to ET onset, ET onset, ET completion, and 12-h after ET completion. 250-hPa wind speed (ms^{-1}) for NATL (top row) present-day, (second row) future, (third row) future minus present-day composite ET events at (a)–(d) 24-h prior to ET onset, (e)–(h) 12-h prior to ET onset, (i)–(l) time of ET onset, (m)–(p) time of ET completion, and (q)–(t) 12-h after ET completion. Distance from the storm center in degrees are shown on the ordinate and abscissa with an asterisk at (0,0) marking the storm center. The number of cases included in each composite is shown at the top-right of each panel in the top two rows. Contours in the top two rows are shaded every 2.5-ms^{-1} and contours in the last row are shaded every 1-ms^{-1} . Stippling in the bottom row panels indicate where the differences are significant at the 95% confidence level using the Wilcoxon rank sum significance test.

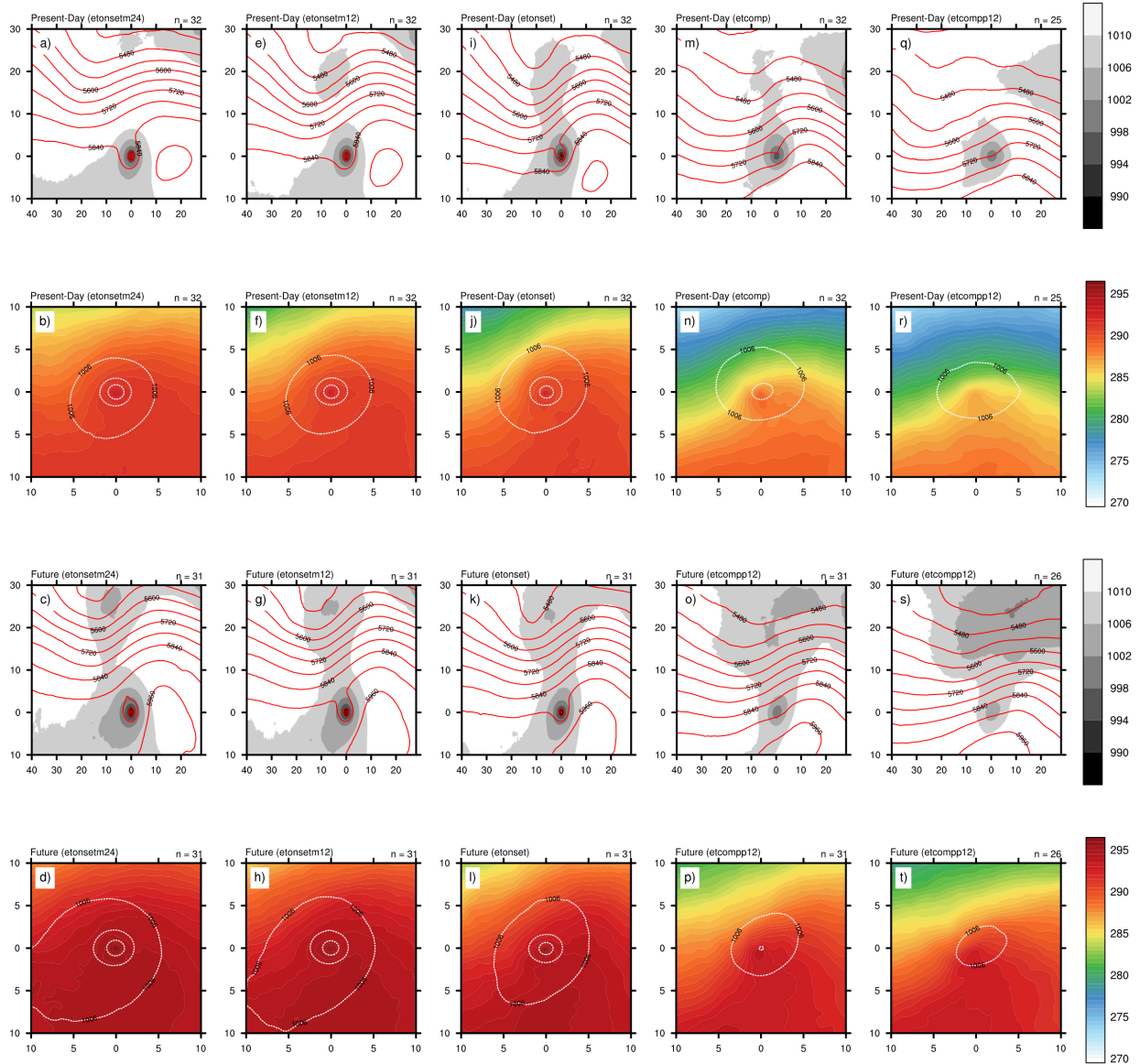


Figure 5.13: 500-hPa height, SLP, and 850-hPa temperature showing an overview of the ET process for present-day and future WNP composite events. (first and third rows) 500-hPa heights (m; red contours; every 60-m) and SLP (hPa; shaded below 1010-hPa; every 4-hPa) and (second and fourth rows) 850-hPa temperature (K; shaded; every 0.5-K) and SLP (hPa; dashed contours; every 8-hPa) for WNP (top two rows) present-day and (bottom two rows) future composite ET events at (a)–(d) 24-h prior to ET onset, (e)–(h) 12-h prior to ET onset, (i)–(l) time of ET onset, (m)–(p) time of ET completion, and (q)–(t) 12-h after ET completion. Distance from the storm center in degrees are shown on the ordinate and abscissa with (0,0) marking the storm center. The number of cases included in each composite is shown at the top-right of each panel.

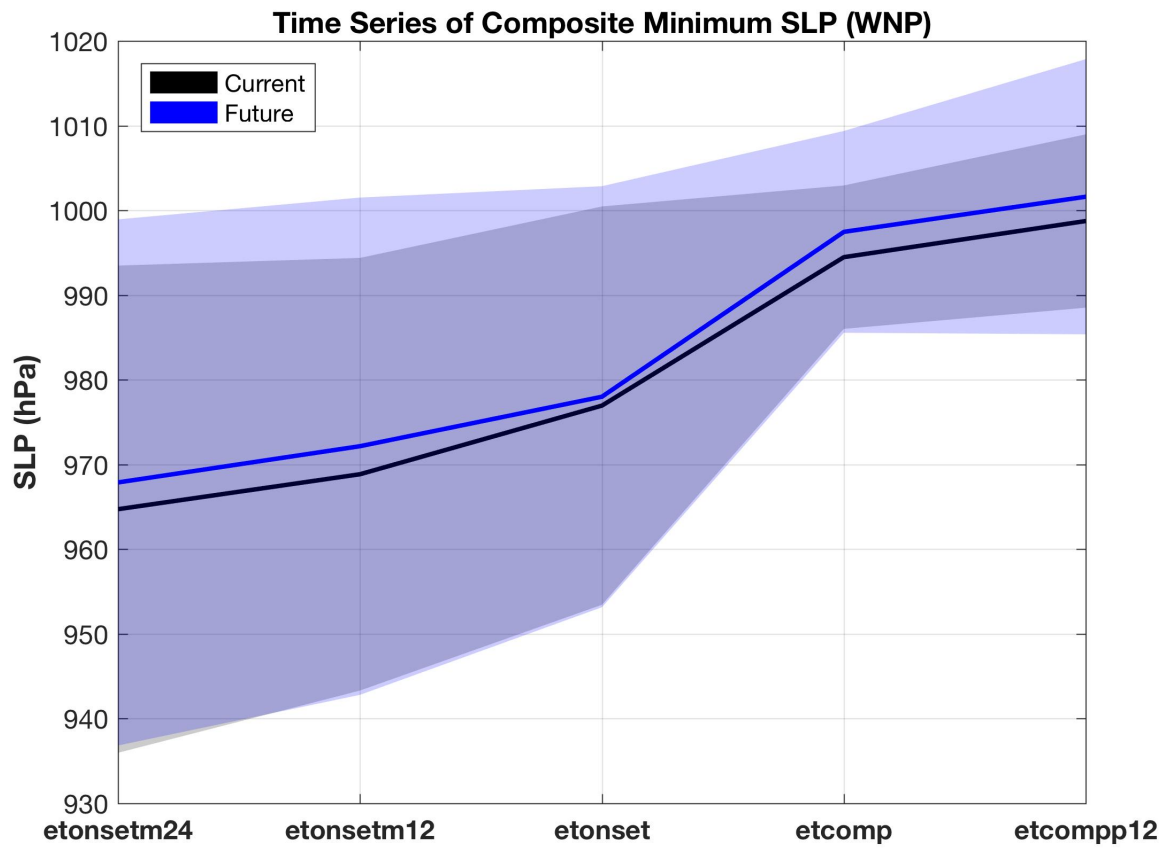


Figure 5.14: Time series of minimum SLP for present-day and future WNP composite ET events. Time series of minimum SLP (hPa) over all composite times for the WNP composite ET events. Present-day (future) time series is shown in black (blue). Shading indicates ± 1 -standard deviation.

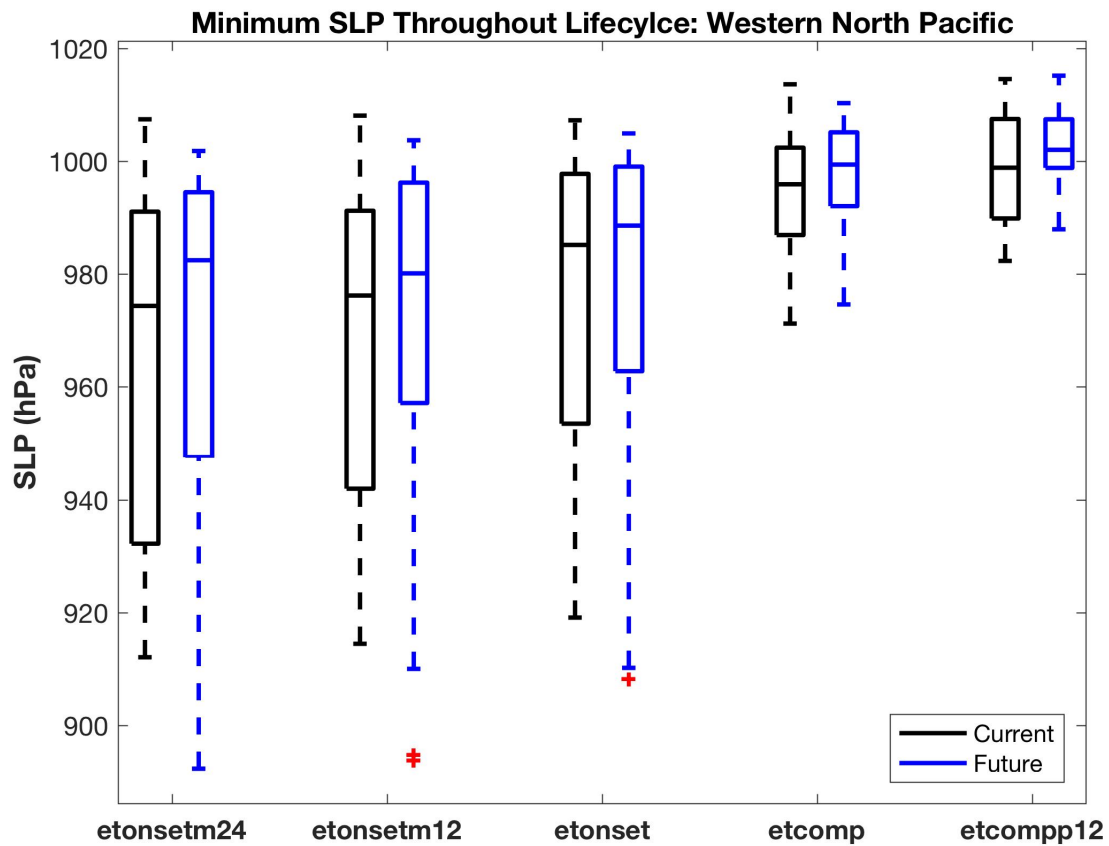


Figure 5.15: Boxplots of minimum SLP at various stages of the cyclone lifecycle for present-day vs. future WNP composite ET events. Boxplots showing SLP (hPa) reached 24-h prior to ET onset, 12-h prior to ET onset, at the time of ET onset, at the time of ET completion, and 12-h after ET completion for the NATL composited ET events. Present-day (future) distributions are shown in black (blue). The bottom whisker indicates the minimum intensity. The top whisker indicates the maximum intensity. The bottom, middle, and top lines associated with each box represent the 25th, 50th, and 75th percentile intensity. The red asterisks represent outliers that fall outside of $\pm 2.7\sigma$ range.

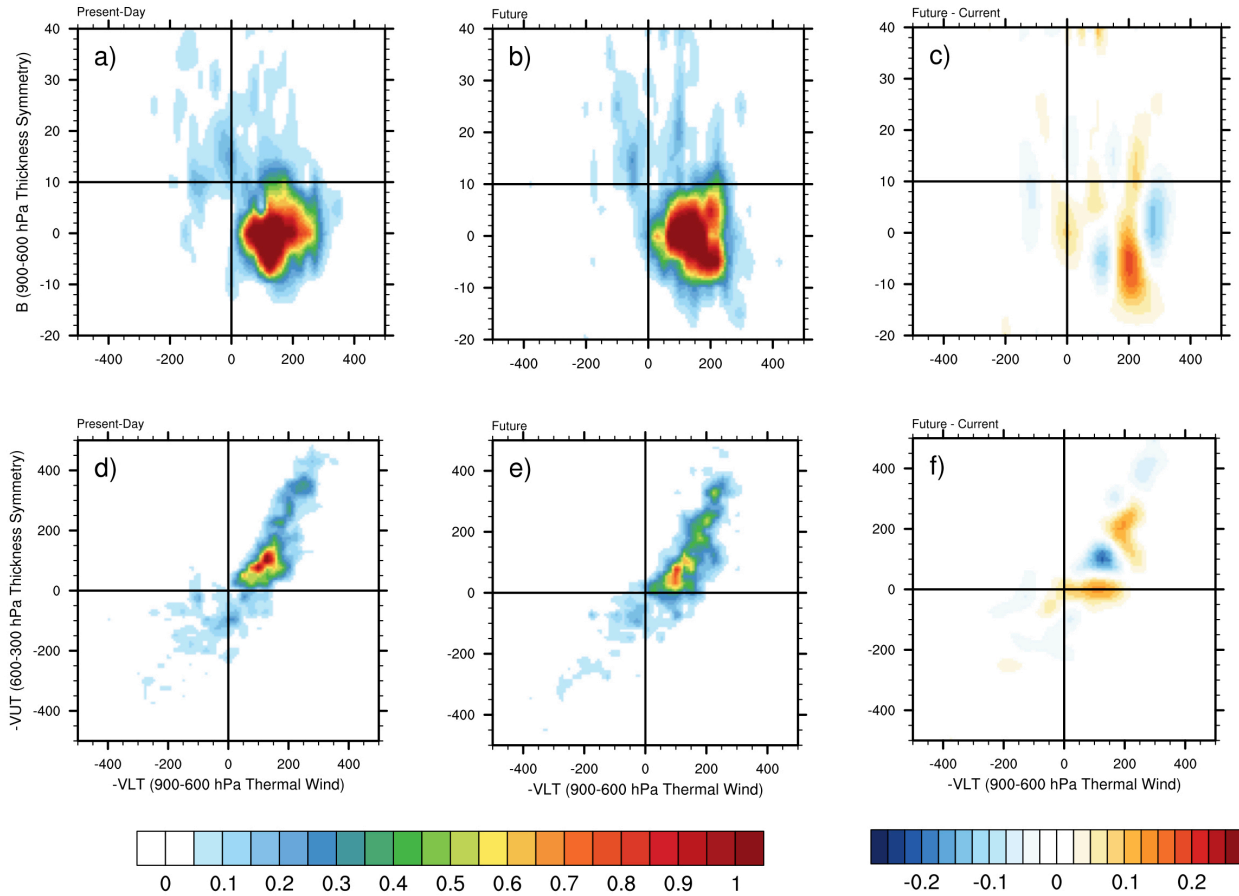


Figure 5.16: Cyclone phase space frequency diagrams for present-day vs. future NATL composite ET events. Cyclone phase space frequency diagrams for composited WNP ET events in the (a,d) present-day simulations, (b,e) future simulations, and (c,f) future minus present-day. $-VLT$ vs. B is shown on the top row. $-VLT$ vs. $-VUT$ is shown on the bottom row. Frequencies are normalized by the number of storms.

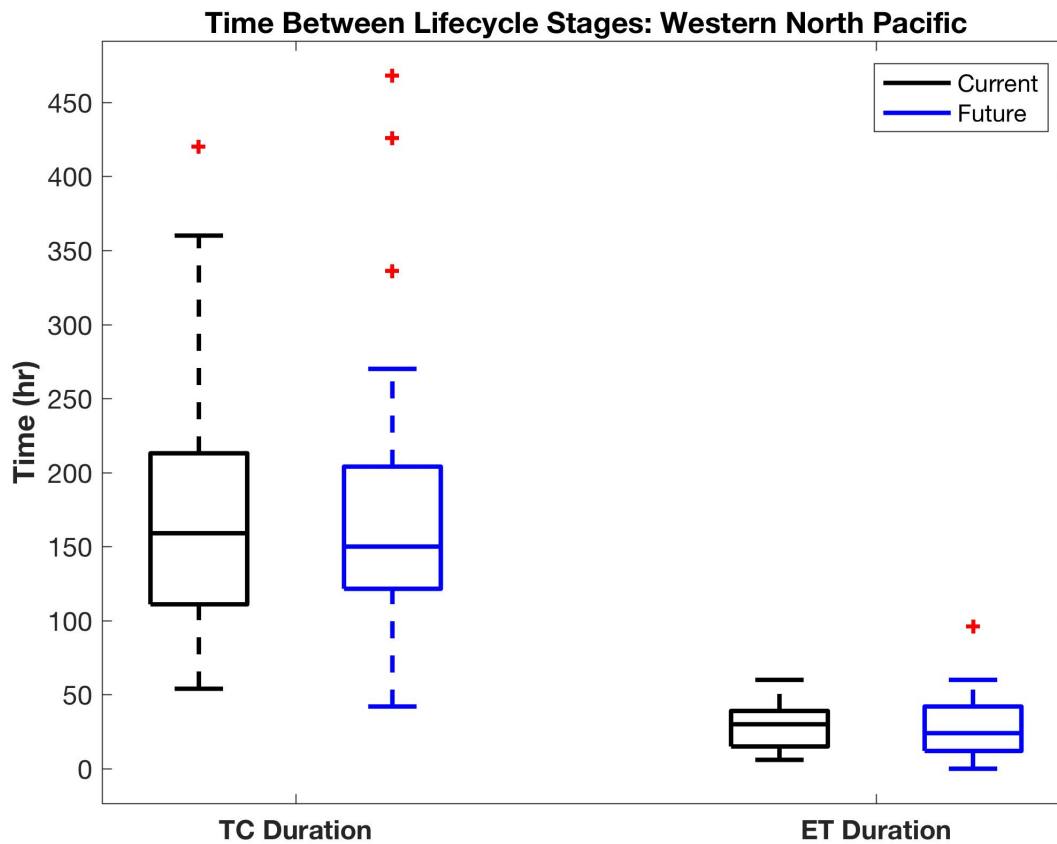


Figure 5.17: Boxplots of TC and ET durations for present-day vs. future NATL composite ET events. Boxplots showing time (hr) between TC genesis and ET onset (TC duration) and ET onset and ET completion (ET duration) for the WNP composited ET events. Present-day (future) distributions are shown in black (blue). The bottom whisker indicates the minimum duration. The top whisker indicates the maximum duration. The bottom, middle, and top lines associated with each box represent the 25th, 50th, and 75th percentile duration. The red asterisks represent outliers that fall outside of $\pm 2.7\sigma$ range.

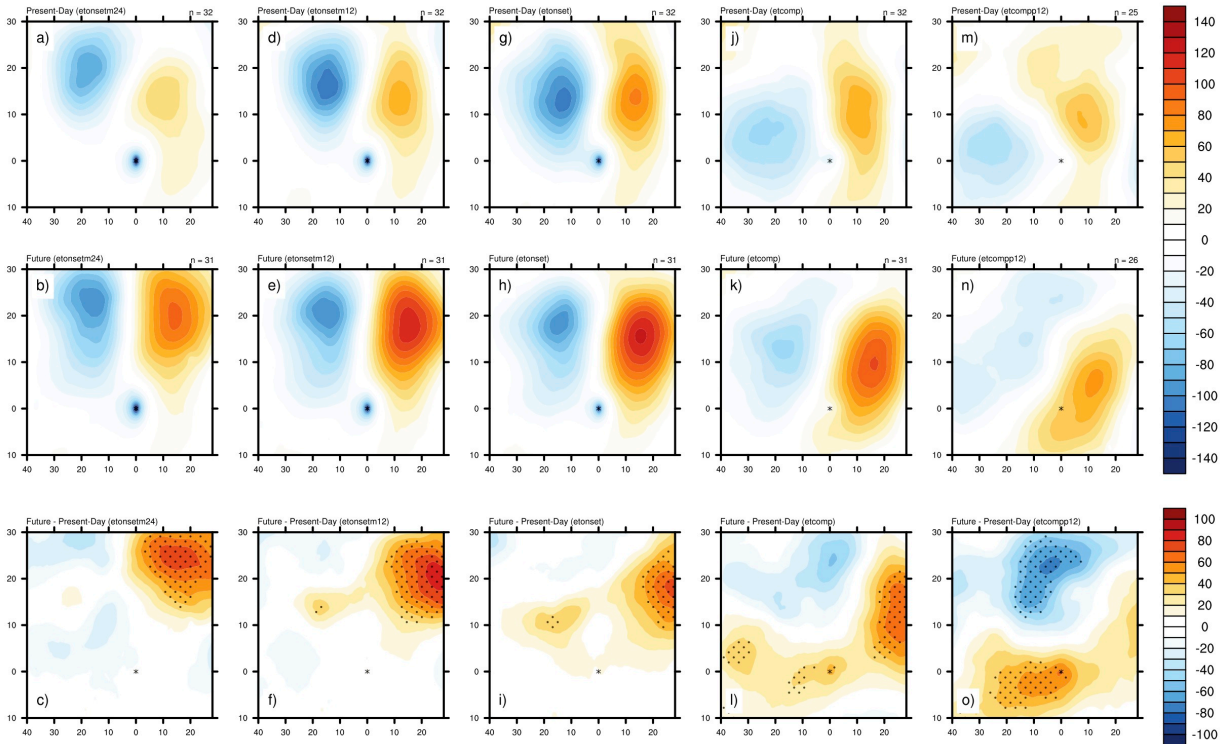


Figure 5.18: 500-hPa height anomaly for present-day vs. future WNP composite ET events at 24-h prior to ET onset, 12-h prior to ET onset, ET onset, ET completion, and 12-h after ET completion. 500-hPa height anomaly for WNP (top row) present-day, (middle row) future, and (bottom row) future minus present-day composite ET events at (a)–(c) 24-h prior to ET onset, (d)–(f) 12-h prior to ET onset, (g)–(i) time of ET onset, (j)–(l) time of ET completion, and (m)–(o) 12-h after ET completion. Distance from the storm center in degrees are shown on the ordinate and abscissa with an asterisk at (0,0) marking the storm center. The number of cases included in each composite is shown at the top-right of each panel in the top two rows. Contours are shaded every 10-m in all panels. Stippling in the bottom row panels indicate where the differences are significant at the 95% confidence level using the Wilcoxon rank sum significance test.

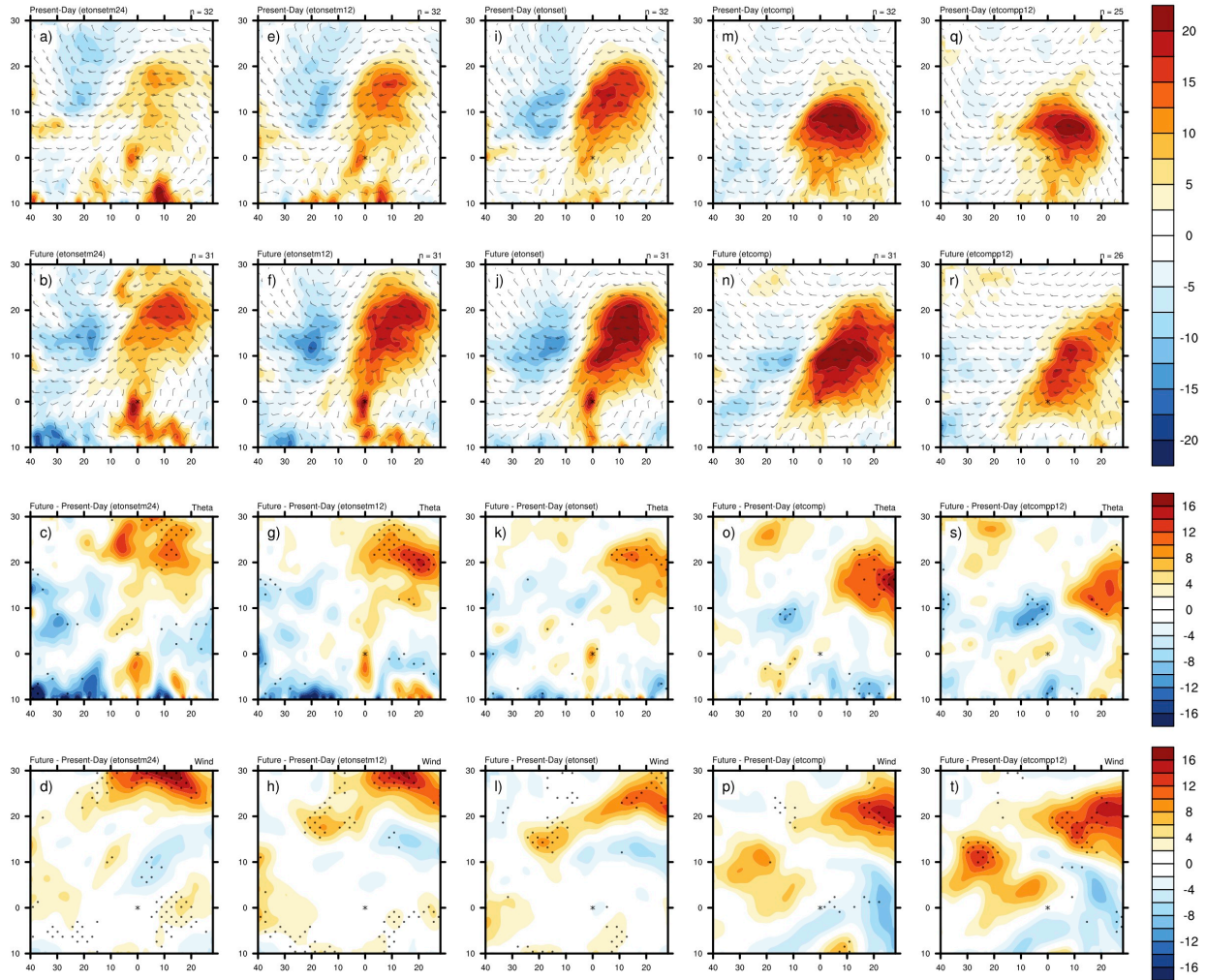


Figure 5.19: Potential temperature anomaly and winds on the dynamic tropopause for present-day vs. future WNP composite ET events at 24-h prior to ET onset, 12-h prior to ET onset, ET onset, ET completion, and 12-h after ET completion. Potential temperature (θ) anomaly (shaded) and winds (vectors) on the dynamic tropopause for WNP (top row) present-day, (second row) future, (third row) future minus present-day (θ) and (bottom row) future minus present-day (wind speed) composite ET events at (a)–(d) 24-h prior to ET onset, (e)–(h) 12-h prior to ET onset, (i)–(l) time of ET onset, (m)–(p) time of ET completion, and (q)–(t) 12-h after ET completion. Distance from the storm center in degrees are shown on the ordinate and abscissa with an asterisk at (0,0) marking the storm center. The number of cases included in each composite is shown at the top-right of each panel in the top two rows. Contours are shaded every 2.5-K in the top two rows, every 2-K in the third row, and every 2- m s^{-1} in the bottom row. Stippling in the bottom row panels indicate where the differences are significant at the 95% confidence level using the Wilcoxon rank sum significance test.

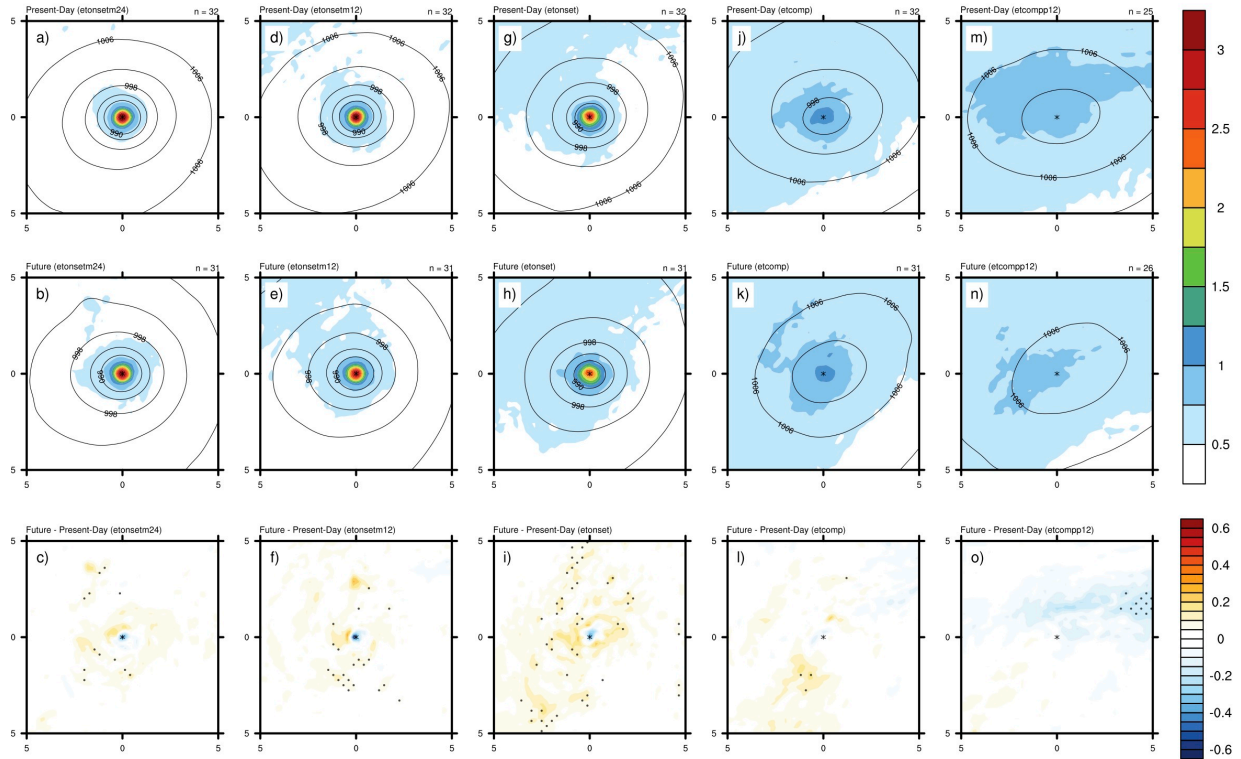


Figure 5.20: 900–700-hPa layer average PV and SLP for present-day vs. future WNP composite ET events at 24-h prior to ET onset, 12-h prior to ET onset, ET onset, ET completion, and 12-h after ET completion. 900–700-hPa layer average PV (PVU; shaded) and SLP (hPa; contours) for WNP (top row) present-day, (middle row) future, and (bottom row) future minus present-day composite ET events at (a)–(d) 24-h prior to ET onset, (e)–(h) 12-h prior to ET onset, (i)–(l) time of ET onset, (m)–(p) time of ET completion, and (q)–(t) 12-h after ET completion. Distance from the storm center in degrees are shown on the ordinate and abscissa with an asterisk at (0,0) marking the storm center. The number of cases included in each composite is shown at the top-right of each panel in the top two rows. PV contours are shaded every 0.25-PVU and SLP contours are drawn every 4-hPa in the top two rows; PV contours are shaded every 0.05-PVU in the bottom row. Stippling in the bottom row panels indicate where the differences are significant at the 95% confidence level using the Wilcoxon rank sum significance test.

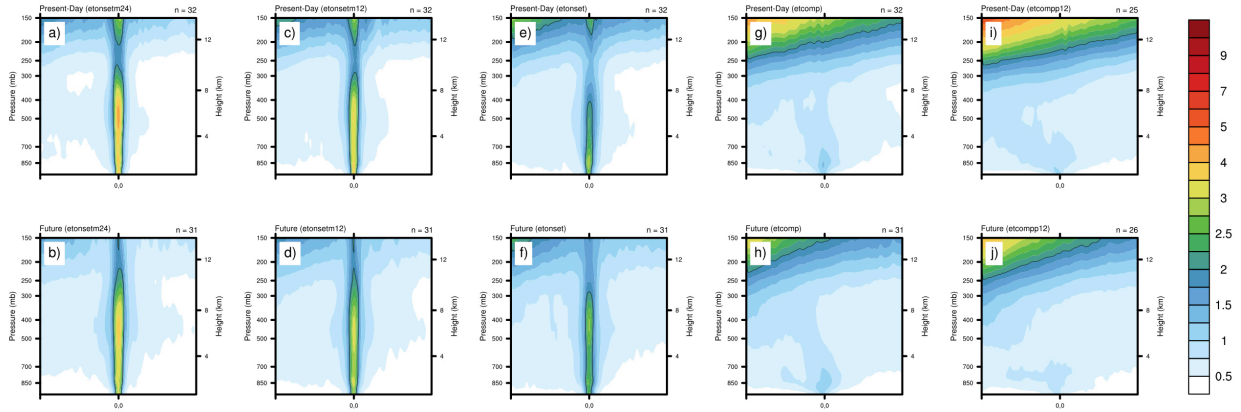


Figure 5.21: Vertical cross-section of PV for present-day vs. future WNP composite ET events at 24-h prior to ET onset, 12-h prior to ET onset, ET onset, ET completion, and 12-h after ET completion. Vertical northwest-to-southeast cross-section of PV (PVU) for WNP (top row) present-day and (bottom row) future composite ET events at (a)–(b) 24-h prior to ET onset, (c)–(d) 12-h prior to ET onset, (e)–(f) time of ET onset, (g)–(h) time of ET completion, and (i)–(j) 12-h after ET completion. Distance from the storm center in degrees are shown on the ordinate and abscissa with (0,0) marking the storm center. The number of cases included in each composite is shown at the top-right of each panel in the top two rows. PV contours are shaded every 0.25-PVU from 0.5-PVU to 3-PVU, every 0.5-PVU from 3-PVU to 5-PVU, and every 1-PVU from 5-PVU to 10-PVU.

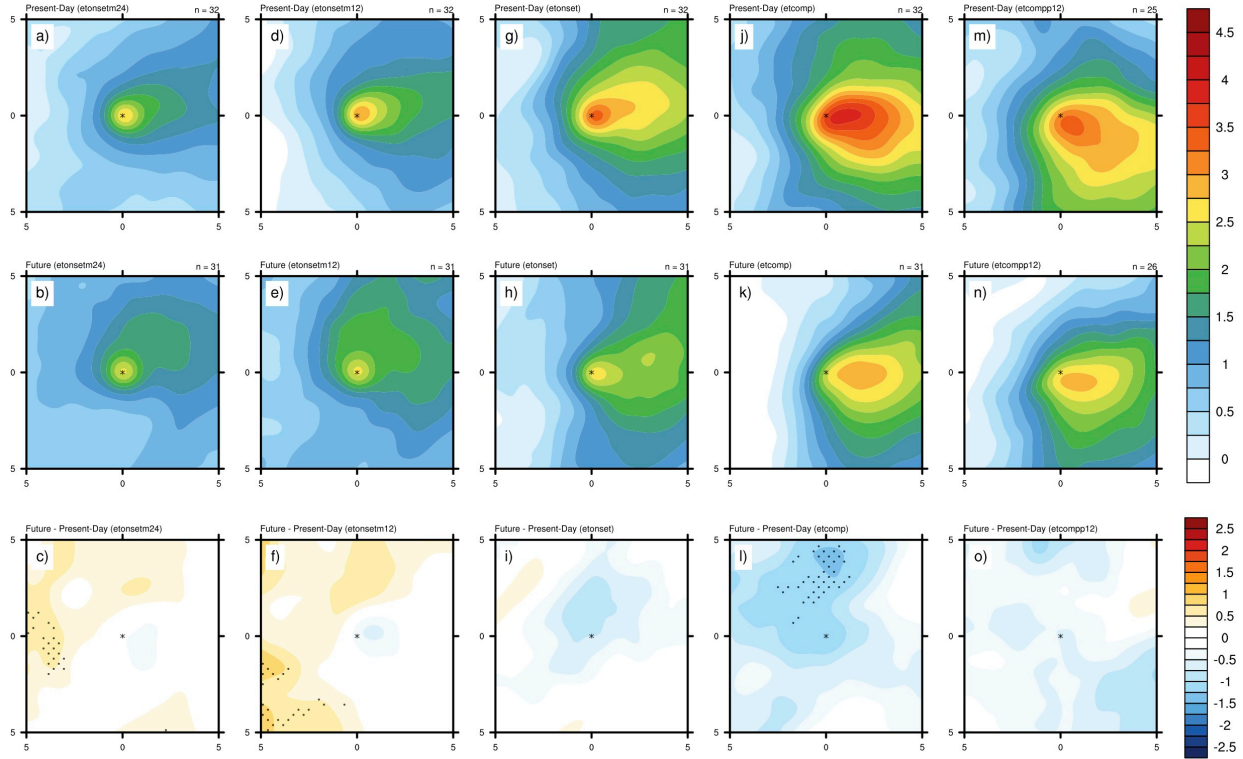


Figure 5.22: θ'_{2-m} for present-day vs. future WNP composite ET events at 24-h prior to ET onset, 12-h prior to ET onset, ET onset, ET completion, and 12-h after ET completion. θ'_{2-m} (K) for WNP (top row) present-day, (middle row) future, and (bottom row) future minus present-day composite ET events at (a)–(c) 24-h prior to ET onset, (d)–(f) 12-h prior to ET onset, (g)–(i) time of ET onset, (j)–(l) time of ET completion, and (m)–(o) 12-h after ET completion. Distance from the storm center in degrees are shown on the ordinate and abscissa with an asterisk at (0,0) marking the storm center. The number of cases included in each composite is shown at the top-right of each panel in the top two rows. Contours are shaded every 0.25-K in all panels. Stippling in the bottom row panels indicate where the differences are significant at the 95% confidence level using the Wilcoxon rank sum significance test.

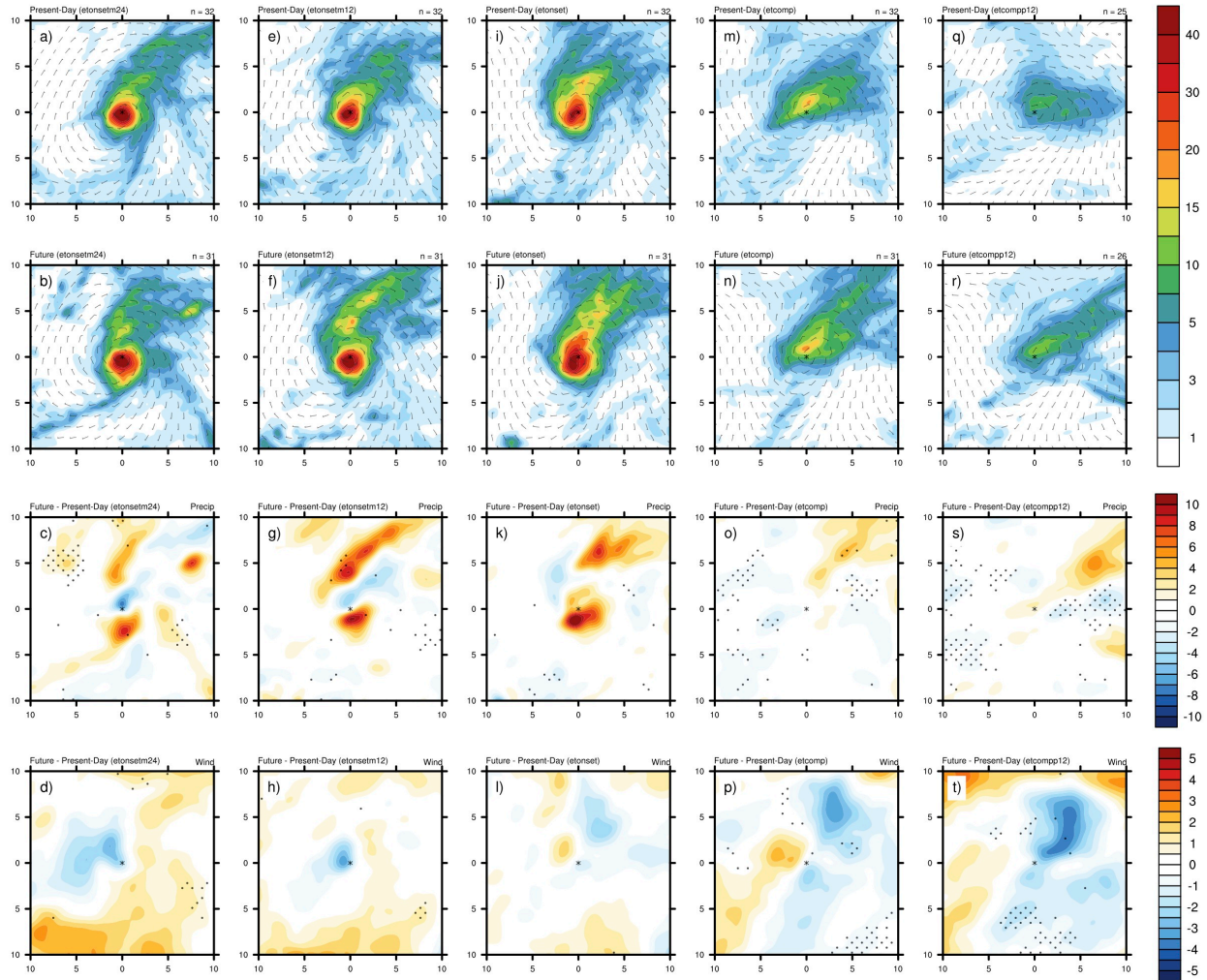


Figure 5.23: 6-hourly precipitation and 10-m winds for present-day vs. future WNP composite ET events at 24-h prior to ET onset, 12-h prior to ET onset, ET onset, ET completion, and 12-h after ET completion. 6-hourly precipitation (mm; shaded) and 10-m winds (ms^{-1} ; vectors) for WNP (top row) present-day, (second row) future, (third row) future minus present-day (precipitation) and (bottom row) future minus present-day (wind speed) composite ET events at (a)–(d) 24-h prior to ET onset, (e)–(h) 12-h prior to ET onset, (i)–(l) time of ET onset, (m)–(p) time of ET completion, and (q)–(t) 12-h after ET completion. Distance from the storm center in degrees are shown on the ordinate and abscissa with an asterisk at (0,0) marking the storm center. The number of cases included in each composite is shown at the top-right of each panel in the top two rows. Contours in the top two rows are shaded every 1-mm from 1-mm to 5-mm, every 2.5-mm from 5-mm to 20-mm, and every 5-mm from 20-mm to 40-mm. Contours in the third row are shaded every 1-mm. Contours in the last row are shaded every 0.5- m s^{-1} in the bottom row. Stippling in the bottom row panels indicate where the differences are significant at the 95% confidence level using the Wilcoxon rank sum significance test.

6. Summary and Conclusions

ET events pose a unique threat to areas such as the northeast US and Western Europe by bringing TC-like weather conditions these regions are typically unaccustomed to. Additionally, the outflow from ET events can modify midlatitude flow, leading to high-impact weather far downstream from the original TC (e.g., e.g., Harr and Dea 2009; Archambault et al. 2013; Archambault et al. 2015; Keller et al. 2018). A considerable amount of prior research has examined TCs in the context of climate change, and the ET process itself, but there remains a gap in the literature regarding climate change effects on ET events. Of the few studies that have examined this question, most have found evidence for an increase in the percentage of NATL TCs undergoing ET due to a more favorable background environment, an eastward and poleward extension of the TC development region, and/or an increase in TC strength (Haarsma et al. 2013; Baatsen et al. 2015; Liu et al. 2017). Furthermore, Jung and Lackmann (2018, in review) found, for the case of Hurricane Irene (2011), reduced vertical wind shear and reduced meridional SST gradients, among other factors, enabled the storm to maintain its tropical characteristics longer, thus increasing the time between ET onset and completion. On the contrary, a case study by Ito et al. (2016) showed that weakened baroclinicity in the WNP created an environment less favorable for ET in the future.

Current GCMs are too coarse to resolve TCs and therefore, ET. Therefore, to further examine how ET may be affected by climate change, we conduct a novel set of model simulations using MPAS in present-day and future thermodynamic environments that is designed to maximize our ability to analyze changes in high-impact weather systems, including ET events. Our use of a global model eliminates the lateral boundary constraints of regional models, while inclusion of high-resolution, analyzed SSTs preserves realistic SST gradients throughout the duration of the simulations. Furthermore, a grid length of 15 km provides an advantage over coarser modeling studies to better represent the atmospheric mesoscale. The future climate simulations employ a technique that combines methods associated with PGW and time-slice experiments; this allows for the inclusion of high-resolution SSTs, plausible future sea ice fields, and seamless simulation of non-consecutive years without excessive spin-up time.

We first evaluate the model climate in regard to present-day large-scale circulations as well as the large-scale responses to warming in our climate change experiments; these aspects must be reasonably represented to justify moving forward in investigating ET or other high-

impact weather phenomena in these simulations. The future simulations replicate two key warming signatures produced by GCMs: Arctic amplification and the warming maximum in the tropical upper-troposphere (Fig. 2.3), indicating an appropriate large-scale response to the imposed warming. MPAS is able to realistically reproduce Northern Hemispheric wintertime midlatitude storm tracks (Fig. 3.1) and annual precipitation patterns over the CONUS (Fig. 3.4a,d,g,j). The dry bias in summertime precipitation over the Great Plains discussed in other modeling studies also appears here (Fig. 3.4i,l), highlighting a need for future research on how to alleviate this bias. Our simulations do suffer from a substantial cold-season wet bias over continental North America (Fig. 3.4h,k). Tropical characteristics, such as precipitation along the ITCZ in the equatorial Pacific, are also well simulated ($r \sim 0.95$), although the ITCZ representation in the Atlantic does not compare as favorably to observations (Fig. 3.2).

Simulated TCs are tracked with the TempestExtremes tracking algorithm (Ullrich and Zarzycki 2017; Zarzycki and Ullrich 2017). TempestExtremes initially tracks candidate TCs as minima in SLP and retains cyclones that meet additional criteria, such as the presence of a warm core (Table 2.3). While MPAS overestimates TC activity in the WNP, TC frequency in other Northern Hemispheric basins is within the range of observations (Fig. 3.6). The largest discrepancy in the simulated spatial distribution of TCs is the lack of TC genesis in the eastern NATL (Fig. 3.7), likely due to a positive bias in vertical wind shear there (Fig. 3.8). Otherwise, TC track density patterns match observations reasonably well ($r \sim 0.7$). Additionally, with the exception of the ENP, the seasonal cycles for the Northern Hemispheric basins are well reproduced (Fig. 3.9). Regarding TC strength, MPAS is able to produce several tropical cyclones of Cat4 strength, as defined by traditional maximum 10-m wind speed thresholds of the Saffir-Simpson scale (Fig. 3.5 and Fig. 3.6b). Categorizing TCs using the minimum SLP thresholds of Roberts et al. (2015), on the other hand, shows simulated TCs across the full intensity spectrum, including Cat_p5 storms (Fig. 3.5 and Fig. 3.6a).

Trajectories from TempestExtremes are continued into the extratropical phase using the ExTraTracks tracking algorithm (Zarzycki et al. 2017), which also computes the CPS parameters over each cyclone's lifetime to identify ET events. The simulated estimates of percentage of TCs undergoing ET in the NATL and WNP basins are well within the observed range of variability (Table 3.1). MPAS does produce more variation in ET location compared to observations (Fig. 3.13a–b), but the median location of ET in both basins matches reasonably well (Table 3.2).

The number of ET events in the NATL increases by ~40% in the future simulations while the fraction of TCs undergoing ET increases ~6% (Table 4.1). Reduced vertical wind shear, warmer SSTs, and lower MPI minimum SLP in the NATL subtropics along with increased overlap of the tropically favorable and baroclinically favorable regions, defined as 960-hPa MPI and Eady growth rate of 0.25 day^{-1} , respectively, creates an environment in the NATL that is more conducive for ET in the future simulations (Fig. 4.1–4.4). Furthermore, a significant poleward shift in the location of TC genesis and peak intensity (Table 4.3; Fig. 4.10) reduces the distance future TCs need to travel in an unfavorable environment while a shift towards stronger warm cores as tropical systems (Fig. 4.14) increases the chance of survival in unfavorable conditions. All of these factors increase the likelihood of ET in the NATL and thus, are consistent with the simulated increase in ET percentage, and with previous work. Similar changes in the background environment occur in the WNP (Fig. 4.1–4.4), but there are not significant shifts towards stronger warm cores (Fig. 4.15) or in the location of TC genesis or peak intensity (Table 4.3; Fig. 4.10), resulting in little change in ET percentage for WNP events (Table 4.1).

Consistent with the shift in TC genesis and peak intensity location (Torres-Vasquez 2018), and a poleward expansion of the tropics, the locations of ET onset and completion in the NATL are also shifted significantly poleward in the future simulations by 4.6° and 5° , respectively (Table 4.2; Fig. 4.9). Additionally, future NATL ET events are shown to be stronger at later stages of the cyclone lifecycle, particularly as post-transition ETCs where the median minimum SLP is ~6-hPa lower (Table 4.6; Fig. 4.12). WNP events, on the other hand, show no significant change in ET location (Table 4.2; Fig. 4.9), and are only significantly more intense as tropical systems where future storms are ~12-hPa stronger (Table 4.6; Fig. 4.12).

Storm-relative composites of a subset of ET events chosen to represent a “traditional” ET synoptic environment featuring a prominent upstream trough and substantial downstream ridge allows us to delve further into potential changes in the storm dynamics and impacts. For NATL events, there are several factors that suggest a slower future ET process, including a shift towards stronger warm cores (Fig. 4.12; Fig. 5.4), stronger and deeper PV towers (Fig. 5.9), warmer underlying SSTs (Fig. 2.2), and environmental conditions supporting continued maintenance of tropical characteristics (Fig. 4.1–4.4). Despite this, no significant changes in the median duration of ET were found (Table 4.4; Table 5.2). This is likely due to a combination of a strengthening

and equatorward shift of the upper-level trough maximum and a poleward shift of the storm center in the times leading up to ET onset (Table 5.3; Fig. 5.6), which both allow for enhanced trough-TC interaction, thus likely speeding up the transition process (Hart et al. 2006; Ritchie and Elsberry 2007). The opposite is true for WNP events in that a slight poleward shift in the upper-level trough at ET onset (Fig. 5.18) could be hindering the trough-TC interaction, thus acting to slow the transition process. As with the NATL, however, no significant change in ET duration was found for WNP events (Table 4.4; Table 5.10).

The upstream trough in the future NATL composite is significantly stronger and more organized at ET completion and post-completion (Fig. 5.6), allowing for continued interaction between the trough and resultant ETC after ET is completed. The closer in proximity the post-transition cyclone is to the upper-level trough axis, the more likely reintensification is to occur (Hart et al. 2006; Ritchie and Elsberry 2007). While both present-day and future NATL events weaken between ET completion and 12 h after completion, they do so at a slower rate in the future; therefore, future events are significantly more intense as post-transition ETCs (Table 5.1; Fig. 5.2). Enhanced θ'_{2-m} and 10-m wind speeds after ET completion (Table 5.6; Table 5.8; Figs. 5.10–5.11) indicate a significantly stronger cyclonic circulation in the future composite, which is consistent with the increased post-transition intensity of NATL ET events in the future (Table 4.6; Table 5.1).

Composites for both NATL and WNP events show a significant enhancement and eastward extension of the downstream ridge in the future simulations (Figs. 5.6–5.7; Figs. 5.18–5.19). Additionally, on the northern edge of the ridge, the wind speed on the dynamic tropopause is stronger (Fig. 5.7; Fig. 5.19), which, along with enhanced LPV in broad areas around the storm center (Fig. 5.8; Fig. 5.20), indicate that future ET events in both basins are accompanied by stronger diabatic outflow. Additionally, 6-hourly precipitation in the future NATL composite increases at all composite times, and does so at a super-Clausius-Clapeyron rate (Table 5.7; Fig. 5.11). While precipitation does, on average, increase in the future WNP composite (Table 5.15), it does so at a sub-Clausius-Clapeyron rate.

To conclude, we have shown that, in our simulations, the *overall process* of ET is largely unchanged in the future simulations: in both basins, the process begins with a distinct tropical system that, over time, interacts with an approaching upper-level trough, and eventually merges completely into the midlatitude flow (Fig. 5.1; Fig. 5.13). However, with a projected future

environment in the NATL that is more conducive to ET, along with a poleward shift in TC genesis, peak tropical intensity, and ET, these systems have a better chance of undergoing ET and reaching the midlatitudes intact. This, combined with a significantly more intense post-transition ETC and strengthened precipitation, near-surface wind speed, and outflow ridge, indicates that ET events in the NATL are likely to pose more severe threats to midlatitude locations in the future, both locally and farther downstream. The WNP events show less significant changes, and therefore, no concrete conclusions can be drawn for that basin. The most drastic difference between the two regions is the significant poleward shift in TC location for NATL events, which does not occur in the WNP, and leads us to believe that this shift is the primary factor influencing the observed change in ET frequency. Future work will examine this hypothesis, and further explore this regional dependency to help diagnose the main mechanisms contributing to future changes in ET. Additionally, investigating the interannual variability in ET changes (e.g., comparing years with the largest changes to years with the smallest changes) will help shed light on the primary factors affecting ET in future climate conditions.

As this study is, to the author's knowledge, one of the first to examine climate change effects on ET, the results presented here provide a substantial contribution to this field of research. It is necessary, though, to further reconcile our results by conducting a physics and/or initial condition ensemble with our current model configuration, and compare with other high-resolution studies before our results can be considered robust. Additionally, we would like to look more closely into potential changes in post-transition reintensification pathways. For example, Baatsen et al. (2015) suggests that enhanced diabatic effects could lead to an increased likelihood of warm seclusion reintensification in the future, which could further increase the severity of impacts associated with ET events.

Beyond TCs and ET described here, we anticipate these simulations, in conjunction with similar efforts, will have great value in projecting and understanding changes in high-impact weather phenomena for which dynamics on sub-synoptic scales are important. Research involving these simulations is currently underway investigating climate change effects on TC seasonality, midlatitude precipitation, and persistent anomalies. Many more aspects of these simulations, however, remain to be explored.

REFERENCES

- Archambault, H. M., L. F. Bosart, D. Keyser, and J. M. Cordeira, 2013: A climatological analysis of the extratropical flow response to recurving western North Pacific tropical cyclones. *Mon. Wea. Rev.*, **141**, 2325–2346, doi:10.1175/MWR-D-12-00257.1.
- Archambault, H. M., D. Keyser, L. F. Bosart, C. A. Davis, and J. M. Cordeira, 2015: A composite perspective of the extratropical flow response to recurving western North Pacific tropical cyclones. *Mon. Wea. Rev.*, **143**, 1122–1141, doi:10.1175/MWR-D-14-00270.1.
- Arnott, J. M., J. L. Evans, and F. Chiaromonte, 2004: Characterization of extratropical transition using cluster analysis. *Mon. Wea. Rev.*, **132**, 2916–2937, doi:10.1175/MWR2836.1.
- Baatsen, M., R. J. Haarsma, A. J. Van Delden, and H. De Vries, 2015: Severe autumn storms in future western Europe with a warmer Atlantic Ocean. *Climate Dyn.*, **45**, 949–964, doi:10.1007/s00382-014-2329-8.
- Bacmeister, J. T., K. A. Reed, C. Hannay, P. Lawrence, S. Bates, J. E. Truesdale, N. Rosenbloom, and M. Levy, 2018: Projected changes in tropical cyclone activity under future warming scenarios using a high-resolution climate model. *Climatic Change*, **146**, 547–560, doi:10.1007/s10584-016-1750-x.
- Bacmeister, J. T., M. F. Wehner, R. B. Neale, A. Gettelman, C. Hannay, P. H. Lauritzen, J. M. Caron, and J. E. Truesdale, 2014: Exploratory high-resolution climate simulations using the Community Atmosphere Model (CAM). *J. Climate*, **27**, 3073–3099, doi:10.1175/JCLI-D-13-00387.1.
- Ban, N., J. Schmidli, and C. Schär, 2014: Evaluation of the convection-resolving regional climate modeling approach in decade-long simulations. *J. Geophys. Res. Atmos.*, **119**, 7889–7907, doi:10.1002/2014JD021478.
- Bell, R., J. Strachan, P. L. Vidale, K. Hodges, and M. Roberts, 2013: Response of tropical cyclones to idealized climate change experiments in a global high-resolution coupled general circulation model. *J. Climate*, **26**, 7966–7980, doi:10.1175/JCLI-D-12-00749.1.

- Bengtsson, L., K. I. Hodges, and N. Keenlyside, 2009: Will extratropical storms intensify in a warmer climate? *J. Climate*, **22**, 2276–2301, doi:10.1175/2008JCLI2678.1.
- Bengtsson, L., K. I. Hodges, and E. Roeckner, 2006: Storm tracks and climate change. *J. Climate*, **19**, 3518–3543, doi:10.1175/JCLI3815.1.
- Bieli, M., S. J. Camargo, A. H. Sobel, J. L. Evans, and T. Hall, 2018: A Global Climatology of Extratropical Transition. *J. Climate*, Submitted.
- Booth, J. F., H. E. Rieder, and Y. Kushnir, 2016: Comparing hurricane and extratropical storm surge for the Mid-Atlantic and Northeast Coast of the United States for 1979–2013. *Environ. Res. Lett.*, **11**, 094004, doi:10.1088/1748-9326/11/9/094004.
- Booth, J. F., L. Thompson, J. Patoux, and K. A. Kelly, 2012: Sensitivity of midlatitude storm intensification to perturbations in the sea surface temperature near the Gulf Stream. *Mon. Wea. Rev.*, **140**, 1241–1256, doi:10.1175/MWR-D-11-00195.1.
- Brayshaw, D. J., B. Hoskins, and M. Blackburn, 2009: The basic ingredients of the North Atlantic storm track. Part I: Land–sea contrast and orography. *J. Atmos. Sci.*, **66**, 2539–2558, doi:10.1175/2009JAS3078.1.
- Brayshaw, D. J., B. Hoskins, and M. Blackburn, 2011: The basic ingredients of the North Atlantic storm track. Part II: Sea surface temperatures. *J. Atmos. Sci.*, **68**, 1784–1805, doi:10.1175/2011JAS3674.1.
- Camargo, S. J., A. W. Robertson, A. G. Barnston, and M. Ghil, 2008: Clustering of eastern North Pacific tropical cyclone tracks: ENSO and MJO effects. *Geochem. Geophys. Geosyst.*, **9**, Q06V05, doi:10.1029/2007GC001861.
- Chang, E. K., and Y. Fu, 2003: Using mean flow change as a proxy to infer interdecadal storm track variability. *J. Climate*, **16**, 2178–2196, doi:10.1175/2773.1.
- Chang, E. K., Y. Guo, and X. Xia, 2012: CMIP5 multimodel ensemble projection of storm track change under global warming. *J. Geophys. Res.*, **117**, D23118, doi:10.1029/2012JD018578.
- Chang, E. K., Y. Guo, X. Xia, and M. Zheng, 2013: Storm-track activity in IPCC AR4/CMIP3 model simulations. *J. Climate*, **26**, 246–260, doi:10.1175/JCLI-D-11-00707.1.

- Chang, E. K., S. Lee, and K. L. Swanson, 2002: Storm track dynamics. *J. Climate*, **15**, 2163–2183, doi:10.1175/1520-0442(2002)015<02163;STD>2.0.CO;2.
- Colle, B. A., J. F. Booth, and E. K. Chang, 2015: A review of historical and future changes of extratropical cyclones and associated impacts along the US East Coast. *Current Climate Change Reports*, **1**, 125–143, doi:10.1007/s40641-015-0013-7.
- Daloz, A. S., and Coauthors, 2015: Cluster analysis of downscaled and explicitly simulated North Atlantic tropical cyclone tracks. *J. Climate*, **28**, 1333–1361, doi:10.1175/JCLI-D-13-00646.1.
- Daly, C., M. Halbleib, J. I. Smith, W. P. Gibson, M. K. Doggett, G. H. Taylor, J. Curtis, and P. P. Pasteris, 2008: Physiographically sensitive mapping of climatological temperature and precipitation across the conterminous United States. *Int. J. Climatology*, **28**, 2031–2064, doi:10.1002/joc.1688.
- Davis, C. A., 2018: Resolving tropical cyclone intensity in models. *Geophys. Res. Lett.*, **45**, 2082–2087, doi:10.1002/2017GL076966.
- de Vries, H., T. Woollings, J. Anstey, R. J. Haarsma, and W. Hazeleger, 2013: Atmospheric blocking and its relation to jet changes in a future climate. *Climate Dyn.*, **41**, 2643–2654, doi:10.1007/s00382-013-1699-7.
- Dee, D. P., and Coauthors, 2011: The ERA-Interim reanalysis: Configuration and performance of the data assimilation system. *Quart. J. Roy. Meteor. Soc.*, **137**, 553–597, doi:10.1002/qj.828.
- Deser, C., J. E. Walsh, and M. S. Timlin, 2000: Arctic sea ice variability in the context of recent atmospheric circulation trends. *J. Climate*, **13**, 617–633, doi:10.1175/1520-0442(2000)013<0617;ASIVIT>2.0.CO;2.
- Di Capua, G., and D. Coumou, 2016: Changes in meandering of the Northern Hemisphere circulation. *Environ. Res. Lett.*, **11**, 094028, doi:10.1088/1748-9326/11/9/094028.
- Donlon, C. J., M. Martin, J. Stark, J. Roberts-Jones, E. Fiedler, and W. Wimmer, 2012: The operational sea surface temperature and sea ice analysis (OSTIA) system. *Remote Sens. Environ.*, **116**, 140–158, doi:10.1016/j.rse.2010.10.017.

- Du, Q., V. Faber, and M. Gunzburger, 1999: Centroidal Voronoi tessellations: Applications and algorithms. *SIAM Rev.*, **41**, 637–676, doi:10.1137/S0036144599352836.
- Emanuel, K. A., 1995: Sensitivity of tropical cyclones to surface exchange coefficients and a revised steady-state model incorporating eye dynamics. *J. Atmos. Sci.*, **52**, 3969–3976, doi:10.1175/1520-0469(1995)052<3969;SOTCTS>2.0.CO;2.
- Evans, C., and Coauthors, 2017: The extratropical transition of tropical cyclones. Part I: Cyclone evolution and direct impacts. *Mon. Wea. Rev.*, **145**, 4317–4344, doi:10.1175/MWR-D-17-0027.1.
- Evans, J. L., and R. E. Hart, 2003: Objective indicators of the life cycle evolution of extratropical transition for Atlantic tropical cyclones. *Mon. Wea. Rev.*, **131**, 909–925, doi:10.1175/1520-0493(2003)131<0909;OIOTLC>2.0.CO;2.
- Frei, C., C. Schär, D. Lüthi, and H. C. Davies, 1998: Heavy precipitation processes in a warmer climate. *Geophys. Res. Lett.*, **25**, 1431–1434, doi:10.1029/98GL51099.
- Frierson, D. M., J. Lu, and G. Chen, 2007: Width of the Hadley cell in simple and comprehensive general circulation models. *Geophys. Res. Lett.*, **34**, L18804, doi:10.1029/2007GL031115.
- Gentry, M. S., and G. M. Lackmann, 2010: Sensitivity of simulated tropical cyclone structure and intensity to horizontal resolution. *Mon. Wea. Rev.*, **138**, 688–704, doi:10.1175/2009MWR2976.1.
- Giorgi, F., C. Jones, and G. R. Asrar, 2009: Addressing climate information needs at the regional level: the CORDEX framework. *World Meteorological Organization (WMO) Bulletin*, **58**, 175–183.
- Haarsma, R. J., W. Hazeleger, C. Severijns, H. Vries, A. Sterl, R. Bintanja, G. J. Oldenborgh, and H. W. Brink, 2013: More hurricanes to hit western Europe due to global warming. *Geophys. Res. Lett.*, **40**, 1783–1788, doi:10.1002/grl.50360.
- Han, J., and H. Pan, 2006: Sensitivity of hurricane intensity forecast to convective momentum transport parameterization. *Mon. Wea. Rev.*, **134**, 664–674, doi:10.1175/MWR3090.1.

- Hara, M., T. Yoshikane, H. Kawase, and F. Kimura, 2008: Estimation of the impact of global warming on snow depth in Japan by the pseudo-global-warming method. *Hydrol. Res. Lett.*, **2**, 61–64, doi:10.3178/HRL.2.61.
- Harr, P. A., and J. M. Dea, 2009: Downstream development associated with the extratropical transition of tropical cyclones over the western North Pacific. *Mon. Wea. Rev.*, **137**, 1295–1319, doi:10.1175/2008MWR2558.1.
- Harr, P. A., and R. L. Elsberry, 2000: Extratropical transition of tropical cyclones over the western North Pacific. Part I: Evolution of structural characteristics during the transition process. *Mon. Wea. Rev.*, **128**, 2613–2633, doi:10.1175/1520-0493(2000)128<2613;ETOTCO>2.0.CO;2.
- Hart, R. E., 2003: A cyclone phase space derived from thermal wind and thermal asymmetry. *Mon. Wea. Rev.*, **131**, 585–616, doi:10.1175/1520-0493(2003)131<0585;ACPSDF>2.0.CO;2.
- Hart, R. E., and J. L. Evans, 2001: A climatology of the extratropical transition of Atlantic tropical cyclones. *J. Climate*, **14**, 546–564, doi:10.1175/1520-0442(2001)014<0546;ACOTET>2.0.CO;2.
- Hart, R. E., J. L. Evans, and C. Evans, 2006: Synoptic composites of the extratropical transition life cycle of North Atlantic tropical cyclones: Factors determining posttransition evolution. *Mon. Wea. Rev.*, **134**, 553–578, doi:10.1175/MWR3082.1.
- He, J., and B. J. Soden, 2016: The impact of SST biases on projections of anthropogenic climate change: A greater role for atmosphere-only models? *Geophys. Res. Lett.*, **43**, 7745–7750, doi:10.1002/2016GL069803.
- Hill, K. A., 2010: *Climate and Tropical Cyclones*, North Carolina State University, 217pp.
- Hill, K. A., and G. M. Lackmann, 2011: The impact of future climate change on TC intensity and structure: A downscaling approach. *J. Climate*, **24**, 4644–4661, doi:10.1175/2011JCLI3761.1.

- Hogan, T. F., and R. L. Pauley, 2007: The impact of convective momentum transport on tropical cyclone track forecasts using the Emanuel cumulus parameterization. *Mon. Wea. Rev.*, **135**, 1195–1207, doi:10.1175/MWR3365.1.
- Huffman, G. J., and Coauthors, 2007: The TRMM multisatellite precipitation analysis (TMPA): Quasi-global, multiyear, combined-sensor precipitation estimates at fine scales. *J. Hydrometeor.*, **8**, 38–55, doi:10.1175/JHM560.1.
- IPCC, 2013: Climate Change 2013: The Physical Science Basis. Contribution of Working Group I to the Fifth Assessment Report of the Intergovernmental Panel on Climate Change [Stocker, T.F., D. Qin, G.-K. Plattner, M. Tignor, S.K. Allen, J. Boschung, A. Nauels, Y. Xia, V. Bex and P.M. Midgley (eds.)]. Cambridge University Press, Cambridge, United Kingdom and New York, NY, USA, 1535 pp.
- IPCC, 2014: Climate Change 2014: Synthesis Report. Contribution of Working Groups I, II and III to the Fifth Assessment Report of the Intergovernmental Panel on Climate Change [Core Writing Team, R.K. Pachauri and L.A. Meyer (eds.)]. IPCC, Geneva, Switzerland, 151 pp.
- Ito, R., T. Takemi, and O. Arakawa, 2016: A possible reduction in the severity of typhoon wind in the northern part of Japan under global warming: A case study. *SOLA*, **12**, 100–105, doi:10.2151/sola.2016-023.
- Jones, S. C., and Coauthors, 2003: The extratropical transition of tropical cyclones: Forecast challenges, current understanding, and future directions. *Wea. Forecasting*, **18**, 1052–1092, doi:10.1175/1520-0434(2003)018<1052:TETOTC>2.0.CO;2.
- Jung, C., G. M. Lackmann, 2018: Extratropical Transition of Hurricane Irene (2011) in a Changing Climate. *J. Climate*, in review.
- Kang, S. M., J. Lu, 2012: Expansion of the Hadley cell under global warming: Winter versus summer. *J. Climate*, **25**, 8387–8393, doi:10.1175/JCLI-D-12-00323.1.
- Keller, J. H., and Coauthors, 2018: The Extratropical Transition of Tropical Cyclones Part II: Interaction with the midlatitude flow, downstream impacts, and implications for predictability. *Mon. Weather Rev.*, doi:10.1175/MWR-D-17-0329.1.

- Kim, D., J. Kug, I. Kang, F. Jin, and A. T. Wittenberg, 2008: Tropical Pacific impacts of convective momentum transport in the SNU coupled GCM. *Climate Dyn.*, **31**, 213–226, doi:10.1007/s00382-007-0348-4.
- Kimura, F., and A. Kitoh, 2007: Downscaling by pseudo global warming method. *The Final Report of ICCAP*, **4346**, doi:10.3178/hrl.2.61.
- Kirtman, B. P., and Coauthors, 2012: Impact of ocean model resolution on CCSM climate simulations. *Climate Dyn.*, **39**, 1303–1328, doi:10.1007/s00382-012-1500-3.
- Kitabatake, N., 2011: Climatology of extratropical transition of tropical cyclones in the western North Pacific defined by using cyclone phase space. *J. Meteor. Soc. Japan*, **89**, 309–325, doi:10.2151/jmsj.2011-402.
- Klein, P. M., P. A. Harr, and R. L. Elsberry, 2000: Extratropical transition of western North Pacific tropical cyclones: An overview and conceptual model of the transformation stage. *Wea. Forecasting*, **15**, 373–395, doi:10.1175/1520-0434(2000)015<0373;ETOWNP>2.0.CO;2.
- Klein, P. M., P. A. Harr, and R. L. Elsberry, 2002: Extratropical transition of western North Pacific tropical cyclones: Midlatitude and tropical cyclone contributions to reintensification. *Mon. Wea. Rev.*, **130**, 2240–2259, doi:10.1175/1520-0493(2002)130<2240;ETOWNP>2.0.CO;2.
- Klein, S. A., X. Jiang, J. Boyle, S. Malyshev, and S. Xie, 2006: Diagnosis of the summertime warm and dry bias over the US Southern Great Plains in the GFDL climate model using a weather forecasting approach. *Geophys. Res. Lett.*, **33**, L18805, doi:10.1029/2006GL027567.
- Knapp, K. R., M. C. Kruk, D. H. Levinson, H. J. Diamond, and C. J. Neumann, 2010: The international best track archive for climate stewardship (IBTrACS) unifying tropical cyclone data. *Bull. Amer. Meteor. Soc.*, **91**, 363–376, doi:10.1175/2009BAMS2755.1.
- Knutson, T. R., and R. E. Tuleya, 1999: Increased hurricane intensities with CO₂-induced warming as simulated using the GFDL hurricane prediction system. *Climate Dyn.*, **15**, 503–519, doi:10.1007/s003820050296.

- Knutson, T. R., and Coauthors, 2010: Tropical cyclones and climate change. *Nat. Geosci.*, **3**, 157–163, doi:10.1038/ngeo779.
- Knutson, T. R., and R. E. Tuleya, 2004: Impact of CO₂-induced warming on simulated hurricane intensity and precipitation: Sensitivity to the choice of climate model and convective parameterization. *J. Clim.*, **17**, 3477–3495, doi:10.1175/1520-0442(2004)017<3477;IOCWOS>2.0.CO;2.
- Kofron, D. E., E. A. Ritchie, and J. S. Tyo, 2010a: Determination of a consistent time for the extratropical transition of tropical cyclones. Part I: Examination of existing methods for finding “ET time”. *Mon. Wea. Rev.*, **138**, 4328–4343, doi:10.1175/2010MWR3180.1.
- Kofron, D. E., E. A. Ritchie, and J. S. Tyo, 2010b: Determination of a consistent time for the extratropical transition of tropical cyclones. Part II: Potential vorticity metrics. *Mon. Wea. Rev.*, **138**, 4344–4361, doi:10.1175/2010MWR3181.1.
- Kossin, J. P., S. J. Camargo, and M. Sitkowski, 2010: Climate modulation of North Atlantic hurricane tracks. *J. Climate*, **23**, 3057–3076, doi:10.1175/2010JCLI3497.1.
- Kossin, J. P., K. A. Emanuel, and G. A. Vecchi, 2014: The poleward migration of the location of tropical cyclone maximum intensity. *Nature*, **509**, 349–352, doi:10.1038/nature13278.
- Kossin, J. P., T. L. Olander, and K. R. Knapp, 2013: Trend analysis with a new global record of tropical cyclone intensity. *J. Climate*, **26**, 9960–9976, doi:10.1175/JCLI-D-13-00262.1.
- Lackmann, G. M., 2013: The south-central US flood of May 2010: Present and future. *J. Climate*, **26**, 4688–4709, doi:10.1175/JCLI-D-12-00392.1.
- Lackmann, G. M., 2015: Hurricane Sandy before 1900 and after 2100. *Bull. Amer. Meteor. Soc.*, **96**, 547–560, doi:10.1175/BAMS-D-14-00123.1.
- Lee, M., S. D. Schubert, M. J. Suarez, J. E. Schemm, H. Pan, J. Han, and S. Yoo, 2008: Role of convection triggers in the simulation of the diurnal cycle of precipitation over the United States Great Plains in a general circulation model. *J. Geophys. Res. Atmos.*, **113**, D02111, doi:10.1029/2007JD008984.

- Liu, C., and Coauthors, 2017: Continental-scale convection-permitting modeling of the current and future climate of North America. *Climate Dyn.*, **49**, 71–95, doi:10.1007/s00382-016-3327-9.
- Liu, M., G. A. Vecchi, J. A. Smith, and H. Murakami, 2017: The present-day simulation and twenty-first-century projection of the climatology of extratropical transition in the North Atlantic. *J. Climate*, **30**, 2739–2756, doi:10.1175/JCLI-D-16-0352.1.
- Lu, J., G. A. Vecchi, and T. Reichler, 2007: Expansion of the Hadley cell under global warming. *Geophys. Res. Lett.*, **34**, L06805, doi:10.1029/2006GL028443.
- Mallard, M. S., G. M. Lackmann, and A. Aiyyer, 2013: Atlantic hurricanes and climate change. Part II: Role of thermodynamic changes in decreased hurricane frequency. *J. Climate*, **26**, 8513–8528, doi:10.1175/JCLI-D-12-00183.1.
- Mallard, M. S., G. M. Lackmann, A. Aiyyer, and K. Hill, 2013: Atlantic hurricanes and climate change. Part I: Experimental design and isolation of thermodynamic effects. *J. Climate*, **26**, 4876–4893, doi:10.1175/JCLI-D-12-00182.1.
- Malmquist, D. L., 1999: Meteorologists and insurers explore extratropical transition of tropical cyclones. *Eos Trans. Amer. Geophys. Union*, **80**, 79–80, doi:10.1029/99EO00055.
- Marciano, C. G., 2014: Climate Change and Wintertime East Coast Cyclones, North Carolina State University, 167pp.
- Maue, R. N., 2010: Warm Seclusion Extratropical Cyclones, The Florida State University.
- McTaggart-Cowan, R., J. R. Gyakum, and M. K. Yau, 2003: The influence of the downstream state on extratropical transition: Hurricane Earl (1998) case study. *Mon. Wea. Rev.*, **131**, 1910–1929.
- McTaggart-Cowan, R., J. R. Gyakum, and M. K. Yau, 2004: The impact of tropical remnants on extratropical cyclogenesis: Case study of Hurricanes Danielle and Earl (1998). *Mon. Wea. Rev.*, **132**, 1933–1951, doi:10.1175/1520-0493(2004)132<1933;TIOTRO>2.0.CO;2.

- Meinshausen, M., and Coauthors, 2011: The RCP greenhouse gas concentrations and their extensions from 1765 to 2300. *Climatic Change*, **109**, 213–241, doi:10.1007/s10584-011-0156-z.
- Michaelis, A. C., G. M. Lackmann, and W. A. Robinson, 2018: High-Resolution Climate Change Simulations for Analysis of High-Impact Weather using the Model for Prediction Across Scales (MPAS). *Geo. Sci. Model Dev.*, submitted.
- Mizielinski, M. S., and Coauthors, 2014: High resolution global climate modelling; the UPSCALE project, a large simulation campaign. *Geosci. Model Dev.*, **7**, 1629–1640, doi:10.5194/gmd-7-1629-2014.
- Overland, J. E., and M. Wang, 2010: Large-scale atmospheric circulation changes are associated with the recent loss of Arctic sea ice. *Tellus*, **62**, 1–9, doi:10.1111/j.1600-0870.2009.00421.x.
- Park, S., J. B. Klemp, and W. C. Skamarock, 2014: A comparison of mesh refinement in the global MPAS-A and WRF models using an idealized normal-mode baroclinic wave simulation. *Mon. Wea. Rev.*, **142**, 3614–3634, doi:10.1175/MWR-D-14-00004.1.
- Petterssen, S., and S. J. Smebye, 1971: On the development of extratropical cyclones. *Quart. J. Roy. Meteor. Soc.*, **97**, 457–482, doi:10.1002/qj.49709741407.
- Plant, R. S., G. C. Craig, and S. L. Gray, 2003: On a threefold classification of extratropical cyclogenesis. *Quart. J. Roy. Meteor. Soc.*, **129**, 2989–3012, doi:10.1256/qj.02.174.
- Prein, A. F., and Coauthors, 2015: A review on regional convection-permitting climate modeling: Demonstrations, prospects, and challenges. *Rev. Geophys.*, **53**, 323–361, doi:10.1002/2014RG000475.
- Previdi, M., and B. G. Liepert, 2007: Annular modes and Hadley cell expansion under global warming. *Geophys. Res. Lett.*, **34**, L22701, doi:10.1029/2007GL031243.
- Rasmussen, R., and Coauthors, 2011: High-resolution coupled climate runoff simulations of seasonal snowfall over Colorado: A process study of current and warmer climate. *J. Climate*, **24**, 3015–3048, doi:10.1175/2010JCLI3985.1.

- Richter, J. H., and P. J. Rasch, 2008: Effects of convective momentum transport on the atmospheric circulation in the Community Atmosphere Model, version 3. *J. Climate*, **21**, 1487–1499, doi:10.1175/2007JCLI1789.1.
- Ritchie, E. A., and R. L. Elsberry, 2003: Simulations of the extratropical transition of tropical cyclones: Contributions by the midlatitude upper-level trough to reintensification. *Mon. Wea. Rev.*, **131**, 2112–2128, doi:10.1175/1520-0493(2003)131<2112;SOTETO>2.0.CO;2.
- Ritchie, E. A., and R. L. Elsberry, 2007: Simulations of the extratropical transition of tropical cyclones: Phasing between the upper-level trough and tropical cyclones. *Mon. Wea. Rev.*, **135**, 862–876, doi:10.1175/MWR3303.1.
- Roberts, M. J., and Coauthors, 2015: Tropical cyclones in the UPSCALE ensemble of high resolution global climate models. *J. Climate*, **28**, 574–596, doi:10.1175/JCLI-D-14-00131.1.
- Schade, L. R., and K. A. Emanuel, 1999: The ocean's effect on the intensity of tropical cyclones: Results from a simple coupled atmosphere–ocean model. *J. Atmos. Sci.*, **56**, 642–651, doi:10.1175/1520-0469(1999)056<0642;TOSEOT>2.0.CO;2.
- Schär, C., C. Frei, D. Lüthi, and H. C. Davies, 1996: Surrogate climate–change scenarios for regional climate models. *Geophys. Res. Lett.*, **23**, 669–672, doi:10.1029/96GL00265.
- Screen, J. A., and I. Simmonds, 2013: Exploring links between Arctic amplification and mid latitude weather. *Geophys. Res. Lett.*, **40**, 959–964, doi:10.1002/grl.50174.
- Shen, W., R. E. Tuleya, and I. Ginis, 2000: A sensitivity study of the thermodynamic environment on GFDL model hurricane intensity: Implications for global warming. *J. Clim.*, **13**, 109–121, doi:10.1175/1520-0442(2000)013<0109;ASSOTT>2.0.CO;2.
- Shepherd, T. G., 2016: A common framework for approaches to extreme event attribution. *Curr. Climate Change Rep.*, **2**, 28–38, doi:10.1007/s40641-016-0033-y.
- Sherwood, S., and Q. Fu, 2014: A drier future? *Science*, **343**, 737–739, doi:10.1126/science.1247620.

- Simpson, I. R., T. A. Shaw, and R. Seager, 2014: A diagnosis of the seasonally and longitudinally varying midlatitude circulation response to global warming. *J. Atmos. Sci.*, **71**, 2489–2515, doi:10.1175/JAS-D-13-0325.1.
- Siqueira, L., and B. P. Kirtman, 2016: Atlantic near-term climate variability and the role of a resolved Gulf Stream. *Geophys. Res. Lett.*, **43**, 3964–3972, doi:10.1002/2016GL068694.
- Skamarock, W. C., and Coauthors, 2008: A description of the advanced research WRF Version 3. *NCAR Tech. Note NCAR/TN-4751STR*, , 113 pp., doi:10.5065/D68S4MVH.
- Skamarock, W. C., J. B. Klemp, M. G. Duda, L. D. Fowler, S. Park, and T. D. Ringler, 2012: A multiscale nonhydrostatic atmospheric model using centroidal Voronoi tessellations and C-grid staggering. *Mon. Wea. Rev.*, **140**, 3090–3105, doi:10.1175/MWR-D-11-00215.1.
- Small, R. J., and Coauthors, 2014: A new synoptic scale resolving global climate simulation using the Community Earth System Model. *J. Adv. Model. Earth Sys.*, **6**, 1065–1094, doi:10.1002/2014MS000363.
- Strachan, J., P. L. Vidale, K. Hodges, M. Roberts, and M. Demory, 2013: Investigating global tropical cyclone activity with a hierarchy of AGCMs: The role of model resolution. *J. Climate*, **26**, 133–152, doi:10.1175/JCLI-D-12-00012.1.
- Studholme, J., K. I. Hodges, and C. M. Brierley, 2015: Objective determination of the extratropical transition of tropical cyclones in the Northern Hemisphere. *Tellus*, **67**, 24474, doi:10.3402/tellusa.v67.24474.
- Torres-Vasquez, A. P., 2018: Evaluating the effects of a warming climate on the spatiotemporal characteristics of tropical cyclones, North Carolina State University, 134pp.
- Trapp, R. J., and K. A. Hoogewind, 2016: The realization of extreme tornadic storm events under future anthropogenic climate change. *J. Climate*, **29**, 5251–5265, doi:10.1175/JCLI-D-15-0623.1.
- Trenberth, K. E., J. T. Fasullo, and T. G. Shepherd, 2015: Attribution of climate extreme events. *Nat. Climate Change*, **5**, 725, doi:10.1038/NCLIMATE2657.

- Ullrich, P. A., and C. M. Zarzycki, 2017: TempestExtremes: a framework for scale-insensitive pointwise feature tracking on unstructured grids. *Geosci. Model Dev.*, **10**, 1069–1090, doi:10.5194/gmd-10-1069-2017.
- Vecchi, G. A., and B. J. Soden, 2007: Increased tropical Atlantic wind shear in model projections of global warming. *Geophys. Res. Lett.*, **34**, L08702, doi:10.1029/2006GL028905.
- Walsh, K. J., and Coauthors, 2016: Tropical cyclones and climate change. *WIREs Climate Change*, **7**, 65–89, doi:10.1002/wcc.371.
- Wang, Y., L. R. Leung, J. L. McGregor, D. Lee, W. Wang, Y. Ding, and F. Kimura, 2004: Regional climate modeling: progress, challenges, and prospects. *J. Meteor. Soc. Japan*, **82**, 1599–1628, doi:10.2151/jmsj.82.1599.
- Willison, J., W. A. Robinson, and G. M. Lackmann, 2013: The importance of resolving mesoscale latent heating in the North Atlantic storm track. *J. Atmos. Sci.*, **70**, 2234–2250, doi:10.1175/JAS-D-12-0226.1.
- Willison, J., W. A. Robinson, and G. M. Lackmann, 2015: North Atlantic storm-track sensitivity to warming increases with model resolution. *J. Climate*, **28**, 4513–4524, doi:10.1175/JCLI-D-14-00715.1.
- Wood, K. M., and E. A. Ritchie, 2014: A 40-year climatology of extratropical transition in the eastern North Pacific. *J. Climate*, **27**, 5999–6015.
- Woollings, T., 2010: Dynamical influences on European climate: an uncertain future. *Philos. Trans. R. Soc., A*, **368**, 3733–3756, doi:10.1098/rsta.2010.0040.
- Yin, J. H., 2005: A consistent poleward shift of the storm tracks in simulations of 21st century climate. *Geophys. Res. Lett.*, **32**, L18701.
- Zarzycki, C. M., D. R. Thatcher, and C. Jablonowski, 2017: Objective tropical cyclone extratropical transition detection in high-resolution reanalysis and climate model data. *J. Adv. Model. Earth Sys.*, **9**, 130–148, doi:10.1002/2016MS000775.
- Zarzycki, C. M., and P. A. Ullrich, 2017: Assessing sensitivities in algorithmic detection of tropical cyclones in climate data. *Geophys. Res. Lett.*, **44**, 1141–1149, doi:10.1002/2016GL071606.

Zhang, G. J., and H. Wang, 2006: Toward mitigating the double ITCZ problem in NCAR CCSM3. *Geophys. Res. Lett.*, **33**, L06709, doi:10.1029/2005GL025229.

Zhang, G. J., and N. A. McFarlane, 1995: Role of convective scale momentum transport in climate simulation. *J. Geophys. Res. Atmos.*, **100**, 1417–1426, doi:10.1029/94JD02519.

Zhao, M., and I. M. Held, 2012: TC-permitting GCM simulations of hurricane frequency response to sea surface temperature anomalies projected for the late-twenty-first century. *J. Climate*, **25**, 2995–3009, doi:10.1175/JCLI-D-11-00313.1.